



**HAL**  
open science

# Laminar-to-turbulent transition in supersonic boundary layer : different scenarios and possible control

Sushank Sharma

► **To cite this version:**

Sushank Sharma. Laminar-to-turbulent transition in supersonic boundary layer : different scenarios and possible control. Fluids mechanics [physics.class-ph]. Normandie Université, 2019. English. NNT : 2019NORMIR16 . tel-02924479

**HAL Id: tel-02924479**

**<https://theses.hal.science/tel-02924479>**

Submitted on 28 Aug 2020

**HAL** is a multi-disciplinary open access archive for the deposit and dissemination of scientific research documents, whether they are published or not. The documents may come from teaching and research institutions in France or abroad, or from public or private research centers.

L'archive ouverte pluridisciplinaire **HAL**, est destinée au dépôt et à la diffusion de documents scientifiques de niveau recherche, publiés ou non, émanant des établissements d'enseignement et de recherche français ou étrangers, des laboratoires publics ou privés.



Normandie Université

## THÈSE

Pour obtenir le titre de  
Docteur

Spécialité : *Mécanique des fluides*

Préparée au sein de l'Institut National des Sciences Appliquées (INSA) de Rouen,  
Normandie, France

# Transition laminaire turbulent dans les couches limites supersoniques : Différents scénarios et contrôle possible

Présentée et soutenue par  
Sushank SHARMA

Thèse soutenue publiquement le 17 Oct. 2019  
devant le jury composé de

Marc BUFFAT	Professeur, Université Claude Bernard, Lyon, France	Rapporteur
Francesco GRASSO	Professeur, CNAM, Paris, France	Rapporteur
Françoise BATAILLE	Professeure, Université de Perpignan, France	Examineur
Antoine DUCOIN	Maître de Conférences, École Centrale de Nantes, France	Examineur
Dany VANDROMME	Professeur Émérite, INSA de Rouen, France	Examineur
Mostafa S. SHADLOO	Maître de Conférences, INSA de Rouen, France	Co-encadrant
Abdellah HADJADJ	Professeur, INSA de Rouen, France	Directeur de thèse

Thèse dirigée par Prof. Abdellah HADJADJ  
Co-encadrée par Dr. Mostafa Safdari SHADLOO  
Département TASC, Laboratoire CORIA UMR – 6614, CNRS







Normandie Université

## DISSERTATION

submitted in the partial fulfillment for the award of  
Doctor of Philosophy

Specialized in : *Fluid Mechanics*

For the work performed at the National Institute of Applied Sciences (INSA) of  
Rouen, Normandy, France

# Laminar-to-turbulent transition in supersonic boundary layer: Different scenarios and possible control

Presented and defended by  
**Sushank SHARMA**

Thesis defended publicly on the 17th Oct. 2019  
in front of the jury comprising of

Marc BUFFAT	Professor, Claude Bernard University, Lyon, France	Reporter
Francesco GRASSO	Professor, CNAM, Paris, France	Reporter
Françoise BATAILLE	Professor, University of Perpignan, France	Examiner
Antoine DUCOIN	Assistant professor, École Centrale de Nantes, France	Examiner
Dany VANDROMME	Professor Emeritus, INSA de Rouen, France	Examiner
Mostafa S. SHADLOO	Assistant professor, INSA de Rouen, France	Co-supervisor
Abdellah HADJADJ	Professor, INSA de Rouen, France	Thesis Director

Supervised by Prof. Abdellah HADJADJ

Co-supervised by Dr. Mostafa Safdari SHADLOO

TASC Department, CORIA laboratory UMR – 6614, CNRS





# Acknowledgements

---

First and foremost, I would like to express my gratitude towards my esteemed supervisors Prof. Abdellah HADJADJ and Dr. Mostafa S. SHADLOO for providing me the opportunity to work on this deeply interesting topic of compressible boundary layer transition. Their sense of direction and guidance kept me motivated throughout the course of my research work. They helped me learn the basic and advanced concepts related to the compressible flows. I would also like to massively thank Dr.-Ing. Markus J. Kloker at Institute of Aerodynamics and Gas-dynamics (IAG), University of Stuttgart for proving me with the necessary knowledge related to compressible transition and hosting me for a three months research stay under his supervision. His pushing support provided a good sense of direction to my research work. I am also grateful to the reviewers of my thesis namely, Prof. Marc BUF-FAT and Prof. Francesco GRASSO, and also the jury members Dr. Françoise BATAILLE, Dr. Antoine DUCOIN and Prof. Dany VANDROMME for investing their valuable time in evaluating this manuscript.

I would like to acknowledge the access to French HPC resources provided by the French regional computing center of Normandy CRIANN (1998022 and 2017002) and IDRIS (2017-100752, by GENCI (Grand Equipment National de Calcul Intensif) - A0022A10103). The funding resources are provided by European projects FEDER and NEPTUNE 1. The funding resources provided by DAAD (German Academic Exchange Service) for the fruitful three-months research stay at IAG, University of Stuttgart, program ID. 57381332 (personal reference no. 91708728), hosted by Dr. Kloker are deeply appreciated. Moreover, I would also like to thank Dr. Johan LARSSON and Prof. James WALLACE for hosting me during the J. M. Burgers summer school at University of Maryland, United States of America.

Furthermore, I would also like to extend my thanks to the former PhD/postdocs of our group i.e. Dr. Vineet SONI, Dr. Arthur PIQUET and Dr. Minh-Quan NGUYEN for their precious support and fruitful discussions. Dr. Soni helped me a lot to familiarize the structure of our solver which definitely sped-up the progress of the work, so thanks a lot for always being there to help like 911. I am thankful to my lab buddies Margio, Nassim and Boubakr with whom I started this journey of PhD. And, also Ms. Fatemeh who joined us later on. Special thanks to Dr. Michael GAUDING and Mr. Yacine BRAHAMI for all the thought provoking tea-time discussions. Furthermore, I am extremely thankful to my friends - Dr. Irfan, Dr. Mukesh, Jigyasa, Dr. Deewakar, Biraj, Gareema, Megha, Haasanthi, Shalini, Saksham and Jay with whom I have cherished my time in Rouen.

Finally, I could not thank enough to my lovely parents; Prof. Rajnesh K. Sharma and Dr. Manju B. Sharma for bearing with me through the highs and lows of this journey. They are an endless source of motivation, encouragement, and support. They endured me throughout my life and also during this journey being my backbone, and made the things worthwhile.

# Abstract

---

## *English*

Direct numerical simulations (DNS) of both adiabatic and isothermal (heated and cooled) supersonic boundary layers are performed. Two different transition scenarios, namely the Oblique-type breakdown and the By-pass transition are presented in detail. For the oblique-type transition scenario, the results show that the control modes with four to five times the fundamental wavenumber are beneficial for controlling the transition. In the first region, after the control-mode forcing, the beneficial mean-flow distortion (MFD) generated by inducing the control mode is solely responsible for hampering the growth of the fundamental-mode. Globally, the MFD and the three-dimensional part of the control contribute equally towards controlling the oblique breakdown. Effects of physical parameters like wall-temperature, perturbation intensity and baseflow are investigated for the By-pass transition. The results regarding the by-pass scenario reveal that increasing the perturbation intensity moves the transition onset upstream and also increases the length of the transition region. Additionally, below 1% perturbation levels, wall-cooling stabilizes the flow while inverse happens at higher values. The existence of the thermo-mechanical non-equilibrium advances the onset of transition for the heated cases while the cooled wall behaves in the opposite sense. The analyses of the turbulent boundary layer show that the thermal factors influence the topology and inclination of the vortical structures. Moreover, regarding the heat flux, different transfer process is dominant in the near-wall region for the cooled wall.

## *Français*

Les simulations numériques directes (DNS) des couches limites supersoniques adiabatiques et isothermes (chauffées et refroidies) sont effectuées. Deux différents scénarios de transition, à savoir la décomposition de type oblique et la transition de type 'by-pass', sont présentés en détail. Pour le scénario de transition de type oblique, les résultats montrent que les modes contrôlés avec un nombre d'onde quatre à cinq fois supérieur au nombre fondamental se révèlent être bénéfiques pour contrôler la transition. Dans la première région après le forçage du mode de contrôle, la distorsion de flux moyenne (MFD) bénéfique générée en induisant le mode de contrôle est uniquement responsable de l'entrave à la croissance du mode fondamental. Globalement, le MFD et la partie tri-dimensionnelle du contrôle contribuent également à contrôler la rupture oblique. Les effets de paramètres physiques tels que la température de paroi, l'intensité de la perturbation et le 'baseflow' sont étudiés pour la transition de 'By-pass'. Les résultats concernant le scénario de by-pass révèlent que l'augmentation de l'intensité de la perturbation déplace le début de la transition en amont et augmente également la longueur de la région de transition. De plus, en dessous de 1 % des niveaux de perturbation, le refroidissement de la paroi stabilise le flux, tandis que l'inverse se produit à des valeurs plus élevées. L'existence d'un non-équilibre thermo-mécanique avance le début de la transition pour les cas chauffés alors que la paroi refroidie se comporte dans le sens opposé. Les analyses de la couche limite turbulente montrent que les facteurs thermiques influencent la topologie et l'inclinaison des structures tourbillonnaires. De plus, en ce qui concerne le flux de chaleur, un processus de transfert différent est dominant dans la région proche paroi pour la paroi refroidie.

# Contents

---

<b>List of Symbols and Abbreviations</b>	<b>v</b>
<b>List of Figures</b>	<b>viii</b>
<b>List of Tables</b>	<b>x</b>
<b>List of Algorithms</b>	<b>xi</b>
<b>List of Publications</b>	<b>xii</b>
<b>Sommaire</b>	<b>xiii</b>
0.1 Contexte: projet Neptune . . . . .	xiii
0.2 Motivation . . . . .	xiii
0.3 Portée de la recherche . . . . .	xiv
0.4 Contenu de la thèse . . . . .	xiv
0.5 Conclusions . . . . .	xvi
0.6 Perspectives . . . . .	xx
<b>1 Introduction</b>	<b>1</b>
1.1 Context: Neptune project . . . . .	1
1.2 Motivation . . . . .	1
1.3 Basic notions regarding the boundary layer . . . . .	2
1.3.1 Thermal boundary layer . . . . .	3
1.4 Transition . . . . .	4
1.4.1 Transition in pipe flows . . . . .	5
1.4.2 Transition over a curved wall . . . . .	5
1.5 Transition over a flat plate . . . . .	8
1.5.1 Incompressible transitional boundary layers . . . . .	8
1.5.2 Classical breakdown scenarios . . . . .	10
1.5.3 Compressible transitional boundary layers . . . . .	15
1.5.4 Global linear stability analysis . . . . .	21
1.5.5 Effect of wall-heat transfer . . . . .	21
1.6 Transition control techniques: A general overview . . . . .	23
1.6.1 Controlling oblique-type transition . . . . .	24
1.7 Turbulent boundary layer . . . . .	25
1.8 Scope of the present study . . . . .	28
1.9 Outline of the dissertation . . . . .	29

<b>2 Numerical methodology and validation</b>	<b>31</b>
2.1 Governing equations . . . . .	31
2.2 Numerical solver . . . . .	32
2.3 Treatment of the convective flux . . . . .	32
2.3.1 WENO scheme . . . . .	32
2.3.2 Conservative skew-symmetric central scheme . . . . .	34
2.3.3 Hybrid scheme . . . . .	37
2.4 Treatment of the viscous terms . . . . .	38
2.5 Time-stepping . . . . .	39
2.6 Boundary conditions . . . . .	39
2.7 Validation . . . . .	40
2.7.1 Simulation setup . . . . .	41
2.7.2 Simulating the baseflow . . . . .	42
2.7.3 Oblique type transition . . . . .	43
<b>3 Control of the oblique-type breakdown</b>	<b>47</b>
3.1 Introduction . . . . .	47
3.2 Calculating the contribution of the MFD . . . . .	67
3.3 Evolution of the induced streak amplitude . . . . .	69
<b>4 Factors influencing the by-pass transition</b>	<b>70</b>
<b>5 Effects of the baseflow variation on the onset of the transition</b>	<b>92</b>
<b>6 Implications of the wall temperature on the turbulent flow topology</b>	<b>106</b>
<b>7 Conclusions and perspectives</b>	<b>126</b>
7.1 Conclusions . . . . .	126
7.2 Perspectives . . . . .	129
<b>Bibliography</b>	<b>131</b>

# List of Symbols and Abbreviations

---

## English symbols

$\hat{u}_{st}$	Streak amplitude
$d$	Tuning weights
$E^*$	Energy (J)
$f(u)$	Characteristic flux
$f_0^*$	Fundamental frequency (Hz)
$f_x$	Numerical flux
$G$	Görtler number
$h$	Multiple of fundamental frequency
$H_s$	Shape factor
$k$	Multiple of fundamental spanwise wavenumber
$M$	Mach number
$p^*$	Pressure (Pa)
$Pr$	Prandtl number
$q^*$	Heat flux ( $W/m^2$ )
$R^*$	Gas constant ( $J/Kkg^{-1}$ )
$Re_x$	Reynolds number at a distance $x^*$ (in m) from the leading edge
$Ri^*$	Radius of curvature (m)
$S$	Stencil for WENO scheme
$S^*$	Sutherland's temperature for air (110.4 K)
$T^*$	Temperature (K)
$t^*$	Time (s)
$u_\infty^*$	Freestream velocity (m/s)
$u_{99}$	99% of the freestream velocity (edge of the boundary layer).
$w_l$	Weighting coefficient
$(h,k)$	Frequency/spanwise wavenumber tuple

**Greek symbols**

$\beta_0^*$	Fundamental spanwise wavenumber (/m)
$\delta^*$	Boundary-layer thickness (m)
$\delta_1^*$	Displacement thickness (m)
$\delta_2^*$	Momentum thickness (m)
$\delta_t^*$	Thermal boundary-layer thickness (m)
$\delta_{ii}^*$	Kronecker delta
$\delta_{in}^*$	Boundary-layer thickness at the inlet (m)
$\gamma$	Specific heat ratio
$\mu^*$	Dynamic viscosity (kg/ms)
$\nu^*$	Kinematic viscosity ( $m^2/s$ )
$\omega_0^*$	Fundamental frequency (rad/s)
$\phi$	Wave angle with respect to the flow direction
$\rho^*$	Density ( $kg/m^3$ )
$\tau$	Symmetric viscous stress tensor

**Superscripts**

*	Dimensional quantity
---	----------------------

**Subscripts**

$\infty$	Free-stream quantity
$in$	Inlet quantity
$r$	Reference quantity
$w$	Wall quantity

**Abbreviations**

2DP	2-D disturbance part
CNRS	Centre National de la Recherche Scientifique
CORIA	Complexe de Recherche Interprofessionnel en Aérothermochimie
DMD	Dynamic Mode Decomposition
DNS	Direct numerical simulation

---

ENO	Essentially Non-Oscillatory
ERDF	European Regional Development Fund
EU	European Union
GIP	Generalized Inflection Point
GREAh	Groupe de Recherche en Electrotechnique et Automatique du Havre
H-	Hebert
INSA	Institut National des Sciences Appliquées
JPDF	Joint probability density function
K-	Klebanoff
LST	Linear Stability Theory
MFD	Mean-flow distortion
NSE	Navier-Stokes equations
O-	Oblique
PSE	Parabolized Stability Equations
RK	Runge-Kutta
RME	Renewable Marine Energies
SBL	Supersonic boundary layer
TS	Tollmein-Schlichting
UAC	Ultrasonic Absorptive Coating
UFD	Upstream Flow Deformation
UNFCCC	United Nations Framework Convention on Climate Change
WENO	Weighted Essentially Non-Oscillatory

# List of Figures

---

1.1	Schematic depiction of boundary-layer development over a flat plate. . . . .	2
1.2	Thermal boundary layer profiles for adiabatic (—), and isothermal (heated (—) and cooled (—)) walls in laminar regime for compressible boundary layers at Mach 2.2. . . . .	4
1.3	Axial velocity time sequence obtained from the DNS ((a)-(c)) compared to the corresponding time instances in the experiments ((f)-(i)). As shown in <a href="#">Lebon et al. (2018)</a> . . . . .	6
1.4	Inception of Görtler vortices for different turbulent intensities ( <a href="#">Sharma &amp; Ducoin (2018)</a> ). . . . .	7
1.5	Schematic of different stages of flow evolution over a flat-plate. ( <i>Image source: <a href="http://clasfaculty.ucdenver.edu/rtagg/CLARIfstyle/CLARIfstyle_02.html">http://clasfaculty.ucdenver.edu/rtagg/CLARIfstyle/CLARIfstyle_02.html</a></i> ). . . . .	8
1.6	(a) Instantaneous iso-Q structures ( <a href="#">Sayadi et al. 2013</a> ), and (b) wave vector diagram (in blue are the principal and input secondary modes, while red ones are nonlinearly generated) for the K-type breakdown scenario. . . . .	12
1.7	K-type transition in an experimental study, see <a href="#">Saric et al. (2002)</a> . . . . .	13
1.8	(a) Instantaneous iso-Q structures ( <a href="#">Sayadi et al. 2013</a> ), and (b) wave vector diagram (in blue are the principal and input secondary modes, while red ones are nonlinearly generated) for the H- or the N-type breakdown scenario. . . . .	14
1.9	H-type transition in an experimental study, see <a href="#">Saric et al. (2002)</a> . . . . .	15
1.10	(a) Instantaneous iso-Q structures, and (b) wave vector diagram (in blue are the input principal modes, while red ones are nonlinearly generated) for the O-type breakdown scenario. . . . .	16
1.11	O-type transition in an experimental study, see <a href="#">Kloker (2018)</a> . . . . .	17
1.12	An example of by-pass transition in the case of a supersonic adiabatic flat plate with $M_\infty = 2.2$ . . . . .	17
1.13	A Road Map of boundary-layer transition ( <a href="#">Morkovin (1994)</a> , <a href="#">Fedorov (2011)</a> ). . . . .	18
1.14	(a) Influence of viscosity on the growth rate of different modes. Here, the x-axis represents the Mach numbers, and (b) Disturbance growth rate of various modes as a function of Mach number ( <a href="#">Kloker 2018</a> ). $\phi$ represents the wave angle with respect to the flow direction ( <a href="#">White &amp; Corfield 2006</a> , <a href="#">Kloker 2018</a> ). . . . .	19
1.15	Iso-contours of phase-velocity showing the acoustic modes ( <a href="#">Kloker (2002)</a> ). . . . .	20
2.1	Schematic representation of the computational domain and the boundary conditions. . . . .	40
2.2	Instantaneous snapshot of the baseflow: contours of (a) $u^*/u_\infty^*$ shown at $y^*/\delta_{in}^* = 0.48$ , and (b) $p^*/p_\infty^*$ shown at $z^*/\delta_{in}^* = 12$ . . . . .	42
2.3	Self-similar (a) velocity profiles, and (b) temperature profiles at $Re_x = 2 \times 10^5$ (—) and $Re_x = 6 \times 10^5$ (—), and (c) represents the profile obtained from the shooting method. . . . .	43
2.4	Comparison of the streamwise evolution of the maximum disturbance amplitudes of various modes with <a href="#">Fezer &amp; Kloker (2000)</a> (marked by symbols). . . . .	44

---

2.5	Instantaneous flow-field for the validation case: contours of $u^*/u_\infty^*$ , shown at $y^*/\delta_{in}^* = 0.44$ . . . . .	44
2.6	(a) Longitudinal cut at $z^*/\delta_{in}^* = 50$ ; (b) top view at $y^*/\delta_{in}^* = 0.60$ : contours, and (c) perspective view of the surface of the disturbance ( $u^* - u_{bf}^*$ ). . . . .	45
3.1	Instantaneous flow-field for (a) (0,2), and (b) (0,4) control mode: contours of $u^*/u_\infty^*$ , shown at $y^*/\delta_{in}^* = 0.44$ . Control modes are induced using time independent blowing/suction without the induction of the Principal mode for $M_\infty = 2.0$ . . . . .	47
3.2	Streamwise evolution of streak amplitude for various cases in transition region. . . . .	69

# List of Tables

---

2.1 Coefficients of central schemes from second to eighth order. . . . .	37
--	----

# List of Algorithms

---

2.1 : Spectral approach, or Fourier analysis . . . . .	46
3.2 : Reducing the 2-D part . . . . .	67
3.3 : Reducing the 3-D control part . . . . .	68
3.4 : The LST approach . . . . .	68
3.5 : Approximate strategy . . . . .	68

# List of Publications

---

## Peer-reviewed journals:

1. **Sharma S.**, Shadloo M. S., Hadjadj A. & Kloker M. J. (2019), Control of oblique-type breakdown in a supersonic boundary layer employing streaks, *Journal of Fluid Mechanics*, **873**, 1072-1089.
2. **Sharma S.**, Shadloo M. S. & Hadjadj A., Turbulent flow topology in supersonic boundary layer with heat transfer, *International Journal of Heat and Fluid Flow*, **78**, 1-19.
3. **Sharma S.**, Shadloo M. S. & Hadjadj A. (2018), Effect of thermo-mechanical non-equilibrium on the onset of transition in supersonic boundary layers, *Heat and Mass transfer*, DOI: [doi.org/10.1007/s0023](https://doi.org/10.1007/s0023).
4. **Sharma S.**, Shadloo M. S. & Hadjadj A. (2018), Laminar-to-turbulent transition in supersonic boundary layer: Effects of initial perturbation and wall heat-transfer, *Numerical Heat Transfer, Part A: Applications*, **73**(9), 583-603.

## International conference:

1. **Sharma S.**, Shadloo M. S. & Hadjadj A. (2018), Effect of thermo-mechanical non-equilibrium on the onset of transition in supersonic boundary layers, *12th European Fluid Mechanics Conference (EFMC 12)*, 9-13 September 2018, Vienna, Austria.

# Sommaire

---

## 0.1 Contexte: projet Neptune

Cette thèse de recherche fait partie d'un projet Européen intitulé Neptune, consacré au développement de la recherche universitaire nationale et internationale dans le domaine des Énergies Marines Renouvelables (EMR). Le projet englobe différents aspects du EMR tels que la mécanique, l'aéro/hydrodynamique, l'électricité et le contrôle. Actuellement, le projet en est à sa première phase, à savoir Neptune 1, et pour cette étape, l'accent est mis sur la construction de trois plates-formes, à savoir : les sources éoliennes, l'énergie marine en mer et l'énergie électrique. Neptune 1 favorise les travaux de recherche en vue du développement et de l'optimisation de EMR. Afin de faciliter les recherches scientifiques, le projet comprend quatre tâches/groupes d'action. Cette thèse fait donc partie du deuxième groupe d'action axé sur la génération de la turbulence compressible. Pour mieux comprendre les fondamentaux, le cas d'une couche limite le long d'une plaque plane est choisi pour notre étude.

Le consortium comprend des instituts de recherche renommés comme CORIA (Complexe de Recherche Interprofessionnel en Aérothermochimie), GREAH (Groupe de Recherche en Electrotechnique et Automatique du Havre), Laboratoire Ondes et Milieux Complexes, CNRS (Centre National de la Recherche Scientifique), Université de Rouen, Université le Havre et INSA (Institut National des Sciences Appliquées) de Rouen. Ce projet est cofinancé par l'Union Européenne (UE) par le biais du Fonds Européen de Développement Régional (FEDER) et du conseil régional de la région de Normandie. Le budget global alloué au projet est de 2,8 millions € qui comprend un financement de l'UE de 1,38 million €.

## 0.2 Motivation

La transition vers la turbulence a toujours été un domaine de recherche difficile et est relativement moins bien comprise que les écoulements laminaires ou turbulents pleinement développés. Il est bien connu que l'existence de la couche limite turbulente augmente sensiblement la résistance au frottement, provoque un mélange en masse avec l'écoulement environnant et produit également du bruit. En outre, pour les régimes super/hypersoniques, l'échauffement de la paroi par frottement est une préoccupation essentielle. Le scénario de transition à grande vitesse devient donc un sujet complexe à traiter. Par conséquent, il est indispensable de contrôler le début de la turbulence pour les couches limites à grande vitesse. Une prévision précise de la transition laminaire en turbulence dans l'écoulement de couche limite supersonique est indispensable pour la conception et l'optimisation des avions supersoniques modernes. Avec un accent croissant sur la réduction des émissions imposées par les normes strictes en matière de pollution et d'efficacité, la prochaine génération d'engins supersoniques doit non seulement être plus efficace, mais également moins polluante. Ces

objectifs sont bien formalisés dans l'esprit du fameux accord de Paris sur le climat ([UNFCCC 2015](#)) signé par divers pays pour faire baisser la hausse de la température mondiale.

Par conséquent, ce scénario nécessite des travaux de recherche fondamentaux approfondis dans les domaines de l'aérodynamique compressible, du contrôle d'écoulement, de la stabilité et de la réduction de la traînée, ce qui nous aiderait à atteindre les objectifs susmentionnés avec une meilleure compréhension de la physique des écoulements. Par conséquent, cette étude de recherche vise à fournir une meilleure compréhension des différents mécanismes d'apparition de la transition, des paramètres d'influence et de la stratégie de contrôle possible pour les couches limites supersoniques.

### 0.3 Portée de la recherche

Notre analyse de la littérature existante présentée jusqu'à présent montre clairement que des recherches approfondies ont été menées sur la couche limite compressible, mais que les questions fondamentales concernant l'impact de divers paramètres physiques sur le début de la transition sont très rares. Comme indiqué précédemment, la décomposition de type oblique est la principale voie de transition dans les couches limites supersoniques. Cependant, aucune étude expérimentale ni numérique n'a été rapportée concernant le contrôle de la rupture de type O dans un environnement à transition contrôlée. Par conséquent, afin de comprendre les principes fondamentaux des couches limites supersoniques compressibles, nous définissons les objectifs suivants à explorer :

1. Comprendre la décomposition de type O dans un scénario d'entrée de perturbation contrôlée et présenter une méthode efficace, telle que les modes de traînée de grande amplitude pour supprimer le passage à la turbulence. Déterminer également quelle partie du contrôle (2D ou 3D) est responsable du contrôle effectif.
2. Étude des implications de différents paramètres physiques, tels que l'amplitude de perturbation initiale, les variations de la température de la paroi et l'écoulement de base, au début de la transition pour les couches limites à grande vitesse.
3. Étude des impacts de la température des parois sur la topologie des écoulements, ainsi que d'importants paramètres physiques tels que la contrainte de cisaillement et les différentes composantes du flux thermique de la couche limite turbulente entièrement développée à l'aide de la distribution JPDF et des analyses de covariance.

### 0.4 Contenu de la thèse

Comme mentionné précédemment, un aperçu complet de la littérature révèle que de nombreuses questions importantes concernant la caractérisation et le contrôle des couches limites transitoires compressibles sont encore ouvertes. Par conséquent, dans notre étude, nous voudrions aborder en détail certains des thèmes ouverts. Cette thèse est organisée

comme suit :

**Chapitre 2 :** Ce chapitre décrit de manière détaillée les équations principales ainsi que les détails numériques du solveur DNS. Le chapitre contient également des informations sur l'analyse de Fourier utilisée pour obtenir la tendance évolutive des différents modes. Vers la fin de ce chapitre, quelques résultats concernant la validation du code et les résultats du de l'écoulement de base sont également présentés.

**Chapitre 3 :** Dans ce chapitre, nous présentons le contrôle du scénario de décomposition de type O à l'aide des modes de contrôle streak. Seul le cas adiabatique est considéré. Au meilleur de notre connaissance, ce chapitre présente la première étude DNS sur le contrôle du scénario de décomposition oblique à l'aide des modes streak. Le chapitre porte sur l'efficacité des modes de traînée dans le contrôle de la décomposition de type oblique dans la couche limite supersonique. Les résultats révèlent que les parties 2D et 3D du mode de contrôle sont responsables de la suppression du passage à la turbulence. Les résultats sont publiés dans : *Journal of Fluid Mechanics* (Sharma, Shadloo, Hadjadj & Kloker 2019).

**Chapitre 4 :** Le scénario de transition du type 'by-pass' est présenté dans ce chapitre. Les implications des différents phénomènes physiques, dont l'intensité de la perturbation et la température de la paroi au début de la transition, sont présentées. Les résultats sont publiés dans: *Numerical Heat Transfer, Part A: Applications* (Sharma et al. 2018a).

**Chapitre 5 :** Ce chapitre poursuit la discussion sur le scénario de transition 'by-pass' et les effets des variations de débit de l'écoulement de base (nommés ici non-équilibre thermo-mécanique) sur le début de la transition sont discutés en détail. Le DMD est utilisé pour révéler le comportement des modes prescrits utilisés pour exciter l'écoulement vers la turbulence. Les résultats sont publiés dans : *Heat and Mass Transfer* (Sharma et al. 2018b).

**Chapitre 6 :** Ce chapitre traite des couches limites turbulentes supersoniques, dans lesquelles les analyses JPDF et de covariance sont utilisées pour clarifier les mécanismes physiques responsables du transfert de chaleur dans les directions de l'écoulement et des parois. Différentes analyses de quadrant d'intégrants de covariance ont été proposées pour déterminer le processus de transfert le plus significatif et de l'orientation des structures vorticales (qui affectent la topologie du flux) et du flux de chaleur turbulent. Les résultats sont publiés dans : *International Journal of Heat and Fluid Flow* (Sharma, Shadloo & Hadjadj 2019).

**Chapitre 7 :** Ce chapitre contient le résumé des travaux de recherche menés ainsi que les conclusions. Cela expose également les possibilités pour que les travaux futurs envue d'une meilleure compréhension des couches limites de transition compressibles

supersoniques.

## 0.5 Conclusions

Ce travail de recherche a pour objectif de mieux appréhender la physique des écoulements de paroi. Des scénarios de transition complexes tels que la décomposition de type O et la transition by-pass dans la couche limite supersonique ont été étudiés. Les implications des différents paramètres physiques, tels que la température à la paroi, l'intensité de la perturbation initiale et les variations de l'écoulement porteur ont été étudiées. L'étude a également porté sur le contrôle en décomposition de type O à l'aide des modes streak.

Le solveur numérique utilisé dans cette thèse a été validé avec les résultats DNS existants de Fezer & Kloker (2000), Mayer et al. (2011) (rupture de type O) à  $M_\infty = 2.0$ . La même configuration a été utilisée pour démontrer le contrôle via une décomposition de type oblique complet d'une couche limite supersonique adiabatique à l'aide des traînées de contrôle. Les traînées étudiées avec, dans divers cas, trois à six fois le nombre d'ondes dans le sens fondamental des modes fondamentaux en fonctionnement oblique et des amplitudes maximales de 20 à 10% ont été introduites par aspiration/soufflage périodique constant dans le sens perpendiculaire à l'écoulement dans une ou deux bandes de contrôle. En général, les nombres d'ondes plus élevés des traînées en décomposition s'avèrent plus efficaces pour supprimer le mode fondamental le plus amplifié et le plus instable (1,1), mais nécessitent des amplitudes initiales plus élevées en raison d'une plus forte décroissance en direction de l'écoulement. Cela peut provoquer une onde de pression constante préjudiciable, de type onde choc. Le mode de balayage oblique (0,2) n'est pas directement influencé, mais par l'abaissement des modes de déplacement oblique (1,1) qui l'alimentent.

Il a été constaté que la longueur d'onde dans le sens de la largeur des bandes de contrôle efficaces se situe entre 20 et 25% du mode oblique fondamental. Un DNS modifié avec des parties de perturbation bi-dimensionnelles supprimées et donc une distorsion de l'écoulement moyen (MFD) pourrait montrer que, pour que la partie tri-dimensionnelle soit efficace dans l'atténuation de la croissance, la longueur d'onde dans le sens de l'envergure doit être inférieure à environ 2,5 fois l'épaisseur de la couche limite locale ( $\lambda_{control}^*/\delta^* < 2,5$ ). Cette valeur est proche de celle des modes avec une croissance transitoire optimale en théorie. Au nombre de Reynolds considéré,  $Re_x = 2 \times 10^5$ , de la première bande de contrôle d'aspiration/soufflage dans le sens contraire de l'envergure, tous les modes de contrôle permanent se désintègrent de manière monotone directement en aval de la bande, lorsque la longueur d'onde est courte. Commencer par l'idéal  $\lambda_{control}^*/\delta^*$  conduirait à une dégradation rapide des stries et aucun contrôle significatif ne peut être réalisé. Pour les traînées trouvées globalement efficaces, l'idéal  $\lambda_{control}^*/\delta^*$  est atteint en aval près de  $Re_x = 5.5 - 6 \times 10^5$  lorsque leur contrôle  $\rho u$ -amplitudes se sont désintégréées d'initialement d'environ 20% à 10%, mais dans le même temps, les effets bénéfiques induits par le MFD tombent au-dessous de 3% et deviennent inactifs. Dans la première partie en aval de la bande de contrôle, l'amplitude du MFD varie

de 10% à 3%, et la suppression de mode oblique observée est donc uniquement fournie par le MFD. Globalement, le MFD et la partie 3D du contrôle contribuent chacun avec une part comparable à la réduction de l'amplitude du mode fondamental.

Le MFD peut devenir dommageable (localement) si la partie soufflante est trop forte et pas assez pointue; des points d'inflexion généralisés apparaissent dans les profils de vitesse moyennés dans le sens de la largeur, invoquant une instabilité non visqueuse. Lors du rafraîchissement de la bande de contrôle en aval, les traînées à faible vitesse ne doivent pas être élargies localement, ce qui déclencherait une transition. Les pénalités initiales liées au cisaillement pariétal et à l'augmentation de la température des parois sont marginales par le contrôle, décalant leur augmentation de manière turbulente en aval. Des simulations avec un spectre de perturbations plus large comprenant des nombres d'ondes supérieurs  $k$  et des fréquences  $h$ , des modes ( $h = 1 - 2, k = 1 - 3$ ) et une amplitude totale considérablement accrue montrent que les mécanismes de suppression de base fonctionnent également dans ce cas. Les modes de streak supplémentaires générés ( $0, k = 4, 6$ ) sont beaucoup plus proches du mode de contrôle et considérés a priori comme critiques, sans dégradation du contrôle (Sharma, Shadloo, Hadjadj & Kloker 2019).

Les simulations DNS concernant le scénario de transition de contournement ont également été effectuées. Les implications de divers facteurs, tels que l'intensité de la perturbation initiale et le transfert de chaleur sur la transition, ont été étudiées. Nous avons quantifié le début et la fin de la région de transition en utilisant différentes quantités, à savoir l'évolution du coefficient de frottement pariétal, la distribution des contraintes de cisaillement de Reynolds et flux de chaleur de Reynolds de paroi normale, la décomposition modale et l'évolution du nombre de Stanton en fonction de  $Re_x$ .

Il a été observé qu'une augmentation de l'intensité de perturbation du soufflage et de la succion a déplacé l'emplacement de début de transition en amont des parois adiabatiques. Les analyses ont prédit une augmentation de la longueur de la région de transition avec des niveaux croissants de perturbation. Les résultats DNS des effets du transfert de chaleur sur les parois ont été comparés aux prévisions de Théorie de la Stabilité linéaire (TSL) (initialement rapportés par Shadloo & Hadjadj (2017)). Les résultats de DNS et de TSL étaient en bon accord. Il a également été constaté qu'à faible intensité de perturbation, c'est-à-dire 0,5%, le refroidissement de la paroi tend à stabiliser l'écoulement et il reste laminaire, tandis que le chauffage de la paroi a avancé le début du passage à la turbulence par rapport à la paroi adiabatique.

Les effets conjoints de l'intensité de la perturbation et du transfert de chaleur dans la paroi ont été analysés pour déterminer des intensités de perturbation plus fortes de 1% et 2,4%. À 1%, le refroidissement de la paroi a stabilisé l'écoulement et l'emplacement de la transition s'est déplacé vers l'aval, mais il n'y avait pas de différence significative entre les parois chauffées et adiabatiques. En raison du taux de croissance plus faible de la paroi refroidie, comme prédit par le LST, la paroi refroidie avait une région de transition plus longue. Mais pour le régime non linéaire, avec une intensité de perturbation de 2,4%, le

refroidissement du paroi déstabilisait le flux, qui passait en amont par rapport au paroi adiabatique. Cependant, le chauffage de la plaque entraînait une transition retardée. Ces résultats sont en accord avec les résultats DNS obtenus par [Shadloo et al. \(2016\)](#), [Shadloo & Hadjadj \(2017\)](#). Ce comportement est en contraste direct avec celui observé pour 0.5% montrant la limitation de la LST pour l'écoulement fortement perturbé. Les interactions non linéaires dans l'écoulement pourraient être prises en compte pour cette tendance contrastée. Il a également été observé que l'impact du refroidissement des parois était plus amplifié que celui des murs, ce qui pourrait s'expliquer par la manière dont la perturbation a été imposée, c'est-à-dire en perturbant la composante  $v$  au niveau de la paroi. Le produit  $\rho v$  devrait rester constant, mais dans un régime compressible, la masse volumique varie. En raison de la variation de la masse volumique, la valeur de ce produit diminue dans la région proche de la paroi pour les parois chauffées et augmente pour celles refroidies, ce qui entraîne une différence de réceptivité. En ce qui concerne la partie turbulente du domaine, il a été constaté que les parois refroidies et chauffées atteignent différentes valeurs du facteur d'analogie de Reynolds qui diffèrent de la valeur donnée par  $Pr^{-2/3}$ . L'analyse dimensionnelle a révélé que multiplier cette valeur par le produit des rapports de masse volumique et de viscosité du cas isotherme au cas adiabatique,  $Pr^{-2/3} \times \frac{\rho_w}{\rho_{aw}} \frac{\mu_w}{\mu_{aw}}$  présente une bonne approximation de la valeur moyenne du facteur d'analogie de Reynolds atteint à la fois par les parois refroidies et chauffées dans la région entièrement turbulente ([Sharma et al. 2018a](#)).

La réceptivité de la couche limite aux variations de l'écoulement de base a été analysée en utilisant l'évolution du coefficient de frottement pariétal, du nombre de Stanton et de la DMD dans le sens de la largeur. Les cas ont été étudiés pour des intensités de perturbation de 0,5% et de 2,4%. Les résultats ont révélé que l'existence du non-équilibre thermo-mécanique déstabilisait l'écoulement et que le début de la transition était déplacé vers l'amont, quelle que soit l'intensité de la perturbation induite pour les parois chauffées. De plus, il a également été constaté que les parois chauffées avec le non-équilibre thermo-mécanique avaient une longueur de transition plus courte. De la tendance évolutive du nombre de Stanton dans le sens du courant, il était clair que malgré la grande différence entre les valeurs du nombre de Stanton dans la partie laminaire, les parois chauffées avec non-équilibre thermo-mécanique finissaient par atteindre l'équilibre thermique la partie turbulente du domaine résultant du mélange turbulent. Les parois refroidies ne présentaient aucun signe de transition et le flux restait laminaire dans tout le domaine de calcul pour une intensité de perturbation de 0,5%. Contrairement à la paroi chauffée, pour une intensité de perturbation de 2,4%, il a été constaté que le non-équilibre thermo-mécanique retardait l'emplacement du début de la transition et qu'une région de transition plus longue était également observée pour les parois refroidies. Cependant, les parois refroidies n'ont jamais atteint l'équilibre thermique, ni pour des intensités de perturbation de 0,5% ni de 2,4%. De plus, les courbes d'évolution du nombre de Stanton en fonction de  $Re_x$  ont révélé que les cas de non-équilibre thermo-mécanique dépassaient plus que leurs équivalents d'équilibre thermo-mécaniques en raison de la quantité accrue de transfert de chaleur ([Sharma et al.](#)

2018b).

Les résultats obtenus à partir de l'analyse DMD montrent deux voies d'évolution distinctes pour les harmoniques impairs et pairs de la fréquence de forçage. Il a été constaté que l'évolution de ces harmoniques était indépendante des paramètres physiques imposés tels que la température de la paroi ou le non-équilibre thermo-mécanique. Cependant, pour la paroi refroidie avec une intensité de perturbation de 0,5%, les modes ont disparu vers la fin du domaine, mais le manière de propagation était le même que dans les autres cas pour les modes correspondants. Il a également été constaté que le mode considéré avait fortement progressé et était devenu dominant dans la région en transition avant de se transformer en structures plus petites dans le régime turbulent. Le tracé et les retards dans les fronts d'ondes se propageant ont été révélés par la représentation graphique des angles de phase qui a révélé que chaque mode de propagation était constitué des fronts d'ondes aux angles de phase opposés (Sharma et al. 2018b).

Les études DNS pour les couches limites supersoniques turbulentes ont également été effectuées afin de comprendre les effets de la température de paroi sur la topologie en écoulement turbulent des SBL. Les implications sur les paramètres physiques importants tels que la contrainte de cisaillement turbulente, l'orientation des projections des structures cohérentes dans différents plans et les différentes composantes du flux de chaleur turbulent ont été analysées à l'aide de la distribution JPDF et des analyses des intégrands de covariance (Sharma, Shadloo & Hadjadj 2019).

Les résultats ont montré que les balayages étaient le phénomène physique dominant contribuant en grande partie due à la contrainte de cisaillement turbulente dans la couche tampon. Mais, pour la paroi chauffée, les éjections et les balayages sont devenus des processus de transfert comparables. Dans la région logarithmique, les éjections jouent un rôle prépondérant dans la contrainte de cisaillement, quelle que soit la température de la paroi. Ces tendances ont montré des similitudes avec les résultats rapportés par Wallace et al. (1972), Ong & Wallace (1998) en ce qui concerne les couches limites incompressibles adiabatiques. Les résultats présentés ont également mis en évidence différentes tendances pour les angles d'inclinaison ( $\alpha$  et  $\beta$ ) des projections des structures cohérentes dans le cas d'une paroi chauffée, en raison du transfert de chaleur accru de la surface de la paroi. Les tendances de  $\alpha$  et  $\beta$  ont montré un bon accord avec les contreparties compressibles et incompressibles rapportées dans la littérature.

Les courbes des intégrales de covariance des  $u'$  et  $T'$  ont montré que pour les parois adiabatiques et chauffés, les  $Q_2$  et  $Q_4$  étaient les quadrants dominants impliquant la contribution principale du fluide à refroidissement rapide vers la composante dans le sens du courant du transfert de chaleur à paroi turbulente s'étendant de la sous-couche visqueuse à la région de bûche. Alors que pour la paroi refroidie, les  $Q_1$  et  $Q_3$  étaient les principaux contributeurs de la sous-couche visqueuse. Une tendance similaire a été observée à nouveau pour la paroi refroidie, pour la composante de paroi normale du flux de chaleur turbulent dans la sous-couche visqueuse où le  $Q_2$  était dominant par rapport au  $Q_4$ , ce qui signifie que

le fluide chauffé vers la paroi contribuait davantage au flux de chaleur normal à la paroi turbulente. Pour le reste, les  $Q_1$  et  $Q_3$  étaient les quadrants dominants.

## 0.6 Perspectives

Tenant compte des travaux présentés dans cette thèse, de nombreux résultats importants ont été avancés, ce qui a permis d'améliorer notre connaissance des couches limites supersoniques en transition. De plus, les implications des paramètres physiques sur le comportement et la topologie de l'écoulement étaient également intéressantes.

Cette étude a été l'une des toutes premières entreprises de notre Shock-Waves Research Group à CORIA, Rouen dans le domaine des écoulements en transition. Elle a ouvert les axes suivantes pour la poursuite des travaux futurs :

- Comme présenté au chapitre 3, le mécanisme de contrôle pour contrer le décomposi-tion de type O peut être approfondi. Des simulations avec un spectre de perturba-tions plus large comprenant un nombre d'ondes plus élevés dans l'envergure  $k$  et des fréquences  $h$ , modes ( $h = 1 - 2, k = 1 - 3$ ) ont montré que les modes de traînées supplé-mentaires générés par les modes de contrôle ( $0, k = 4, 6$ ) ne dégradent pas le contrôle. Par conséquent, la robustesse des chaînes de contrôle pour faire face à des situations de perturbation plus complexes doit faire l'objet d'études à court terme.
- La prochaine étape consiste à étudier l'efficacité du mode de contrôle pour supprimer la transition en cas de parois légèrement chauffés/refroidis. Il convient de noter ici que seulement de légers changements de température doivent être étudiés au début, sinon les effets thermiques détruiraient l'amplification des modes.
- Il serait intéressant d'étudier l'applicabilité des modes "streak" à des nombres de Mach plus élevés,  $M_\infty = 4$  par exemple, car avec de tels régimes, les instabilités des modes secondaire (modes Mack) dominant l'écoulement.
- Certains cas impliquant un réchauffement/refroidissement progressif de la paroi pour-raient également être examinés. Ces scénarios représentent la phase de descente/mon-tée de l'avion. Le changement progressif de la température de la paroi devrait décaler de manière dynamique l'emplacement du début de la transition.
- Une simulation numérique directe (DNS) avec les conditions en vol peut également être utilisé pour un cas d'écoulement transversal qui représente la configuration en flèche de l'avion supersonique.

# Chapter 1

## Introduction

---

### 1.1 Context: Neptune project

This research study is part of a European project entitled Neptune which is dedicated towards the development of National and International academic research in the Renewable Marine Energy (RME) domain. The mission of the project encompasses different aspects of RME such as the mechanical, aero/hydrodynamic, electrical and control. Currently, the project is in its first phase i.e. Neptune 1, and for this stage the focus is on building three platforms, namely; the wind sources, the off-shore marine energy and the electric power. Neptune 1 promotes the research works towards the development and optimization of RME. In order to facilitate the scientific investigations, the project underlays four tasks/action-groups. This doctoral research study is part of the second action-group focusing on the generation of compressible turbulence. To better understand the fundamentals, the basic case of a flat-plate is chosen for our study.

The consortium comprises of the renowned research institutes like CORIA (Complexe de Recherche Interprofessionnel en Aérothermochimie), GREAh (Groupe de Recherche en Electrotechnique et Automatique du Havre), Laboratoire Ondes et Milieux Mocomplexes, CNRS (Centre National de la Recherche Scientifique), Université de Rouen, Université le Havre and INSA (Institut National des Sciences Appliquées) de Rouen. This project is co-financed by the European Union (EU) through European Regional Development Fund (ERDF), and the regional council of the region of Normandy. The overall allocated budget for the project is 2.8 million € comprising of the EU funding of 1.38 million €.

### 1.2 Motivation

Transition to turbulence has always been a challenging field of research, and is comparatively less understood than the laminar or the fully developed turbulent flows. It is well-known that existence of the turbulent boundary layer substantially increases the friction drag, causes mass mixing with the surrounding flow and also produces noise. Additionally, for the super/hypersonic regimes, the frictional heating of the wall is a critical concern, hence, the high-speed transition scenario becomes an even complex topic to address. Therefore, it has become of vital, topical interest to control the onset of turbulence for high-speed boundary layers. Precise prediction of laminar breakdown to turbulence in the supersonic boundary-layer flow is indispensable for the design and the optimization of the modern supersonic aircraft. With an ever-increasing focus on cutting emissions laid by the stringent norms of pollution and efficiency, the next-generation of supersonic flying engines have not

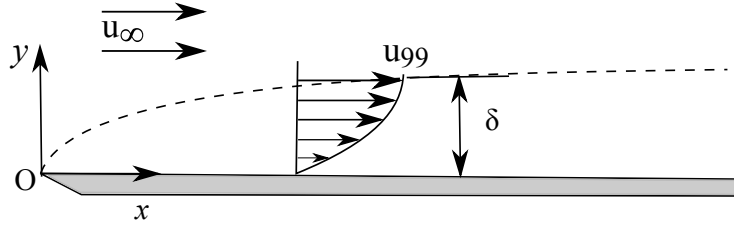


Figure 1.1: Schematic depiction of boundary-layer development over a flat plate.

only to be more efficient but also less polluting. These objectives are well-formalized in the spirit of the famous Paris climate accord (UNFCCC 2015) signed by various countries to bring down the rising global temperature.

Therefore, this scenario demands the in-depth fundamental research works in the fields of compressible aerodynamics, flow-control, stability, and drag-reduction which would help us in achieving the above-mentioned goals with better understanding of the flow physics. Hence, this research study aims to provide a better understanding of different mechanisms of the onset of transition, the influencing parameters, and possible control strategy for the supersonic boundary layers.

### 1.3 Basic notions regarding the boundary layer

For any fluid motion over a smooth or a rough fixed surface, the portion of the fluid present directly at the surface is actually at rest (no-slip condition). Therefore, there exists a thin layer extending from the wall-surface towards the freestream where the fluid actually gains velocity from typically zero to the exact freestream velocity. This layer is known as the boundary layer. A strong velocity gradient exists in this region which is responsible for the existence of high shear-stress because of the strong viscous forces. The boundary layer extends from the surface of the wall to a height where the velocity in the streamwise direction becomes 99% of the freestream velocity of the flow;  $u_{99}$  (see figure 1.1). This height is also known as the edge of the boundary layer. The distance of the boundary layer edge from the wall surface constitutes the **boundary-layer thickness**, denoted by  $\delta^*$  (the superscript \* signifies the dimensional quantities). In the laminar flow regime, the general expression for the boundary layer thickness at any point  $x^*$  can be given as:

$$\delta^* \approx 4.91 \frac{x^*}{\sqrt{Re_x}}. \quad (1.1)$$

where,  $Re_x$  is the Reynolds number at  $x^*$  distance from the leading edge of the plate and is defined as:

$$Re_x = \frac{u_\infty^* x^*}{\nu_\infty^*}. \quad (1.2)$$

where,  $u_\infty^*$  and  $\nu_\infty^*$  are the freestream velocity, and the kinematic viscosity respectively. However, for the turbulent regime, the boundary layer thickness can be stated as:

$$\delta^* \approx 0.37 \frac{x^*}{Re_x^{1/5}} \quad (1.3)$$

This formulation assumes that the flow is turbulent from the beginning. Therefore, it can be stated from equations 1.1 and 1.3 that the boundary-layer thickness is directly proportional to  $x^*$  in both laminar and turbulent regimes.

**Displacement thickness**  $\delta_1^*$  is another important quantity for boundary layer flows. From the physical point of view, it can be defined as a distance to which the wall should be displaced in the wall-normal direction in an inviscid fluid moving at  $u_\infty^*$ . Analytically, it can be given as:

$$\delta_1^* = \int_0^\infty \left( 1 - \frac{\rho^*(y)u^*(y)}{\rho_\infty^*u_\infty^*} \right) dy \quad (1.4)$$

where  $\rho_\infty$  is the free-stream density.

For the turbulent boundary layers, the displacement thickness is calculated in the statistical sense i.e. averaging over both spanwise direction and time.

Another important quantity which needs to be defined is the **momentum thickness** ( $\delta_2^*$ ). It can be quantified as the distance by which the surface should be displaced in order to compensate for the reduction in the momentum of the fluid on account of the boundary layer formation. The momentum thickness can be calculated as:

$$\delta_2^* = \int_0^\infty \frac{\rho^*(y)u^*(y)}{\rho_\infty^*u_\infty^*} \left( 1 - \frac{u^*(y)}{u_\infty^*} \right) dy \quad (1.5)$$

The **shape factor** ( $H_s$ ) determines the nature of the flow, and is defined as the ratio of the displacement thickness ( $\delta_1^*$ ) and the momentum thickness ( $\delta_2^*$ ):

$$H_s = \frac{\delta_1^*}{\delta_2^*} \quad (1.6)$$

### 1.3.1 Thermal boundary layer

The thermal counterpart of the boundary layer also exists, known as the thermal boundary layer, which is vital for investigating the effects of wall-heat transfer. The profile of the thermal boundary layer is greatly affected by the wall temperature (see figure 1.2). This figure shows that the slope at the wall is equal to zero for a typical adiabatic profile. However, for the cooled and the heated wall, these slopes are positive and negative, respectively. It can also be seen from figure 1.2 that with the increasing wall temperature, the thickness of the thermal boundary layer also increases locally.

**Thermal boundary layer thickness:** The distance across the boundary layer in the wall-normal direction where the temperature reaches 99% of the freestream temperature

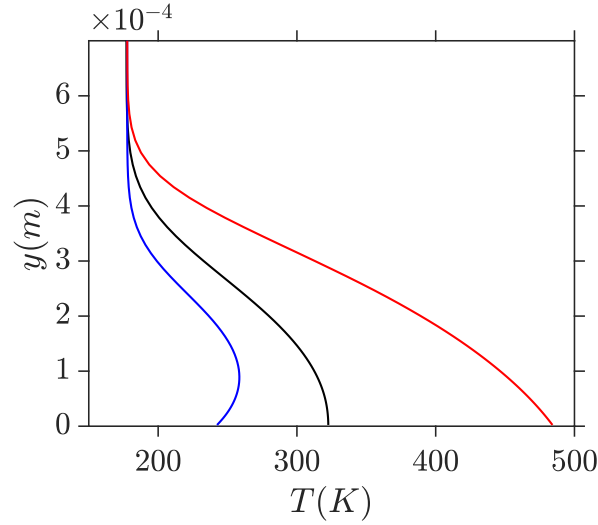


Figure 1.2: Thermal boundary layer profiles for adiabatic (—), and isothermal (heated (—) and cooled (—)) walls in laminar regime for compressible boundary layers at Mach 2.2.

$(T_\infty^*)$  is known as the thermal boundary layer thickness ( $\delta_t^*$ ). For laminar flow,  $\delta_t^*$  is defined as:

$$\delta_t^* = 5 \sqrt{\frac{\nu^* x^*}{u_\infty^*}} Pr^{-1/3} \quad (1.7)$$

where  $Pr$  is the Prandtl number which is defined as the ratio of momentum diffusivity to thermal diffusivity.

Whereas, for the turbulent flow,  $\delta_t^*$  can be written as:

$$\delta_t^* \approx 0.37 \frac{x^*}{Re_x^{1/5}}. \quad (1.8)$$

In the similar fashion, **Thermal displacement thickness** also exists which can be defined as:

$$\delta_{t1}^* = \int_0^\infty \left( \frac{T^*(y) - T_\infty^*}{T_w^* - T_\infty^*} \right) dy \quad (1.9)$$

where  $T_w^*$  is the temperature at the surface of the wall.

## 1.4 Transition

Transition from laminar to turbulent regime is important for design and optimization of numerous engineering applications such as pipe flow in heat exchangers, boundary layer instability for aerodynamics applications, flow separation in nozzles, and many other applications. For the fluid dynamics community, the transition to turbulence has presented a lot of challenges because it represents an intermediate region in between the two distinctively different states; laminar and turbulent. In slightly varied physical scenarios, such as

higher speeds, the situation changes dramatically and a different mechanism of transition comes into play. The importance of the topical interest on understanding the fundamentals of transition can be precisely captured by the research study of [Barkley et al. \(2015\)](#) published in the *Nature* who took on the challenging topic of explaining the origin of turbulence in the wall-bounded shear flows. They found a bifurcation scenario explaining the transition to turbulence, and explained the dynamics of the various stages involved using the theory, experiments and simulations for pipe-flows. Moreover, the recent investigation of [Kubacki et al. \(2019\)](#) regarding the transitional flows around the linear cascade of turbine blades indicates that the topic is still an active area of research.

### 1.4.1 Transition in pipe flows

Historically, the earliest experiments about transition are documented by [Reynolds \(1883\)](#) for the pipe flow. Later on, [Oliveira & Pinho \(1997\)](#), [Rennels & Hudson \(2012\)](#) provided an exhaustive overview of the turbulent flow properties for various applications like the combustion chamber and heat exchangers regarding the sudden-expansion problem. The linear stability analysis of the 1:2 sudden expansion pipe flow performed by [Cliffe et al. \(2012\)](#), [Sanmiguel-Rojas et al. \(2010\)](#) showed the existence of very high Reynolds number before transition. Numerical investigations for the zero-disturbance pipe-flow performed by [Selvam et al. \(2015\)](#) reported the presence of the longer recirculation regions. For the perturbed pipe-flows, [Peixinho & Mullin \(2007\)](#) found the lower bound for the velocity ratio of disturbance to the main flow velocity. In the recent study performed by [Lebon et al. \(2018\)](#) compares the experimental and the DNS results regarding the finite-amplitude disturbances for transition to turbulence. Their study has reported a new mechanism of periodic bursting of the recirculating region, where the secondary recirculation region breaks in to localized turbulence (see the supporting material provided by [Lebon et al. \(2018\)](#) for details). [Figure 1.3](#) shows the comparison of the experimental and the DNS results ([Lebon et al. \(2018\)](#)).

### 1.4.2 Transition over a curved wall

The topography of the surface over which the fluid flows, has implications on the transition mechanisms. In the presence of the curvature of the wall, the secondary centrifugal instabilities arise, known as the Görtler vortices which trigger the breakdown to turbulence in the downstream. This scenario is interesting for various engineering applications like airfoils (e.g. [Dagenhart & Mangalam \(1986\)](#)), nozzles, inlet of the aircraft engines and many more. The understanding of this phenomenon is important because of its applications in the field of renewable energy, like transition over the blades of a wind-turbine (Savonius Style Wind-turbine in particular). The secondary instabilities induced due to the curvilinear geometry of the blade may trigger the natural transition to turbulence (see [Ducoin et al. \(2017\)](#)) and hence deteriorate the efficiency of the whole system. [Görtler \(1940\)](#) was the first to document these longitudinal vortical instabilities, and proposed a non-dimensional parameter which

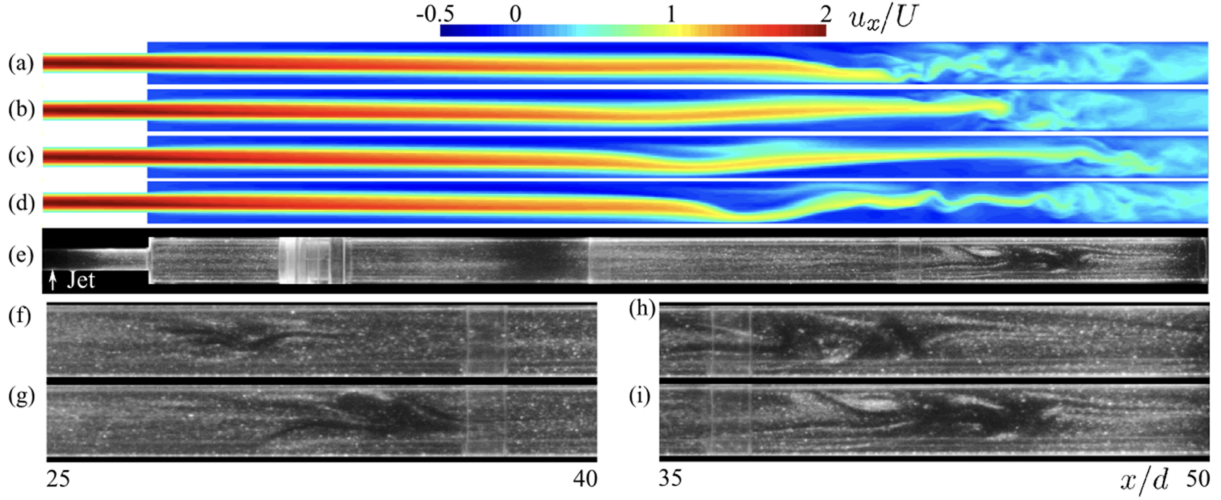


Figure 1.3: Axial velocity time sequence obtained from the DNS ((a)-(c)) compared to the corresponding time instances in the experiments ((f)-(i)). As shown in [Lebon et al. \(2018\)](#).

determines their emergence. This parameter is known as the Görtler number, which can be defined as:

$$G = \frac{u_{\infty}^* \delta_2^*}{\nu^*} \sqrt{\frac{\delta_2^*}{Ri^*}}, \quad (1.10)$$

where,  $Ri^*$  is the radius of curvature of the surface.

The breakdown to turbulence induced by the Görtler instability has been investigated in both the experimental ([Tandiono & Shah \(2009\)](#), [Tandiono et al. \(2013\)](#)) as well as the numerical investigations (e.g. [Schrader et al. \(2011\)](#)). For both compressible and incompressible regimes, [Ren & Fu \(2015\)](#) investigated the governance of different modes affecting the Görtler vortices. Recent numerical investigation of [Sharma & Ducoin \(2018\)](#) regarding the incompressible flow over a curved wall revealed that the induction of the Görtler vortices was very sensitive to the inlet conditions i.e. the freestream turbulence intensity. The results also revealed that with the increase in the freestream turbulence intensity at the inlet, the transition became faster and sharper, characterized by random longitudinal streak distribution. Figure 1.4 shows the inception of the Görtler vortices for different turbulence intensities considered by [Sharma & Ducoin \(2018\)](#). [Méndez et al. \(2018\)](#) have investigated the impacts of the height of the roughness element, and the radius of curvature on the onset of transition. Their results revealed that the transition got delayed with increasing radius of curvature whereas an advancement of transition was observed with increasing height of the roughness elements. For more details, and comprehensive overview of the topic, readers can refer to [Schrader et al. \(2011\)](#), [Ducoin et al. \(2017\)](#), [Sharma & Ducoin \(2018\)](#).

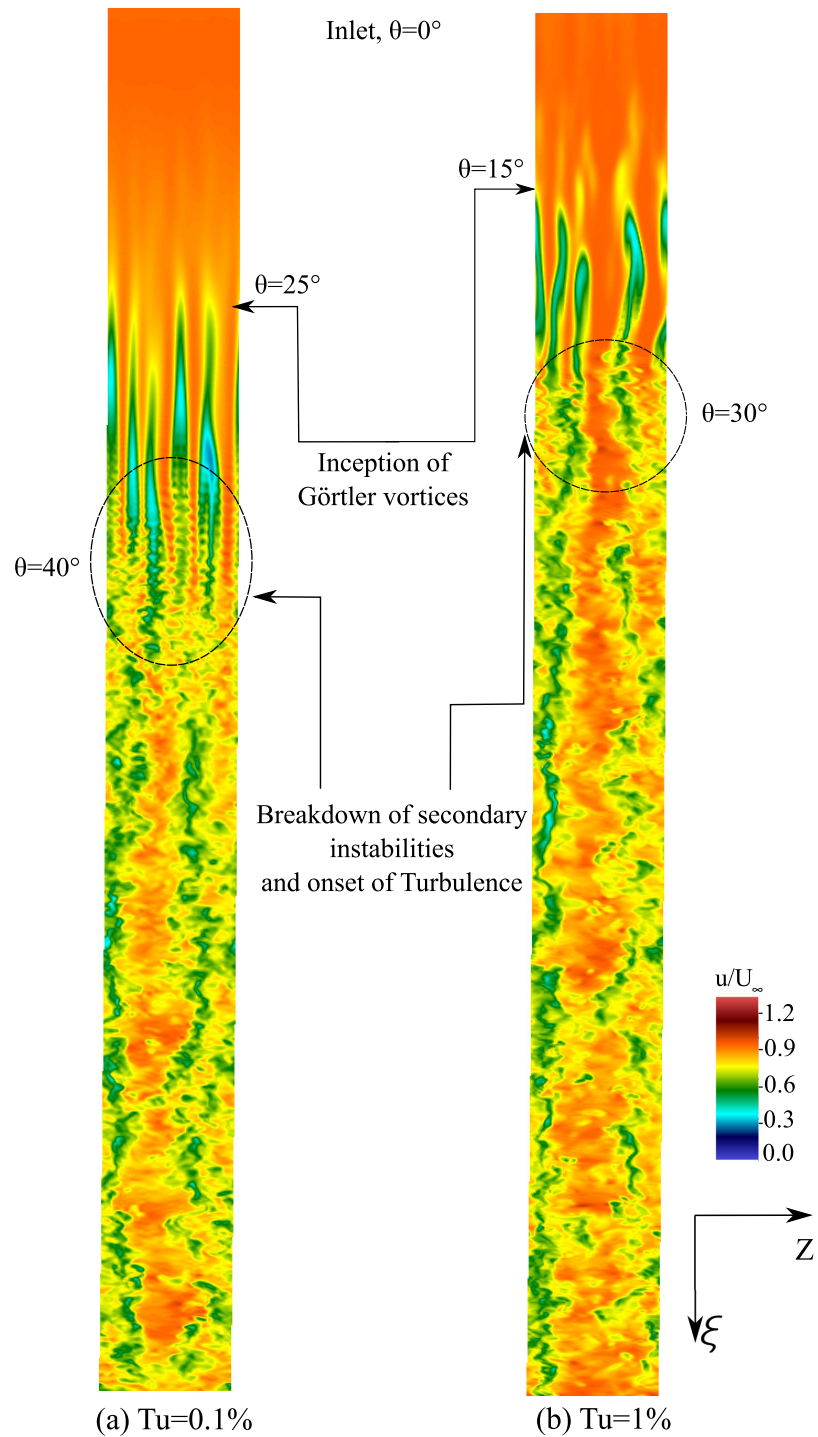


Figure 1.4: Inception of Görtler vortices for different turbulent intensities (Sharma & Ducoin (2018)).

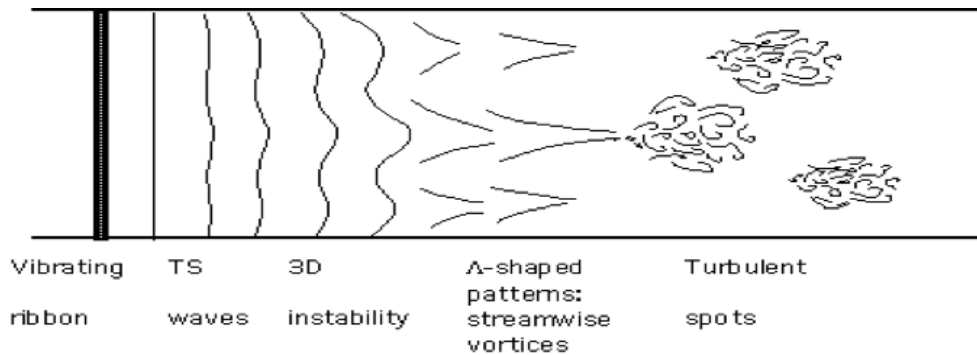


Figure 1.5: Schematic of different stages of flow evolution over a flat-plate. (Image source: [http://clasfaculty.ucdenver.edu/rtagg/CLARIfstyle/CLARIfstyle\\_02.html](http://clasfaculty.ucdenver.edu/rtagg/CLARIfstyle/CLARIfstyle_02.html)).

## 1.5 Transition over a flat plate

With an interest of investigating the fundamentals of the transitional boundary layers, throughout this study, we would focus our attention on the simple case of transition over a flat surface. However, the objectives of this research work would be laid subsequently in §1.8.

### 1.5.1 Incompressible transitional boundary layers

A typical laminar-to-turbulent transition scenario consists of three stages of flow evolution; starting with the initial amplification of a primary instability, then followed by the appearance and growth of the secondary instabilities or the secondary modes. In the later stages, the growth rates become nonlinear, finally setting-in the onset of turbulence (as shown in the schematic in figure 1.5). This description was first reported by Kleiser & Zang (1991) for the study concerning the incompressible controlled breakdown to turbulence. The research approach employed for investigating the transition problems is fundamentally from the ones used for studying the fully developed turbulence because the considered method should correctly predict the growth rate of different modes. Most of the times a deterministic (or controlled) instability scenario is considered because the boundary layer flows are receptive to any form of disturbance (external or internal) which may trigger the transition to turbulence. These disturbances could be induced through numerous ways like vibrating ribbon, introducing roughness elements, a blowing and suction strip at the wall, a free-stream grid turbulence close to the inlet or sometimes a suitable combination of these techniques. It is a well-known fact that the transition is affected by various parameters such as: Reynolds number, shear strength, pressure gradient, Mach number, wall-temperature, wall-roughness and geometry.

The experimental investigation of Schubauer & Skramstad (1947) confirmed the existence of the low-amplitude two-dimensional (2-D) unsteady Tollmein-Schlichting (TS) waves in a low-turbulence wind tunnel which may grow up to an amplitude as high as 2% of the

free-stream velocity. These 2-D TS-waves dominate the transition scenario for the incompressible boundary layers. These waves grow in the downstream and finally breakdown to turbulence (Kleiser & Zang 1991). Higher modes generated nonlinearly by the primary TS-waves do not significantly impact the onset of the secondary instabilities, therefore, the shape assumption holds. Controlling the transition has been a subject of interest in the field of fluid dynamics and many comprehensive investigations have been performed on the same. Earlier attempts to control transition include either a trail-and-error approach or a physical intuition. Comprehensive overview about the systematic approach for flow-control can be found in Moin & Bewley (1994), Joslin et al. (1996), Bewley (2001), Kim & Bewley (2007). Many control strategies have been employed over the course of years to check the flow transition, such as wave cancellation which involves the suppression of the TS-waves by introducing anti-phase signals. Earlier reviews regarding this method can be found in Thomas (1990), their method was experimentally demonstrated by Thomas (1983). In low freestream turbulence flight conditions, even the very subtle surface roughness may trigger the steady crossflow vortical modes (Wassermann & Kloker 2002). As a result of downstream amplitude saturation, crossflow vortices with high-amplitude are formed in the streamwise direction, which distort the flow by causing strong shear layer setting-in an explosive secondary instability mechanism, finally causing the laminar breakdown.

The experimental works regarding the transitional boundary layers utilize a controlled disturbance input to excite the flow. The disturbances are well-defined and could be introduced using various techniques like blowing/suction, hot-air blowing or just the wall-heating. The experimental investigations of DLR Göttingen, Germany emphasize on the nonlinear interaction between the steady and unsteady crossflow modes and their corresponding transition scenarios (see Saric et al. (1998), Bippes (1999) for comprehensive overview). It has been reported that the steady vortices dominate in low-turbulence conditions while for high-turbulence environment, unsteady crossflow waves dominate the flow. For the vortex-dominated scenarios, a high-frequency secondary instability undergoes an explosive growth and causes transition. However, for the regimes dominated by single crossflow wave, slow but steady widening of the Fourier disturbances takes place (Lerche 1996, Bippes 1999). Some experimental studies have been focused on the vortex-dominated transition scenario over a modelled wing in the low-turbulence conditions. The nonlinear development and crossflow vortices excited by varied controlled disturbance input was investigated by Reibert et al. (1996, 1997), Radeztsky et al. (1999). For different steady initial conditions White et al. (2001), White & Saric (2005) have investigated in detail the secondary high-frequency instability which was first discovered by Kohama et al. (1991). Crossflow-vortex induced secondary instability with controlled disturbance excitation for both the primary steady and the secondary unsteady instabilities were experimentally investigated by Kawakami et al. (1999).

Numerous theoretical investigations have also been performed on the topic of boundary layer transition and its control. In a typical theoretical approach, the parabolized stability

equations (PSE) are used to estimate the nonlinear states of the primary modes such as the crossflow vortices. A general overview on this topic is put forward in the study of [Reed et al. \(1998\)](#). In addition to the PSE, [Koch et al. \(2000\)](#) also used the nonlinear equilibrium solutions and compared the saturation amplitudes of both PSE and equilibrium solutions with the DNS results of [Bonfigli & Kloker \(1999\)](#) which had a reasonably good agreement. For more details about the PSE, one can refer to the works of [Malik et al. \(1994, 1999\)](#), [Haynes & Reed \(1996, 2000\)](#), [Janke & Balakumar \(2000\)](#).

[Nolan & Zaki \(2013\)](#) proposed an extreme value model regarding the distribution of streak amplitudes. The proposed model is able to successfully identify the streaks which would breakdown to form turbulent spots. Their study found that the onset of turbulence was due to the high-amplitude streaks of typically more than 20% of the free-stream velocity. Their results also revealed that the volumetric growth rate of turbulent spots was insensitive to the pressure-gradient. Linear growth of the amplitude of disturbance over time, followed by their decay because of the viscous dissipation ([Hultgren & Gustavsson 1981](#)). [Zaki et al. \(2010\)](#) investigated the interactions of streaks with the TS-waves leading to transition. They concluded that the transition onset location was controlled by two mechanisms i.e. the streak distortion inherent in the baseflow which reduce the growth rate of the TS-waves, and direct resonance happening between the 2-D and 3-D instabilities in presence of a wide streak. Recently, [Kurz & Kloker \(2016\)](#) studied the effects of a spanwise row of finite-sized cylindrical roughness elements over a swept-wing boundary layer and reported the changeover from a purely convective to a global instability near the critical height of the roughness element. Recent investigation of [Sundaram et al. \(2019\)](#) has reported that the constant excitation of the TS waves are not always necessary to set-in the transition to turbulence.

### 1.5.2 Classical breakdown scenarios

In a typical controlled transition scenario, after the receptivity, primary-instability modes advance from a linear stage to a weakly nonlinear one before the laminar breakdown (or the fully nonlinear stage). The primary instability modes having the finite amplitudes ( $\approx 0.1-1\%$ ) account for the spectral secondary instability with respect to the secondary modes which grow exponentially as per the findings of [Herbert \(1988\)](#). Fourier approach is usually utilized to study the growth and the behavior of the modes. The modes are labelled based on their contents i.e. the  $(h, k)$  designating the frequency/spanwise wavenumber tuple. Here,  $(h, k)$  denotes the mode with frequency  $hf_0^*$  and spanwise wavenumber  $k\beta_0^*$ , and  $f_0^*$  (or  $\omega_0^*$ ) and  $\beta_0^*$  are the fundamental frequency and the fundamental spanwise wavenumber, respectively. The  $f_0^*$  and  $\beta_0^*$  are obtained from the contours of frequency-spanwise wavenumber plot computed by the linear stability theory (LST) which indicates the combinations of the unstable frequency-spanwise wavenumber tuple. The modes  $(0, k)$  are known as the steady modes,  $(h > 0, k)$  modes are referred as the unsteady or the travelling modes, and  $(h, 0)$  modes are the 2-D modes. The mean-flow distortion (MFD) is given by the  $(0, 0)$  mode. Breakdown

to turbulence can broadly be classified in the following four categories; (i) K-type (Klebanoff) breakdown, (ii) H- (Hebert) or N-type (Novosibirsk) breakdown, (iii) O-type (Oblique) breakdown, and (iv) the By-pass transition.

### **K-type breakdown**

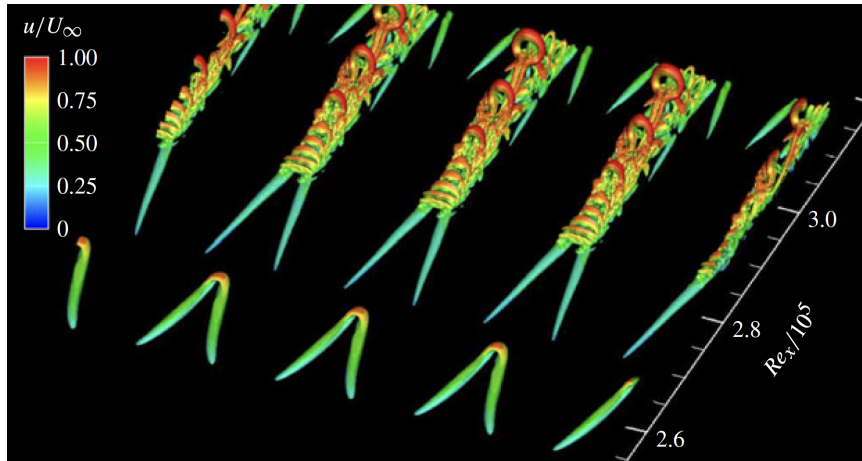
[Klebanoff \(1971\)](#), in his pioneering work observed the emergence of elongated streamwise streaks in the laminar boundary layers as a consequence of the free-stream disturbances. The principal findings of [Klebanoff et al. \(1962\)](#) suggest that two oblique waves bearing the same frequency as that of the fundamental frequency of the TS-waves may interact amongst themselves to produce the higher harmonics but with weaker nonlinear dynamics. This transition scenario is referred to as the K-type (Klebanoff) transition ([Kendall 1985](#)), and is characterized by the in-line arrangement of the  $\Lambda$ -vortices in the transition region (see figure 1.6a), which are precursors of the laminar breakdown. This is a fundamental resonance breakdown scenario (figure 1.7 shows the K-type breakdown in an experimental investigation). The primary mode  $(1,0) > 1.0\%$  intensity and the secondary modes  $(1,\pm 1)$  or  $(0,1)$  are introduced while the missing secondary modes are nonlinearly generated in the downstream ([Kloker 2018](#)). Figure 1.6b shows the wave vector diagram for K-type breakdown; here the principal mode  $(1,0)$  and the secondary modes  $(1,\pm 1)$  are used as the input modes which generate the missing  $(0,1)$  (see figure 1.6b). Also, the subharmonic resonance with  $(2,0)$  is shown which adds the combination resonance ([Kloker 2018](#)) and finally a closed wave-triad is formed (shown by the dotted red arrows in figure 1.6b).

### **H-type breakdown**

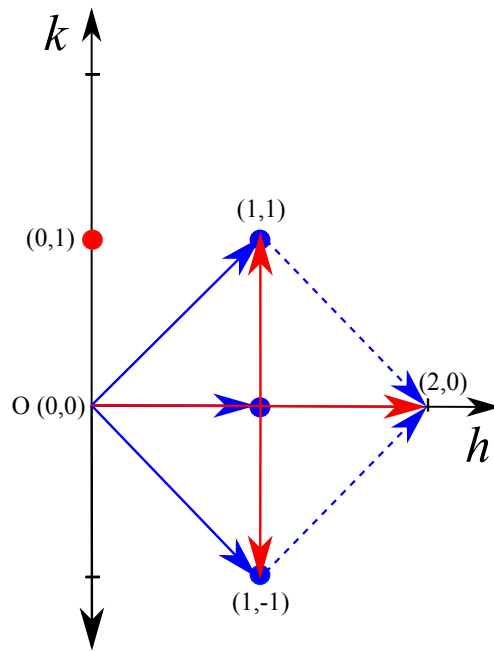
Another type of transition scenario exists which begins with the excitation of the subharmonic fluctuations which are disproportionate to the fundamental TS-wave frequency. For this case, the generalized formulation of the sub-harmonic instability was presented by [Herbert \(1988\)](#). Hence, this scenario is known as the H-type (Hebert) transition, also sometimes referred as the N-type (Novosibirsk) which is characterized by the staggered arrangement of  $\Lambda$  vortices (see figure 1.8a). Figure 1.9 shows the arrangement of  $\Lambda$  vortices in an experimental study. However, the onset of turbulence in the H-type scenario is delayed in comparison to the K-type. The H-type scenario is the subharmonic resonance breakdown scenario where the Principal mode  $(1,0)$ , with more than  $0.1\%$  intensity along with the secondary modes  $(1/2,\pm 1)$ , are excited (see the wave-vector diagram in figure 1.8b). Both the H- and the K-type breakdown scenarios are the consequence of the 2-D mode excitation and are more important in the case of incompressible flows.

### **O-type breakdown**

In the case of supersonic boundary layers, 3-D modes are the most dominant ones, running obliquely with respect to the streamwise direction. Therefore, it is known as the O-type



(a)



(b)

Figure 1.6: (a) Instantaneous iso-Q structures (Sayadi et al. 2013), and (b) wave vector diagram (in blue are the principal and input secondary modes, while red ones are nonlinearly generated) for the K-type breakdown scenario.

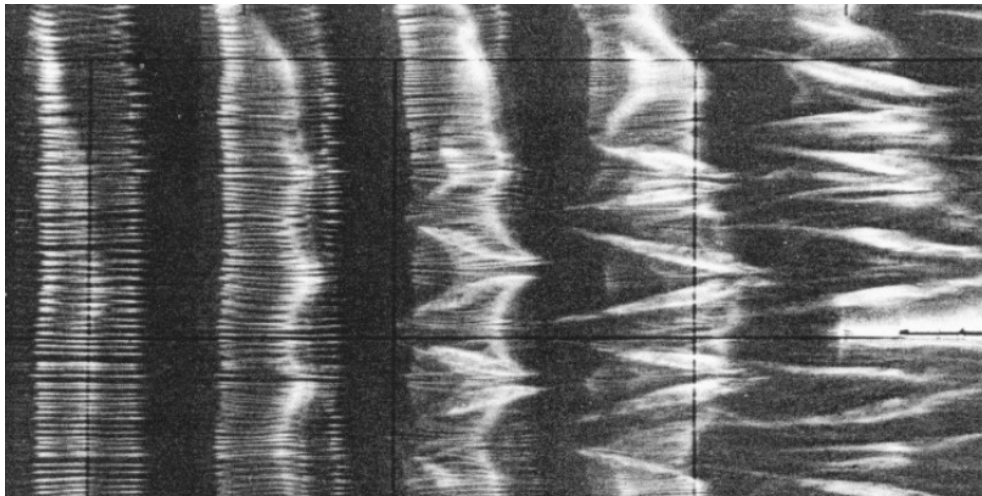
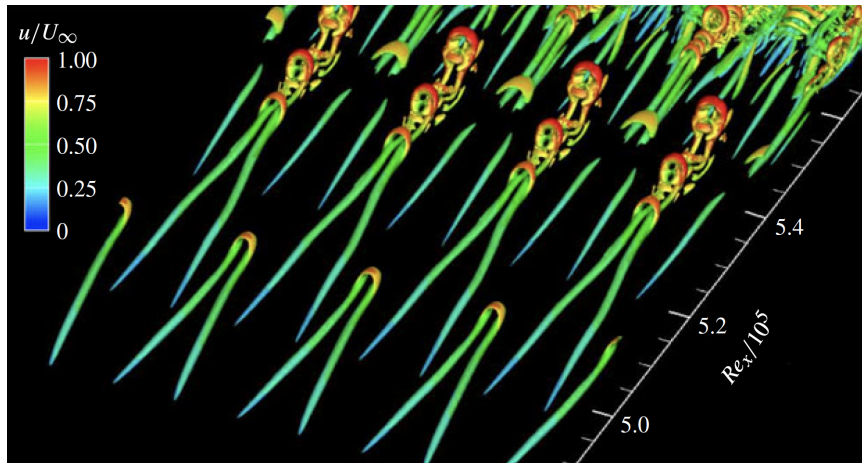
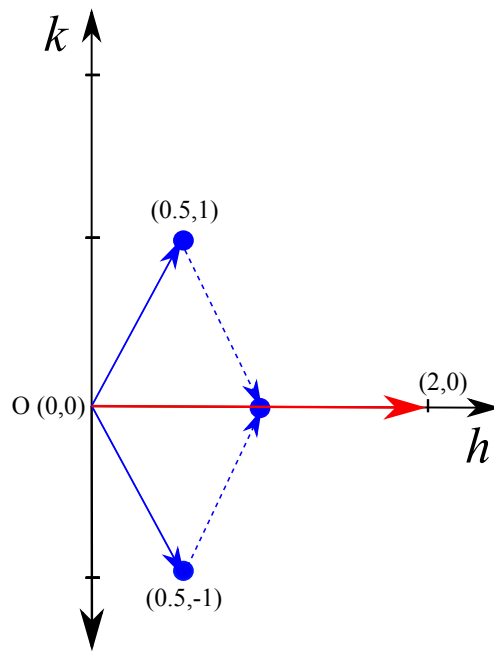


Figure 1.7: K-type transition in an experimental study, see [Saric et al. \(2002\)](#).

(oblique) transition. These waves are also known as the first-mode instabilities. The oblique resonance is generated by the Principal modes  $(1, \pm 1)$  which nonlinearly generate the secondary modes  $(0, 2)$ ,  $(1, \pm 3)$ ,  $(1, \pm 5)$  ... (see the wave triad diagram in figure 1.10b for details). This breakdown is characterized by the linked staggered  $\Lambda$ -vortices (cf. figure 1.10a). DNS studies of [Thumm \(1991\)](#) and [Fasel et al. \(1993\)](#) for supersonic boundary layers at Mach number 1.6 were the first ones that reported the oblique-type breakdown mechanism. [Fezer & Kloker \(2000\)](#) investigated the standard oblique-type breakdown with its velocity-streak modes generated by the fundamental unsteady oblique wave pair(s) in combination with subharmonic 3-D modes using DNS at Mach 2. They found that the growth rates of 3-D subharmonic modes were less significant than those of the fundamental mode, and hence, the standard oblique-type breakdown was found to be dominant. However, the study also concluded that the presence of subharmonic modes did speed-up the transition process. Their findings contradicted the conclusions of [Kosinov et al. \(1994\)](#) who did not document steady modes at that time. Later on, [Mayer et al. \(2011\)](#) replicated the DNS for the conditions of [Kosinov et al. \(1994\)](#) and confirmed the importance of oblique-type breakdown mechanism in the experiments (see figure 1.11). Nowadays, it is very clear that the streak modes inherent in oblique breakdown play an essential role as their amplitude grows strongly, fed by non-linear generation of the unsteady modes and some continuous add-up by a transient-growth mechanism, see [Laible & Fasel \(2016\)](#). Streak instability finally causes the laminar breakdown. When these streaks attain nonlinear amplitude, a localized secondary instability is induced on either side of the streak with sinuous- or varicose-type disturbances which modulate sinuous or varicose type streaks, respectively. Moreover, streaks would definitely form in the boundary layer if the turbulence intensity in the free-stream is  $> 1\%$  ([Zaki 2013](#)).



(a)



(b)

Figure 1.8: (a) Instantaneous iso-Q structures (Sayadi et al. 2013), and (b) wave vector diagram (in blue are the principal and input secondary modes, while red ones are nonlinearly generated) for the H- or the N-type breakdown scenario.

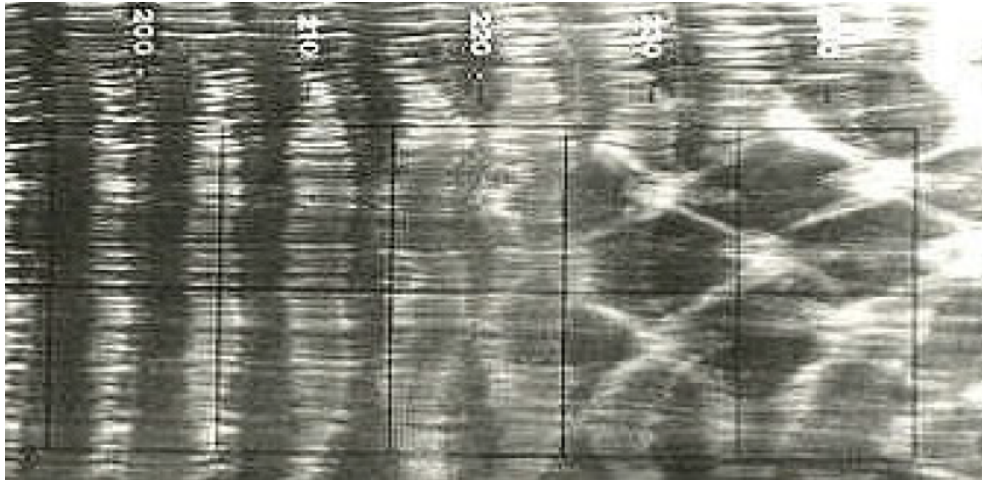


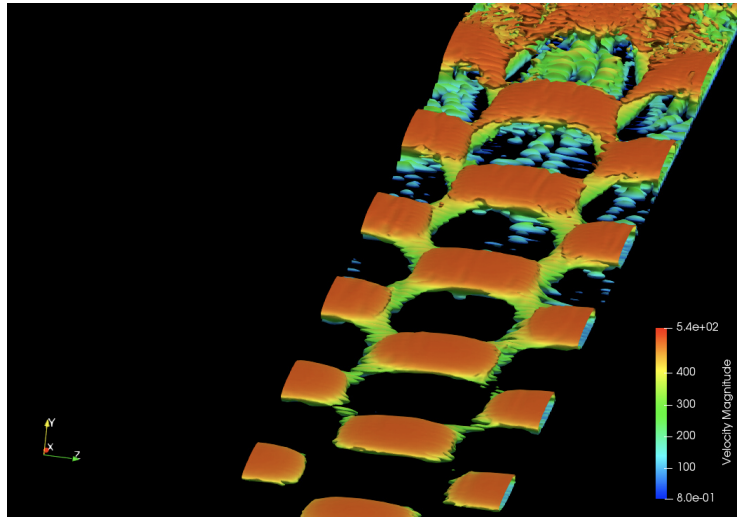
Figure 1.9: H-type transition in an experimental study, see [Saric et al. \(2002\)](#).

### By-pass transition

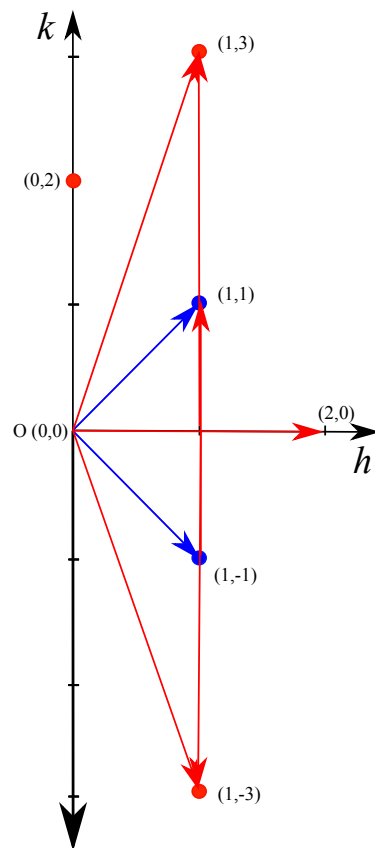
In case of strong transient growth, a distinctive secondary instability is not formed (or is bypassed) and a turbulent spot appears directly ([Kloker 2018](#)). This scenario is termed as the by-pass transition (cf. figure 1.12). After passing-by, the turbulent spots leave a wake region behind. This phenomenon can be observed in the cases of high turbulence intensity caused by strong localized blowing and suction. The medium-amplitude streaks may hinder the growth of the TS-waves and hence can delay TS-wave induced transition ([Fransson et al. 2006](#)). [Durbin & Wu \(2007\)](#) found that some streaks in case of the by-pass transition did indeed go through the stage of formation of the secondary instability before the breakdown. These turbulent spots finally merge together in the downstream to form the fully developed turbulent region. The very random and localized nature of this type of transition makes it challenging to investigate.

### 1.5.3 Compressible transitional boundary layers

Knowledge of high-speed boundary layer flows poses fundamental challenges in the fluid dynamics community and are equally important to be investigated at the same time. For the high-speed applications like the supersonic aircraft and spacecraft, the temperature of the wall becomes an important parameter to be incorporated in the study ([Duan et al. 2010](#)). The wall temperature of a speeding aircraft is significantly lower than the adiabatic temperature of the wall, but on the other hand in case of the atmospheric reentry of a spacecraft, the wall temperature becomes way too higher than the adiabatic wall temperature as a result of the frictional heating by the atmosphere. Moreover, the high-temperature of the exhaust gases over the blade of a gas turbine ([Tutar & Sönmez 2010](#)) or the wall of any propulsive nozzle ([Bensayah et al. 2014](#)) also mimic the heated wall scenario. Prediction of the onset of turbulence is of the utmost importance for designing the thermal protection system for the



(a)



(b)

Figure 1.10: (a) Instantaneous iso-Q structures, and (b) wave vector diagram (in blue are the input principal modes, while red ones are nonlinearly generated) for the O-type breakdown scenario.



Figure 1.11: O-type transition in an experimental study, see [Kloker \(2018\)](#).

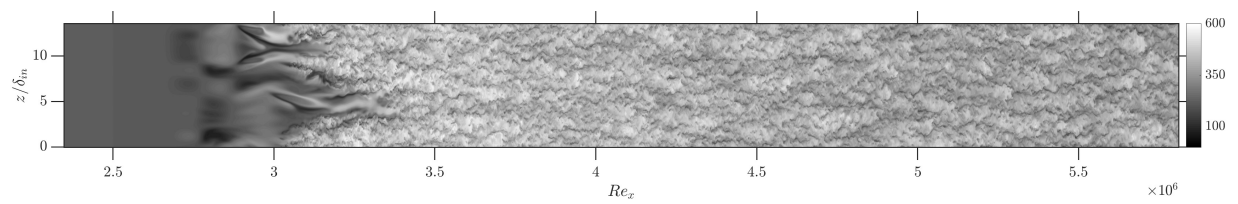


Figure 1.12: An example of by-pass transition in the case of a supersonic adiabatic flat plate with  $M_\infty = 2.2$ .

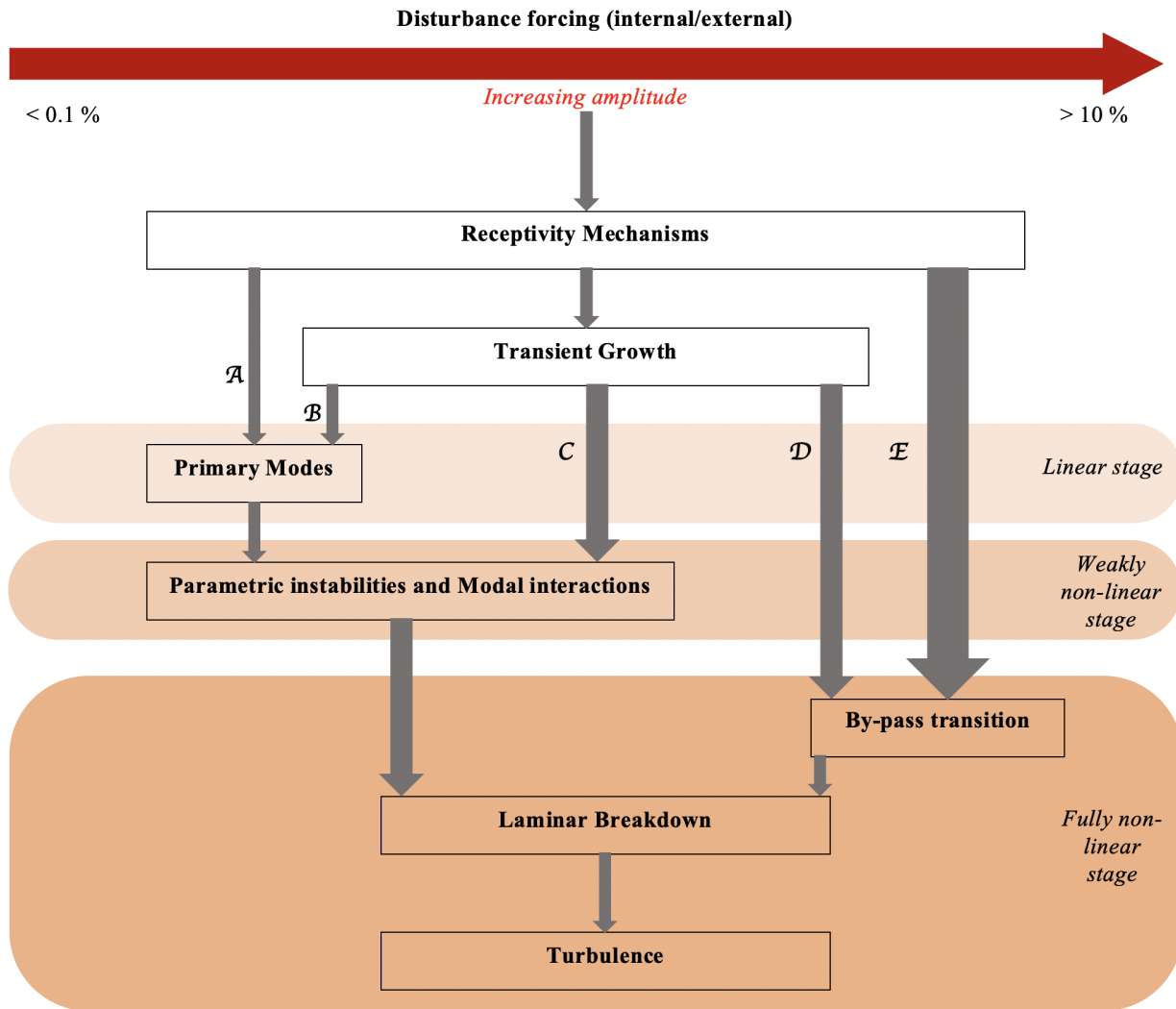


Figure 1.13: A Road Map of boundary-layer transition (Morkovin (1994), Fedorov (2011)).

spacecraft, see Berry et al. (2001). For a spacecraft, the initial laminar flow could be tripped to turbulence because of the surface roughness and the turbulence intensity (Reda et al. 2010). Despite of the numerous numerical and experimental investigations (Duan et al. 2018, Horvath et al. 2002, Kosinov et al. 1997), the mechanisms of transition for the supersonic boundary layers is poorly understood due to the difficulties in accurate measurements (Schneider 2001).

For the high-speed compressible boundary layers, transitional and stability characteristics have been investigated comprehensively through various experimental and numerical investigations. Based on the initial levels of the disturbance amplitude, Fedorov (2011) presented different paths leading to transition (as shown in figure 1.13). The figure shows five different paths leading to turbulence (paths A to E). Path A represents the classical path of modal growth which starts with a low-disturbance level followed by the linear, weakly

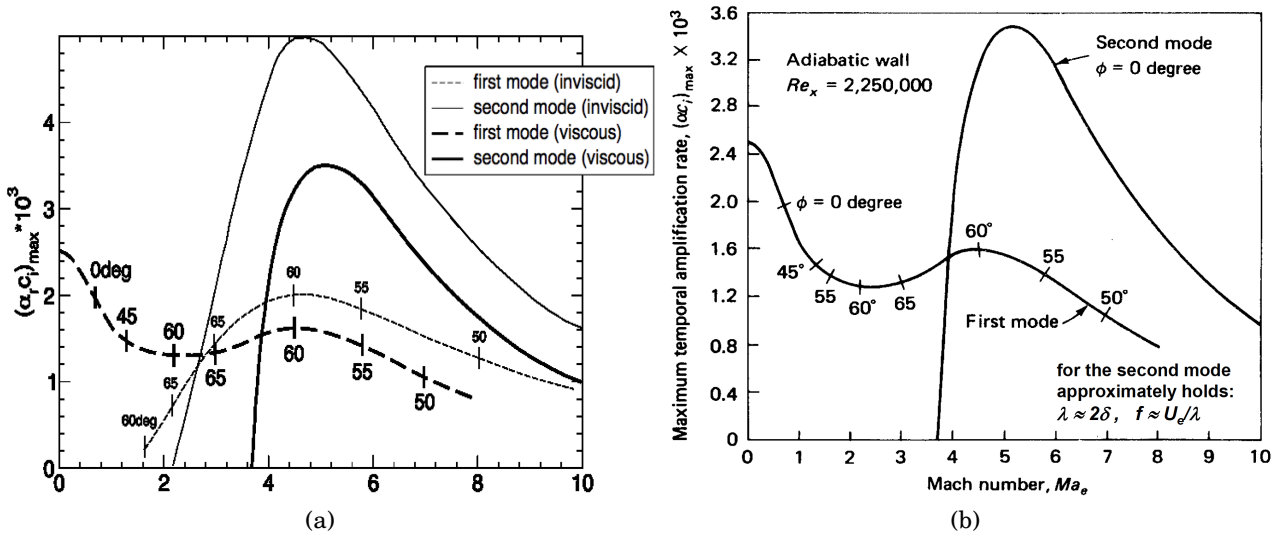


Figure 1.14: (a) Influence of viscosity on the growth rate of different modes. Here, the x-axis represents the Mach numbers, and (b) Disturbance growth rate of various modes as a function of Mach number (Kloker 2018).  $\phi$  represents the wave angle with respect to the flow direction (White & Corfield 2006, Kloker 2018).

non-linear and fully non-linear stages before the onset of turbulence. No transient growth is seen in this case, classical K- and H-type mechanisms follow this path. However, with the increase in the disturbance amplitude transient growth mechanisms happens soon after the receptivity, followed by the usual sequence of events of path A (path B). Oblique-type transition scenario involves transient growth on-top of a nonlinear generation (see Laible & Fasel (2016)) which constantly increases the amplitude somewhat but causes no extra growth-rate increase (as discussed earlier regarding the O-type transition scenario). For larger levels of disturbance amplitude, the transient growth becomes dominant i.e. paths C and D. However, for very large amplitudes of initial disturbance, the flow instantly breaks down without passing through the usual linear disturbance evolution pathways forming a localized turbulent spot. This spot sets-in fully developed turbulence. Hence, this scenario is known as the by-pass transition scenario (path E).

As discussed earlier, the 2-D TS-waves dominate the transition scenario for the incompressible boundary layers. However, sometimes it is falsely concluded that the 2-D modes are always more amplified than the 3-D ones (Kloker 2018). 3-D modes are the most-amplified modes in the supersonic regimes. Up to the free-stream Mach number  $M_\infty = 3.5$  (subscript  $\infty$  represents the free-stream quantities), the TS-(like) modes are stabilized. For the flow with  $M_\infty > 1.5$ , a generalized inflection point (GIP) exists near the edge of the boundary layer causing the inviscid instability which causes the flow to transit to turbulence (cf. figure 1.14a, for more details, see Kloker (2018)). For high-speed flows with  $M_\infty > 3.5$ , the acoustic mode instabilities or the Mack modes dominate the flow (see Mack (1984, 1987))

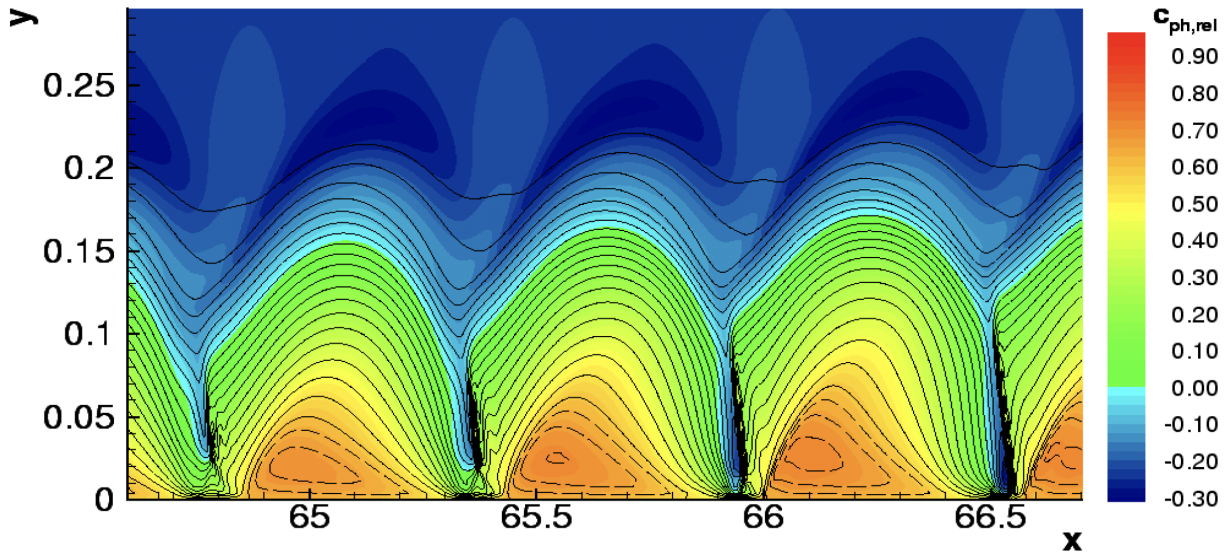


Figure 1.15: Iso-contours of phase-velocity showing the acoustic modes (Kloker (2002)).

for comprehensive overview). The growth rate of these modes is twice as large as that of the first mode instabilities (see figure 1.14b) because of the bouncing back and forth of the trapped acoustic modes between the wall and the sonic line. These modes are also known as the trapped modes (as can be seen in figure 1.15). In these regions, the disturbance travels faster locally than the sound waves with a typical high frequency (300 – 1000  $kHz$ ). The studies have shown that the wall cooling tends to stabilize the vorticity (or the first) mode instability and destabilize the second mode because of the larger supersonic region (Kloker 2018). Moreover, the temperature profile has to be taken into consideration for determining the instability because retarded-flow scenarios may occur which could be stabilized by wall cooling. For high-speed boundary layer transition, numerical investigations are mainly focused on transition through roughness elements. Bernardini et al. (2014) and Van den Eynde & Sandham (2015) have analyzed the effects of different shapes of roughness elements on transition. The results of Van den Eynde & Sandham (2015) reveal that the frontal shape of the roughness element and the shape in streamwise direction had a large impact on the onset of transition in the hypersonic regime. Bernardini et al. (2014) have also investigated the dominant instability modes in the near field past the roughness element and have given a new parameter for the prediction of transition. Groskopf & Kloker (2016) highlighted the impact of the orientation of the roughness element on the laminar streak breakdown scenario. They found that obliquely placed roughness element did generate more pronounced low-speed streaks in the roughness wake. For a given height of a roughness element, the unstable wake modes of various types have been investigated by De Tullio et al. (2013) where the results reveal that varicose modes are the most unstable ones. The main objective of these studies was to better understand the mechanisms responsible for laminar to turbulent transition in high-speed flows. However, it seems that many voids are still present

in the knowledge of such mechanisms in particular for supersonic and hypersonic regimes as compared to the incompressible flows. [Schneider \(2008\)](#) has presented an exhaustive overview of current state-of-the-art for flow transition for high-speed flows.

#### 1.5.4 Global linear stability analysis

The classical LST depends on the eigen-functions based on the wall-normal direction. However, the underlying theory dealing with the flow instability has now been extended to other spatial dimensions too. [Theofilis \(2011\)](#) presented an exhaustive overview of the theoretical approaches, numerics and physical applications of the LST for 2-D and 3-D flows. In the traditional LST approaches, the growth of small-amplitude perturbations in a 3-D laminar baseflow is studied by solving the initial value problem or an eigen-value problem. This problem set-up arises from the linearization of different equations like the continuity, momentum and energy equations based on the bi-global (2-D problem), or the tri-global (3-D problem) LST problem. [Åkervik et al. \(2006\)](#) generated the steady flow by utilizing the selective frequency damping in order to investigate the unsteady flows consisting of steady set-up and boundary conditions. [Marxen et al. \(2010\)](#) applied the classical LST to study the mechanisms of disturbance amplification past a 2-D roughness element in hypersonic regimes. Various investigations regarding the incompressible swept-wing configuration with crossflow instabilities in flight conditions was put forward by [Koch et al. \(2000\)](#), [Bonfigli & Kloker \(2007\)](#). The investigation of [Bonfigli & Kloker \(2007\)](#) validated the results of the LST against the DNS results, and found three dominant eigen-modes of crossflow vortices. However, only two of the considered modes were successfully confirmed by the DNS counterparts. Non-local downstream marching of the PSE along with the bi-global LST can be used for overcoming the parallel-flow assumption (see [De Tullio et al. \(2013\)](#) for a comprehensive overview). For further information regarding the bi-global LST applied to super/hypersonic flows, one can refer to the works of [Groskopf et al. \(2010\)](#), [Schmidt & Rist \(2011\)](#), [Choudhari et al. \(2010, 2013\)](#), [Groskopf & Kloker \(2012\)](#).

#### 1.5.5 Effect of wall-heat transfer

Regarding the incompressible flows, many studies have been undertaken to understand the effects of heat-transfer on the onset of turbulence. [Lee et al. \(2013\)](#) have investigated the influence of viscosity stratification by wall heating on skin-friction reduction in turbulent boundary layers for heated and super-heated walls. Their study utilized the incompressible flow considering water as the medium. The results of their DNS revealed a reduction in the skin-friction coefficient for heated and super-heated walls, which implies that wall-heating tends to stabilize the flow ([Lee et al. 2013](#)).

For high-speed flows, growth mechanism discussed by [Redford et al. \(2012\)](#) highlights that the mainstream Mach number is the main governing parameter in determining the lateral growth rate of the turbulent spots, while the wall temperature being the secondary

one. They have also revealed that instability of the lateral jets which show up close to the turbulent zone in the domain serve as a trigger for generation of the new turbulent spots further downstream. Redford et al. (2011) have utilized a thermal wall model which is coupled at high Mach number and showed that due to the frictional heating of the wall resulting from the fluid flow, the flow tends to re-laminarize with time. An investigation regarding the implications of wall heat transfer on Klebanoff modes and TS-waves has been performed by Ricco et al. (2009). They have highlighted various scenarios in which whether the wall cooling or heating will stabilize the flow. The results suggest that laminar streaks are stabilized by wall cooling when spanwise wavelength is quite large in comparison to the boundary layer thickness. Whereas for the Klebanoff modes, when the spanwise diffusion is comparable to the wall-normal diffusion, they are stabilized by wall heating. Franko & Lele (2014) investigated the effects of adverse pressure gradient on laminar to turbulent transition of high speed flows, typically for Mach 6. They have studied three different transition mechanisms namely the first mode oblique breakdown, the second mode oblique breakdown and the second mode fundamental resonance. Their results showed that the adverse pressure gradient did not fundamentally alter the process of transition nor the heat transfer overshoot. However, it did prepone the transition process and augmented the growth rate for both the first and the second mode instabilities. Their results also highlight that the fundamental disturbances lead to immediate transition to turbulence in case of the first mode oblique breakdown scenario because of the interaction of two oblique first mode instabilities which generate large streamwise vorticity producing an overshoot in heat transfer and generation of large amplitude streaks of velocity and temperature. These streaks breakdown soon owing to their large magnitude. The skin friction and the heat transfer overshoot in the transition region have been observed in many experimental studies like in Wadhams et al. (2008). The numerical investigation about the heat transfer overshoot and breakdown mechanisms for high speed boundary layers was done by Franko & Lele (2013) involving different types of transition mechanisms as in Franko & Lele (2014) but with zero pressure gradient. They uncovered that for all the three mechanisms the breakdown to turbulence was preceded by growth of the streamwise streaks. It was also observed that the second mode instabilities tend to dominate the flow with decrease in the wall temperature. Franko & Lele (2014) also found that the second mode fundamental resonance mechanism did not change with decreasing temperature. The study concluded that the first mode oblique breakdown was the most-likely mechanism of heat transfer overshoot found in the experimental studies before.

Shadloo et al. (2016) investigated the effects of wall heat transfer on transition onset for supersonic flows at freestream Mach number of 2.2. Good agreement was observed in the results of the LST and the DNS for the adiabatic case. On contrary to the LST predictions, for the isothermal cases it was found that heating up the wall actually stabilized the flow and it transit farther downstream to turbulence when compared to the adiabatic wall, while on the other hand, cooling down the wall did destabilize the flow and it transited

upstream in comparison to the adiabatic case. It is noted that the main reason accounted for this discrepancy was the mismatch of the baseflow, because all of the investigated cases had adiabatic baseflow regardless of the wall temperature. [Shadloo & Hadjadj \(2017\)](#) also showed the evolution of the disturbance energy in the streamwise direction and found that the growth-rate slopes remain the same and merge together in turbulent area, regardless of the wall temperature. Both previous works have considered high perturbation intensities of 2.4% and 4% of the freestream velocity which resulted in the by-pass transition. [Shadloo & Hadjadj \(2017\)](#) plotted the evolution of the disturbance energy, which is the energy associated with the unsteady streamwise velocity fluctuations, in the streamwise direction and uncovered that the slopes of the growth rate did not change and tend to merge together in turbulent part regardless of the wall temperature. [Sharma et al. \(2018a\)](#) investigated the effects of different physical mechanisms like perturbation intensity and wall temperature on transition onset location and transition length for compressible supersonic boundary layers. They found that below 1% perturbation intensity, wall cooling stabilized the flow and it remained laminar while wall heating had a destabilizing impact causing the flow to transit upstream in comparison to the adiabatic wall. Beyond the 1% perturbation intensity, wall cooling instead of stabilizing the boundary layer it destabilized it resulting in the upstream shift of transition onset location [Sharma et al. \(2018a\)](#) and inverse was found for the heated wall.

Dynamic mode decomposition (DMD) method has been utilized to reveal the behavior and evolution of induced perturbation frequency and its super-harmonics throughout the computational domain. This method was introduced by [Schmid \(2010\)](#), focusing on extracting the information about fluid dynamical and transport processes. Various methods and algorithms were developed later on as mentioned by [Tu et al. \(2013\)](#) and [Kutz et al. \(2015\)](#). This method tracks modal growth in the computational domain. See [Zhang & Zheng \(2018\)](#) for an overview and application to the airfoils. The results obtained from the DMD analysis of [Sharma et al. \(2018b\)](#) uncover two distinct ways of evolution for odd and even harmonics of the perturbation frequency. DMD results also show that the fundamental evolution of the modes is not affected by the physical flow parameters like wall temperature or existence of thermo-mechanical non-equilibrium. It is observed that the imposed frequency mode or the principal mode is dominant in the transition region and eventually breakdown to smaller structures in the turbulent regime.

## 1.6 Transition control techniques: A general overview

The existence of turbulent flow causes penalties in form of increased skin friction and rise in wall temperature (in compressible flows) due to the aerodynamic heating. Several countermeasures have been devised in order to suppress or significantly delay the onset of turbulence. Some of the control techniques are discussed below in brief:

1. **Baseflow modification:** A baseflow modification is introduced in order to suppress

or delay the primary instability. In this technique, a favorable (0,0) mode is added, for example by 2-D boundary layer to get a more fuller velocity profile, which moves the unstable region downstream (Kloker 2018). For hypersonic flow, the second mode can be stabilized by weakly blowing a light gas (Kloker 2018).

2. **Steady control disturbances:** Nonlinear control disturbances that do not trigger a localized instability but hinder the growth of the natural disturbances are forced. 3-D boundary layer can be seeded with upstream vortices causing the upstream flow distortion (UFD) (Wassermann & Kloker 2002) or the distributed roughness elements (Wassermann & Kloker 2002, 2000, Saric et al. 2003). And, the 2-D boundary layer could be seeded with the useful streaks (Fransson et al. 2006).
3. **Unsteady control disturbance needing sensors:** This control technique classically comprises of forcing an out of phase disturbance by blowing and suction or by vibrating ribbon in an unsteady manner. It is best suited for the early linear stages of the TS-waves. However, in the nonlinear regions, for example, the mode (0,1) in case of the K-type breakdown is insensitive to this type of control (Kloker 2018).
4. **Localized control needing sensors:** This is a mixture of techniques 1 to 3 which is used to counter large amplitude disturbances. Large-amplitude crossflow vortices can be countered with the local application of suction at the spot of the possible updraft in order to hinder it. This is also known as the pinpoint suction (Friederich & Kloker 2012, Kloker 2008) and could be accompanied by the plasma actuators (Dörr & Kloker 2015).
5. **Passive disturbance damping:** This method is utilized for the hypersonic flow stabilization. It involves the weakening of the growth rate of the second mode instability by the porous wall which is formed by the Ultrasonic Absorptive Coating (UAC). The damping can be further enhanced by the quarter-pipe effect which means that the reflected wave from the bottom of the porous surface superimposes with the oncoming pressure wave in an anti-phased manner. On the downside, this technique can slightly amplify the growth of the first mode (Wagner et al. 2014, Fedorov et al. 2003).

### 1.6.1 Controlling oblique-type transition

Regarding the control of transition in cases where 2-D TS-waves dominate (incompressible flow), the forcing of control streaks has been investigated, see, e.g., Cossu & Brandt (2002), Bagheri & Hanifi (2007), Shahinfar et al. (2012). Only the streak amplitude must not be too high - otherwise localized shear-layer instabilities cause rapid transition (Andersson et al. (2001)). For oblique breakdown with its inherent streak modes the additional forcing of such modes does not look promising at first, and was only investigated recently in a first study on the interaction of modes by Paredes et al. (2017).

On the other hand, Saric et al. (2003) and Wassermann & Kloker (2002) successfully investigated the control strategy using appropriate steady control vortex modes for the generic base flow on a swept wing, where crossflow instability leads to exponential amplification of

such steady modes. The findings also report that closely-spaced vortices can suppress the wider spaced modes responsible for the natural breakdown. Importantly, [Wassermann & Kloker \(2002\)](#) attributed the suppression of the most-amplified steady modes to the mean-flow distortion (MFD) generated nonlinearly by the UFD by the control modes. It was found that the 2-D part of the UFD weakened the growth while the 3-D part the receptivity of the naturally most growing modes; for Blasius flow similar findings concerning the MFD are reported, see, e.g., [Dörr & Kloker \(2017\)](#). Stabilization of a supersonic 2-D boundary layer using optimally growing streaks has been discussed in the recent study by [Paredes et al. \(2017\)](#). They utilized the nonlinear plane-marching PSE to predict the development of finite, stationary disturbances and their interaction with oblique waves. The study concludes that the spanwise wavelength of the control streaks must be smaller than the one of the naturally most growing oblique travelling modes by a factor of two at least, in order not to reinforce the streak mode inherent in the oblique-breakdown scenario. However, neither DNS nor experiments have so far been reported for successful control of supersonic boundary-layer oblique breakdown.

Although the PSE study of [Paredes et al. \(2017\)](#) provides a conceptual model for characterizing a stabilization provided by transiently growing optimal streaks, still some important questions need to be addressed. As later transition stages are completely nonlinear and unsteady, the situation needs a deeper analysis using full DNS. The full effects of "control" streaks, possibly not growing but decaying, are not known for the O-type breakdown. How effective are they in the full scenario to turbulence, and which spanwise spacing is useful?

## 1.7 Turbulent boundary layer

Scientific community is trying to characterize the turbulent flows from a very long period of time. The physical aspects of the turbulent flows are comparatively well-understood and explored than the transitional flows. The study performed by [Theodorsen \(1952\)](#) brings out the importance of the coherent structures in incompressible turbulent wall-bounded flows. Their results shed light on the fact that these structures are responsible for low-momentum fluid transport and Reynolds shear-stress production. The morphology of these structures were experimentally verified by [Head & Bandyopadhyay \(1981\)](#). The investigation presented by [Stanislas et al. \(2008\)](#) suggests that in the turbulent boundary layer, asymmetric one-legged hairpin vortex is the most-probable shape of the coherent structures. Later on, the numerical study performed by [Wu & Moin \(2009\)](#) stated that the forests of hairpin vortices dominate the turbulent boundary layer. Experimentally, the events of ejections and sweeps which are responsible for Reynolds shear-stress production were visualized by [Corino & Brodkey \(1969\)](#). [Wallace et al. \(1972\)](#) quantified the turbulent processes and provided further insight about Reynolds stress production in the near-wall region for the incompressible turbulent channel flows. Their results revealed that ejections and sweeps together contribute more than 100% to the Reynolds shear-stress and the additional stress was countered by other

contributing factors named interactions.

For the incompressible turbulent channel flows, [Wallace & Brodkey \(1977\)](#) performed the joint probability density distribution function (JPDF) and covariance integrands analyses for streamwise and wall-normal velocity fluctuations in order to find out the contribution of different transport processes towards the Reynolds shear-stress. Their results suggest that when moving from near wall-region i.e.  $y^+ = 5$  to the end of the log region, there exist different physical phenomena which dominate the transfer processes. They also showed that the most-probable velocity pairs did not have the largest contribution towards the shear-stress. Major contribution of ejections towards Reynolds shear stress was also reported by the experimental investigation of [Willmarth & Lu \(1972\)](#). The results presented by [Ong & Wallace \(1998\)](#) highlighted the ability of JPDF and covariance analyses in determining the topology of the turbulent flows. The results of this study helped in determining the most probable angle of inclination of the vorticity filaments using the covariance integrands' analyses. The events of vortex stretching and compression were also discussed in detail. It was found that the average stretching of the filaments was greater than compression at all of the considered locations ([Ong & Wallace 1998](#)). DNS of [Le et al. \(2000\)](#) investigated the changes in three-dimensional turbulent boundary layer by employing a combination of different statistical and visualization techniques. Their results uncovered that mean three-dimensionality was responsible for breaking up the symmetry and alignment of near-wall coherent structures disrupting their self-sustaining mechanisms, and resulting in the reduction of the turbulent kinetic energy.

Fewer investigations have been performed so-far for the compressible turbulent boundary layers. For low Mach number turbulent boundary layers, the DNS results of [Bechlars & Sandberg \(2017b\)](#) found the potential backscatter mechanism for the transfer of the kinetic energy from smaller scales to the larger scales. The effects on the first three invariants of the velocity gradient tensor with wall-normal distance for weakly compressible flow are studied by [Bechlars & Sandberg \(2017a\)](#). Recent investigation of [Avellaneda et al. \(2019\)](#) regarding the low Mach number channel flows with high temperature gradient arising due to the non-symmetric heating from the temperature-dependent fluid properties revealed that the mean temperature stays the same, and positions of the zero shear-stress and the maximum mean longitudinal velocity slightly tend to move towards the hotter side of the channel. The experimental database available for this type of problem is scarce due to the difficulty in measurements. The experimental investigation of [Spina et al. \(1994\)](#) revealed that the compressibility has little impact on the statistical properties of the flow. One of the first investigations reported by [Morkovin \(1962\)](#) suggests that the effects of compressibility on turbulence are due to the variations of the thermodynamic properties across the boundary layer. The experimental data also confirms that the supersonic boundary layers bear close similarities to the incompressible ones ([Smits & Dussauge 2006](#), [Li & Xi-Yun 2011](#)) from the statistical point of view. [Li & Xi-Yun \(2011\)](#) have reported that the angles of inclination of the vortical structures with the streamwise direction increases from the sub-layer to

the buffer layer and then decreases from the buffer layer to the wake region. [Maeder et al. \(2001\)](#), [Pirozzoli et al. \(2004\)](#) have investigated the structural characteristics of supersonic turbulence and found the presence of organized motions in the outer layer. The study presented by [Pirozzoli et al. \(2008\)](#) quantitatively characterized the statistical features of coherent structures for the case of turbulent supersonic boundary layer and found that the inner layer was mostly populated by quasi-streamwise vortices while the outer layer (including log and wake region) was populated by different types of structures such as hairpin vortices and hairpin packets. Recent study of [Zhang et al. \(2017\)](#) has investigated the impacts of wall temperature on single- and multi-point statistics of pressure fluctuations at different wall-normal locations for hypersonic case  $M_\infty = 6$ . Their results revealed that the acoustic sources were mainly concentrated in the near-wall region and wall cooling was found to significantly influence the nonlinear component of the acoustic term by enhancing dilatational fluctuations in the sublayer while damping vortical fluctuations in the buffer and log layers. [Shadloo et al. \(2015\)](#) investigated the impacts of wall heat-transfer on the statistical properties of the supersonic turbulent boundary layers. They found out that the behavior of near-wall turbulence was affected by wall heat-transfer for turbulent Mach numbers less than 0.3. [Tong et al. \(2017\)](#) have studied the impact of wall cooling on turbulent structures and shock motions. Their results suggest that wall cooling significantly affects the log region of mean velocity profile downstream of the interaction region. The streamwise coherence of the streaks did increase with decrease in temperature, but the shapes of dynamic modes were not sensitive to the wall temperature ([Tong et al. 2017](#), [Hadjadj et al. 2015](#)).

The careful examination of the existing scientific literature reveals that the studies pertaining to the effects of wall-heat transfer on turbulent flow topology for compressible supersonic boundary layer are scarce. The study investigating supersonic cooled turbulent channel flows in [Lechner et al. \(2001\)](#) deals with effects of compressibility on pressure-strain correlation and the dissipation rate tensors in Reynolds stress budgets. The results of this study revealed that fluctuations conditioned on ejections and sweeps in wall-layer were instructive, and showed that positive temperature fluctuations were mainly due to sweeps in case of the cooled wall. Moreover, the comparison with the incompressible flow data underlined that compressibility effects persisted in wall-layer only. Relevant statistical properties of compressible turbulent flows (including the heated wall) are assessed in [Shadloo et al. \(2015\)](#). This study found that Morkovin's hypothesis was neither valid for the heated walls nor for the cooled walls. The analysis of the turbulent kinetic energy budget showed that the dilatational to solenoidal dissipation ratio increases/decreases with heating/cooling of the wall. Later on, [Trettel & Larsson \(2016\)](#) proposed the transformations of velocity and wall coordinate simultaneously for the supersonic isothermal turbulent channel flows and turbulent boundary layers relating compressible mean velocity profile at any given Mach number. For low-Mach number heated channel flows, [Patel et al. \(2017\)](#) found that the van Driest transformed mean temperature profiles of variable property cases collapsed with constant property cases if semi-local Reynolds number and local Prandtl number distributions

are constant across the channel. [Chu et al. \(2013\)](#) studied the effects of wall temperature on the orientation of vortical structures and other statistical properties like Morkovin's scaling. It was found that with the increase in temperature, spanwise distance between the legs of the hairpin vortex increased, the mean swirling strength and the angle of the vorticity filament with the wall also increased in the inner layer. However, the statistical properties of vortical structures were nearly insensitive to the wall temperature in the outer layer. They also put forward new criteria for better characterizing the angles of inclination of the vortical structures. Other works characterized the factors influencing the transition scenarios for compressible supersonic flows [Shadloo et al. \(2016\)](#), [Shadloo & Hadjadj \(2017\)](#), [Sharma et al. \(2018a\)](#). However, for the supersonic boundary layers, it is important to address the impacts of wall heating and cooling on arrangement and orientation of vortical structures and heat-transfer mechanisms, which are the fundamental and still open questions for the community.

## 1.8 Scope of the present study

From our discussion of the existing literature presented so far, it is clear that although comprehensive research investigations have been performed regarding the compressible boundary layer, but the fundamental questions concerning the impacts of various physical parameters on the onset of transition are very scarce. As discussed earlier, the oblique-type breakdown is the main route to transition in supersonic boundary layers. However, there has not been any study neither experimental nor numerical reported concerning the control of the O-type breakdown in a controlled transition environment. Therefore, in order to understand the fundamentals of the compressible supersonic boundary layers, we define the following main objectives to investigate:

1. Understanding the O-type breakdown in a controlled disturbance input scenario, and to present an effective method such as the large-amplitude decaying streak modes to suppress the transition to turbulence. Also, finding out which part of the control (2-D or 3-D) is responsible for the effective control.
2. Investigating the implications of different physical parameters like the initial perturbation amplitude, wall-temperature and baseflow variations on the onset of transition for high-speed boundary layers.
3. Studying the impacts of wall temperature on the flow topology, and important physical parameters like the shear stress and different components of heat flux of the fully developed turbulent boundary layer using the JPDF distribution and the covariance intergrads analyses.

## 1.9 Outline of the dissertation

As mentioned earlier that a comprehensive overview of the literature reveals that many important questions regarding the characterization and the control of compressible transitional boundary layers are still open. Therefore, in our study we would like to address some of the open topics in detail. This thesis is organized as follows:

**Chapter 2:** This chapter elaborately describes the governing equations as well as the numerical details of the DNS solver. The chapter also contains the information regarding the employed Fourier analysis to obtain the evolutionary trend of different modes. Towards the end of the this chapter, some results concerning the code validation, and results of baseflow are also presented.

**Chapter 3:** In this chapter, we present the control of the O-type breakdown scenario using control streak modes. Only the adiabatic case is considered. To the best of our knowledge, this chapter reports the first DNS study concerning the control of oblique breakdown scenario using the streak modes. The chapter focuses on the effectiveness of the streak modes in controlling the oblique-type breakdown in supersonic boundary layer. The results reveal that both the 2-D and the 3-D parts of the control mode are responsible for suppressing the transition to turbulence. The results are published in: *Journal of Fluid Mechanics* (Sharma, Shadloo, Hadjadj & Kloker 2019).

**Chapter 4:** The by-pass transition scenario is focused in this chapter. Implications of different physical phenomena including the intensity of perturbation and wall-temperature on the onset of transition are presented. The results are published in: *Numerical Heat Transfer, Part A: Applications* (Sharma et al. 2018a).

**Chapter 5:** This chapter continues the discussion about the by-pass transition scenario and the effects of baseflow variations (named as thermo-mechanical non-equilibrium here) on the onset of transition are discussed in detail. The DMD is used to reveal the behavior of the prescribed modes used to excite the flow to turbulence. The results are published in: *Heat and Mass Transfer* (Sharma et al. 2018b).

**Chapter 6:** This chapter deals with the supersonic turbulent boundary layers, in which JPDF and covariance analyses are utilized to unravel the physical mechanisms responsible for heat transfer in the streamwise and the wall-normal directions. Various quadrant analyses of covariance integrands have been put forward to find out the most-significant and contributing transfer process responsible for turbulent shear stress, vortical structures' orientation (which affect the topology of the flow) and the turbulent heat flux. The results are published in: *International Journal of Heat and Fluid Flow* (Sharma,

Shadloo & Hadjadj 2019).

**Chapter 7:** The summary of the research work undertaken along with the concluding remarks are given in this chapter. This also lays out the possibilities for different perspective works further in the direction of better understanding supersonic compressible transitional boundary layers.

**Chapter 8:** A short summary of the thesis in French language is presented in this chapter.

# Chapter 2

## Numerical methodology and validation

---

### 2.1 Governing equations

The motion of a Newtonian fluid is governed by the set of equations known as the *Navier – Stokes equations* (NSE) comprising of the equations of conservation of mass, momentum and total energy. The NSE can be non-dimensionalized using for instance the freestream quantities and the incoming boundary layer thickness at the inlet  $\delta_{in}^*$  as the reference length:

$$\frac{\partial \rho}{\partial t} + \frac{\partial \rho u_j}{\partial x_j} = 0, \quad (2.1)$$

$$\frac{\partial \rho u_i}{\partial t} + \frac{\partial \rho u_i u_j}{\partial x_j} = -\frac{\partial p}{\partial x_i} + \frac{\partial \tau_{ij}}{\partial x_j}, \quad (2.2)$$

$$\frac{\partial \rho E}{\partial t} + \frac{\partial (\rho E + p) u_i}{\partial x_i} = -\frac{\partial q_i}{\partial x_i} + \frac{\partial u_i \tau_{ij}}{\partial x_j}, \quad (2.3)$$

where, density  $\rho = \rho^*/\rho_\infty^*$ , velocity  $u = u^*/u_\infty^*$ , time  $t = t^* u_\infty^*/\delta_{in}^*$ , pressure  $p = p^*/(\rho_\infty^* u_\infty^{*2})$  and energy  $E = E^*/u_\infty^{*2}$ . The free-stream quantities are marked by the subscript  $\infty$  and the dimensional quantities are marked by the asterisk superscript (\*).

$\tau$  being the symmetric viscous stress tensor, which is given by:

$$\tau_{ij} = \frac{\mu}{Re} \left( \frac{\partial u_j}{\partial x_i} + \frac{\partial u_i}{\partial x_j} - \frac{2}{3} \frac{\partial u_k}{\partial x_k} \delta_{ij} \right). \quad (2.4)$$

where, viscosity  $\mu = \mu^*/\mu_\infty^*$ , Reynolds number  $Re = \rho_\infty^* u_\infty^* \delta_{in}^*/\mu_\infty^*$  and  $\delta_{ij}$  is the Kronecker delta. The pressure and the heat-flux are computed using the equation of state and the Fourier law of heat conduction, respectively:

$$p = (\gamma - 1) \left( \rho E - \frac{1}{2} \rho u_i u_i \right) = \frac{1}{\gamma M_\infty^2} \rho T, \quad (2.5)$$

and

$$q = \frac{-\mu}{(\gamma - 1) M_\infty^2 Re Pr} \frac{\partial T}{\partial x_j}. \quad (2.6)$$

with temperature  $T = T^*/T_\infty^*$ , constant specific heat ratio  $\gamma = 1.4$  and Mach number  $M_\infty = u_\infty^*/\sqrt{\gamma R^* T_\infty^*}$  with gas constant  $R^* = 287 \text{ J/Kkg}^{-1}$  and Prandtl number  $Pr = 0.72$ .

The Sutherland's law is used to calculate the dynamic viscosity:

$$\mu^*(T^*) = \frac{C_1^* T^{*3/2}}{T^* + S^*}, \quad (2.7)$$

where,  $S^* = 110.4$  K is Sutherland's temperature for air and  $C_1^*$  is a constant,  $1.458 \times 10^{-6}$  kg/ms $\sqrt{K}$  which can be written as:

$$C_1^* = \frac{\mu_r^*}{T_r^{*3/2}}(T_r^* + S^*), \quad (2.8)$$

where  $\mu_r^*$  is the reference dynamic viscosity of the air,  $1.716 \times 10^{-5}$  kg/ms at the reference temperature,  $T_r^*$  of 273.15 K. The subscript  $r$  refers to the reference values.

## 2.2 Numerical solver

We have utilized a well-validated DNS - LES numerical solver named CHOC-WAVES which stands for **C**ompressible **H**igh-**O**rders **C**ode using **W**eno **A**dapti**V**E **S**tencils to solve the 3-D, compressible, unsteady NSE for perfect gases. This solver discretizes the convective fluxes by a hybrid conservative sixth-order central scheme with a fifth-order Weighted Essential Non-Oscillatory (WENO) scheme [Jiang & Shu \(1996\)](#), [Chaudhuri et al. \(2011\)](#). Convective terms are splitted in a skew-symmetric form to minimize the aliasing error and to enforce discrete conservation of the kinetic energy which results in better numerical stability. Approximation of the diffusive terms is done with either fourth or sixth order formulas, and they are expanded in the Laplacian form to achieve better stability. The time integration is performed using the third-order Runge-Kutta (RK-3) scheme. More details on the validation for the different studies can be found in ([Ngomo et al. \(2010\)](#), [Chaudhuri et al. \(2012\)](#), [Ben-Nasr et al. \(2016\)](#)). In order to simplify the problem, the single-species version of the code has been utilized considering air as a perfect gas. The validation case for the compressible supersonic transitional boundary layer is presented in §2.7.

## 2.3 Treatment of the convective flux

Strong gradients and contact discontinuities are present in compressible fluids. Therefore, the numerical scheme often should be robust enough in the vicinity of these zones like shocks and shocklets, to ensure that the solver runs smoothly without blowing-up.

### 2.3.1 WENO scheme

The Essentially Non-Oscillatory (ENO) schemes are based on the idea of determining the numerical flux from the higher-order reconstruction based on the single adaptive stencil selected in such a way to avoid the interpolation through the discontinuities. However, these schemes have inherent problem of convergence towards a stationary solution, and also a lack of precision (see [Pirozzoli \(2010\)](#) for details). This drawback of the ENO scheme can be countered with help of the WENO scheme which is based on the idea of construction of a high-order numerical flux from a convex linear combination of a weighted reconstruction of the lower-order polynomials known as the stencils. The stencils are weighted in order

to maximize the accuracy of pattern in the so-called smooth regions, while negating the impacts of adaptive stencil near the discontinuity.

In the CHOC-WAVES code, multiple variants of WENO schemes are available like the classic WENO scheme of [Jiang & Shu \(1996\)](#), the bandwidth-optimized WENO of [Martín et al. \(2006\)](#), the Mapped-WENO of [Henrick et al. \(2005\)](#), and the hybrid scheme combining a WENO scheme with a sixth order central finite difference scheme. Different orders of accuracies i.e. third, fourth or fifth order can be utilized in the solver. For the description of the WENO scheme, we would consider a one-dimensional scalar conservation equation<sup>1</sup>:

$$\frac{\partial u}{\partial t} + \frac{\partial f(u)}{\partial x} = 0 \quad (2.9)$$

where  $f(u)$  is the characteristic flux which can be decomposed into a positive and a negative parts, as shown:

$$f(u) = f^+(u) + f^-(u) \quad (2.10)$$

These two flux represent the non-negative and non-positive velocities of propagation, respectively:

$$\frac{df^+(u)}{du} \geq 0, \quad \frac{df^-(u)}{du} \leq 0 \quad (2.11)$$

This decomposition has been carried out in accordance with the Lax-Friedrichs scheme which can be written as:

$$f^\pm(u) = \frac{1}{2}(f(u) \pm \alpha u) \quad (2.12)$$

where  $\alpha = \max_u |f'(u)|$  is the greatest value along the concerned mesh element.

Similarly, the numerical flux at the interface ( $f_{i+1/2}$ ) can be decomposed as:

$$f_{i+1/2} = f_{i+1/2}^+ + f_{i+1/2}^- \quad (2.13)$$

The flux  $f_{i+1/2}^+$  (similarly  $f_{i+1/2}^-$ ) is reconstructed by interpolating the flux  $f_i^+$  (similarly  $f_i^-$ ) from three stencils  $S = \{S_1, \dots, S_3\}$ . The WENO utilizes a convex combination of the three flux in order to obtain the maximum possible accuracy in the regions of weak or negligible gradients:

$$\begin{cases} f_{i+1/2}^{+(1)} &= \frac{2}{6}f_{i-2}^+ - \frac{7}{6}f_{i-1}^+ + \frac{11}{6}f_i^+ \\ f_{i+1/2}^{+(2)} &= -\frac{1}{6}f_{i-1}^+ + \frac{5}{6}f_i^+ + \frac{2}{6}f_{i+1}^+ \\ f_{i+1/2}^{+(3)} &= \frac{2}{6}f_i^+ + \frac{5}{6}f_{i+1}^+ - \frac{11}{6}f_{i+2}^+ \end{cases} \quad (2.14)$$

Therefore, the numerical flux at the interface for the 5th order WENO scheme is calculated

<sup>1</sup>The mathematical expressions and equations have been presented in the same way as in [Ben-Nasr \(2012\)](#)

as follows:

$$f_{i+1/2} = \sum_{l=1}^r w_l^+ f_{i+1/2}^{+(l)} \quad (2.15)$$

The nonlinear weighting coefficients are defined as:

$$w_l^+ = \frac{\alpha_l^+}{\sum_{l=1}^r \alpha_l^+}, \quad \alpha_l^+ = \frac{d_l^+}{(\epsilon + \beta_l^+)^2}. \quad (2.16)$$

where  $d_l^+ = d_l^- = d_l$  are the weights tuned in such a way to obtain the optimal precision of the WENO scheme (5th order here). In our case, the weights are;  $d_1 = 1/10$ ,  $d_2 = 6/10$ , and  $d_3 = 3/10$ .  $\epsilon$  is a small number ( $\epsilon = 10^{-6}$ ) which is introduced to avoid division by zero (see [Jiang & Shu \(1996\)](#) for more details). And  $\beta_l^+$  are the indicators which are used to decrease the weight of the stencils containing the discontinuity. They can be defined as the sum of the norms of all the derivatives of the polynomials used for interpolation and can be written as:

$$\begin{cases} \beta_1^+ &= \frac{13}{12} (f_{i-2}^+ - 2f_{i-1}^+ + f_i^+)^2 + \frac{1}{4} (f_{i-2}^+ - 4f_{i-1}^+ + f_i^+)^2 \\ \beta_2^+ &= \frac{13}{12} (f_{i-1}^+ - 2f_i^+ + f_{i+1}^+)^2 + \frac{1}{4} (f_{i-1}^+ - 4f_i^+ + f_{i+1}^+)^2 \\ \beta_3^+ &= \frac{13}{12} (f_i^+ - 2f_{i+1}^+ + f_{i+2}^+)^2 + \frac{1}{4} (f_i^+ - 4f_{i+1}^+ + f_{i+2}^+)^2 \end{cases} \quad (2.17)$$

The negative part of the numerical flux i.e.  $f_{i+1/2}^-$  for WENO is calculated in the same manner as mentioned above for the positive part, just by replacing the  $f^+$  by  $f^-$ . The numerical expressions and derivations are presented as in [Ben-Nasr \(2012\)](#).

### 2.3.2 Conservative skew-symmetric central scheme

It has been shown in various studies that the use of centered finite-difference approach gives rise to numerical instabilities even in the absence of discontinuities. For continuous flows, several methods have been proposed for ensuring the numerical stability of the schemes (see [Pirozzoli \(2010\)](#) for a comprehensive review). One of the commonly used methods involves the use of the fractional (or the splitted) forms of the derivatives of the convective terms in the Navier-Stokes equations. This method is based on the idea of writing the convective terms in the skew-symmetric form. However, the obtained approximations can be written in the divergence form but not in the local conservative one. [Pirozzoli \(2010\)](#) has developed a local conservative approximation of the convective terms of the compressible Navier-Stokes equations which can be written as:

$$\frac{\partial \rho u_k \varphi}{\partial x_k} \quad (2.18)$$

where  $\varphi$  is a generic scalar reduced to unity in the continuity equation, to the velocity vector  $u_i$  ( $i = 1, 2, 3$ ) for the momentum equation, and the enthalpy  $H = \frac{\gamma}{\gamma-1} \frac{p}{\rho} + \frac{u^2}{2}$  for the energy equation.

### Basic numerical formulation

For the analysis concerning one-dimensional problems, and equally spaced grid points i.e.  $x_j = jh$ , the conservative finite-difference approximations are of the type<sup>2</sup>:

$$\left. \frac{\partial \rho u_k \varphi}{\partial x_k} \right|_{x=x_j} \approx \frac{1}{h} (f_{i+1/2} - f_{i-1/2}) \quad (2.19)$$

where  $f_{i+1/2}$  is the numerical flux.

The expanded form of equation 2.19 representing the split form of the convective derivatives can be expressed as:

$$\frac{\partial \rho u \varphi}{\partial x} = \frac{1}{2} \frac{\partial \rho u \varphi}{\partial x} + \frac{1}{2} \varphi \frac{\partial \rho u}{\partial x} + \frac{1}{2} \rho u \frac{\partial \varphi}{\partial x} \quad (2.20)$$

or

$$\frac{\partial \rho u \varphi}{\partial x} = \frac{1}{2} \frac{\partial \rho u \varphi}{\partial x} + \frac{1}{2} u \frac{\partial \rho \varphi}{\partial x} + \frac{1}{2} \rho \varphi \frac{\partial u}{\partial x} \quad (2.21)$$

On replacing the continuous derivative operators in equations 2.20, 2.21 with the finite-difference ones, we get:

$$\left. \frac{\partial ab}{\partial x} \right|_{x=x_j} \approx D_s(ab)_j \equiv \frac{1}{2} D(ab)_j + \frac{1}{2} a_j D b_j + \frac{1}{2} b_j D a_j \quad (2.22)$$

where  $D_s$  represents the discrete approximation of the split convective derivative,  $D a_j$  is the discrete approximation of the first derivative of  $a$  at node  $x_j$ , and ( $a = \rho u$ ,  $b = \varphi$ ) or ( $a = \rho \varphi$ ,  $b = u$ ) in the split forms, as shown in equations 2.20, 2.21 respectively.

Here, the standard central difference approximations of the first derivative operator would be considered, which can be written as:

$$D a_j = \sum_{l=1}^L c_l D^l a_j \quad (2.23)$$

where  $c_l$  can be obtained by either acquiring the exact order of accuracy of the approximation, or from what the discrete phase velocity approximates closest to the exact one over a wide range of wavenumbers (see Pirozzoli (2010) for details). And,

$$D^l a_j = \frac{1}{h} (a_{j+l} - a_{j-l}) \quad (2.24)$$

For the simple case of second-order approximation corresponding to  $L = 1$ , we obtain:

$$f_{i+1/2} = \frac{1}{4} (a_j + a_{j+l}) (b_j + b_{j+l}) \quad (2.25)$$

Whereas, the conservative approximation of the convective form shown in equation 2.19

---

<sup>2</sup>Numerical developments are given as shown in Pirozzoli (2010), Ben-Nasr (2012)

would give:

$$f_{i+1/2} = \frac{1}{2} (a_j b_j + a_{j+l} b_{j+l}) \quad (2.26)$$

If we consider the single term  $D^l$ , in equation 2.23, and replace it in equation 2.22 which would yield:

$$D_s^l(ab)_j = \frac{1}{2} D^l(ab)_j + \frac{1}{2} (a)_j D^l(b)_j + \frac{1}{2} (b)_j D^l(a)_j \quad (2.27)$$

where

$$D_s^l(ab)_j = \frac{2}{h} \left\{ (\widehat{a, b})_{j,l} - (\widehat{a, b})_{j-l,l} \right\} \quad (2.28)$$

And,

$$(\widehat{a, b})_{j,l} = \frac{1}{4} (a_j + a_{j+l}) (b_j + b_{j+l}) \quad (2.29)$$

is a two-point, two-variable discrete averaging operator.

It is to be noted that the equation 2.27 is not written directly in the conservative form. However, after certain mathematical manipulations and developments, it can be rewritten as:

$$D_s^l(ab)_j = \frac{1}{4} (f_{i+1/2}^l - f_{i-1/2}^l) \quad (2.30)$$

with

$$f_{i+1/2}^l = 2 \sum_{m=0}^{l-1} (\widehat{a, b})_{j-m,l} \quad (2.31)$$

Hence, the expression of the total flux obtained by summing up all the partial fluxes can be written as:

$$f_{i+1/2} = \sum_{l=1}^L c_l f_{i+1/2}^l \quad (2.32)$$

Consequently, we obtain:

$$f_{i+1/2} = 2 \sum_{l=1}^L c_l \sum_{m=0}^{l-1} (\widehat{\rho u, \varphi})_{j-m,l} \quad (2.33)$$

and

$$f_{i+1/2} = 2 \sum_{l=1}^L c_l \sum_{m=0}^{l-1} (\widehat{\rho \varphi, u})_{j-m,l} \quad (2.34)$$

Therefore, it can be seen that these two equations are of the form of equations 2.20, and 2.21 respectively, with  $c_l = c_1 = 1/2$ .

### Generalized form

Additional robustness for the flows with large density variations can be achieved by expanding the triple products appearing in equation 2.19 (see Pirozzoli (2010) for details). The obtained generalized split form can be written as:

$$\frac{\partial \rho u \varphi}{\partial x} = \alpha \frac{\partial \rho u \varphi}{\partial x} + \beta \left( u \frac{\partial \rho \varphi}{\partial x} + \rho \frac{\partial u \varphi}{\partial x} + \varphi \frac{\partial \rho u}{\partial x} \right) + (1 - \alpha - 2\beta) \left( \rho u \frac{\partial \varphi}{\partial x} + \rho \varphi \frac{\partial u}{\partial x} + u \varphi \frac{\partial \rho}{\partial x} \right) \quad (2.35)$$

Table 2.1: Coefficients of central schemes from second to eighth order.

Order (L)	$i = 1$	$i = 2$	$i = 3$	$i = 4$
1	$c_1 = 1/2$	–	–	–
2	$c_1 = 8/12$	$c_2 = -1/12$	–	–
3	$c_1 = 45/60$	$c_2 = -9/60$	$c_3 = 1/60$	–
4	$a_1 = 672/840$	$c_2 = -168/840$	$c_3 = -/840$	$c_4 = 3/840$

It has been found by Pirozzoli (2010) that the conservative split form of the expression given by equation 2.35 can be recovered for a particular set of conditions. For example, for  $\alpha = \beta = 1/4$  one obtains:

$$f_{i+1/2} = 2 \sum_{l=1}^L c_l \sum_{m=0}^{l-1} (\widehat{\rho, u, \varphi})_{j-m,l} \quad (2.36)$$

where the two-point three-variable discrete averaging operator can be defined as:

$$(\widehat{a, b, d})_{j,l} = \frac{1}{8} \{(a_j + a_{j+l}) (b_j + b_{j+l}) (h_j + h_{j+l})\} \quad (2.37)$$

Table 2.1 summarized the constant values for  $c_l$  for different orders. It should be noted here that the variation of density is also taken into account, which is independent of the other two variables of  $u$  and  $\varphi$ .

### 2.3.3 Hybrid scheme

It is well-known that the WENO schemes have an upwind formulation and are somehow dissipative. The use of pure centered difference scheme may arise some stability issues in the regions of weak shocks or shocklets, like the ones generated in turbulent regions. Therefore, a hybrid scheme has been utilized to address this issue which switches between the WENO and the skew-symmetric central schemes. This method provides the dissipation in the strong gradient regions from the WENO scheme, and uses the skew-symmetric central difference scheme in rest of the region to ensure the accuracy and stability of the solver. The hybrid scheme can be defined as:

$$\frac{\partial \varphi}{\partial x}^{Hybrid} = (1 - \Theta) \frac{\partial \varphi}{\partial x}^{Skew-symmetric} + \Theta \frac{\partial \varphi}{\partial x}^{WENO}. \quad (2.38)$$

The main challenge in a hybrid scheme is to properly tune the shock sensor such that the schemes can be switched at the right location. Ducros et al. (1999) devised a shock sensor based on the Jameson's sensor presented by Jameson et al. (1981):

$$\theta = \frac{(\vec{\nabla} \cdot \vec{u})^2}{(\vec{\nabla} \cdot \vec{u})^2 + (\vec{\nabla} \times \vec{u})^2 + \epsilon} \quad (2.39)$$

where  $\epsilon = 10^{-30}$  is a small parameter used to prevent numerical divergence.

Pirozzoli (2011) proposed a new value of  $\epsilon$  in order to improve the original formulation for the wall-bounded flows. They defined it as:

$$\epsilon = \left( \frac{u_\infty}{\delta_0} \right)^2. \quad (2.40)$$

Numerous tests of the Riemann problem i.e. the shock tube problem have revealed that this new parameter provides unstable results in the shock regions. The Ducros sensor uses a coefficient value ranging from 0 to 1. However, in our solver, the coefficient  $\Theta$  is set as a switch equal to 0 or 1, with  $\theta_0$  being the limiter value (0.02 for our case);  $\Theta = 1$ , if  $\theta > \theta_0$ , and 0 otherwise.

For other versions and numerical schemes present in the solver, the readers can refer to Mouronval (2004), Soni (2016), Piquet (2017).

## 2.4 Treatment of the viscous terms

In the CHOC-WAVES code, the viscous fluxes are approximated by using a fourth or sixth order central scheme, in which the derivative  $(\partial F_v / \partial x)_{i,j,k}$  can be written as:

$$\frac{\partial F_v}{\partial x} \Big|_{i,j,k} = \frac{F_{v_{i-2,j,k}} - 8F_{v_{i-1,j,k}} + 8F_{v_{i+1,j,k}} - F_{v_{i+2,j,k}}}{12\Delta x} + \mathcal{O}(\Delta x^4) \quad (2.41)$$

The components of the flux  $F_v$  contain the derivatives of the type  $\partial()/\partial x$ ,  $\partial()/\partial y$  and  $\partial()/\partial z$ . In the wall-normal ( $y$ ), and the spanwise ( $z$ ) directions of the flow, the approximation of the derivatives are computed based on the standard central formulation. However, in the streamwise ( $x$ ) direction, the derivatives are computed by using a different formulation of the fourth order over a reduced stencil  $S = \{i-2, i-1, i, i+1, i+2\}$ , which yields:

$$\begin{aligned} \frac{\partial u}{\partial x} \Big|_{i-2,j,k} &= \frac{-25u_{i-2,j,k} + 48u_{i-1,j,k} - 36u_{i,j,k} + 16u_{i+1,j,k} - 3u_{i+2,j,k}}{12\Delta x} + \mathcal{O}(\Delta x^4) \\ \frac{\partial u}{\partial x} \Big|_{i-1,j,k} &= \frac{-3u_{i-2,j,k} - 10u_{i-1,j,k} + 18u_{i,j,k} - 6u_{i+1,j,k} + u_{i+2,j,k}}{12\Delta x} + \mathcal{O}(\Delta x^4) \\ \frac{\partial u}{\partial x} \Big|_{i+1,j,k} &= \frac{-u_{i-2,j,k} + 6u_{i-1,j,k} - 18u_{i,j,k} + 10u_{i+1,j,k} + 3u_{i+2,j,k}}{12\Delta x} + \mathcal{O}(\Delta x^4) \\ \frac{\partial u}{\partial x} \Big|_{i+2,j,k} &= \frac{3u_{i-2,j,k} - 16u_{i-1,j,k} + 36u_{i,j,k} - 48u_{i+1,j,k} + 25u_{i+2,j,k}}{12\Delta x} + \mathcal{O}(\Delta x^4) \end{aligned} \quad (2.42)$$

The advantage of the so-called compact scheme is that it produces the same order of precision as the standard central scheme, while using a limited number of points between the two blocks of calculations.

## 2.5 Time-stepping

The time-integration schemes implemented in the solver are mainly explicit solvers which are of the TVD Runge-Kutta type. These schemes obey a restriction on the temporal increment which must be sufficiently small to accommodate the unsteady nature of the turbulent part of the domain. For this study, a third-order Runge-Kutta scheme has been used. The time-integration procedure is performed over three time-steps as shown below:

$$\begin{cases} U^{(1)} = U^n + \Delta t \mathcal{L}(U^n) \\ U^{(2)} = \frac{1}{4} \left[ 3U^n + U^{(1)} + \Delta t \mathcal{L}(U^{(1)}) \right] \\ U^{n+1} = \frac{1}{3} \left[ U^n + 2U^{(2)} + 2\Delta t \mathcal{L}(U^{(2)}) \right] \end{cases} \quad (2.43)$$

where  $\Delta t$  is the time-step,  $U^n$  is the value of the variable  $U$  at an instant  $n$ , and  $U^{(k)}$  are the intermediate values of  $U$  ( $k = 1, 2$ ).

The stability criteria used for the time-stepping can be given as:

$$\Delta t = \mathcal{CFL} \cdot \min(\Delta t_x, \Delta t_y, \Delta t_z) \quad (2.44)$$

where the first term on the right hand side of the equation represents the convective time while the other one corresponds to the diffusion time (laminar and turbulent). The Courant-Friedrichs-Lewy (CFL) number should be less than one in order to ensure the global numerical stability. For this study, the CFL value is set as 0.9. And, the time step in  $x$  direction is computed as

$$\Delta t_x = \min \left[ \frac{\Delta x}{|u| + c}, \frac{1}{2} \frac{\Delta x^2}{\gamma (\mu / Pr)} \right] \quad (2.45)$$

## 2.6 Boundary conditions

The boundary conditions are satisfied by imposing the finite values on the ghost cells (three in our case) lying outside of the computational domain. Depending on the physical condition to be satisfied, the conservative variables of the system of equations governing the flow are defined on these mesh points.

Figure 2.1 shows the schematic of the computational domain with the boundary conditions. At the inlet of the domain, physical quantities like the streamwise and wall-normal velocity, and the density profiles obtained from the similarity solution of a laminar compressible adiabatic, or isothermal boundary layer are specified (without any perturbations) which are obtained by using the Illingworth transformation (White & Corfield (2006), Masatsuka (2009)). Supersonic inflow and outflow conditions are chosen at the inlet and outlet of the domain at  $x_{in}^*$  and  $x_{out}^* = x_{in}^* + L_x^*$ , respectively (where  $L_x^*$  is the length of the domain in the streamwise direction). Periodic boundary conditions are used for the side-walls of the do-

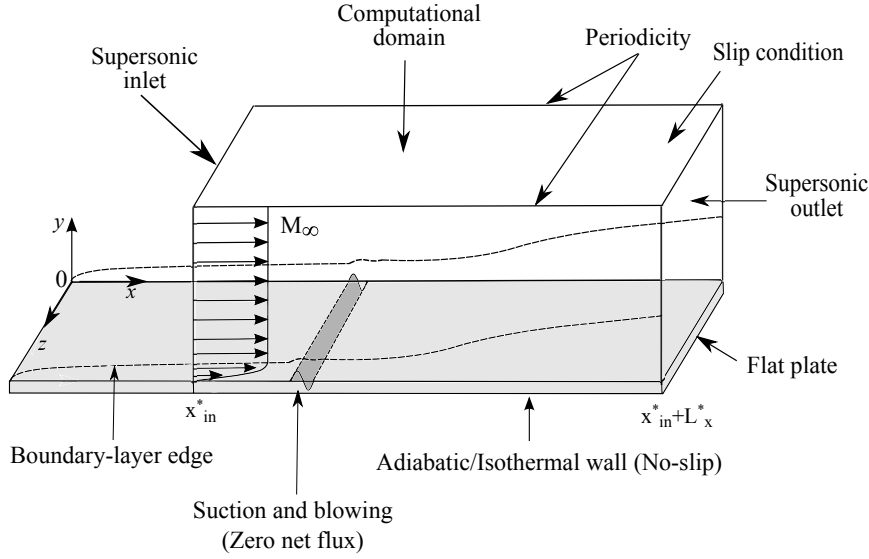


Figure 2.1: Schematic representation of the computational domain and the boundary conditions.

main. The no-slip and no-penetration condition is used at the surface of the wall except for the blowing-suction and control strips (see following chapters for details) which are used to excite the test-modes and introduce the stabilization streaks respectively in the domain. The temperature at the wall is calculated considering the adiabatic zero-gradient condition everywhere for adiabatic walls, while a constant wall-temperature is forced for the isothermal cases. For the top surface, a slip condition with zero boundary-normal gradient is imposed.

It is to be noted that an equidistant grid spacing is utilized in streamwise ( $x$ ) and spanwise ( $z$ ) directions. A grid stretching function is used in the wall-normal direction which is defined as:

$$y^* = L_y^* \left( 1 + \frac{\tanh \kappa y^*}{\tanh \kappa} \right), \quad (2.46)$$

where  $\kappa = 3$  is the grid stretching parameter, and  $L_y^*$  is the length of the domain in the wall-normal direction.

## 2.7 Validation

The solver has been previously used for simulating quite complex flow scenarios such as the turbulent boundary layer (Shadloo et al. (2015), Ben-Nasr et al. (2016), Ben-Nasr (2012), Hadjadj et al. (2015)), shock waves (Chaudhuri et al. (2011, 2012), Shadloo et al. (2014), Soni (2016), Soni et al. (2017)), nozzle flows (Piquet (2017)) using both Large-eddy simulation (LES) and Direct numerical simulation (DNS). However, the solver has not been validated yet for the transition scenarios. Therefore, we now present the validation of the solver for compressible transitional boundary layer.

### 2.7.1 Simulation setup

A supersonic boundary layer with free-stream Mach number  $M_\infty = 2.0$  is investigated using DNS. The fluid is supposed to be a perfect gas with constant specific heats. The setup is designed to keep the flow conditions of [Fezer & Kloker \(2000\)](#) and [Mayer et al. \(2011\)](#). The free-stream temperature is  $T_\infty^* = 160$  K, velocity  $u_\infty^* = 507.1$  m/s, viscosity  $\nu^* = 2.1067 \times 10^{-5}$  m<sup>2</sup>/s, pressure  $p_\infty^* = 23.786$  kPa and Prandtl number  $Pr = 0.72$ . The flow domain is free of any shocks generated from the leading edge of the plate because the inlet of the domain is kept downstream of the leading edge at  $x_{in}^* = 0.004154$  m with inlet Reynolds number  $Re_{x_{in}} = 10^5$  and unit Reynolds number  $Re_u^* = 2.407 \times 10^7/\text{m}$ . The boundary-layer thickness at the inlet is  $\delta_{in}^* = 7.958 \times 10^{-5}$  m. The length and height of the domain are  $L_x^* = 0.055$  m ( $L_x^*/\delta_{in}^* = 691.13$ ) and  $L_y^* = 0.0102$  m ( $L_y^*/\delta_{in}^* = 128.17$ ), respectively. The width of the domain corresponds to four times of the fundamental wavelength  $L_z^* = 4 \times \lambda_z^*$  (where,  $\lambda_z^* = 0.002153$  m, and  $L_z^*/\delta_{in}^* = 108.2$ ) of the disturbed mode to include the subharmonic modes considered by [Fezer & Kloker \(2000\)](#). The total number of points in  $x$ ,  $y$  and  $z$  directions are  $N_x = 800$ ,  $N_y = 180$  and  $N_z = 80$ , respectively.

### Blowing and suction

The laminar boundary layer is perturbed using the blowing and suction technique which introduces an excitation in  $(\rho v)_w/\rho_\infty u_\infty$ . This strip extends from  $x_1^* = (x_{in}^* + 0.004154)$  m to  $x_2^* = (x_{in}^* + 0.009654)$  m, and can be expressed as:

$$\rho v(x, y = 0, z, t) = A \rho_\infty u_\infty f(x) g(z) h_1(t), \quad (2.47)$$

$$f(x) = 4 \sin \theta (1 - \cos \theta) / \sqrt{27}, \quad (2.48)$$

$$\theta = 2 \pi (x - (x_1^* - x_{in}^*)) / (x_2^* - x_1^*), \quad (2.49)$$

$$g(z) = (-1)^k \cos \left( \frac{2\pi k z^*}{L_z^*} \right), \quad (2.50)$$

$$h_1(t) = \sin(h\omega^* t). \quad (2.51)$$

where  $A$  is the disturbance amplitude given as  $(\rho v)_w/(\rho_\infty u_\infty)$ ,  $\omega^*$  is the angular frequency of the excitation mode,  $h$  is the multiple of the fundamental frequency, and  $k$  is the multiple of the fundamental spanwise wavenumber. The expressions for  $f(x)$ ,  $\theta$  and  $h_1(t)$  are taken from [Pirozzoli et al. \(2004\)](#). Here,  $A = 0.065\%$ , the fundamental frequency,  $f_0^* = 73.83$  kHz and wavenumber,  $\beta_4^* = 2\pi/(4\lambda_z^*) = 729.42/\text{m}$  which correspond to their non-dimensional counterparts used by [Fezer & Kloker \(2000\)](#), are excited in this study, i.e. modes (1,4) and (1,-4), designating the frequency/spanwise wavenumber tuple. Moreover, the subharmonic modes (1/2,3) and (1/2,-3) are also excited. However, for the subharmonic modes  $A = 4.043 \times 10^{-3}\%$ . Here  $(h,k)$  denotes the mode with frequency  $hf_0^*$  and spanwise wavenumber  $k\beta_0^*$ . In the following  $(h,k)$  stands for the sum of  $(h,+k)$  and  $(h,-k)$ .

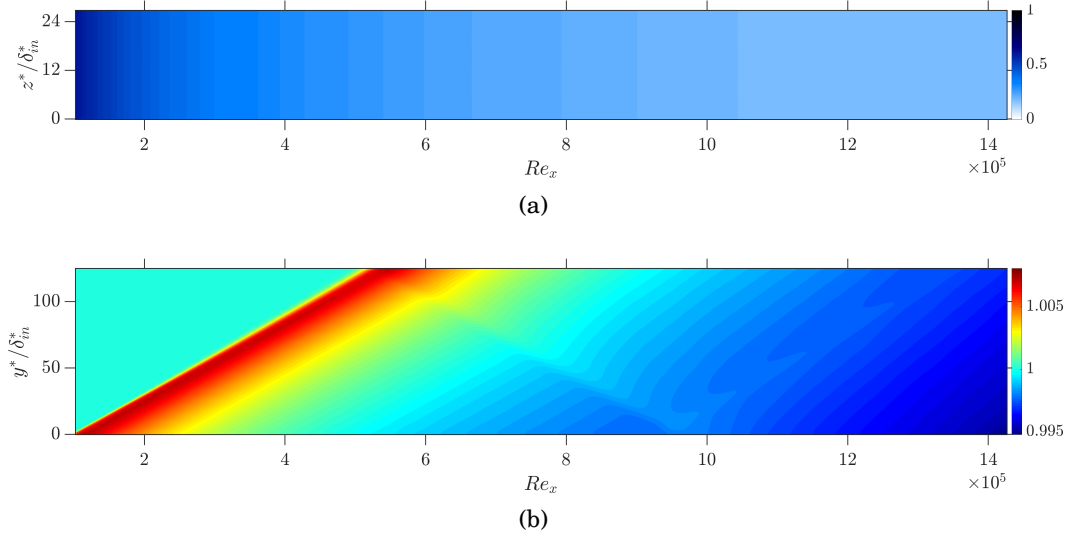


Figure 2.2: Instantaneous snapshot of the baseflow: contours of (a)  $u^*/u_\infty^*$  shown at  $y^*/\delta_{in}^* = 0.48$ , and (b)  $p^*/p_\infty^*$  shown at  $z^*/\delta_{in}^* = 12$ .

### 2.7.2 Simulating the baseflow

Before going into details of the full case of validation, we would like to verify whether the solver correctly runs a case without any perturbation input i.e. the laminar case. This simple test case would permit us to verify very basic but important parameters, for example, the correctness of the periodic boundary condition of the side-walls. Moreover, it could also be verified that are there any strong shock-reflections present in the domain, generating from the leading edge of the flat-plate. In case of a strong pressure wave, there exists a risk of strong reflections due to the upper boundary of the domain which may inflict the shock-induced transition to turbulence, and therefore, the generated results would not be physically significant.

The results of the 3-D DNS of the fully-laminar case show that the periodic boundary condition is working perfectly because the contours of the instantaneous velocity do not show any variation in the spanwise direction (see figure 2.2a). The contours of pressure ( $p^*/p_\infty^*$ ) depicted in figure 2.2b show a weak compression wave ( $\approx 0.5\% \Delta p$ ) originating straight from the inlet of the domain which is because of the similarity solution used at the inlet of the domain. In fact, this small change in the pressure field does not have any implication on the evolution of the boundary layer, as is revealed by comparing figures 2.2a and b. Therefore, it can be concluded that the chosen height of the domain is large enough to inhibit any harmful reflections inside the domain and hence, we may now proceed towards the full validation case.

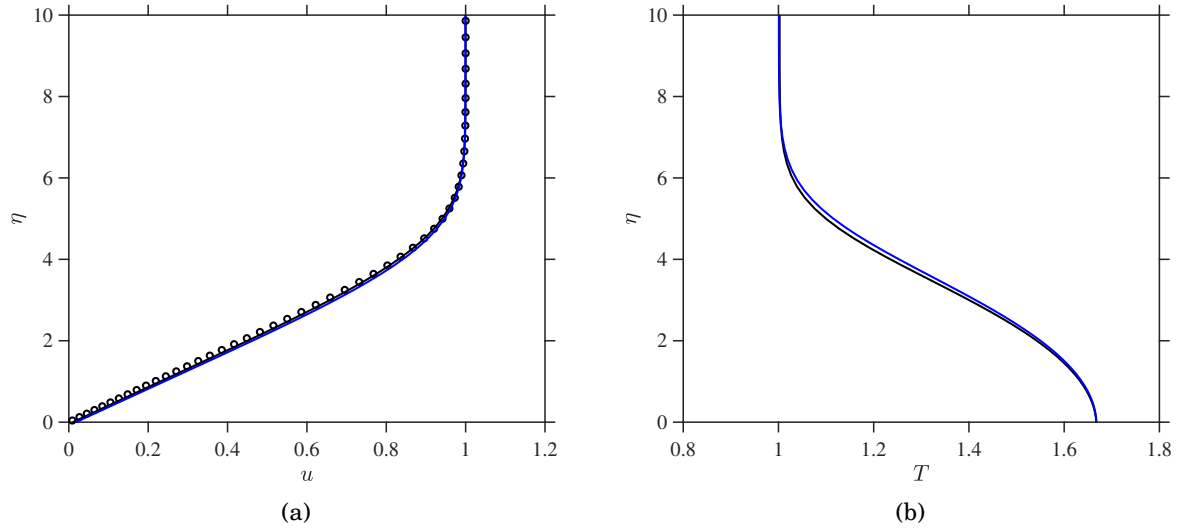


Figure 2.3: Self-similar (a) velocity profiles, and (b) temperature profiles at  $Re_x = 2 \times 10^5$  (—) and  $Re_x = 6 \times 10^5$  (—), and (o) represents the profile obtained from the shooting method.

### Laminar boundary layer properties

Figure 2.3a compares the velocity profiles at different streamwise locations i.e. at  $Re_x = 2 \times 10^5$  and  $Re_x = 6 \times 10^5$  of the baseflow against the profile obtained from the shooting method using the Illingworth transformation in terms of the similarity coordinates  $\eta = y^* \sqrt{\frac{u_\infty^*}{\nu_\infty^* x^*}}$ . As can be seen from this figure that the profiles collapse well with each-other signifying that the existence of the self-similar Blasius profiles at different streamwise locations. Similarly, figure 2.3b shows the adiabatic temperature profiles for the same streamwise locations, and it can be clearly seen that like the velocity profiles, these profiles are also self-similar. The self-similarity of temperature profiles at different streamwise locations indicates that the flow is in thermal equilibrium. Hence, it can be seen that the solver correctly establishes the Blasius profile in the laminar regime.

### 2.7.3 Oblique type transition

In order to validate the solver for growth rates of various modes in the boundary layer, 'Case 1', computed by Fezer & Kloker (2000) (or Mayer et al. (2011)), is taken as the reference benchmark. The readers may refer to Mayer et al. (2011) for an overview of the stability characteristics of the flow as obtained by the LST. Modes (1,4) and (1/2,3) are excited using blowing-suction. It should be noted here that the details of blowing and suction used by Fezer & Kloker (2000) are not provided in their study. Therefore, the amplitudes of both fundamental and subharmonic modes are adjusted to match with the respective initial amplitudes. Figure 2.4 compares various modes of current DNS with their counterparts by Fezer & Kloker (2000), marked by symbols. The curves show a good collapse assuring that

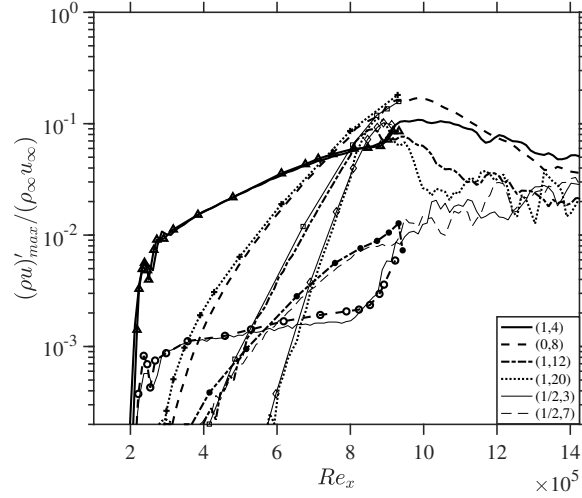


Figure 2.4: Comparison of the streamwise evolution of the maximum disturbance amplitudes of various modes with Fezer & Kloker (2000) (marked by symbols).

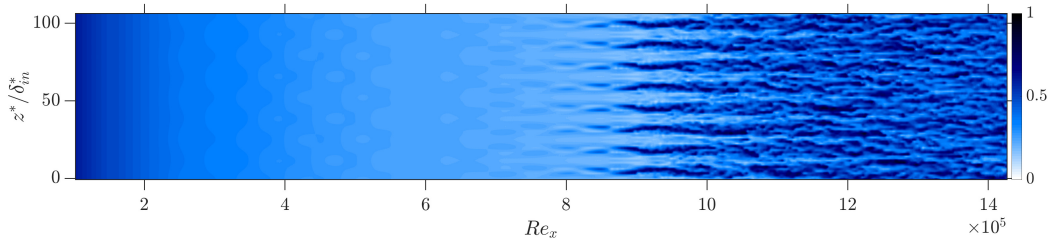


Figure 2.5: Instantaneous flow-field for the validation case: contours of  $u^*/u_\infty^*$ , shown at  $y^*/\delta_{in}^* = 0.44$ .

the DNS correctly predicts the growth of various modes. Each mode is computed as per algorithm 2.1, i.e. by time sampling over two fundamental periods. Then performing Fourier transform in spanwise direction followed by in time and then obtaining the maximum value in wall-normal direction at a given streamwise station. It should be noted here that for getting the exact Fourier amplitudes of the modes, the amplitude of the modes ( $h > 0, k > 0$ ) should be multiplied by four because these modes contain  $\pm k$  modes (signifying right and left travelling waves) and also the complex conjugate. Therefore, in the same sense, the amplitudes of  $(0, k)$  or the  $(h, 0)$  modes should be multiplied by two, but for the mean-flow distortion (MFD)  $(0, 0)$  mode, the amplitude is not multiplied by any factor. The instantaneous flow field for the validation case is shown in figure 2.5 which prominently displays the oblique-type breakdown close to  $Re_x = 9 \times 10^5$ . Figure 2.6 shows different views of the contours of the instantaneous disturbance growth, which is calculated by subtracting the baseflow from the instantaneous flow field ( $u^* - u_{bf}^*$ ). Only the stages leading up to the laminar breakdown are shown. The disturbance contours increase in amplitude as well as in size when moving downstream (see figure 2.6a). It can be seen from figures 2.5 and 2.6b that a

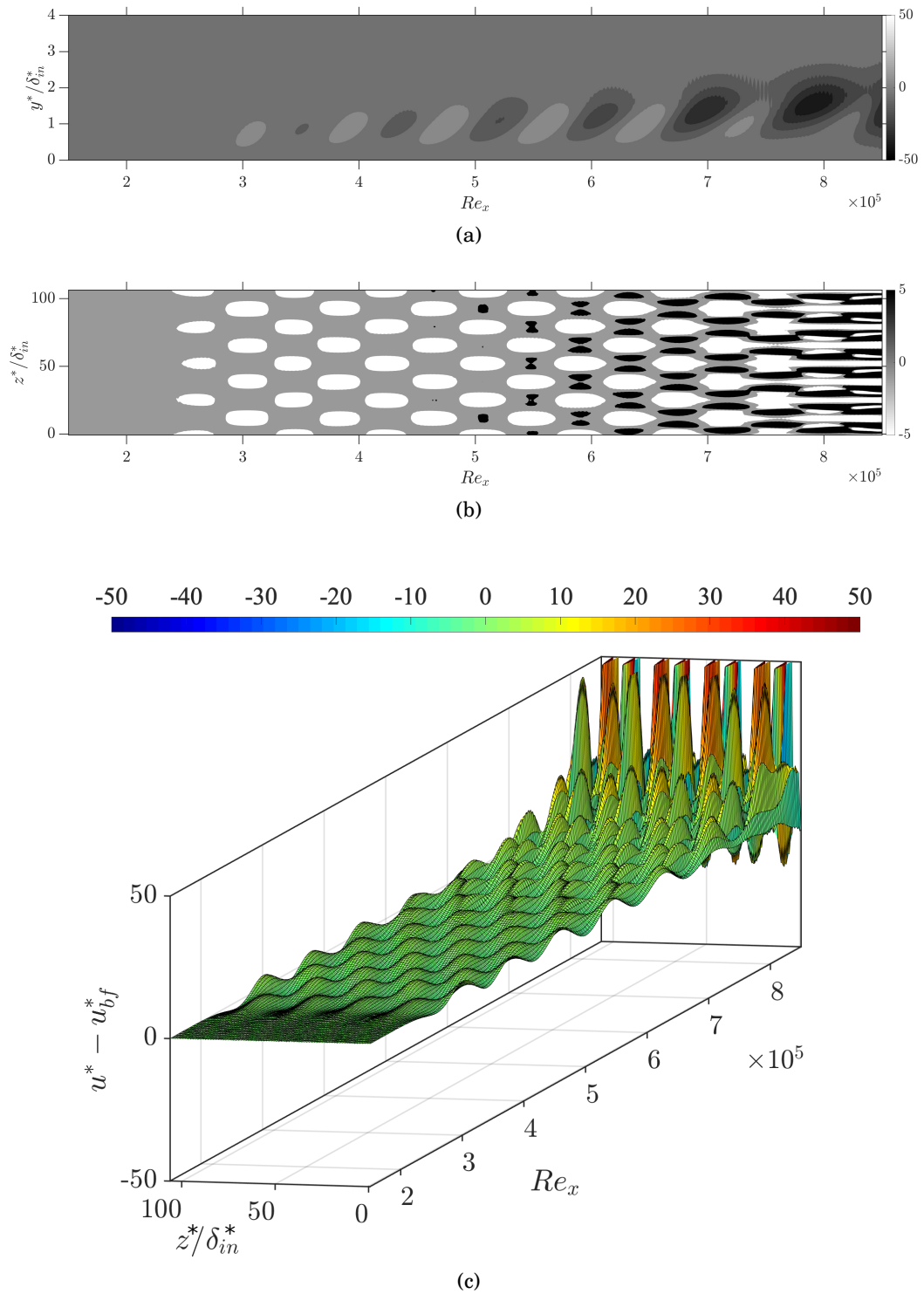


Figure 2.6: (a) Longitudinal cut at  $z^*/\delta_{in}^* = 50$ ; (b) top view at  $y^*/\delta_{in}^* = 0.60$ : contours, and (c) perspective view of the surface of the disturbance  $(u^* - u_{bf}^*)$ .

---

**Algorithm 2.1** : Spectral approach, or Fourier analysis

---

- 1: **Run** DNS for 4-6 cross-over times.
  - 2:       Check the time-step from log.dat file.
  - 3: **Post-process** the instantaneous flow-field
  - 4:       Verify  $\lambda_x^*$ .
  - 5: **Open** Slice.dat and put 6 to 8 slices per streamwise wavelength, and set output frequency at 40 slices per fundamental time-period.
  - 6: **Restart** COMPUTATION
  - 7:       Run for two fundamental time-periods (to capture the subharmonic frequency).
  - 8: **STOP** COMPUTATION
  - 9: **Extract** all slice\*.h5 files
  - 10: **Run** modal\_dcmp.m
  - 11:       **Read** all slice.h5 files and baseflo.h5
  - 12:       **Reduce** baseflo.h5 from all the slice.h5 files to get MFD or (0,0) mode.
  - 13:       **FFT** in z-direction
  - 14:       **FFT** in time
  - 15:       **Get** the maximum along y-direction
  - 16:       **Plot** desired  $(h,k)$  mode in x-direction.
  - 17: **STOP** modal\_dcmp.m
- 

total of eight streaks show-up at  $Re_x \approx 8 \times 10^5$  which is the (0,8) mode. Figure 2.4 shows that the amplitude of the (0,8) mode shoots up rapidly, and at this point, the amplitude reaches 10% of  $\rho_\infty u_\infty$ , ultimately resulting in the laminar breakdown at  $Re_x = 9 \times 10^5$ . Figure 2.6c shows the perspective view of the disturbance growth which provides a better insight on the growth of disturbance in a 3-D sense. Therefore, from all the discussion presented in §2.7, it can be concluded that the solver correctly predicts the growth rates for different modes and hence can be used for investigating the compressible supersonic transitional boundary layers.

**Note:** The following four chapters of the manuscript are the reprints/submitted copies of the journal publications produced from this research work. Therefore, the upcoming chapters may have different naming conventions for nomenclature, as well as the dimensional and non-dimensional parameters enlisted in the list of nomenclature presented in the beginning of the write-up.

# Chapter 3

## Control of the oblique-type breakdown

### 3.1 Introduction

Published in: *Journal of Fluid Mechanics*

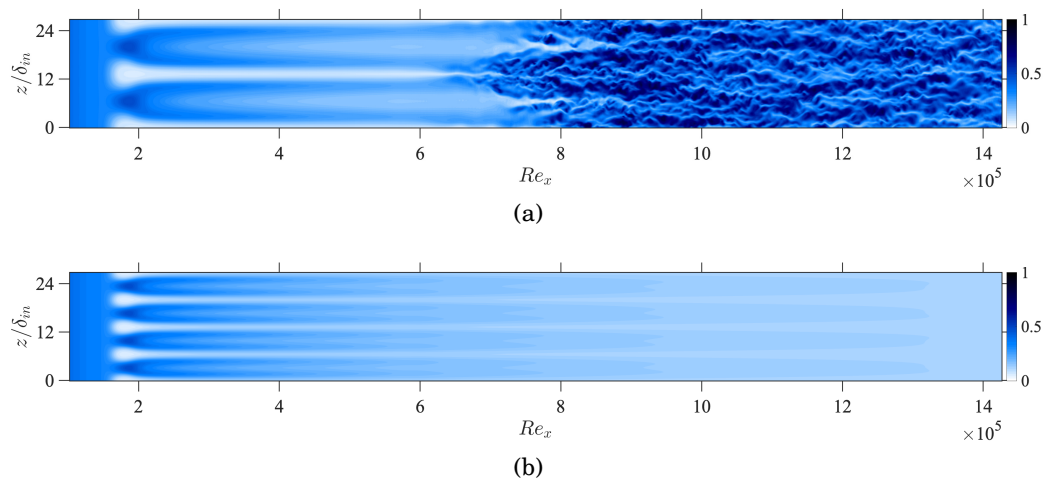


Figure 3.1: Instantaneous flow-field for (a) (0,2), and (b) (0,4) control mode: contours of  $u^*/u_\infty^*$ , shown at  $y^*/\delta_{in}^* = 0.44$ . Control modes are induced using time independent blowing/suction without the induction of the Principal mode for  $M_\infty = 2.0$ .

This chapter deals with O-type breakdown and its control. The effectiveness of streak modes in suppressing the laminar breakdown for a supersonic boundary layer at  $M_\infty = 2.0$  has been presented in detail. For this study, only a quarter of the domain is considered to lower the computational cost. No subharmonic modes are used, only the fundamental mode (1,1) which peaks the growth rate in the frequency-spanwise wavenumber spectrum is excited.

Initially, various streak modes are considered to be used as the control modes like (0,2), (0,3), (0,4), (0,5), and (0,6). However, there are certain criteria which need to be fulfilled before any streak mode can qualify as a control mode:

1. The streak mode itself should not be of detrimental nature i.e. it should not destabilize the flow and does not induce transition to turbulence.
2. It should generate high enough beneficial mean-flow distortion to satisfactorily suppress the growth of the primary test mode (1,1).

Figure 3.1 shows the instantaneous fields for the cases using (0,2) and (0,4) control modes without the test modes. It can be seen that (0,2) is detrimental in nature and breakdown

to turbulence at  $Re_x \approx 7 \times 10^5$ , hence it could not be used as a control mode whereas the (0,4) mode remains stable. However, all other mentioned streak modes ( $0, k = 3 - 6$ ) are not of detrimental nature (not all cases shown here) and qualify as the control mode (see the following for more details).

# Control of oblique-type breakdown in a supersonic boundary layer employing streaks

Sushank Sharma<sup>1</sup>, Mostafa S. Shadloo<sup>1</sup>, Abdellah Hadjadj<sup>1</sup>  
and Markus J. Kloker<sup>2,†</sup>

<sup>1</sup>CORIA-UMR 6614, CNRS-University, INSA of Rouen and Normandie University, 76000 Rouen, France

<sup>2</sup>Universität Stuttgart, Institut für Aerodynamik und Gasdynamik, Pfaffenwaldring 21,  
D-70550 Stuttgart, Germany

(Received 19 December 2018; revised 22 May 2019; accepted 22 May 2019)

The effectiveness of streak modes in controlling the oblique-type breakdown in a supersonic boundary-layer at Mach 2.0 is investigated using direct numerical simulations. Investigations in the literature have shown the effectiveness of streak modes in delaying the onset of transition dominated by two-dimensional waves, but in oblique breakdown, three-dimensional waves and a strong streak mode dominate the transition process. Paredes *et al.* (*J. Fluid Mech.*, vol. 831, 2017, pp. 524–553) discussed the possible stabilization of supersonic boundary layers by optimally growing streaks using parabolized stability equations. However, no study has as yet been reported regarding direct nonlinear control of oblique breakdown. This study deals with the effects of large-amplitude decaying streak modes generated by a blowing–suction strip at the wall to control full breakdown in a reference case. Modes with four to five times the fundamental wavenumber are found to be beneficial for controlling the transition. In the first region after the control-mode forcing, the beneficial mean-flow distortion (MFD), generated by inducing the control mode, is solely responsible for hampering the growth of the fundamental-mode. On the whole, the MFD and the three-dimensional part of the control contribute equally towards controlling the oblique breakdown. The results show significant suppression of transition, and substantial improvements have been observed in the levels of the skin-friction coefficient and wall-temperature in comparison to the uncontrolled case. Moreover, refreshing the control using an additional downstream control strip increases the gain. However, the forcing amplitude must be carefully chosen in order not to introduce a generalized inflection point in the spanwise averaged mean flow invoking enhanced disturbance growth.

**Key words:** boundary layer stability, drag reduction, high-speed flow

---

## 1. Introduction

Precise prediction of laminar breakdown to turbulence in the boundary-layer flow is indispensable for the design of modern supersonic aircraft, not only due to drag and

† Email address for correspondence: [markus.kloker@iag.uni-stuttgart.de](mailto:markus.kloker@iag.uni-stuttgart.de)

separation control but also wall heating by friction. With an ever-increasing focus on cutting emissions and increasing the efficiency of the next-generation of supersonic carriers, it has therefore become of vital, topical interest to control the onset of turbulence for high-speed boundary layers.

The oblique-type, first-mode instabilities, breakdown scenario is dominant for the supersonic boundary layer while the acoustic-mode instabilities (Mack modes, Mack (1984)) often dominate in the hypersonic regime. The direct numerical simulation (DNS) studies of Thumm (1991) and Fasel, Thumm & Bestek (1993), for the supersonic boundary layers at Mach number 1.6, were the first ones to report the oblique-type breakdown mechanism. Fezer & Kloker (2000) have investigated the standard oblique-type breakdown with its velocity-streak modes generated by the fundamental unsteady oblique wave pair(s) in combination with subharmonic three-dimensional modes using DNS at Mach 2. They found that the growth rates of three-dimensional subharmonic modes were less significant than those of the fundamental mode and, hence, the standard oblique-type breakdown was found to be dominant. However, the study also concluded that the presence of subharmonic modes did speed-up the transition process. Their findings contradicted the conclusions of Kosinov *et al.* (1994) who did not document steady modes at that time. Later on, Mayer, Wernz & Fasel (2011) replicated the DNS for the conditions of Kosinov *et al.* (1994) and confirmed the importance of oblique-type breakdown mechanism in the experiments. Nowadays it is very clear that the streak modes inherent in oblique breakdown play an essential role as their amplitude grows strongly, fed by nonlinear generation of the unsteady modes and some continuous add-up by a transient-growth mechanism, see Laible & Fasel (2016). Streak instability finally causes the laminar breakdown.

Regarding the control of transition in cases where two-dimensional Tollmien–Schlichting waves dominate (incompressible flow), the forcing of control streaks has been investigated, see, for example, Cossu & Brandt (2002), Bagheri & Hanifi (2007) or Shahinfar *et al.* (2012). The streak amplitude must not be too high – for otherwise localized shear-layer instabilities cause rapid transition (Andersson *et al.* 2001). For oblique breakdown with its inherent streak modes the additional forcing of such modes does not look promising at first, and was only investigated recently in a first study on the interaction of modes by Paredes, Choudhari & Li (2017). On the other hand, Wassermann & Kloker (2002) and Saric, Reed & White (2003) successfully investigated the control strategy using appropriate steady control vortex modes for the generic base flow on a swept wing, where cross-flow instability leads to exponential amplification of such steady modes. The findings report that closely spaced vortices can suppress the wider spaced modes responsible for the natural breakdown. Importantly, Wassermann & Kloker (2002) attributed the suppression of the most-amplified steady modes to the mean-flow distortion (MFD) generated nonlinearly by the control vortices within the upstream flow deformation (UFD) technique. It was found that the two-dimensional (2-D) part of the UFD weakened the growth while the three-dimensional (3-D) part weakened the receptivity of the naturally most-growing modes; for Blasius-flow similar findings concerning the MFD are reported, see, for example, Dörr & Kloker (2017). Stabilization of a supersonic two-dimensional boundary layer using optimally growing streaks has been discussed in the recent study by Paredes *et al.* (2017). They utilized the nonlinear plane-marching parabolized stability equations (PSE) to predict the development of finite, stationary disturbances and their interaction with oblique waves. The study concludes that the spanwise wavelength of the control streaks must be smaller than the one of the

naturally most-growing oblique travelling modes by a factor of two at least, in order not to reinforce the streak mode inherent in the oblique-breakdown scenario. However, neither DNS nor experiments have so far been reported for the successful control of supersonic boundary-layer oblique breakdown.

Although the PSE study of Paredes *et al.* (2017) provides a conceptual model for characterizing a stabilization provided by transiently growing optimal streaks, still some important questions need to be addressed. As later transition stages are completely nonlinear and unsteady, the situation needs a deeper analysis using full DNS. The full effects of ‘control’ streaks, possibly not growing but decaying, are not known for the oblique-type breakdown. How effective are they in the full transition scenario up to turbulence, and which spanwise spacing is useful?

This paper is structured as follows. Section 2 provides the details about the DNS solver used and the boundary conditions, followed by a validation case in § 3. Various aspects about controlling the oblique-type breakdown are presented in § 4; which include the description of the main scenario in § 4.1, the effects of the disturbance spectrum in § 4.2, the effects of control mode amplitude in § 4.3, implications of the spanwise wavenumber of the control mode in § 4.4, the role of the mean-flow distortion and the 3-D part of the control in § 4.5, reinforcing the control mode in § 4.6 and the effect of controlling transition in § 4.7. And finally, the study is concluded in § 5.

## 2. DNS solver and simulation details

The study utilizes an in-house developed high-order DNS, and large-eddy simulation (LES) code named CHOC-WAVES which solves the three-dimensional, compressible, unsteady Navier–Stokes equations for perfect gases. This code uses a hybrid conservative sixth-order split centred finite-difference scheme with a fifth-order weighted essential non-oscillatory scheme to discretize convective fluxes. Numerical stability is achieved by splitting the convective terms in skew-symmetric form to minimize the aliasing error and to enforce the discrete conservation of the kinetic energy. The diffusive terms are approximated with fourth- or sixth-order schemes and are expressed in Laplacian form. The whole system is time-integrated using a third-order Runge–Kutta scheme. The solver has previously been used for many studies (Shadloo, Hadjadj & Hussain 2015; Sharma, Shadloo & Hadjadj 2018*a,b*). The validation case for the current study is presented in § 3.

### 2.1. Simulation set-up

A supersonic boundary layer with free-stream Mach number  $M_\infty = 2.0$  is investigated using DNS. The fluid is supposed to be a perfect gas with constant specific heats. The set-up is designed to keep the flow conditions of Fezer & Kloker (2000) or Mayer *et al.* (2011). The free-stream temperature is  $T_\infty^* = 160$  K, velocity  $u_\infty^* = 507.1$  m s<sup>-1</sup>, viscosity  $\nu^* = 2.1067 \times 10^{-5}$  m<sup>2</sup> s<sup>-1</sup>, pressure  $p_\infty^* = 23.786$  kPa and Prandtl number  $Pr = 0.72$ . The flow domain is free of any shocks generated from the leading edge of the plate because the inlet of the domain is kept downstream of the leading edge at  $x_{in}^* = 0.004154$  m with inlet Reynolds number  $Re_{x_{in}} = 10^5$  and unit Reynolds number  $Re_u^* = 2.407 \times 10^7$  m<sup>-1</sup>. The boundary-layer thickness at the inlet is  $\delta_{in}^* = 7.958 \times 10^{-5}$  m. The length and height of the domain are  $L_x^* = 0.055$  m ( $L_x/\delta_{in} = 691.13$ ) and  $L_y^* = 0.0102$  m ( $L_y/\delta_{in} = 128.17$ ), respectively. The width of the domain corresponds to the fundamental wavelength  $L_z^* = \lambda_z^* = 0.002153$  m ( $L_z/\delta_{in} = 27.05$ ) of the disturbed mode. But for the validation case, a four times broader domain was chosen to include

Cases	$N_{modes}$	Control mode	FCS	$A_{FCS}$ (%)	SCS	$A_{SCS}$ (%)	$H_{SCS}$
Cref	1	×	OFF	×	OFF	×	×
C31Cw	5	(0,3)	ON	1.69	OFF	×	×
C41C	1	(0,4)	ON	1.95	OFF	×	×
C41Cw	5	(0,4)	ON	1.95	OFF	×	×
C51Cl	1	(0,5)	ON	1.95	OFF	×	×
C51C	1	(0,5)	ON	2.43	OFF	×	×
C51Ch	1	(0,5)	ON	4.88	OFF	×	×
C51Cw	5	(0,5)	ON	2.43	OFF	×	×
C52C	1	(0,5)	ON	2.43	ON	2.43	1
C52Cn	1	(0,5)	ON	2.43	ON	2.43	3
C52Ch	1	(0,5)	ON	2.43	ON	4.88	3
C61Cw	5	(0,6)	ON	2.53	OFF	×	×

TABLE 1. Simulation parameters for various cases.  $N_{modes}$ , FCS, SCS,  $A_{FCS,SCS}$  and  $H_{SCS}$  stand for the number of modes excited, first control strip, second control strip, the amplitudes at the first and the second control strip ( $A_{FCS,SCS} = (\rho v)_{w,max} / \rho_{\infty} u_{\infty}$ ), and the number of harmonics used in the second control strip, respectively. Suffix  $h$ ,  $l$ ,  $n$  and  $w$  represent cases with high, low intensity of the control mode, narrow crests of SCS and wide disturbance spectrum, respectively.

the subharmonic modes considered by Fezer & Kloker (2000). Table 1 lists the various cases investigated in this study. Equidistant grid spacing is utilized in streamwise ( $x$ ) and spanwise ( $z$ ) directions with  $N_x = 800$  and  $N_z = 140$  points, respectively. Grid stretching is used in wall-normal direction, defined as

$$y = L_y^* \left( 1 + \frac{\tanh \kappa y}{\tanh \kappa} \right), \quad (2.1)$$

where,  $\kappa = 3$  is the grid stretching parameter. The number of points in wall-normal ( $y$ ) direction are  $N_y = 180$ .

## 2.2. Boundary conditions

At the inlet of the domain, physical quantities like streamwise and wall-normal velocity, and density profiles obtained from the similarity solution of a laminar compressible adiabatic boundary layer are specified. Supersonic inflow and outflow conditions are chosen at the inlet and outlet of the domain at  $x_{in}^*$  and  $x_{out}^* = x_{in}^* + L_x^*$ , respectively. Periodic boundary conditions are used for the side-walls of the domain. The no-slip and no-penetration condition is used at the surface of the wall except for the blowing–suction and control strips which are used to excite the test-modes and introduce the stabilization streaks, respectively, in the domain. The temperature at the wall is calculated by considering the adiabatic zero-gradient condition everywhere, and for the top surface a slip condition with zero boundary-normal gradient is imposed.

### 2.2.1. Blowing and suction

The laminar boundary layer is perturbed using blowing and suction which introduces an excitation in  $(\rho v)_{wall} / \rho_{\infty} u_{\infty}$ . This strip extends from  $x_1^* = (x_{in}^* + 0.004154)$  m to  $x_2^* = (x_{in}^* + 0.009654)$  m, and can be expressed as

$$\rho v(x, y = 0, z, t) = A \rho_{\infty} u_{\infty} f(x) g(z) h_1(t), \quad (2.2)$$

$$f(x) = 4 \sin \theta (1 - \cos \theta) / \sqrt{27}, \quad (2.3)$$

$$\theta = 2\pi(x - (x_1^* - x_{in}^*)) / (x_2^* - x_1^*), \quad (2.4)$$

$$g(z) = (-1)^k \cos \left( \frac{2\pi kz}{L_z^*} \right), \quad (2.5)$$

$$h_1(t) = \sin(h\omega t), \quad (2.6)$$

where  $A$  is the disturbance amplitude given as  $(\rho v)_{wall} / (\rho_\infty u_\infty)$ ,  $\omega$  is the angular frequency of the excitation mode,  $h$  is the multiple of the fundamental frequency and  $k$  is the multiple of the fundamental spanwise wavenumber. The expressions for  $f(x)$ ,  $\theta$  and  $h_1(t)$  are taken from Pirozzoli, Grasso & Gatski (2004). For all the cases listed in table 1,  $A = 6.5 \times 10^{-4}$ . The fundamental frequency  $f_0^* = 73.83$  kHz and wavenumber  $\beta_0^* = 2\pi/\lambda_z^* = 2.9176 \times 10^3 \text{ m}^{-1}$ , which correspond to their dimensionless counterparts used by Fezer & Kloker (2000), are excited in this study, i.e. modes (1,1) and (1,-1), designating the frequency/spanwise wavenumber tuple. Here,  $(h,k)$  denotes the mode with frequency  $hf_0^*$  and spanwise wavenumber  $k\beta_0^*$ . In the following,  $(h,k)$  stands for the sum of  $(h,+k)$  and  $(h,-k)$ . Various  $(h,k)$  modes are excited for Cx1Cw cases (details in § 4.2).

### 2.2.2. Control streak strips

Control streaks are introduced using additional strips to control the transition process. Their formulation is quite similar to that of the unsteady blowing–suction but these perturbations are steady and the function in  $x$  is altered. Note that no net mass flux is introduced because there is no 2-D part in the wall-function. For all the cases mentioning FCS ‘ON’ in table 1, this strip runs from  $x_{c1.1}^* = (x_{in}^* + 0.002)$  m to  $x_{c1.2}^* = (x_{in}^* + 0.004)$  m,

$$\rho v(x, y = 0, z) = A_{FCS} \rho_\infty u_\infty f(x) g(z), \quad (2.7)$$

$$f(x) = 2.5983(1 - \cos \theta) / \sqrt{27} \quad (2.8)$$

here,  $\theta$  and  $g(z)$  have same formulations as defined earlier in § 2.2.1, see figure 13(a). Additionally, for cases with SCS ‘ON’, another more downstream control strip is used which extends from  $x_{c2.1}^* = (x_{in}^* + 0.01664)$  m to  $x_{c2.2}^* = (x_{in}^* + 0.01864)$  m. For cases C52Cn and C52Ch a different formulation of  $g(z)$  has been used (details will be described in § 4.6), which is given as

$$g(z) = \frac{1}{3} \times \left[ -\cos \left( \frac{2\pi \times 5z}{L_z^*} \right) + \cos \left( \frac{2\pi \times 10z}{L_z^*} \right) - \cos \left( \frac{2\pi \times 15z}{L_z^*} \right) \right]. \quad (2.9)$$

## 3. Validation

In order to validate the solver for growth rates of various modes in the boundary layer, ‘Case 1’ computed by Fezer & Kloker (2000), see also Mayer *et al.* (2011), is taken as the reference benchmark. See the latter paper also for an overview of the stability characteristics of the flow as obtained by linear stability theory. Modes (1,4) and (1/2,3) are excited using blowing–suction. It should be noted here that the details of blowing and suction used by Fezer & Kloker (2000) are not provided in their study, therefore the amplitudes of the fundamental and subharmonic modes are adjusted to match with the respective initial amplitudes. Figure 1 compares various modes of the current DNS with their counterparts by Fezer & Kloker (2000), marked

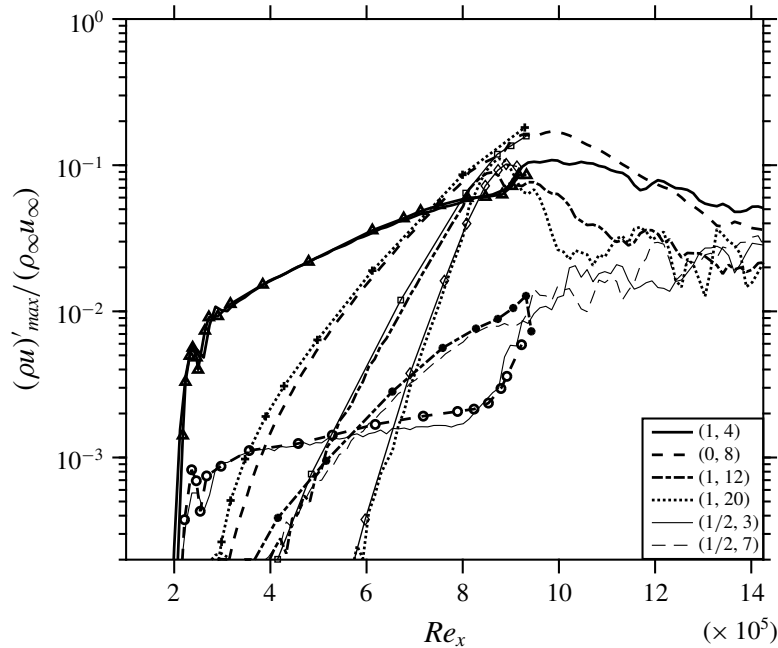


FIGURE 1. Comparison of the streamwise evolution of the maximum disturbance amplitudes of various modes with Fezer & Kloker (2000) (marked by symbols).

by symbols. The curves show a good collapse assuring that the DNS correctly predicts the growth of various modes. Each mode is computed by time-sampling over two fundamental periods, then performing a Fourier transform in the spanwise direction followed by one with respect to time, and then obtaining the maximum value in wall-normal direction at a given streamwise station. In order to cut the computational cost, a quarter of the domain used for validation is considered in the reference case  $C_{ref}$  for the remainder of the study. No subharmonic excitation is employed, only the fundamental mode (1,1), which peaks in growth rate in the frequency-spanwise wavenumber spectrum, is excited. Moreover,  $C_{ref}$  is seven times more refined in the spanwise direction than the original case used for validation. The instantaneous flow-field for  $C_{ref}$  is shown in figure 4(a) which prominently displays the oblique-type breakdown close to  $Re_x = 9 \times 10^5$ .

## 4. Controlling transition

### 4.1. Main scenario

In an attempt to control the transition to turbulence, control mode (0,5) – as a result of various trials, see below – is utilized, which is forced using a control strip running from  $Re_x = 1.48 \times 10^5$  to  $Re_x = 1.96 \times 10^5$  (case C51C). The longitudinal cut for C51C, coloured by the contours of temperature shown in figure 2, clarifies that no local temperature jump is introduced due to the induction of the steady control streak mode. The induced control mode indeed successfully suppresses the transition. It can be seen in figure 3(a) that, as a result of introduction of the control streak mode (location marked by vertical dashed lines) (0,5), a large MFD (0,0) is generated ( $\approx 12\%$  of  $\rho_\infty u_\infty$ ), and the control modes lead to the reduction of the growth rates of the main 3-D modes (1,1) and (0,2) in comparison to  $C_{ref}$ . The MFD is a part of the stabilization of the flow, as will be shown below in §4.5. The evolution of high-frequency modes initiated by the numerical background noise shown in figure 3(b)

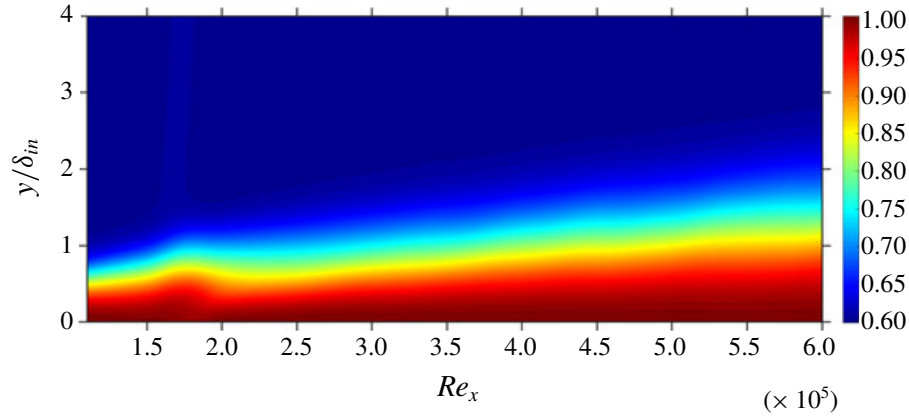


FIGURE 2. (Colour online) Longitudinal cut for C51C: contours of  $T/T_w$  at  $z/\delta_{in} = 13.5$ .

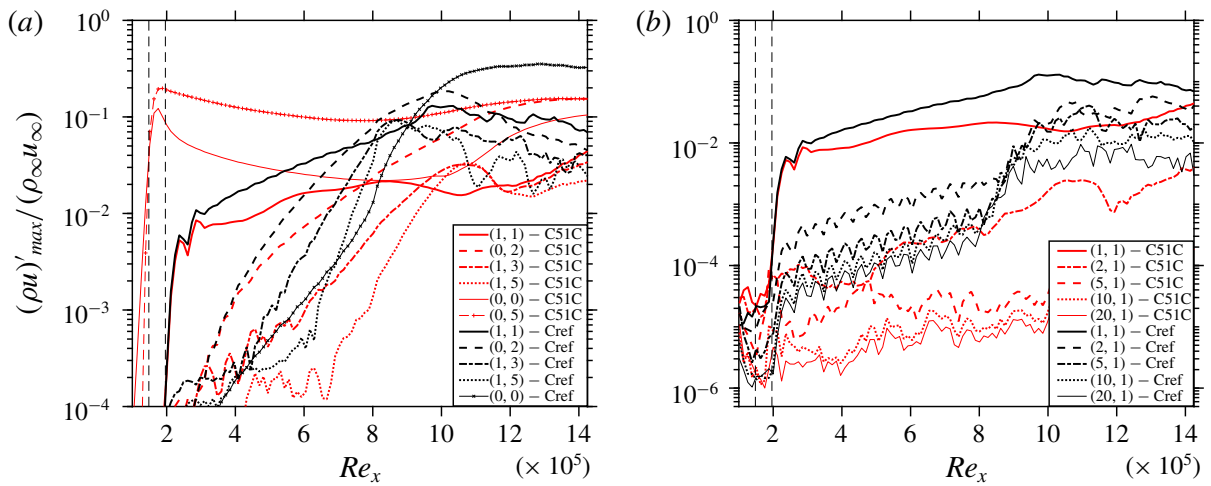


FIGURE 3. (Colour online) Comparison of the streamwise evolution of the maximum (a) disturbance amplitudes of various modes, and (b) amplitudes of high-frequency modes: C51C versus Cref.

depicts significant suppression for C51C. This difference is as large as three orders of magnitude towards the end of the domain because of the missing breakdown with control. The initial noise level generated from the solver is  $\approx 10^{-5}$  of  $\rho_\infty u_\infty$  (see figure 3b). Figure 4(b) shows the instantaneous flow-field for C51C demonstrating complete suppression of the turbulent region. Towards the end of the domain, (0,2) high-speed streaks can be prominently seen as a result of their higher amplitude from  $Re_x = 10^6$  onwards (see figure 3a). It is to be noted that no streak instability sets in despite the large (0,2) amplitude that however is enriched by the (0,5) control mode and (0,0). Flow cross-cuts in figure 5 show the early stage of transition of Cref in figure 5(a) while C51C remains stable at this location (see figure 5b) due to less pronounced low-speed regions. A comparison of figures 5(c) and 5(d) reveals a more stable nature of the streaky boundary layer of C51C compared to Cref due to the existence of the two high-speed streaks intruding into the low-speed near-wall region and preventing the build-up of strong, unstable low-speed regions, cf. figures 5(a) and 5(c).

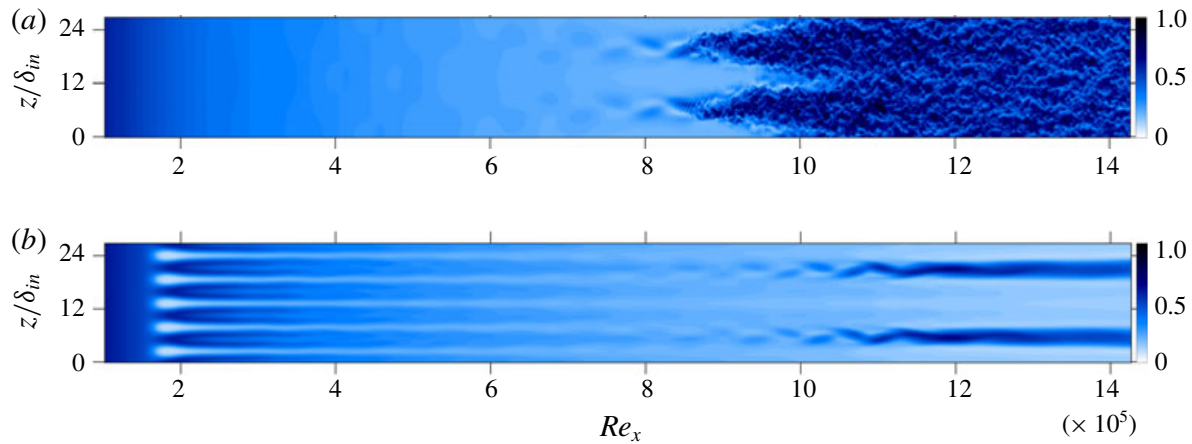


FIGURE 4. (Colour online) Instantaneous flow-fields for (a) Cref, and (b) C51C: contours of  $u/u_\infty$ , shown at  $y/\delta_{in} = 0.48$ .

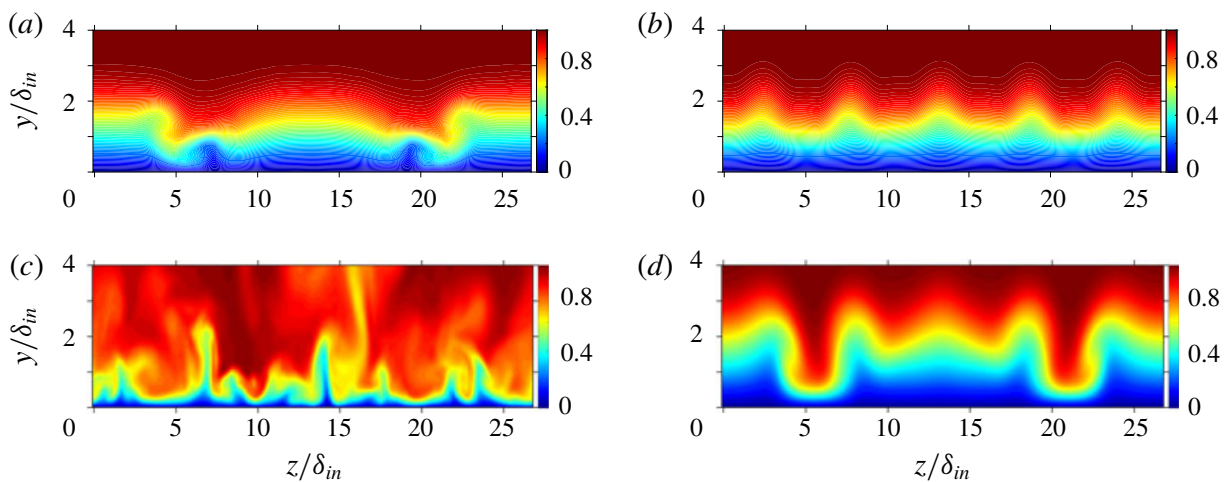


FIGURE 5. (Colour online) Contours of  $u/u_\infty$  for (a,b) at  $Re_x = 8.6 \times 10^5$ , (c) (snapshot) and (d) at  $Re_x = 13 \times 10^5$ , (a,c) case Cref, (b,d) C51C.

#### 4.2. Larger disturbance spectrum

The results presented so far prove the effectiveness of the considered control mode (0,5) in controlling the oblique-type breakdown induced by the fundamental symmetric mode (1,1). To investigate the effect of a broader disturbance input we consider the case C51Cw comprising of a total of five disturbance modes which are forced simultaneously in the same blowing–suction strip, each having the same amplitude as the fundamental mode before. The additional modes are (1,2), (1,3), (2,1), (2,3), to include higher spanwise wavenumbers being closer to the control-mode wavenumber and to provide modes that fill the gaps directly or by the nonlinear interaction that exists in the pure, fundamental case with (1,1) only. Likewise C51C, the transition is successfully suppressed in C51Cw despite the larger total forcing amplitude, see figure 6. It can be seen that (2,1) and (2,3) do not alter the scenario palpably. Modes (1,2) and (1,3) nonlinearly generate the streak modes (0,4) and (0,6), respectively, which are much closer to the spanwise wavenumber of the control mode (0,5), than the (0,2) of the fundamental mode. This may compromise the control strategy according to intuition and the findings of Paredes *et al.* (2017). However, it can be seen from figure 6 that the control mode (0,5), with the applied amplitude

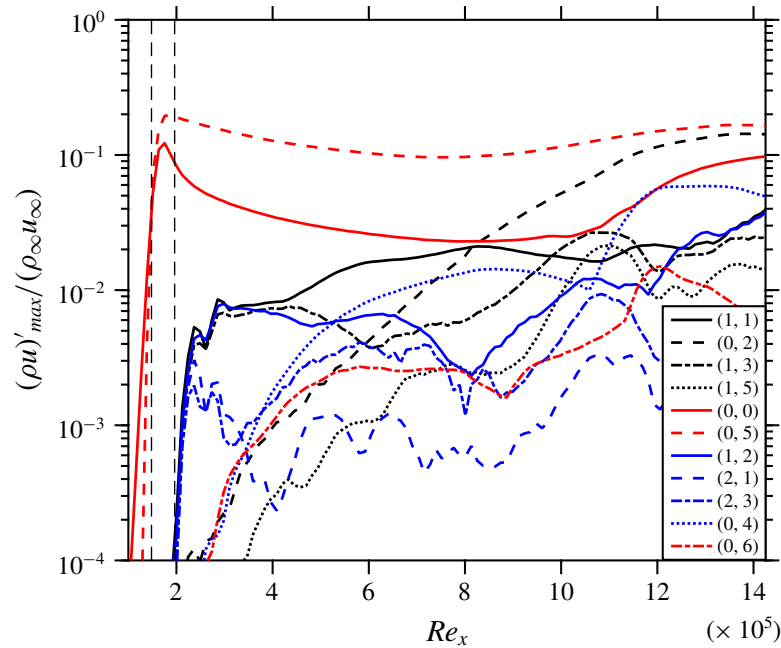


FIGURE 6. (Colour online) Streamwise evolution of the maximum disturbance amplitudes of various modes for C51Cw.

and the generated MFD (0,0), still successfully suppresses the significant growth of the relevant 3-D modes.

#### 4.3. Effects of control-mode amplitude

The two cases C51Cl and C51Ch with lower and higher forcing amplitudes of the control mode, respectively, are compared to C51C. Figure 7(a) shows the evolution of various modes for C51Cl; the sudden shoot-up of (0,0) close to  $Re_x = 8 \times 10^5$  signifies transition to turbulence. It can be implied from this figure that because of both the lower forcing amplitude of the control mode (0,5) and the MFD ( $\approx 9\%$  of  $\rho_{\infty} u_{\infty}$ ) transition cannot be suppressed. On the other hand, the high forcing amplitude of the control mode (0,5) in case C51Ch (figure 7b) causes rapid transition close to  $Re_x = 5 \times 10^5$ , see figure 8, as a result of strong streak-mode instability. The control-effective amplitude window is thus expectedly limited. Streaks with a modal  $\rho u$  amplitude larger than about 25% cause localized high-frequency instability even if they are closely spaced, as here.

#### 4.4. Implications of spanwise wavenumber of control mode

The effect of the spanwise wavenumber is investigated using four cases: C31Cw, C41Cw, C51Cw and C61Cw, employing control modes (0,3), (0,4), (0,5) and (0,6), respectively, with the wide disturbance spectrum. These control modes are induced with different forcing amplitudes (see table 1) in order to have the same effective Fourier amplitude at the end of the control strip (see figure 9). This comparison plot reveals that the streaks and generated MFD (0,0) decay is stronger the higher the spanwise wavenumber of the control mode is, except for C41Cw and C51Cw that behave similarly. On comparing the (0,0) modes further downstream it becomes clear that C31Cw and C61Cw do not show working control because their (0,0) modes shoot-up suddenly at  $Re_x = 10 \times 10^5$  and  $Re_x = 9 \times 10^5$ , respectively, signifying

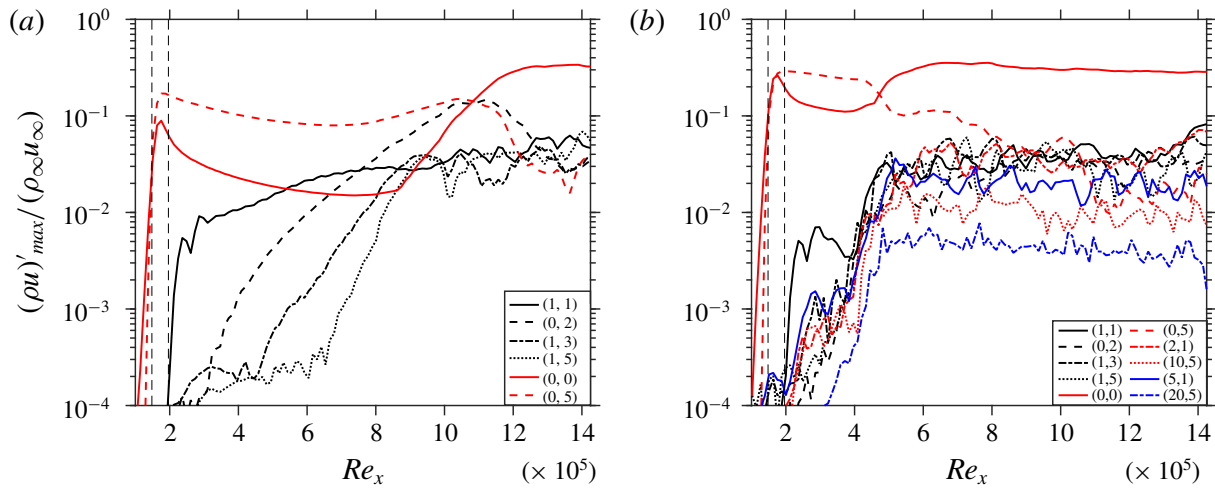


FIGURE 7. (Colour online) Streamwise evolution of the maximum disturbance amplitudes of various modes for cases (a) C51Cl, and (b) C51Ch.

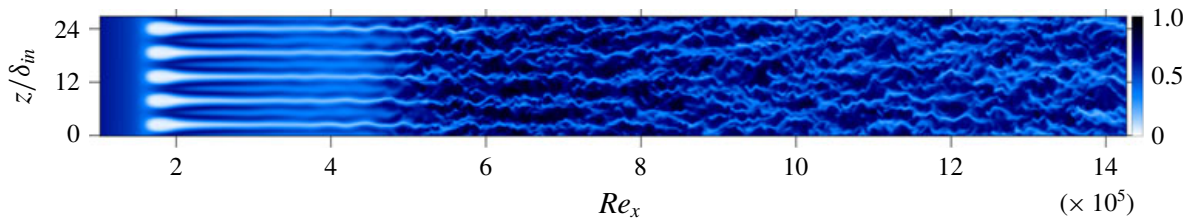


FIGURE 8. (Colour online) Instantaneous flow-field for C51Ch: contours of  $u/u_\infty$ , shown at  $y/\delta_{in} = 0.48$ .

transition. C61Cw generates the lowest of all control MFDs, and as soon as it falls below about 2% of  $\rho_\infty u_\infty$ , the flow shows early signs of transition at about  $Re_x = 8 \times 10^5$ . Hence, the growth rate of (1,1) is strongest for C61Cw. As a result of the high forcing amplitude of the control modes, relevant modes with double spanwise wavenumber are generated nonlinearly. The interaction of the generated (0,6) by control mode (0,3), which is as strong as the (0,3) itself (see figure 9), is responsible for destabilization of the flow towards the end of the domain, therefore, the control fails here. Figure 9 also shows that for C41Cw the amplitude of generated mode (0,8) remains about half as low as the control mode (0,4) while for C51Cw, (0,10) shows exponential decay right from its generation. An instantaneous flow-field of C41Cw is shown in figure 10; four high-speed streaks can be seen towards the end of the domain with more pronounced low-speed streaks, see the edges of the spanwise domain in figure 11, compared to C51C(w), see figures 4(b) and 5(d). Therefore, (0,5) stands out slightly as the best choice for the control mode. Finally, further simulations (not shown) indicated no relevant influence of a spanwise shift of the control modes in relation to the fundamental oblique mode (1,1).

#### 4.5. Role of the mean-flow distortion generated by the control

Here we investigate the contribution of the MFD quantitatively towards its share in the flow stabilization, cf. §5.3 in Wassermann & Kloker (2002). The analysis is performed as follows: the converged working cases are restarted, then the laminar baseflow is subtracted from the spanwise mean of the instantaneous flow which

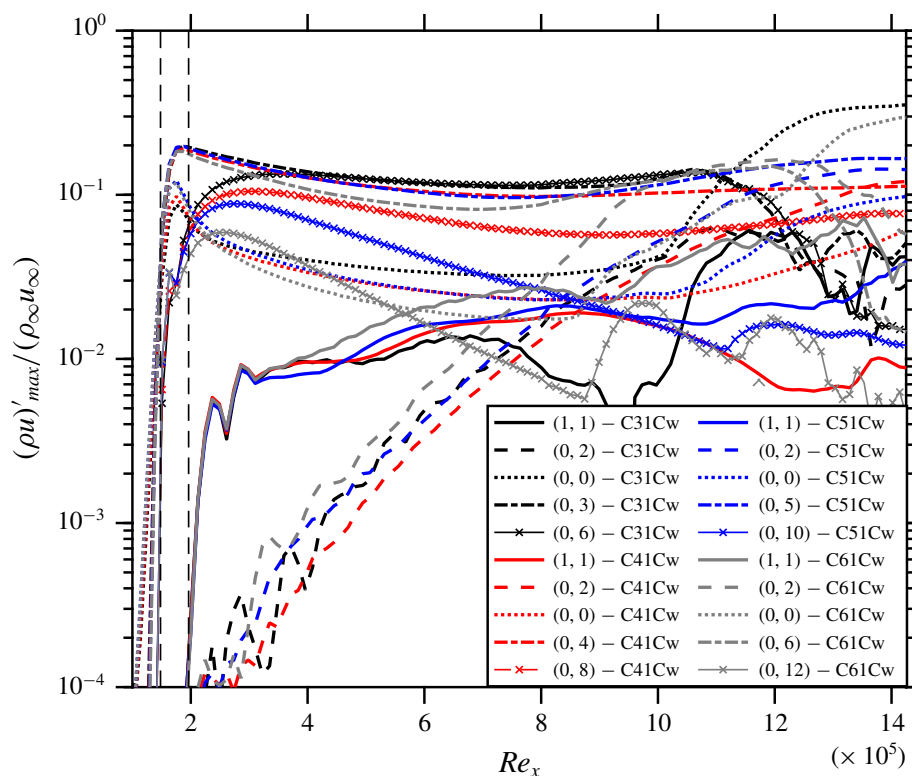


FIGURE 9. (Colour online) Comparison of the streamwise evolution of the maximum disturbance amplitudes of various modes of cases C31Cw, C41Cw, C51Cw and C61Cw.

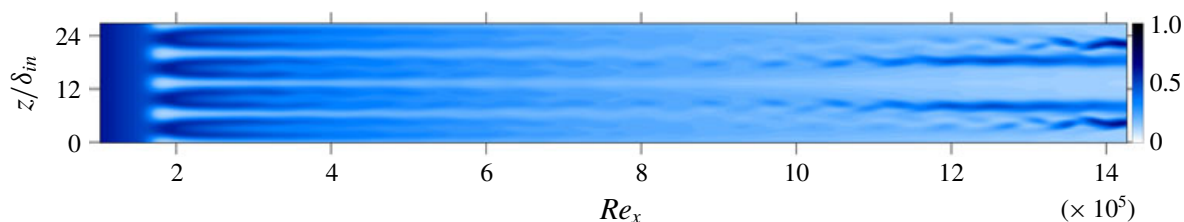


FIGURE 10. (Colour online) Instantaneous flow-field for C41Cw: contours of  $u/u_{\infty}$ , shown at  $y/\delta_{in} = 0.48$ .

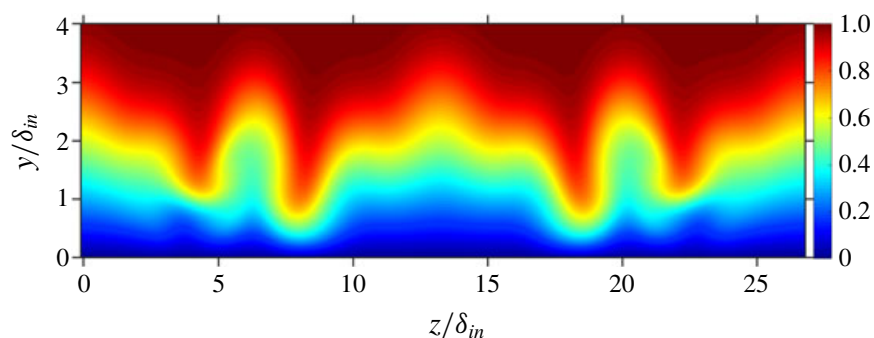


FIGURE 11. (Colour online) Cross-cut of the domain: contours of  $u/u_{\infty}$  for C41Cw at  $Re_x = 13 \times 10^5$ .

gives the 2-D disturbance part (2DP) of the flow including the MFD. Note that for regions where steady modes prevail, the 2DP is equal to the MFD. This 2DP is then subtracted from the instantaneous field, hence only the 3-D part remains in the

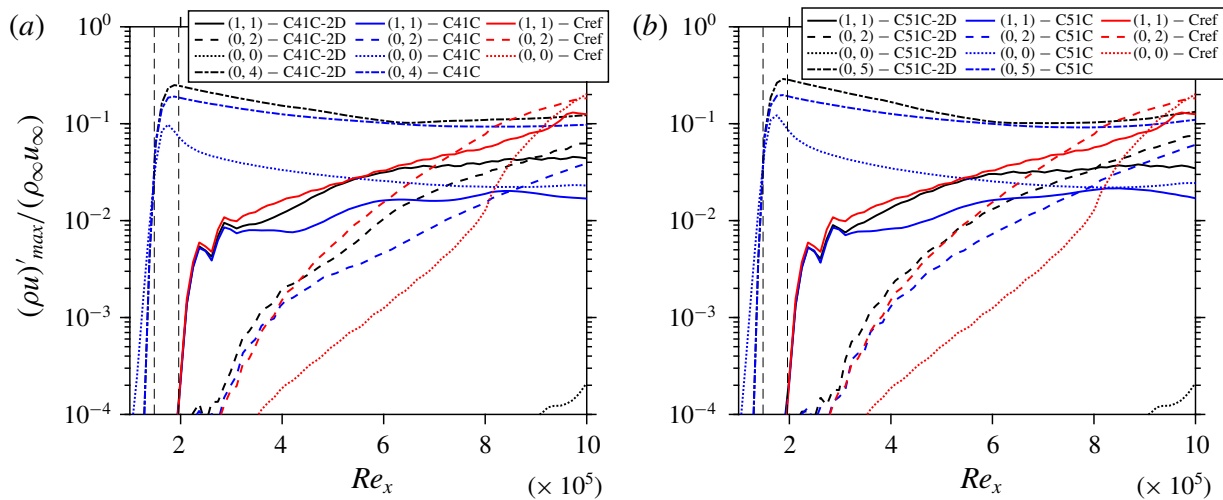


FIGURE 12. (Colour online) Comparison of the streamwise evolution of the maximum disturbance amplitudes of various modes for cases (a) C41C-2D with C41C and Cref, and (b) C51C-2D with C51C and Cref.

flow. The same procedure is repeated at each time-step. The flow is thus deprived of any 2-D part that is nonlinearly generated. This gives interpretable results in the early stages of the scenario where the 2-D modes (2,0) and (0,0) inherent in oblique breakdown without control are not too large. Figures 12(a) and 12(b) compare the modal growth for cases with and without the 2DP with Cref for C41C and C51C, respectively. It can be seen from these figures that the initial control-mode amplitude for both (0,4) and (0,5) gets larger if the respective MFD is suppressed at equal 3-D wall forcing, i.e. the nonlinearly generated MFD reduces the generated streak mode amplitude as qualitatively expected. The initial amplitude of (1,1) is reduced by the 3-D part of the control mode, independent of the existence of the MFD. Directly downstream of the first control strip, the MFD of the control is between 8% and 3%, and weakens the growth rate of the fundamental oblique mode (1,1) considerably. Without MFD its growth is initially even larger than without any control part (Cref case). However, if the amplitude of MFD falls below about 3%, its effect on the growth rate of the fundamental oblique mode (1,1) vanishes. Then, the (growth) development of the fundamental mode is the same with or without the MFD of the control, i.e. the amplitude curves run parallel with a difference caused by the initial suppressing effect of the MFD. The control streaks decay but never fall below 10% in the cases considered, and are eventually responsible for the suppression of the fundamental mode further downstream. Therefore, it may be concluded from figure 12 that the 3-D part of the streaks causes a suppression of the fundamental mode (1,1) when their (fixed) spanwise wavelength gets lower than about 2.3 times the local boundary-layer thickness; this holds for  $Re_x > 5.5 \times 10^5$  for C51C and for  $Re_x > 6 \times 10^5$  for C41C; for  $Re_x < 5 \times 10^5$ , the 3-D part may even cause a growth increase of (1,1). That is why a (0,3) control is here not effective for the fundamental (1,1) oblique mode, the latter being the most amplified mode as for primary instability. We note here that the ratio of spanwise wavelength to boundary-layer thickness that is found effective in control for the 3-D control part is about the same as that for optimally growing streaks, see Paredes *et al.* (2017). The streaks, however, decay here.

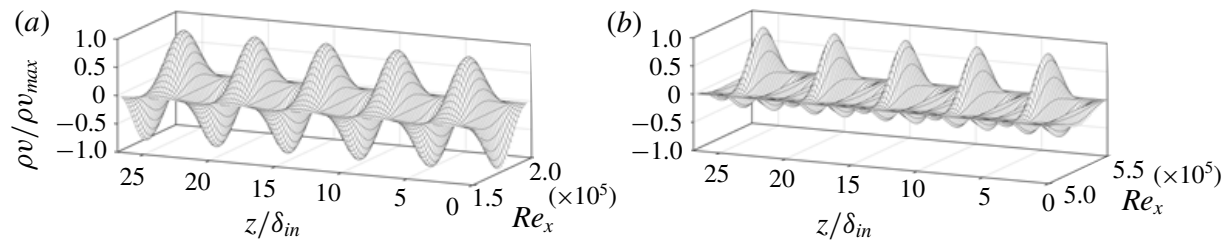


FIGURE 13. 3-D representation of control strip functions at (a) FSC, and (b) SCS for C52Cn and C52Ch.

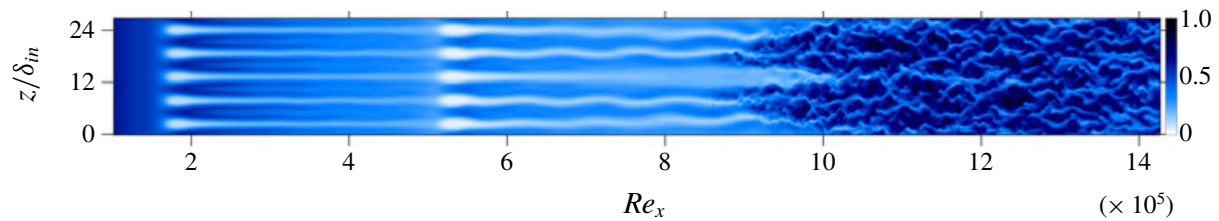


FIGURE 14. (Colour online) Instantaneous flow-field for C52C: contours of  $u/u_\infty$ , shown at  $y/\delta_{in} = 0.48$ .

#### 4.6. Bolstering the control

In order to check for an improvement of the effectiveness of transition control, another control strip is used further downstream extending from  $Re_x = 5.00 \times 10^5$  to  $Re_x = 5.49 \times 10^5$  for the cases C52C and C52Cn. For case C52C, the same control strip function as the first one is used. Its mathematical function is shown in figure 13(a) in a perspective view. Figure 14 shows the instantaneous flow field for C52C and it can be seen that the repetition of the strip turns out to be detrimental, resulting in earlier transition to turbulence. The cross-cut of C52C at  $Re_x = 8 \times 10^5$  in figure 15(b) shows pronounced destabilizing low-velocity streaks in comparison to C51C in figure 5(b). Figure 14 also reveals that after the induction of the streaks from the first control strip they tend to become thinner. At the second control strip the blowing, which is of the same spanwise size of the blowing at the first strip, results in local thickening and destabilization of the streaks and hence causes transition. Note that the blowing (part of the control) induces the low-speed streaks and the wall shear is smaller at the second strip, causing the blowing to effectively penetrate deeper into the boundary-layer. This issue can be addressed by altering the second control strip in such a manner that the blowing parts of the control become narrower and remain contained inside the oncoming streaks from the first control strip. To achieve this, the disturbance function is chosen as the sum of the control mode (0,5) and its first two super-harmonics (0,10) and (0,15), each component having a third of the original amplitude to yield the same peak amplitude of the function, see figure 13(b). In case C52Cn, the flow does, indeed, not show transition, and figure 16(a) shows the effectiveness of having a second control strip, by comparing the growth of various modes for cases C51C and C52Cn. The figure documents that the increase in amplitude of (0,5) at the second control strip reinforces the beneficial MFD (0,0) at the second control strip ( $\approx 5\%$  of  $\rho_\infty u_\infty$ ) which results in stronger suppression of the modes such as (1,1) and (0,2) for C52Cn in comparison to C51C. The instantaneous field is shown in figure 17. On comparing the streaks generated by (0,2) in C52Cn and C51C in figure 4 it can be seen that the ones for C52Cn are

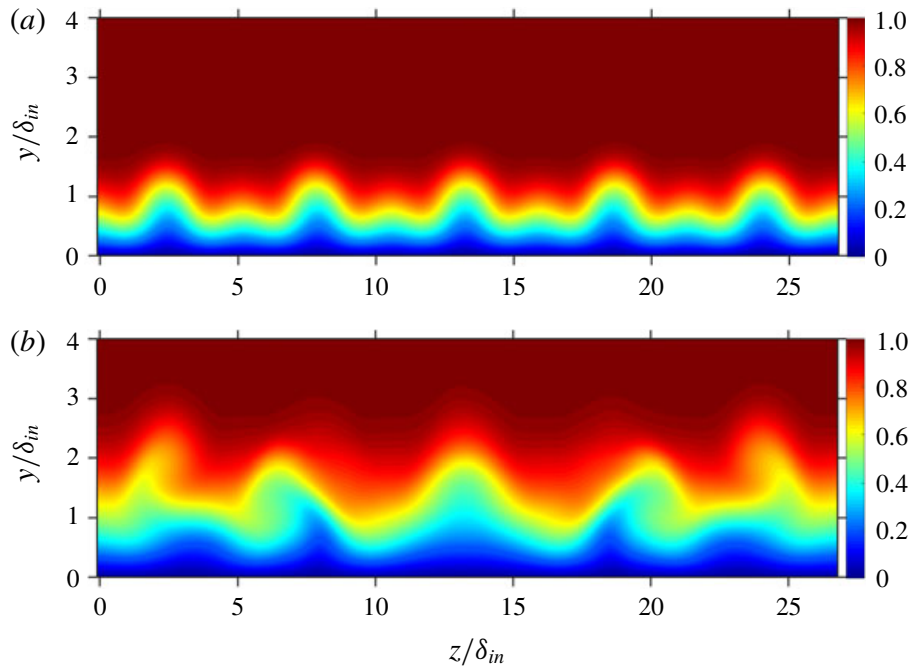


FIGURE 15. (Colour online) Cross-cuts of the C52C: contours of  $u/u_\infty$  at (a)  $Re_x = 3 \times 10^5$ , and (b)  $Re_x = 8 \times 10^5$ .

weaker than for C51C, which is a direct consequence of the stronger suppression of (1,1) due to the second control strip as shown in figure 16(a). If the peaky-blowing function is used for the first and second control strip, the result is the same as with the standard function for strips 1 and 2, C52C: the low-speed streaks are widened by the second strip, and the second strip is detrimental. A higher control amplitude at the second control strip leads to transition even for the peaky-blowing strip (case C52Ch). Figure 16(b) shows the modal evolution for C52Ch, and mode (1,1) is compared with case C52Cn. It is clear that just after the second control strip (1,1) grows strongly for C52Ch while it shows suppression for C52Cn indicating that most probably the mean-flow distortion generated in case C52Ch seems to be no more beneficial.

The assumption of the generation of a detrimental mean-flow distortion could be confirmed by inspecting the existence of a generalized inflection point (GIP) at the first and second control strip for all C5xCx cases. The GIP is defined as (Mack 1984)

$$GIP(y) : \frac{\partial \rho}{\partial y} \frac{\partial u}{\partial y} + \rho \frac{\partial^2 u}{\partial y^2} = 0, \quad (4.1)$$

and signifies the existence of an (additional) inviscid instability in the mean flow. Figure 18(a) depicts the GIP function in the middle of the first control strip ( $Re_x = 1.722 \times 10^5$ ) and in the middle of the second control strip ( $Re_x = 5.311 \times 10^5$ ) for various cases. This figure clarifies that no GIP is generated at the location of the first control strip, however, inflection points do exist at the location of the second control strip for cases C52C and C52Ch. The existence of the GIP is caused by the weaker wall shear at the second strip location due to the thicker boundary layer together with the large blowing amplitude. To assess the stabilizing role of the mean-flow distortion, the velocity and temperature profiles for mode (0,0) are plotted in figure 18(b). Here,  $\Delta T = \langle T_{C51C, C52C}^* \rangle - T_{base\ flow}^*$  and  $\Delta u = \langle u_{C51C, C52C}^* \rangle - u_{base\ flow}^*$  where  $\langle \rangle$  signifies the spanwise and time mean. The  $\Delta u$ -curve signifies that the flow is accelerated close

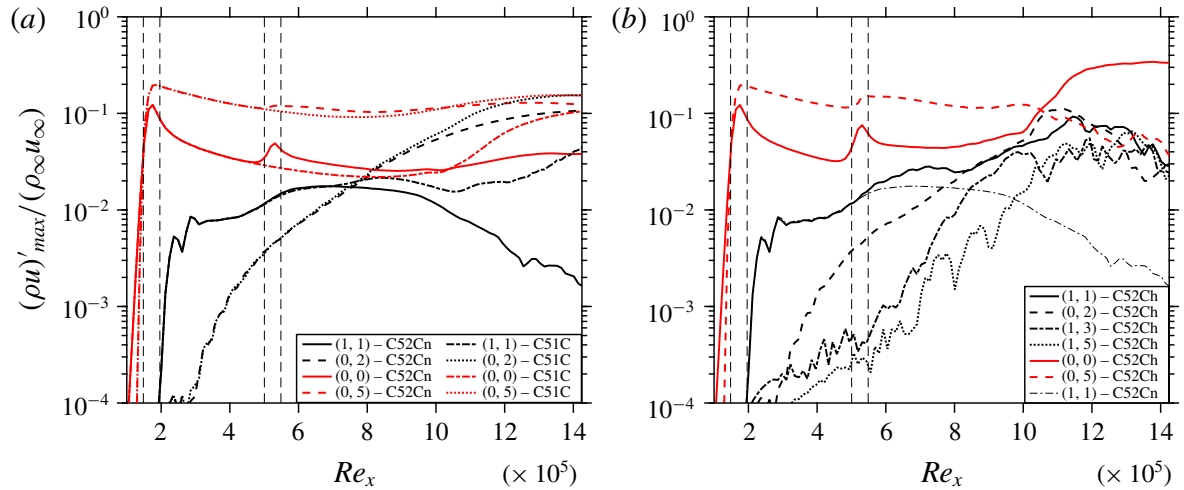


FIGURE 16. (Colour online) Comparison of the streamwise evolution of the maximum disturbance amplitudes of various modes of cases (a) C51C and C52Cn, and (b) C52Ch and C52Cn.

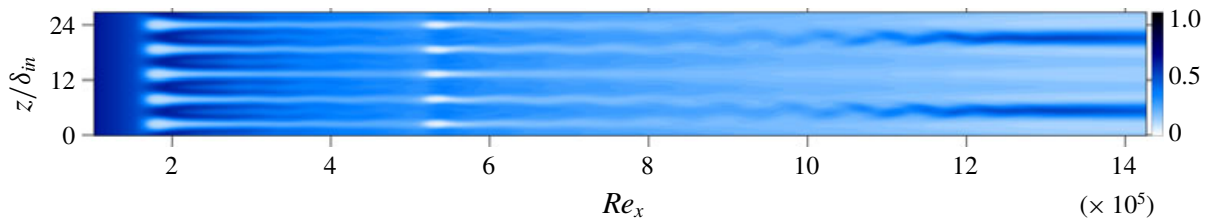


FIGURE 17. (Colour online) Instantaneous flow-field for C52Cn: contours of  $u/u_{\infty}$ , shown at  $y/\delta_{in} = 0.48$ .

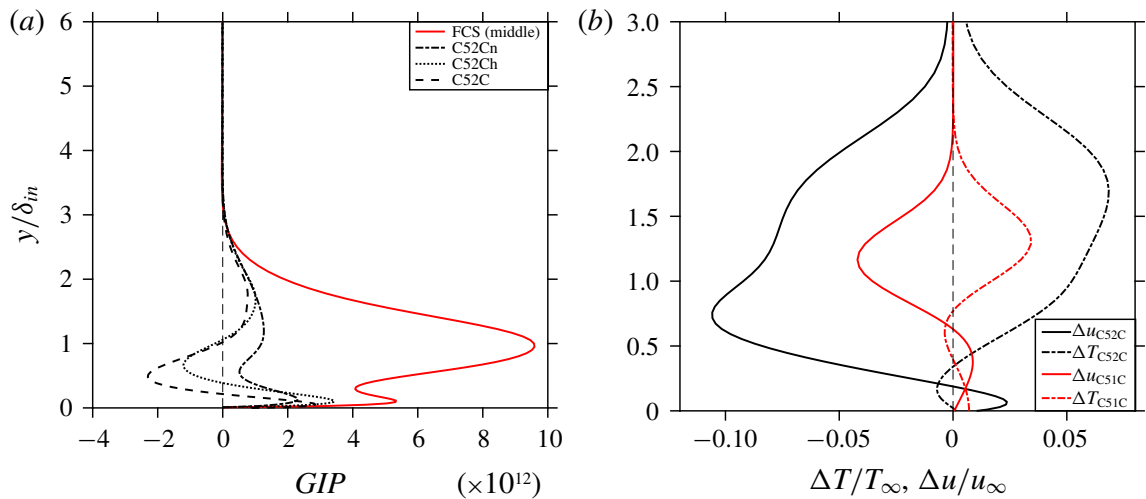


FIGURE 18. (Colour online) (a) Generalised inflection point curves at the middle of the first control strip ( $Re_x = 1.722 \times 10^5$ , red) and the middle of the second control strip ( $Re_x = 5.311 \times 10^5$ , black) and (b) temperature and velocity profiles for case C51C downstream of FCS at  $Re_x = 3 \times 10^5$  (red) and for C52C at SCS (black).

to the wall, and decelerated in the upper two-thirds of the boundary layer, both in line to a fuller, more stable profile (cf. figure 4 of Dörr & Kloker (2017)). From the

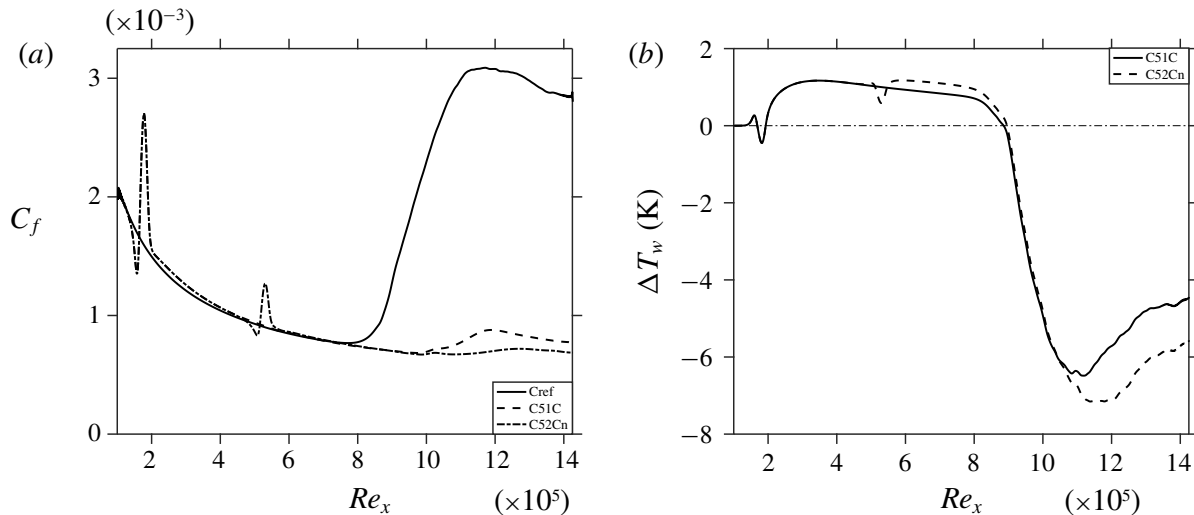


FIGURE 19. Streamwise evolution of (a)  $C_f$  and (b) time and spanwise averaged temperature for corresponding controlled cases with respect to Cref.

$\Delta T$ -profile it can be seen that the flow is slightly heated at the wall and cooled above. Both  $\Delta u$  and  $\Delta T$  point into the direction of a ‘disturbance-saturated’ mean-flow. Note that the existence of a GIP cannot be seen directly from the  $u(y)$  and  $T(y)$  profiles.

#### 4.7. Effects of controlling transition

The skin-friction coefficient  $C_f$  (spanwise and time mean) for cases C51C and C52Cn is compared with Cref in figure 19(a), showing the reduction of the  $C_f$  values for the two controlled cases due to the absence of a turbulent region; the localized peaky increase of  $C_f$  in the control strips is of minor importance. Figure 19(b) represents the temperature difference at the wall for the controlled cases,  $\Delta T_w = \langle T_{wC51C, C52Cn} \rangle - \langle T_{wCref} \rangle$ . It can be seen that due to the existence of streaks there is a slight penalty as for temperature for both cases C51C and C52Cn. Remarkably, for the turbulent portion of Cref, both cases C51C and C52Cn show a significant decrease in wall temperature, being augmented for C52Cn.

## 5. Conclusions

The successful control of full oblique-type breakdown of a supersonic adiabatic boundary layer at  $M_\infty = 2.0$  using control streaks has been demonstrated using DNS. The investigated streaks with, in various cases, three to six times the spanwise wavenumber of the fundamental, obliquely running modes and maximal  $\rho u$ -amplitudes of 20%–10% have been introduced by steady spanwise periodic suction/blowing at the wall within one or two control strips. Generally, higher wavenumbers of the decaying streaks are found to be more effective in suppressing the unsteady most-amplified fundamental mode (1,1) but need higher initial amplitudes due to a stronger streamwise decay, and can cause a significant shock-like, detrimental steady pressure wave. The oblique-breakdown streak mode (0,2) is not much influenced directly, rather by lowering the oblique travelling modes (1,1) that feed it.

It was found that the spanwise wavelength of effective control streaks lies between 20%–25% of the fundamental oblique mode. Modified DNS with suppressed 2-D disturbance parts and thus MFD could show that, for the 3-D part to be effective in

growth attenuation, the spanwise wavelength must be smaller than about 2.5 times the local boundary-layer thickness ( $\lambda_{control}/\delta < 2.5$ ); this value is about that of modes with optimal transient growth in theory. At the considered Reynolds number  $Re_x = 2 \times 10^5$  of the first spanwise blowing–suction control strip, all steady control modes monotonically decay directly downstream of the strip, the stronger the shorter the wavelength is. Starting with the ideal  $\lambda_{control}/\delta$  would lead to a fast decay of the streaks and no significant control can be achieved. For the streaks found effective on the whole, the ideal  $\lambda_{control}/\delta$  is reached downstream near  $Re_x = 5.5\text{--}6 \times 10^5$  when their control  $\rho u$ -amplitudes have decayed from initially about 20% to 10%, but at the same time the beneficial MFD induced falls eventually below 3% and gets inactive. In the first streamwise part downstream of the control strip, the MFD amplitude ranges from 10% to 3%, and the observed oblique-mode suppression is thus solely provided by the MFD. Globally, the MFD and the 3-D part of the control contribute each with a comparable share in the reduction of the fundamental-mode amplitude.

The MFD may become maleficial (locally) if the blowing part is too strong and not pointed enough; generalized inflection points occur in the spanwise-averaged velocity profiles, invoking inviscid instability. In refreshing the control strip downstream, the oncoming low-velocity streaks must not be widened locally which would otherwise trigger transition. The initial penalties in the wall shear and wall temperature increase are marginal by the control, shifting their increase by turbulence significantly downstream. Simulations with a broader disturbance spectrum comprising higher spanwise wavenumbers  $k$  and frequencies  $h$ , modes ( $h = 1\text{--}2$ ,  $k = 1\text{--}3$ ) and significantly increased total amplitude, show that the basic suppressing mechanisms also work in this case. The additional streak modes generated ( $0, k = 4, 6$ ) are much closer to the control mode and were considered critical *a priori*, but they do not degrade the control. Whether control streaks can cope robustly with more complex disturbance situations must be subject of next-step investigations.

### Acknowledgements

The authors acknowledge the access to French HPC resources provided by the French regional computing centre of Normandy (CRIANN) (grant nos 1998022 and 2017002) and Institut du développement et des ressources et informatiques scientifiques (IDRIS) under the allocation no. 2017-100752, by Grand Equipment National de Calcul Intensif (GENCI) under allocation no. A0022A10103. The funding resources are provided by European projects European Regional Development Fund (FEDER), Normandy Regional council, and NEPTUNE 1. S.S. would like to acknowledge the fruitful three-months research stay at IAG, University of Stuttgart, funded by the German Academic Exchange Service (DAAD), programme ID 57381332 (personal reference no. 91708728), hosted by M.J.K. whose ideas and support in finishing this study are appreciated.

### REFERENCES

- ANDERSSON, P., BRANDT, L., BOTTARO, A. & HENNINGSON, D. S. 2001 On the breakdown of boundary layer streaks. *J. Fluid Mech.* **428**, 29–60.
- BAGHERI, S. & HANIFI, A. 2007 The stabilizing effect of streaks on Tollmien–Schlichting and oblique waves: a parametric study. *Phys. Fluids* **19** (7), 078103.
- COSSU, C. & BRANDT, L. 2002 Stabilization of Tollmien–Schlichting waves by finite amplitude optimal streaks in the Blasius boundary layer. *Phys. Fluids* **14** (8), L57–L60.

- DÖRR, P. C. & KLOKER, M. J. 2017 Numerical investigations on Tollmien–Schlichting wave attenuation using plasma-actuator vortex generators. *AIAA J.* **56** (4), 1305–1309.
- FEZER, A. & KLOKER, M. J. 2000 Spatial direct numerical simulation of transition phenomena in supersonic flat-plate boundary layers. In *Laminar-Turbulent Transition*, pp. 415–420. Springer.
- FASEL, H. F., THUMM, A. & BESTEK, H. 1993 Direct numerical simulation of transition in supersonic boundary layers: oblique breakdown. In *Fluids Engineering Conference*, pp. 77–92. ASME.
- KOSINOV, A. D., SEMIONOV, N. V., SHEVELKOV, S. G. & ZININ, O. I. 1994 Experiments on the nonlinear instability of supersonic boundary layers. In *Nonlinear Instability of Nonparallel Flows*, pp. 196–205. Springer.
- LAIBLE, A. C. & FASEL, H. F. 2016 Continuously forced transient growth in oblique breakdown for supersonic boundary layers. *J. Fluid Mech.* **804**, 323–350.
- MACK, L. M. 1984 Boundary-layer linear stability theory. *Tech. Rep.* California Institute of Technology Pasadena Jet Propulsion Lab.
- MAYER, C. S. J., WERNZ, S. & FASEL, H. F. 2011 Numerical investigation of the nonlinear transition regime in a Mach 2 boundary layer. *J. Fluid Mech.* **668**, 113–149.
- PAREDES, P., CHOUDHARI, M. M. & LI, F. 2017 Instability wave–streak interactions in a supersonic boundary layer. *J. Fluid Mech.* **831**, 524–553.
- PIROZZOLI, S., GRASSO, F. & GATSKI, T. B. 2004 Direct numerical simulation and analysis of a spatially evolving supersonic turbulent boundary layer at  $m = 2.25$ . *Phys. Fluids* **16** (3), 530–545.
- SARIC, W. S., REED, H. L. & WHITE, E. B. 2003 Stability and transition of three-dimensional boundary layers. *Annu. Rev. Fluid Mech.* **35** (1), 413–440.
- SHADLOO, M. S., HADJADJ, A. & HUSSAIN, F. 2015 Statistical behavior of supersonic turbulent boundary layers with heat transfer at  $m = 2$ . *Intl J. Heat Fluid Flow* **53**, 113–134.
- SHAHINFAR, S., SATTARZADEH, S. S., FRANSSON, J. H. M. & TALAMELLI, A. 2012 Revival of classical vortex generators now for transition delay. *Phys. Rev. Lett.* **109** (7), 074501.
- SHARMA, S., SHADLOO, M. S. & HADJADJ, A. 2018a Effect of thermo-mechanical non-equilibrium on the onset of transition in supersonic boundary layers. *Heat Mass Transfer* doi:10.1007/s00231-018-2429-9.
- SHARMA, S., SHADLOO, M. S. & HADJADJ, A. 2018b Laminar-to-turbulent transition in supersonic boundary layer: effects of initial perturbation and wall heat transfer. *Numer. Heat Transfer A* **73** (9), 583–603.
- THUMM, A. 1991 Numerische Untersuchungen zum laminar-turbulenten Strömungsumschlag in transsonischen Grenzschichtströmungen. Dissertation, University of Stuttgart.
- WASSERMANN, P. & KLOKER, M. J. 2002 Mechanisms and passive control of crossflow-vortex-induced transition in a three-dimensional boundary layer. *J. Fluid Mech.* **456**, 49–84.

## 3.2 Calculating the contribution of the MFD

As mentioned in §4.5 of chapter 3, the role of the MFD produced by the control in suppressing the growth of the fundamental mode (1,1) is calculated by suppressing the 2-D disturbance part (2DP), see algorithm 3.2 for details. In this algorithm, the *mfd* array is an intermedi-

---

### Algorithm 3.2 : Reducing the 2-D part

---

```

1: Run a full case with all strips (control as well as the test mode) ON.
2: Allocate memory for calculating mean_z of the instantaneous and the baseflow.
3: Procedure COMPUTE MFD
4:   for MPI process in x and y directions do
5:     mfd (1, i, j) = mean_z_inst (1, i, j) - mean_z_base (1, i, j)
6:     mfd (2, i, j) = mean_z_inst (2, i, j) - mean_z_base (2, i, j)
7:     mfd (3, i, j) = mean_z_inst (3, i, j) - mean_z_base (3, i, j)
8:     mfd (4, i, j) = mean_z_inst (4, i, j) - mean_z_base (4, i, j)
9:     mfd (5, i, j) = mean_z_inst (5, i, j) - mean_z_base (5, i, j)
10: ! mfd = z_avg. (instantaneous field) - baseflow
11:   end for
12: end Procedure
13: Procedure UPDATE INSTANTANEOUS FIELD
14:   for MPI process in x, y and z directions do
15:     Q (1, i, j, k) = Q (1, i, j, k) - mfd (1, i, j)
16:     Q (2, i, j, k) = Q (2, i, j, k) - mfd (2, i, j)
17:     Q (3, i, j, k) = Q (3, i, j, k) - mfd (3, i, j)
18:     Q (4, i, j, k) = Q (4, i, j, k) - mfd (4, i, j)
19:     Q (5, i, j, k) = Q (5, i, j, k) - mfd (5, i, j)
20:   end for
21: end Procedure
22: call boundary conditions
23: advance in time (dt)
24: Repeat steps (3) to (23) at each time-step.

```

---

ate array which stores the difference of the spanwise averaged instantaneous flow and the baseflow. The Q array contains the conservative variables, where indices 1, 2, 3, 4 and 5 are the streamwise, the wall-normal, the spanwise velocity components, the density, and the energy, respectively. This method presents the ease of implementation in the CHOC-WAVES solver, but it has certain limitations. Due to the absence of the stabilizing effect provided by (0,0), the turbulence would start to appear and the code may blow-up after running for few fundamental time-periods. Depending on the cases to be investigated, a shorter domain can be considered for computing the role of the MFD so that the flow turns turbulent after longer duration ( $\approx 3$ -4 cross-over times).

Based on the structure of the solver utilized, other methods can also be used to get the contribution of the MFD towards the stabilization. On contrary to algorithm 3.2, instead

of reducing the 2-d part, we may remove the 3-D part of the control to check the effect of (0,0) (algorithm 3.3). The last step mentioned in algorithm 3.3 would prevent the steady

---

**Algorithm 3.3** : Reducing the 3-D control part

---

- 1: **Run** a case with just the control strip ON (deactivate the test mode strip).
  - 2: **Calculate** mean\_z of the flow-field ! This yields laminar baseflow + MFD (0,0)
  - 3: **Restart** the DNS on this field with all strips OFF
  - 4: **Advance** one time-step
  - 5: **STOP** DNS
  - 6: **Store** value of time derivative at any grid point ! This is the force  $F(x, y, z)$
  - 7: **START** DNS with test mode ON (control strip deactivated), and use step (2) as baseflow
  - 8: **SUBTRACT**  $F(x, y, z)$  at any grid point at any time-step.
- 

flow-field to get rid of the (0,0). Afterwards, the solver would compute the evolution of the disturbances in a steady flow that is not the original laminar boundary layer but the flow field enriched by the (0,0) of the control without its 3-D part. This way one can see what is the effect of the (0,0) alone, without the 3-D control part.

There exists another method which takes the route of LST (see algorithm 3.4). This method involves taking the baseflow + MFD for any case with control strip ON as frozen baseflow to be analyzed, followed by the calculation of the growth rate of (1,1) as a function of  $x$ . Then compare with the growth rate of (1,1) if the baseflow is just the laminar baseflow. This way one can see the growth rate weakening by the MFD, and this weakening can be compared to the one in the DNS case (Controlled Case - CREF) where the 3-d effects come additionally into play for the controlled case.

---

**Algorithm 3.4** : The LST approach

---

- 1: **Run** a full case with all strips (control as well as the test mode) ON.
  - 2: **Calculate** the growth rate of (1,1) as a function of  $x$ .
  - 3: **Compare** the growth of (1,1) if the baseflow is laminar.
- 

Another easier way is possible to get the effects of MFD (see algorithm 3.5). Step (3)

---

**Algorithm 3.5** : Approximate strategy

---

- 1: **Run** DNS with all strips (control mode + test mode) ON
  - 2: **Compute** mean\_z only for the control strip region
  - 3: **Replace** the actual flow field by the one of 2) up to the end of the control strip
  - 4: **Deactivate** the control mode strip
  - 5: **Restart** DNS on this new modified field
- 

of this procedure yields a 2-D field until the end of the control strip. After restarting the DNS on the modified flow-field, what happens is that the control mode will start to fade out in time because it is no more perturbed, but its MFD keeps perturbed (along  $y$  also). This simulation must continue until the control mode has died out to an amplitude of  $10^{-3}$  or so. Then, we see eventually the development of the flow influenced only by the MFD forcing.

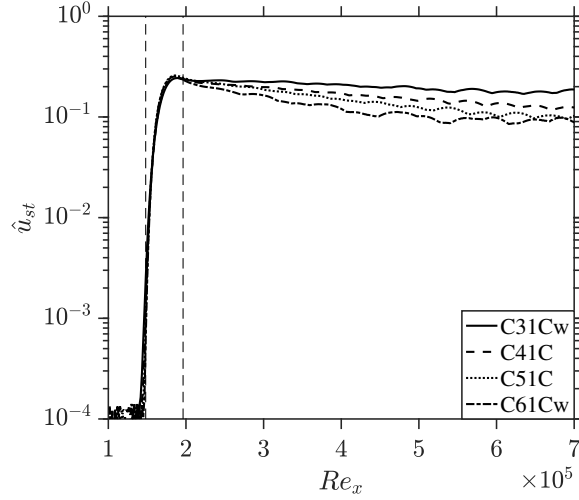


Figure 3.2: Streamwise evolution of streak amplitude for various cases in transition region.

The possible downside of this methodology is that the MFD may decay now stronger than before downstream of the strip; it will decay for sure after the control, but may be faster, or may change its shape along  $y$  (the latter not very likely). This method should show the effect of the MFD on the flow evolution up to  $Re_x = 6 \times 10^5$ .

### 3.3 Evolution of the induced streak amplitude

It would be of great interest to track the evolution of the amplitude of the control modes downstream of their induction. The strength of the generated streaks modes can be evaluated by (Groskopf & Kloker (2016)):

$$\hat{u}_{st} = \frac{1}{2} \left( \max_{yz} [u(x, y, z) - \langle u \rangle(x, y)] - \min_{yz} [u(x, y, z) - \langle u \rangle(x, y)] \right) \quad (3.1)$$

where  $\langle \rangle$  represents the spanwise averaged quantity.

Figure 3.2 shows the evolution of streak amplitude in transition region i.e. up to  $Re_x = 7 \times 10^5$  for different controlled cases. It can be seen from this figure that the streak amplitude of all the control modes decay exponentially right after their induction. Throughout the transition region, no transient growth is seen which should have been the case according to the PSE results of Paredes et al. (2017). Moreover, increase in the wavenumber increases the decay rate of the streaks downstream, therefore, even with lower amplitude forcing the (0,3) shows least decay for C31Cw (see figure 3.2).

# Chapter 4

## Factors influencing the by-pass transition

---

Published in: *Numerical Heat Transfer, Part A: Applications*



# Laminar-to-turbulent transition in supersonic boundary layer: Effects of initial perturbation and wall heat transfer

S. Sharma, M. S. Shadloo  and A. Hadjadj 

CORIA-UMR 6614, CNRS-University, INSA of Rouen and Normandie University, Rouen, France

## ABSTRACT

Direct numerical simulations of supersonic boundary layers (SBLs) over a flat plate for  $M_\infty=2.2$  are performed for adiabatic and isothermal (cooled and heated) walls. Receptivity analysis based on five criteria, namely skin-friction coefficient, Stanton number, Reynolds shear stress, wall-normal Reynolds heat flux, and modal decomposition are performed. Effect of perturbation intensity and wall heat transfer on the receptivity and the transitional growth of SBLs are presented. It is found out that increasing perturbation intensity moves the transition onset location upstream and increases the transition length. Additionally, below 1% perturbation intensity, wall cooling stabilizes the flow while beyond this value it has the opposite effect.

## ARTICLE HISTORY

Received 2 December 2017  
Accepted 10 April 2018

## 1. Introduction

Since the advent of supersonic era of aviation, the understanding of boundary layer flow stability along with attaining the in-depth knowledge of transition of supersonic boundary layer (SBL) flows to turbulence has become vital. The knowledge of high-speed boundary layer flows poses fundamental challenges in fluid dynamics community and is equally important to be investigated at the same time. In high-speed applications like for supersonic aircraft and spacecraft, the temperature of the wall [1] becomes an important parameter to be incorporated in the study. The wall temperature of a speeding aircraft is significantly lower than the adiabatic temperature of the wall, but on the other hand in case of atmospheric reentry of a spacecraft, due to the friction of the atmosphere, the wall temperature becomes way too higher than the adiabatic wall temperature. The high temperature of the exhaust gases over the blade of a gas turbine [2] or the wall of any propulsive nozzle [3] also mimic the heated wall scenario. For a spacecraft, the initial laminar flow could be tripped to turbulence because of the surface roughness and turbulence intensity [4]. Therefore, acquiring the physical insight of the transition of the flow from laminar to turbulent state becomes an absolute necessity.

Boundary layer flows are receptive to any form of disturbance (external or internal) which may trigger the transition of the flow to turbulent. Numerically, these disturbances could be induced through numerous ways like introducing roughness elements, a blowing and suction strip at wall, a physical turbulence model at the inlet, or any suitable combination of these techniques. According to the experimental investigation of Schubauer and Skramstad [5], after receptivity of the boundary layer toward the end of the laminar regime by laminar boundary layer oscillations, the low-amplitude two-dimensional unsteady Tollmien–Schlichting (TS) waves may grow up to

**CONTACT** M. S. Shadloo  [msshadloo@coria.fr](mailto:msshadloo@coria.fr)  CORIA-UMR 6614, CNRS-University, INSA of Rouen and Normandie University, 76000 Rouen, France.

Color versions of one or more of the figures in the article can be found online at [www.tandfonline.com/unht](http://www.tandfonline.com/unht).

an amplitude as high as 2% of the free-stream velocity. Klebanoff [6], in his pioneering work, observed the emergence of elongated streamwise streaks in laminar boundary layers as a consequence of free-stream disturbances. The principal findings of Klebanoff et al. [7] suggest that two oblique waves bearing the same frequency as that of the fundamental frequency of TS waves may interact among themselves to produce higher harmonics but with weaker nonlinear dynamics. This transition scenario is referred to as K-type (Klebanoff) transition [8] and is characterized by the in-line arrangement of  $\Lambda$  vortices in transition region, which are precursors of the turbulent transition. Another type of transition scenario exists which begins with the excitation of subharmonic fluctuations which are disproportionate to the fundamental TS wave frequency. For this case, the generalized formulation of subharmonic instability was presented by Herbert [9]. Hence, this scenario is known as H-type (Hebert) transition, which is characterized by the staggered arrangement of  $\Lambda$  vortices. However, the transition in H-type scenario is delayed in comparison to K-type. Lee et al. [10] have investigated the influence of viscosity stratification by wall heating on skin-friction reduction in turbulent boundary layers for heated and superheated walls. Their study utilized the incompressible flow considering water as the medium. The results of the direct numerical simulations (DNS) revealed a reduction in skin-friction coefficient for heated and superheated walls, which implies that wall heating tends to stabilize the flow [10].

Kurz and Kloker [11] studied the effects of a spanwise row of finite-sized cylindrical roughness elements over a swept-wing boundary layer and found out the changeover from a purely convective to a global instability near the critical height. However, for high-speed boundary layer transition, numerical investigations are mainly focused on transition through roughness elements. Bernardini et al. [12] and Van den Eynde and Sandham [13] have analyzed the effects of different shapes of roughness elements on transition. The results of Van den Eynde and Sandham [13] reveal that the frontal shape of roughness element and the shape in streamwise direction had a large impact on the onset of transition in hypersonic regime. Bernardini et al. [12] have also investigated the dominant instability modes in the near field past the roughness element and have given a new parameter for prediction of transition. Groskopf and Kloker [14] highlighted the impact of the orientation of the roughness element on laminar streak breakdown scenario. They found out that obliquely placed roughness element did generate more pronounced low-speed streaks in the roughness wake. For a given height of a roughness element, the unstable wake modes of various types have been investigated by De Tullio et al. [15] where the results reveal that varicose modes are the most unstable ones. The main objective of these studies on the whole was to better understand the mechanisms responsible for laminar to turbulent transition in high-speed flows. But, it seems that many voids are still present in the knowledge of such mechanisms in supersonic and hypersonic regimes as compared to the incompressible flows. Schneider [16] has presented an exhaustive overview of current state of the art for flow transition in case of high-speed flows.

For high-speed flows, growth mechanism discussed by Redford et al. [17] highlight that main-stream Mach number is the main governing parameter in determining the lateral growth rate of turbulent spots, while wall temperature being secondary one. They have also revealed that instability of the lateral jets which shows up close to the turbulent zone in the domain serves as a trigger for generation of new turbulent spots further downstream. Redford et al. [18] have utilized a thermal wall model which is coupled at high Mach number and showed that due to the frictional heating of the wall resulting from the fluid flow, the flow tends to relaminarize with the passage of time. An investigation regarding the implications of wall heat transfer on Klebanoff modes and TS waves has been performed by Ricco et al. [19]. They have highlighted various scenarios in which whether the wall cooling or heating will stabilize the flow. The results suggest that laminar streaks are stabilized by wall cooling when spanwise wavelength is quite large in comparison with the boundary layer thickness, whereas for Klebanoff modes, when the spanwise diffusion is comparable to the wall-normal diffusion, they are stabilized by wall heating. Franko and Lele [20] investigated the effects of adverse pressure gradient on laminar to turbulent transition of

high-speed flows, typically for Mach 6. They have studied three different transition mechanisms, namely first mode oblique breakdown, second mode oblique breakdown, and second mode fundamental resonance. Their results showed that the adverse pressure gradient did not fundamentally alter the process of transition nor the heat transfer overshoot. However, it did prepone the transition process and augmented the growth rate for both first and second mode instabilities. The results also highlight that the fundamental disturbances lead to immediate transition to turbulence in case of first mode oblique breakdown scenario because of the interaction of two oblique first mode instabilities which generate large streamwise vorticity producing an overshoot in heat transfer and generation of large amplitude streaks of velocity and temperature. These streaks break down soon due to their large magnitude. The skin friction and heat transfer overshoot in transition region have been observed in many experimental studies like in Wadhams et al. [21]. The numerical investigation about the heat transfer overshoot and breakdown mechanisms for high-speed boundary layers was done by Franko and Lele [22] involving different types of transition mechanisms as in Franko and Lele [20] but with zero pressure gradient. They uncovered that for all three mechanisms, the breakdown to turbulence was preceded by growth of streamwise streaks. It was also observed that second mode instabilities tend to dominate the flow as the wall temperature dropped. However, second mode fundamental resonance mechanism did not change with decreasing temperature. The study concluded that first mode oblique breakdown was the most likely mechanism of heat transfer overshoot found in the experimental studies before.

In spite of the discussion of many scientific works so far, the phenomena of supersonic transition to turbulence with wall heat transfer still remains not so well understood. Shadloo et al. [23] investigated the effects of wall heat transfer on transition onset for supersonic flows at free-stream Mach number of 2.2. This specific lower supersonic Mach number was chosen because the effects of thermal modes are not well enhanced in hypersonic regime as other acoustic instabilities like Mack modes start to dominate the flow. The results were also compared against the predictions of linear stability theory (LST). Good agreement was observed in the results of LST and DNS for adiabatic case. On contrary to the LST predictions, for isothermal cases it was found that heating up the wall actually stabilized the flow and it transits farther downstream to turbulence when compared to the adiabatic wall while on the other hand, cooling down the wall did destabilize the flow and it transited upstream in comparison with the adiabatic case. The main reason accounted for this discrepancy was the thermomechanical nonequilibrium of the temperature profiles, as all of the investigated cases had adiabatic inlet temperature profile regardless of the wall temperature. Shadloo and Hadjadj [24] also showed the evolution of the disturbance energy in the streamwise direction and found that the growth rate slopes remain the same and merge together in turbulent area, regardless of the wall temperature. They have considered the perturbation intensities of 2.4% and 4% of the free-stream velocity which actually lie in nonlinear regime. In addition to thermomechanical nonequilibrium, these high turbulence intensities were also accounted as one of the reasons for disagreement from the LST results. Therefore, in our study, we have also considered lower perturbation intensities of 0.5% and 1%, so that the impact of growing nonlinear mechanisms could also be explored.

After having a wholesome view of the available scientific literature, by this study we try to answer some of the vital questions related to transition in SBL flows over adiabatic and isothermal (cooled and heated) walls. In this study, we will be discussing about the receptivity of boundary layer flow transition for changing perturbation intensity and wall heat transfer, and try to understand the physical phenomena responsible for the hence observed behavior. The results obtained would be compared against the available literature.

The rest of the manuscript is organized as follows: The details of the numerical simulation setup including governing equations, numerical solver, boundary conditions, and details regarding the computational domain are given in Section 2. Then, a detailed discussion of the effects of changing perturbation intensity, wall heat transfer, and joint effects of perturbation intensity and

wall heat transfer on transition is presented in Sections 3.1 , 3.2, and 3.3, respectively. Finally, the study is concluded in Section 4.

## 2. Details of the direct numerical simulations

### 2.1. Numerical solver

The motion of any fluid with a given viscosity  $\mu$  and density  $\rho$  can be represented by a set of equations known as the Navier–Stokes equations (NSE). This set of equations essentially comprises of the equations of conservation of mass, momentum, and energy. For this study, we have employed a well-validated DNS–LES numerical solver known as CHOC-WAVES, which solves three-dimensional compressible unsteady NSE for perfect gases. The convective fluxes are discretized by means of a hybrid conservative sixth-order central scheme with fifth-order weighted essential nonoscillatory (WENO) scheme. For better numerical stability, the convective terms are split in a skew-symmetric form in order to minimize the aliasing error and enforce discrete conservation of kinetic energy. The diffusive terms are approximated with fourth- or sixth-order formulas and expanded in Laplacian form. The system of equations is integrated in time using third-order Runge–Kutta (RK-3) scheme. For more details and validation of the solver, the readers can refer to Shadloo et al. [25] and Ben-Nasr et al. [26].

### 2.2. Computational domain and boundary conditions

For current investigation, supersonic flow over a flat plate is considered with free-stream Mach number  $M_\infty = 2.2$ , temperature  $T_\infty = 177$  K, pressure  $p_\infty = 23796$  Pa, and Prandtl number  $Pr = 0.72$ . The subscript  $\infty$  denotes the free-stream values. The velocity, temperature, and density profiles at the inlet of the computational domain are calculated using a dedicated solver to obtain similarity solutions of a laminar compressible boundary layer over adiabatic and isothermal walls. This similarity solution is applied at a certain distance from the beginning of the domain at  $x_{in}$ . For adiabatic case, the wall temperature is kept as  $T_w = T_{aw}$ , while for cooled and heated walls, the temperature is  $T_w = 0.75 T_{aw}$  and  $T_w = 1.5 T_{aw}$ , respectively, where  $T_{aw} \approx 1.82 T_\infty$ . Details about the cases under investigation have been enlisted in Table 1. In this table, A, C, and H stand for adiabatic, cooled, and heated walls; 1, 2, and 3 represent different perturbation intensities of 0.05%, 1%, and 2.4%, respectively with respect to the free-stream velocity. The fluid considered is air with constant specific heats. The dynamic viscosity is calculated using Sutherland’s law  $\mu = C_1 T^{3/2} / (T + S)$ , where,  $S = 110.4$  K is Sutherland’s temperature for air and  $C_1 = 1.458 \times 10^{-6}$  kg/ms  $\sqrt{K}$ . As shown in Table 1, a constant excitation frequency,  $\omega = 150$  krad/s, is chosen for blowing and suction strip for all the cases which corresponds to the most unstable frequency

**Table 1.** Computational parameters of various test cases considered

Cases	$T_w/T_{aw}$	$A/u_\infty$	$\omega$ (krad/s)	$Re_{\theta,max}$	$\Delta x^+$	$\Delta y_{min}^+$	$\Delta z^+$
A1	1.0	0.005	150	6144	11.05	0.34	6.52
A2	1.0	0.010	150	3217	11.05	0.34	6.52
A3	1.0	0.024	150	3675	11.05	0.34	6.52
C1	0.75	0.005	150	1896	16.24	0.5	9.58
C2	0.75	0.010	150	3095	16.24	0.5	9.58
C3	0.75	0.024	150	3935	16.24	0.5	9.58
H1	1.5	0.005	150	2888	6.62	0.21	3.91
H2	1.5	0.010	150	3105	6.62	0.21	3.91
H3	1.5	0.024	150	3474	6.61	0.2	3.90

A, C, and H stand for adiabatic, cooled, and heated walls, respectively.

Subscripts *min* and *max* are the wall-normal spacing and maximum Reynolds number which can be achieved in the domain respectively.

Superscript + denotes the quantities in wall units.

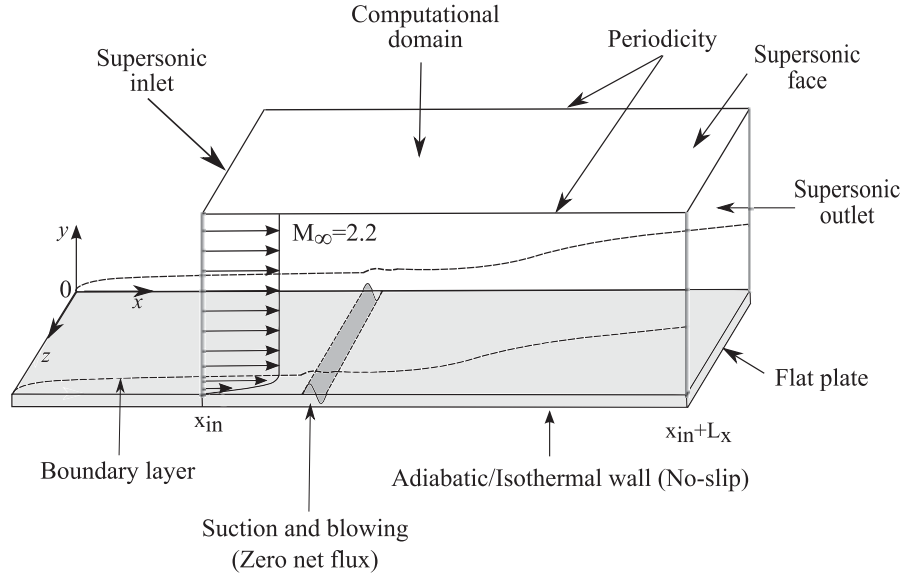


**Figure 1.** Computational domain and boundary conditions.

according to LST [23,24]. However, Shadloo et al. [23] have utilized  $\omega = 75$  krad/s for their study following the work of Pirozzoli et al. [27].

A schematic of the computational domain along with the boundary conditions is presented in Figure 1. The considered domain is large enough ( $L_x/\delta_{in} \approx 390$ ), so that the transition and the turbulent regions of the flow field could be captured satisfactorily except for the case C1 where the flow did not transit to turbulent even in double the length in streamwise direction. The height and the width of the domain are chosen keeping in mind that the flow physics is not compromised by wall-normal outflow and spanwise periodic boundary conditions ( $L_y/\delta_{in} \approx 31$  and  $L_z/\delta_{in} \approx 16$ ). It is noted that this choice is nearly similar to the computational height and accounts for nearly 30% larger domain in both the streamwise and the spanwise directions than the one used by Pirozzoli et al. [27]. Supersonic inflow and outflow boundary conditions are imposed at the inlet ( $x = x_{in}$ ) and at the outlet ( $x = x_{in} + L_x$ ), respectively. For the upper face of the domain, uniform supersonic flow boundary condition is employed, so that the flow may remain undisturbed and no confinement effect is there. It is important to mention here that at the outlet of the domain, no buffer layer has been utilized for compensating the edge effects. This is justified for the scope of this study because here our focus is on the transition region, and far-field turbulent region (toward the end of the domain) is of no interest.

No-slip boundary condition is imposed at the wall ( $y=0$ ), except for the narrow strip between  $x_a = x_{in} + 0.3 \delta_{in}$  and  $x_b = x_{in} + 0.6 \delta_{in}$  where the disturbances are induced by suction and blowing, as used by Shadloo et al. [23]. In this region, the wall-normal component of velocity is prescribed by single-frequency and multiple spanwise wavenumber boundary condition given as  $v(x, z, t) = Af(x)[g(z)/\max(g(z))][h(t)/\max(h(t))]$ , where  $A$  is the amplitude of disturbance,  $f(x)$ ,  $g(z)$ , and  $h(t)$  are the streamwise, spanwise, and time-dependent variations, respectively, and

are defined as  $f(x) = 4\sin\theta(1 - \cos\theta)/\sqrt{27}$ ,  $g(z) = \sum_{l=1}^{l_{max}} Z_l \sin(2\pi l(z/L_z + \phi_l))$ , and

$h(t) = \sum_{m=1}^{m_{max}} T_m \sin(\omega t + \phi_m)$ , with  $\omega$  being the fundamental frequency of the induced disturbance,  $\theta = 2\pi(x - x_a)/(x_b - x_a)$ , and  $\phi_l$  and  $\phi_m$  are the random numbers between 0 and 1. Also,  $\sum_{l=1}^{l_{max}} Z_l = 1$ ,  $Z_l = 1.25Z_{l-1}$ , with  $l_{max} = 20$  and  $\sum_{m=1}^{m_{max}} T_m = 1$ ,  $T_m = 1.25T_{m-1}$ , with  $m_{max} = 20$ . The

method employed here is a modified version of the one used by Pirozzoli et al. [27] and has shown its effectiveness for Shadloo et al. [23] and Shadloo and Hadjadj [24].

Mesh spacing is uniform in both the streamwise and the spanwise directions with  $N_x = 2048$  and  $N_z = 140$  being the number of points considered in stated directions. In wall-normal direction, the total number of points,  $N_y = 150$ , are more concentrated close to the wall in order to capture the details of the boundary layer. The stretching function in wall-normal direction is given by  $y = L_y[1 + \tanh(\kappa_o y)]/\tanh(\kappa_o)$  with,  $\kappa_o \approx 3$  being the stretch parameter.

### 3. Results and discussion

#### 3.1. Effects of changing perturbation intensity

For high-speed flows, the transition location does not possess a unique definition [22]. Various methods have been employed in some experimental studies which necessarily need not agree [28]. Therefore, in this study we try to characterize the transition region parameters using various criteria, namely the streamwise evolution of skin-friction coefficient ( $C_f$ ), contours of Reynolds shear stress (RSS), contours of wall-normal component of Reynolds heat flux (RHF), modal decomposition (MD), and the streamwise evolution of Stanton number ( $St$ ). For exploring the qualitative and quantitative features of supersonic transition, in this section we will focus on the effects that changing perturbation intensity has on the transition onset. Only adiabatic cases have been considered here. Figure 2 depicts the streamwise evolution of skin-friction coefficient for A1, A2, and A3 cases,  $C_f = \tau_w/[(1/2)\rho_\infty U_\infty^2]$ , where  $\tau_w$  is the local shear stress at the wall.

As skin-friction coefficient is the most widely used criterion to quantify the transition location, hence we have utilized the least and the maximum time-averaged values of skin-friction coefficient in the streamwise direction as the beginning and the end of the transition region, respectively. Just at a glance of Figure 2, it is clear that the transition location is receptive to the changes in perturbation intensity. It can be seen that with increase in perturbation intensity, the transition onset location shifts upstream, as A3 begins to transit the earliest at  $Re_x = 3.03 \times 10^6$  followed by A2 and A1 at  $Re_x = 3.64 \times 10^6$  and  $Re_x = 4.12 \times 10^6$ , respectively. The end of transition is marked at  $Re_x = 4.20 \times 10^6$ ,  $Re_x = 4.75 \times 10^6$ , and  $Re_x = 5.32 \times 10^6$  for A3, A2, and A1, respectively. The length of transition region also increases with increase in perturbation intensity, except for A1 and A2 for which it remains almost constant. A closer look to this figure reveals that there exists an overshoot in skin friction in the beginning of turbulent regime for all three cases which could be due to the elongated streamwise vortical structures, also referred as steady modes, as suggested by Franko and Lele [22]. The observed trend of transition onset for changing perturbation intensity is also supported by results of Shadloo et al. [23] and Shadloo and Hadjadj [24].

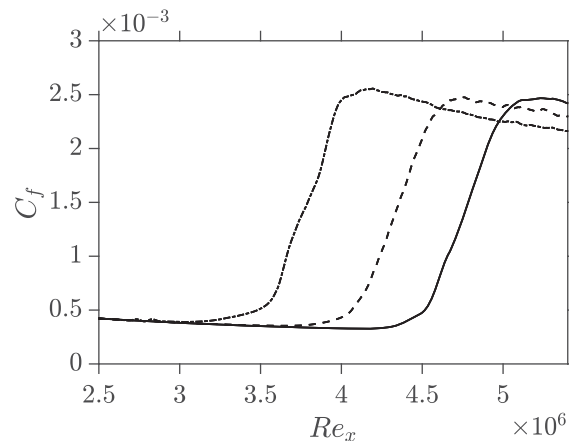
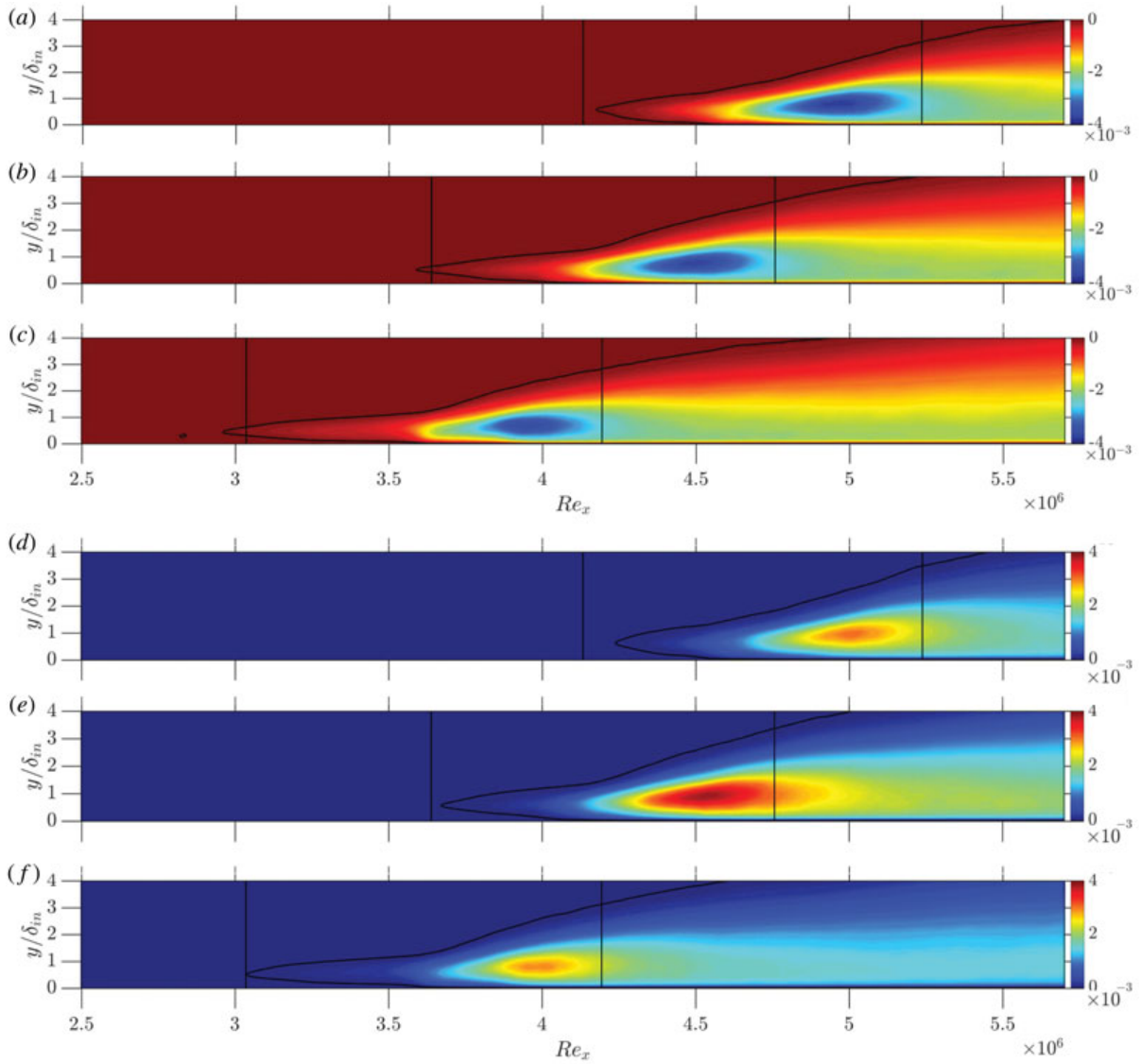
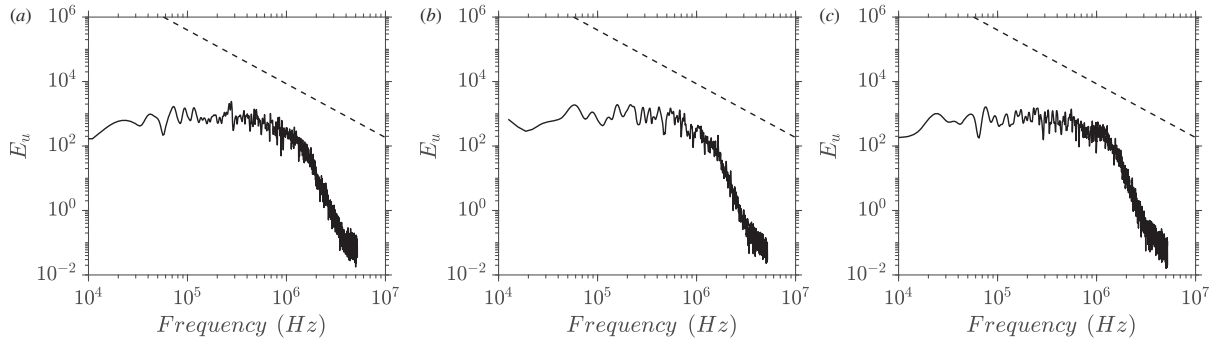


Figure 2. Streamwise evolution of skin-friction coefficient as a function of  $Re_x$  for cases A1(—), A2(---), and A3(-.-) cases.



**Figure 3.** Contours of Reynolds shear stress,  $\frac{\overline{\rho u''v''}}{\rho_w U_\infty^2}$  for (a) A1, (b) A2, and (c) A3 cases, and contours of wall-normal Reynolds heat flux,  $\frac{\overline{\rho v''T''}}{\rho_w U_\infty T_w}$  for (d) A1, (e) A2, and (f) A3 cases.

Figures 3a–3c show the contours of Reynolds shear stress,  $\frac{\overline{\rho u''v''}}{\rho_w U_\infty^2}$  which signifies momentum transport for different perturbation intensities, and here the scale of  $y$ -axis has been exaggerated. The Reynolds shear stress has negative values in the boundary layer region. Higher negative values mean that high momentum fluid is being pushed toward the wall and low momentum fluid is being moved away from the wall. This momentum transport accounts for the increase in the skin-friction coefficient in the domain. In Figure 3, vertical black lines mark the start and the end of transition region based on the  $C_f$  criterion (they have the same meaning throughout this study, unless stated otherwise). The highlighted black contour depicts 1% of the maximum magnitude of Reynolds shear stress attained in the domain. This contour marks the beginning of the preliminary interactions between the fluid layers and gives the very first signs of increase in Reynolds shear stress in the domain. Therefore, the point where this continuous black contour starts appearing for the first time in the streamwise direction would be utilized as the transition onset position for this criterion. The location of the local minimum of the RSS in the streamwise direction would be considered as the end of transition region. Hence, the transition onset locations for A1, A2, and A3 are  $Re_x = 4.17 \times 10^6$ ,  $3.59 \times 10^6$ , and  $2.96 \times 10^6$ , respectively. The least valued Reynolds shear stress region is located at  $Re_x = 4.98 \times 10^6$ ,  $4.48 \times 10^6$ , and  $3.96 \times 10^6$ , respectively, for A1, A2, and A3 which corresponds to rise in the skin-friction coefficient toward the end of transition region followed



**Figure 4.** One-dimensional premultiplied frequency spectra of streamwise velocity fluctuations for (a) A1, (b) A2, and (c) A3 cases at  $Re_x = 4.98 \times 10^6$ ,  $4.48 \times 10^6$ , and  $3.96 \times 10^6$ , respectively, along with  $(-5/3)$  law of turbulence decay, marked by  $(- -)$ .

by an overshoot in  $C_f$ . Figure 4 compares the slopes of premultiplied frequency spectra for all three cases taken at these local minima along with  $-5/3$ rd law of turbulence decay. The similarity of the slopes in Figure 4 confirms the existence of fully developed turbulent flow at the mentioned locations. From Figures 3a–3c, it can be seen that the  $C_f$  criterion points out the existence of fully developed turbulent regime somewhere downstream when compared to the locations shown by RSS criterion. Figures 3a–3c also point out that with increase in perturbation intensity, the location of the peak RSS shifts upstream and hence the transition location moves upstream too, as marked by the  $C_f$  criterion. It is observed that the transition onset locations predicted by  $C_f$  criterion are consistently different from the ones pointed out by the RSS criterion. With the increase in perturbation intensity, the starting point of 1% contour moves closer to the wall with  $y/\delta_{in} = 0.63$  for A1, 0.56 for A2, and 0.49 for A3 in wall-normal direction which means that increasing perturbation intensity tends to intensify Reynolds shear stresses in the near-wall region. As a result of this, the length of the transition region gets elongated as the streaks become longer. Moreover, the difference between the transition lengths predicted by the  $C_f$  criterion and Reynolds shear stress decreases with an increment in perturbation intensity due to the same reason. A comparison between Figures 2 and 3a–3c reveals that transition region's length predicted by the  $C_f$  criterion is constant for A1 and A2 but increases for A3, but on the other hand, RSS predicts increasing length with increase in perturbation intensity. More details regarding transition region comparison would be discussed in Section 3.4.

Figures 3d–3f shows the comparison of contours of the wall-normal Reynolds heat flux (RHF),  $\frac{\rho v'' T''}{\rho_w U_\infty T_w}$ , signifies the heat transfer from the wall in the wall-normal direction as a function of  $Re_x$ . Positive values mean that high temperature fluid is moved away from the wall, while the low temperature fluid is being pushed toward the wall. In contrast to Reynolds shear stress, the high value region corresponds to the rise in heat transfer in transition region. Here, highlighted continuous contours represent the corresponding 1% of the maximum wall-normal Reynolds heat flux, marking the beginning of the transition region. The location of maximum wall-normal Reynolds heat flux gives the end of transition. It can be seen from this figure that with increase in the perturbation intensity, better agreement among the transition onset locations predicted by the  $C_f$  and the RHF criteria is observed. As Reynolds heat flux is the result of increasing Reynolds shear stress in the domain, hence on comparing the corresponding cases in Figure 3 delayed prediction of transition to turbulence is observed for RHF criterion for all of the cases. Like in Figures 3a–3c, with increase in perturbation intensity, the transition onset location moves closer to the wall, signifying an enhanced heat transfer in the near-wall region. Fully turbulent regions are pointed at  $Re_x = 4.98 \times 10^6$ ,  $4.50 \times 10^6$ , and  $3.99 \times 10^6$  for A1, A2, and A3 cases, respectively, which are slightly downstream in comparison with the ones predicted by RSS. RHF also predicts an increase in transition region length with increasing the perturbation intensity, but the length predicted by RHF is the smallest one among the three criteria. It is interesting to note that the high Reynolds heat flux area is unusually intensified for A2 case, signifying the faster and enhanced heat transfer from the wall toward the outer layer. One possible explanation could be, as A2 utilizes 1% perturbation

intensity for excitation, strong interactions of linear and arising nonlinear mechanisms in the flow might be responsible for this unusual behavior.

To unravel more details about the effects of imposed frequency of perturbation throughout the domain, the imposed frequency of perturbation and its superharmonics are traced spatially and temporally using modal decomposition (MD) technique.

Figure 5a represents the premultiplied frequency spectrum of streamwise velocity fluctuations for A1 in early transition region. The imposed frequency of the perturbation along with its first

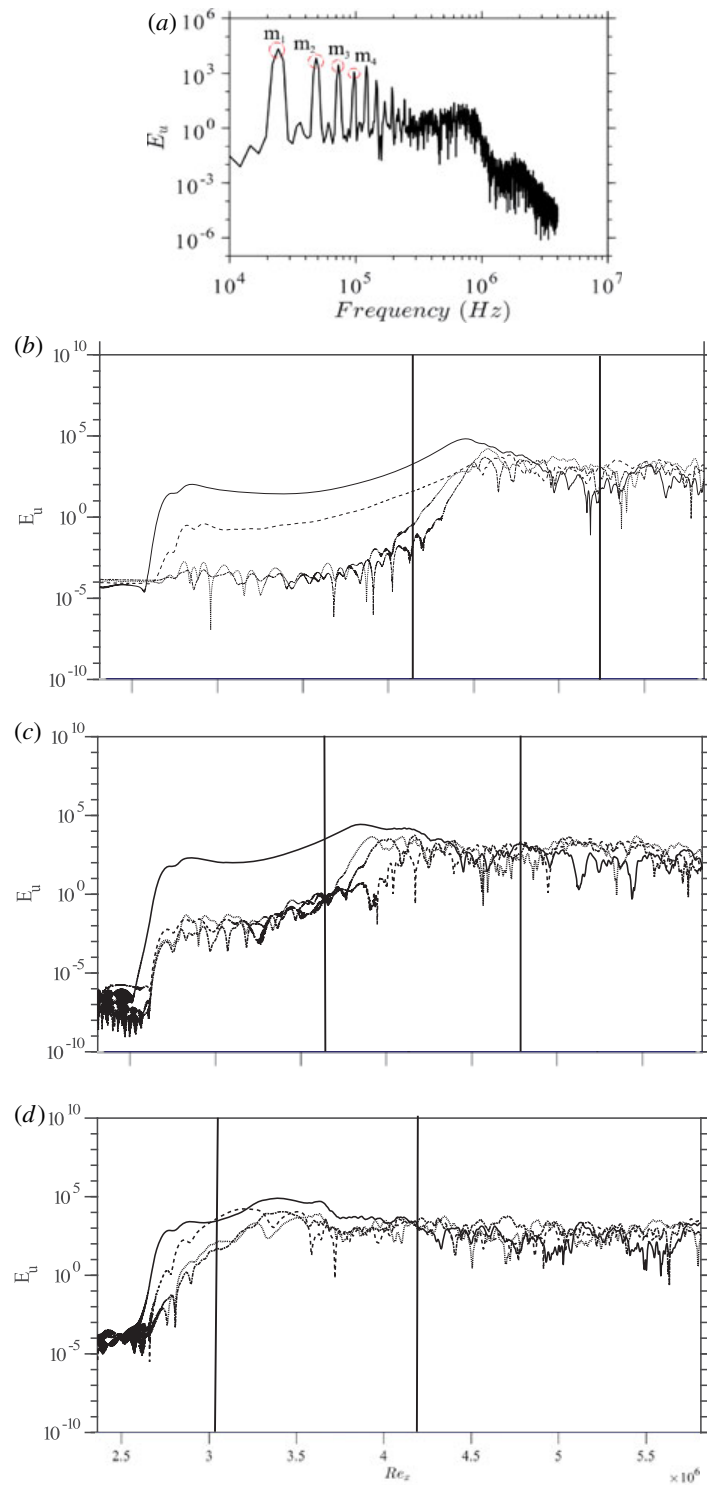


**Figure 5.** (a) Premultiplied frequency spectrum of streamwise velocity fluctuations for A1 case in early transition region. Spatial evolution of different modes throughout the computational domain for (b) A1, (c) A2, and (d) A3 cases, each point is integrated in time. Here, different line topologies represent different modes:  $m_1$  (—),  $m_2$  (---),  $m_3$  (- - - -), and  $m_4$  (· · · ·).

three superharmonics are predominantly visible in this figure and are marked from  $m_1$  to  $m_4$ . The same plots are obtained for all the cases (not shown here) and then the streamwise evolution of each mode is tracked. In order to track the streamwise evolution of these modes, streamwise velocity fluctuations are recorded at each point in the streamwise direction located at mid-span, and then the fast Fourier transform (FFT) is done for a given point in time. Then, the evolution of the amplitude of each mode under investigation is plotted in the streamwise direction. The energy content of different modes is given by,  $E_u(x, y, z, f) = \frac{1}{2} |\hat{u}(x, y, z, f) \hat{u}(x, y, z, f)|$ , where  $\hat{u}(x, y, z, f)$  is the FFT of streamwise velocity fluctuations at a given location,  $\hat{u}(x, y, z, f) = \int u'(x, y, z, t) e^{-ift} dt$ , where  $u'(x, y, z, t)$  is the velocity fluctuation at a given time  $t$  and  $f$  is the frequency.

Figures 5b–5d depict the evolution of imposed frequency of perturbation and its first three superharmonics throughout the computational domain for A1, A2, and A3 cases. It can be seen that soon after the region of blowing and suction strip (from  $Re_x \approx 2.6 \times 10^6$  to  $2.8 \times 10^6$ ), a steep increase in the energy levels of  $m_1$  and  $m_2$  is registered. Based on the modal growth, we define the transition onset location as the point where the energy level of  $m_4$  is equivalent to 1% of the average energy level of all the modes in the turbulent regime. This is the point where the low-energy high-frequency modes get reasonable amount of energy from high-energy lower-frequency modes and start to grow in the streamwise direction. The point where all of the modes coincide with each other for the first time after the excitation would be considered as the starting point of turbulence in the domain. This point shows the existence of high-energy high-frequency modes in the domain signifying the turbulent characteristics. Therefore, it can be seen from Figures 5b–5d that the transition begins at  $Re_x = 4.19 \times 10^6$ ,  $3.66 \times 10^6$ , and  $3.11 \times 10^6$  and ends at  $Re_x = 4.86 \times 10^6$ ,  $4.35 \times 10^6$ , and  $4.01 \times 10^6$  for A1, A2, and A3, respectively. Like other analyses discussed so far, MD also indicates the upstream shift of the transition onset position and increase in the transition region length with an increment in the perturbation intensity. However, MD predicts the shortest transition length among all other criteria employed. The rapid gain in the energy levels of  $m_3$  and  $m_4$  represents the start of secondary instabilities in the domain. However, this trend could not be seen distinctively for A3 case because the flow starts to transit soon after the excitation. Earlier transition for A3 case keeps the energy levels for all of modes monotonically increasing until the start of turbulence, as shown in Figure 5d. From this figure, it can be seen that toward the beginning of the turbulent region, all of the modes start to go toward a constant average energy level. Additionally, the average energy attained by all modes in the turbulent region is approximately 1% of the maximum energy level attained by  $m_1$ . Therefore, it can be concluded that the trend of modal growth throughout the computational domain is not affected by the flow physics arising due to different prescribed perturbation intensities.

On the basis of various analyses discussed so far, it has been observed that the location of transition onset and start of turbulence is not a unique value which could be predicted correctly by just one analysis alone. This emphasizes the fundamental question of unique definition of the transition region in high-speed flows. Therefore, toward the end of this study in Section 3.4, we would provide a comparative overview of the transition region parameters revealed by various analyses.

### 3.2. Effects of wall heat transfer

This section deals with the implications of wall heat transfer on transition region. For underlying comparison, cases with the lowest perturbation intensity, 0.5%, have been considered and the results of DNS have been compared with the predictions of LST. Figure 6 shows the streamwise evolution of  $C_f$  as a function of  $Re_x$  throughout the computational domain for A1, C1, and H1 cases. This figure implies that heating up the wall advances transition onset from  $Re_x = 4.12 \times 10^6$

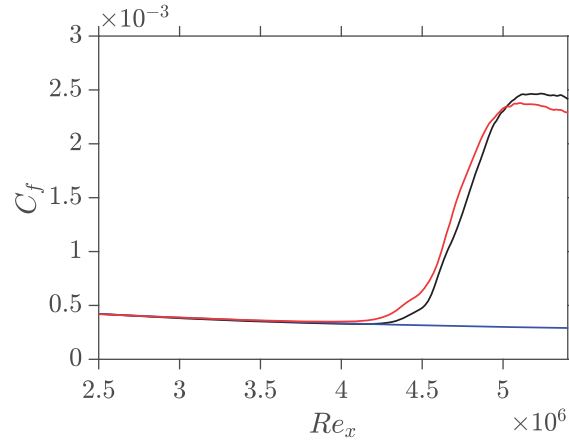


**Figure 6.** Evolution of skin-friction coefficient as a function of  $Re_x$  for A1(—), C1(—), and H1(—) cases.

for adiabatic case to  $Re_x = 3.95 \times 10^6$  and cooling down the wall stabilizes the flow and it remains laminar throughout the computational domain. The end of transition is recorded at  $Re_x = 5.23 \times 10^6$  and at  $Re_x = 5.11 \times 10^6$  for A1 and H1, respectively. **Figure 6** also highlights that the transition length decreases with an increment in the wall temperature. It is worth mentioning here that C1 has also been investigated with a longer domain having twice more size in the streamwise direction, but the flow never showed any precursors of turbulence. According to the investigation of Shadloo et al. [23] and Shadloo and Hadjadj [24], the contours of growth rate are expressed in terms of nondimensional frequency,  $F = \omega \nu_\infty / u_\infty^2$  and spanwise wavenumber,  $\beta = \beta^* x / R$  with  $R = \sqrt{Re_x}$ . The values of  $F$  and  $\beta$  for all the cases are  $F_{150} = 1.12 \times 10^{-6}$  and  $\beta_1 = 0.069$ . Noted that although the DNS results found by Shadloo et al. [23] and Shadloo and Hadjadj [24] for adiabatic wall were consistent with the LST results, their isothermal DNS cases contradicted the LST predictions. From the comparison of **Figure 6** and LST growth plots presented by Shadloo and Hadjadj [24] and Shadloo et al. [23], it can be inferred that the current DNS results are in good agreement with the results of LST. According to the LST, the boundary layer instability region contracts in terms of size exhibiting diminished growth rate for cooled wall while on heating the wall, the boundary layer instability region gets dilated and possesses a higher growth rate. As a result of this decreased growth rate for C1 case, the perturbations get damped and flow remains laminar. It is noted that in both of the previous works, investigated perturbation intensities were superior to 1%. Since the LST results are valid for very small amplification ( $\ll 1\%$ ), hence a clear disagreement was observed between the LST results and the DNS for Shadloo et al. [23] for isothermal walls (heated and cooled cases). The agreement between the DNS results of our study and the LST justifies our choice for investigating 0.5% perturbation intensity. Hence, this comparison clarifies the reason behind the disagreement of the LST and DNS results found in Shadloo and Hadjadj [24].

Contours of Reynolds shear stress for the same cases are shown in **Figures 7a–7c**. It can be seen that heating up the wall intensifies the Reynolds shear stress distribution close to the wall as the size of low Reynolds shear stress region grows tremendously signifying an increased push-up and pull-down of the fluid in the near-wall region. A comparison between **Figures 7a, c** highlights that the starting locations of 1% contour moves from  $y/\delta_{in} = 0.63$  for adiabatic wall to  $y/\delta_{in} = 0.70$  for the heated wall. This means that with increase in wall temperature, the enhanced Reynolds shear stress in the near-wall region augments the boundary layer thickness which results in faster propagation of the perturbations toward the outer layer. Another consequence of the increased Reynolds shear stress for heated case is that the transition onset location predicted by  $C_f$  criterion and RSS criterion is the same for heated wall. As it is observed from **Figures 7a–7c** that RSS criteria point out the transition region extending from  $Re_x = 4.17 \times 10^6$  to  $Re_x = 4.98 \times 10^6$  and from  $3.95 \times 10^6$  to  $4.86 \times 10^6$  for A1 and H1, respectively. Also the difference in

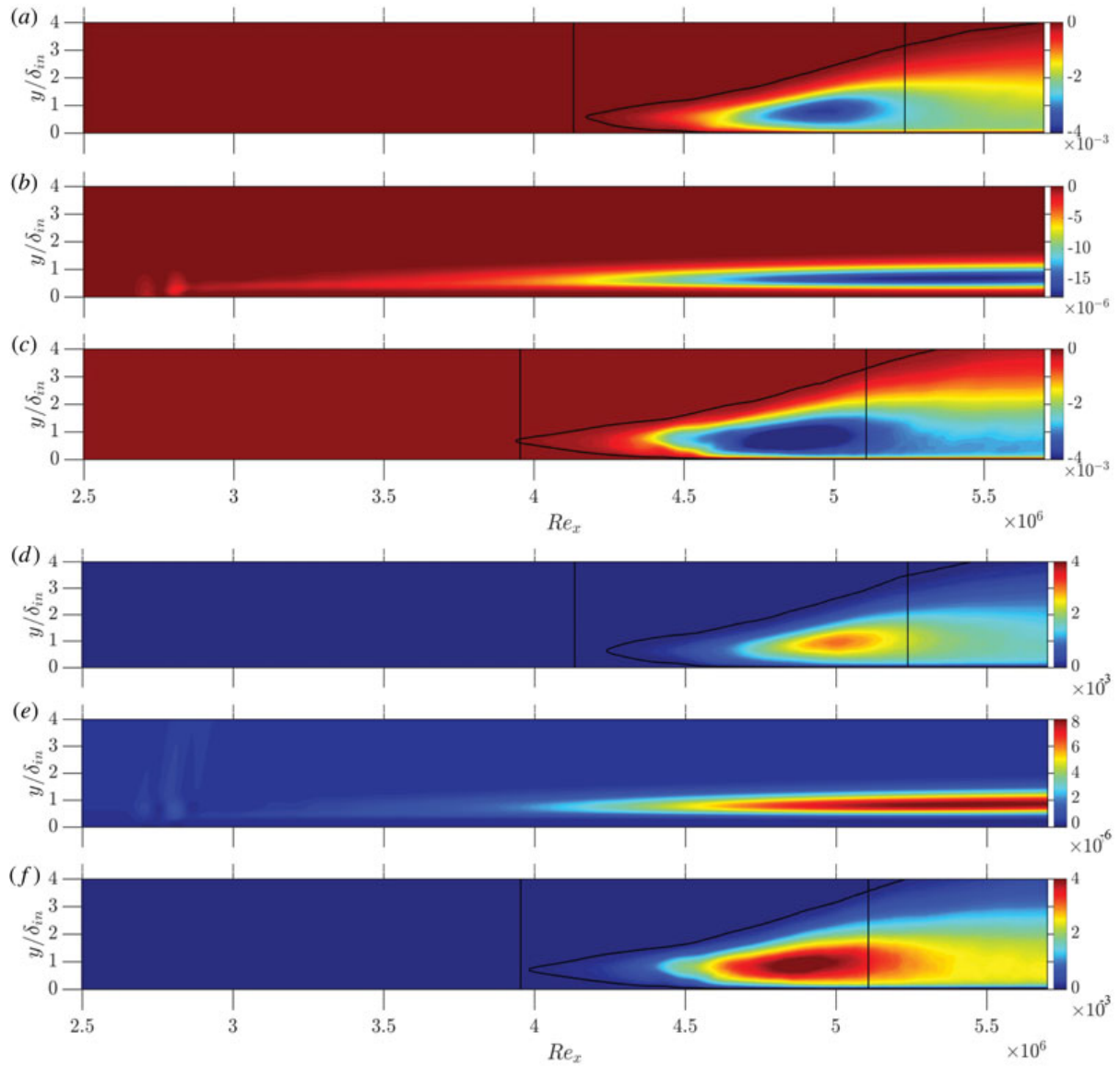


**Figure 7.** Contours of Reynolds shear stress,  $\frac{\rho u'v'}{\rho_w U_\infty^2}$  for (a) A1, (b) C1, and (c) H1 cases, and the contours of wall-normal Reynolds heat flux,  $\frac{\rho v' T''}{\rho_w U_\infty T_w}$  for (d) A1, (e) C1, and (f) H1 cases.

the transition region length predicted by these two criteria is lesser for the heated wall in comparison with the adiabatic wall. For C1, as the flow did not transit to turbulence, different levels for contours have been chosen. Particularly in this case, the perturbations get damped inside of the boundary layer. Figures 7d–7f represents the contours of wall-normal heat flux for the same cases. The effects of wall heat transfer on the Reynolds heat flux are similar in many aspects to that of Reynolds shear stress including the behavior of high Reynolds heat flux area, variations in predicting the transition onset positions by 1% contour, and differences in the transition region length between  $C_f$  and RHF criteria. This criterion points out the beginning and the end of transition region at  $Re_x = 4.24 \times 10^6$  and  $Re_x = 4.98 \times 10^6$ , respectively, for A1 and are  $Re_x = 3.99 \times 10^6$  and  $Re_x = 4.90 \times 10^6$ , respectively, for H1. Additionally, the size of high wall-normal Reynolds heat flux area does grow with the increment of temperature (Figure 7f) but the effects are more contained here when compared to Figure 7c because Reynolds heat flux is a consequence of increasing Reynolds shear stress in the domain. Therefore, the transition lengths predicted by RHF are slightly smaller than the ones predicted by the RSS criterion.

Figure 8 depicts the streamwise evolution of modes  $m_1$  to  $m_4$  for the same cases. The evolutionary trend of the considered modes is actually the same for A1 and H1 as discussed before for

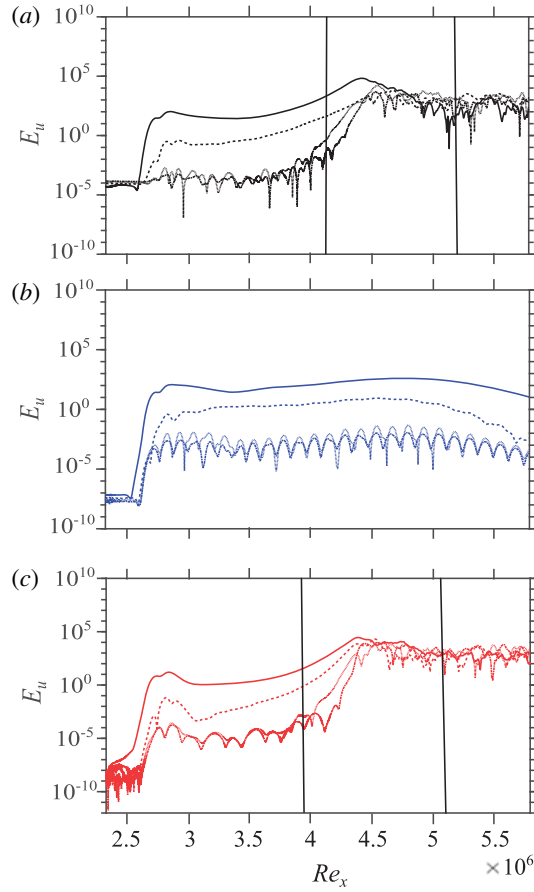


**Figure 8.** Spatial evolution of different modes throughout the computational domain for (a) A1, (b) C1, and (c) H1 cases, each point is integrated in time. Here, different line topologies represent different modes:  $m_1$  (—),  $m_2$  (---),  $m_3$  (· · · · ·), and  $m_4$  (- · - ·).

**Figure 5.** However, it is interesting to see the modal evolution for C1. After the excitation, the energy does increase for some portion in streamwise direction but later on it gets faded off. The maximum energy level reached by  $m_1$  for C1 is less than 1% of the maximum energy level of  $m_1$  for other cases which transit to turbulence. This observation is in accordance with the results shown for C1 in **Figures 7b, e** utilizing low contour levels. We can hence argue that for C1 case, the energy levels are significantly lower than other cases and therefore, the excitation is not ample enough to trigger turbulence. From the results of MD presented in **Figures 5 and 8**, it can be argued that the trend of evolution of the modes is almost the same in all of the cases except for the C1 case as the flow did not show any signs of transition.

### 3.3. Joint effects of perturbation intensity and wall heat transfer

Now we take into account the effects of perturbation intensity over the transition onset along with the effects of wall heat transfer. **Figure 9** compares the streamwise evolution of skin-friction coefficient as a function of  $Re_x$  for the cases with 1% perturbation intensity (A2, C2, and H2) and the cases having 2.4% perturbation intensity (A3, C3, and H3). As can be seen in **Figure 9a**, the cooled wall tends to stabilize the flow as compared to the adiabatic wall and transition onset location moves farther downstream from  $Re_x = 3.64 \times 10^6$  for the adiabatic wall to  $Re_x = 3.74 \times 10^6$  for the cooled wall. However, the heated wall does not show any considerable changes in transition onset location when compared to the adiabatic wall. **Figure 9a** corresponds to the limit of LST with 1% perturbation intensity; therefore, LST can partially predict the flow behavior for the cooled wall but its growth rate predictions do not go very well with the DNS results for the heated wall. Interestingly, for more intense excitation utilizing 2.4% perturbation intensity shown

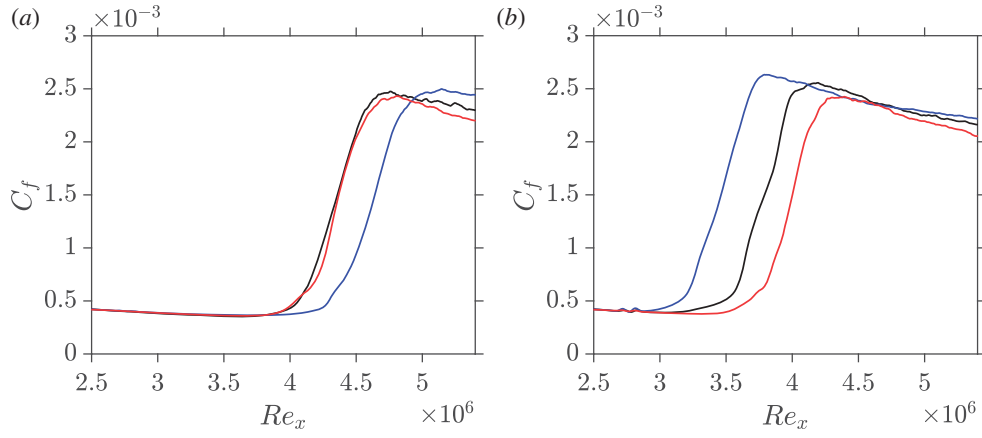


**Figure 9.** Streamwise evolution of skin-friction coefficient as a function of  $Re_x$  for (a) A2, C2, H2 and (b) A3, C3, H3 cases, here blue, black and red lines represent cooled, adiabatic and heated walls, respectively.

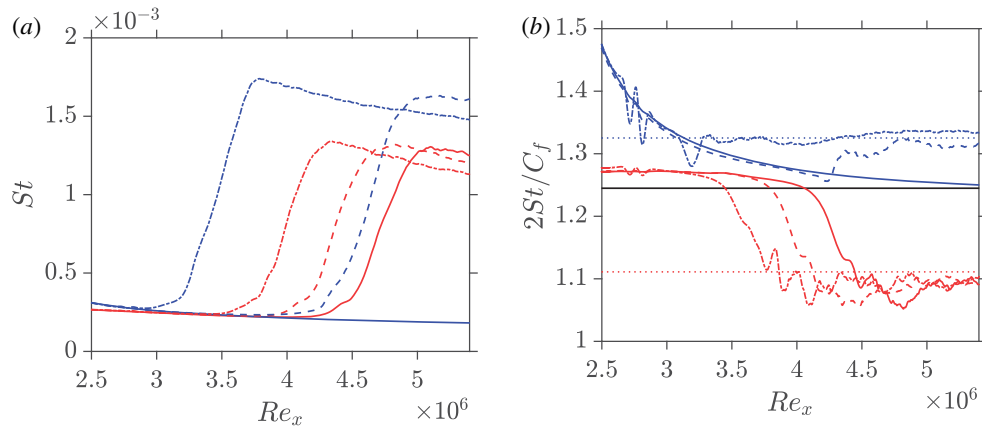


**Figure 10.** Streamwise evolution of (a) Stanton number and (b) Reynolds analogy factor,  $(2St/C_f)$  as a function  $Re_x$ , C1 (—), H1 (—), C2 (---), H2 (---), C3 (---), and H3 (---) cases. These cases are compared with  $Pr^{-2/3}$  (—) and newly introduced factor  $Pr^{-2/3} \times \frac{\rho_w \mu_w}{\rho_{aw} \mu_{aw}}$  for cooled (---) and heated walls (---) in (b).

in [Figure 9b](#), cooling down the wall actually results in destabilization of the flow and it transits sooner at  $Re_x = 2.76 \times 10^6$  as compared to the adiabatic wall at  $Re_x = 3.03 \times 10^6$ . On the other hand, heating up the wall stabilizes the flow and transition onset gets delayed to  $Re_x = 3.32 \times 10^6$ . The latter observation has also been reported by Shadloo et al. [23] and Shadloo and Hadjadj [24]. A comparison between [Figure 6](#) and [Figure 9b](#) reveals that the trend of transition to turbulence actually gets inverted for higher perturbation intensity. The increased nonlinear interactions in the flow field can be accounted for this contrasting behavior. From [Figures 9a, b](#), it can be pointed out that heated wall does not exhibit equal and opposite effect as that of the cooled wall even though the same initial heating/cooling has been utilized (see [Figure 10a](#) in laminar region). This can be explained by the type of blowing and suction utilized to excite the boundary layer. The product of density ( $\rho$ ) and wall-normal velocity component ( $v$ ),  $\rho v$ , must remain constant in the flow field, but for compressible flows, the density changes. Therefore, in the near-wall region, density decreases for the heated wall and increases in case of the cooled wall. As the perturbation model used here is velocity fitted and does not account for the changing density, the product of  $\rho v$  decreases in the near-wall region for the heated wall and increases for the cooled wall which results in lesser receptivity of the heated walls.

[Figure 10a](#) shows the evolution of Stanton number,  $St$  as a function of  $Re_x$  for different cases. The Stanton number characterizes the wall heat transfer and is defined as  $St = q_w / (\rho_\infty U_\infty C_p (T_{aw} - T_w))$ , where  $q_w$  is the heat transfer from the wall. Adiabatic wall temperature,  $T_{aw}$ , for turbulent regime has been calculated by employing the approximation for

recovery factor,  $Pr^{1/3}$  [29],  $T_{aw} = T_{\infty} (1 + Pr^{1/3}(\gamma - 1)/2M_{\infty}^2)$ ,  $Pr$  being the Prandtl number. Likewise the  $C_f$  criterion, the beginning and the end of transition are characterized by the lowest and the highest values of the Stanton number in the domain, respectively. From Figure 10a, it can be seen that there exists a minute difference in the values of  $St$  in laminar region between the heated and the cooled cases. This means that the heat transfer is comparable regardless of its direction, for both the cooled and the heated walls. The overall evolution of  $St$  is quite similar to that of the  $C_f$  for all the cases. However, unlike  $C_f$ , the observed overshoot is higher for the cooled walls than the heated walls. Figure 10a also highlights that with increasing perturbation intensity, the relative upstream shift of transition onset location is considerably large for the cooled walls in comparison with the heated walls. The transition onset location moves from  $Re_x = 3.80 \times 10^6$  for C2 to  $Re_x = 2.89 \times 10^6$  for C3, while it moves from  $Re_x = 4.02 \times 10^6$  for H1 to  $Re_x = 3.73 \times 10^6$  for H2 and  $Re_x = 3.37 \times 10^6$  for H3. In the same way, the endpoint of transition region moves from  $Re_x = 5.15 \times 10^6$  for C2 to  $Re_x = 3.79 \times 10^6$  for C3, and from  $Re_x = 5.10 \times 10^6$  for H1 to  $Re_x = 4.82 \times 10^6$  for H2, and  $Re_x = 4.40 \times 10^6$  for H3. This highlights the difference in the receptivities of the cooled and the heated wall as shown by the  $C_f$  criterion. The lengths of transition region predicted by this criterion are closer to the ones predicted by the  $C_f$  criterion. In the fully developed turbulent region, the values of  $St$  are higher for the cooled walls than the heated ones which signifies more heat transfer in case of the cooled walls than the heated walls.

Another important parameter is the Reynolds analogy factor ( $2St/C_f$ ) that relates skin friction to heat transfer and is expressed as  $Pr^{-2/3} = 2St/C_f$  [29]. Although there is not any agreed value of the Reynolds analogy factor for the high-speed flows [20,22], based on many experimental investigations, it has been found out that it has the value between 0.9 and 1.2 [30,31]. Figure 10b shows the streamwise evolution of Reynolds analogy factor for different cases along with  $Pr^{-2/3}$  shown by black line. It could be seen from this figure that in laminar region, values attained by heated walls is close to  $Pr^{-2/3}$  but for cooled walls, the trend is parabolic from the beginning itself. As the C1 case remains laminar throughout the considered domain, it seems that in extended part of the domain, C1 would eventually converge to  $Pr^{-2/3}$  value. On the other hand in the turbulent region, the values of Reynolds analogy factor attained by the cooled and the heated walls have large deviation from  $Pr^{-2/3}$ . Dimensional analysis reveals that if we multiply  $Pr^{-2/3}$  by the corresponding density ratio and viscosity ratio of the wall with the adiabatic wall,  $Pr^{-2/3} \times \frac{\rho_w \mu_w}{\rho_{aw} \mu_{aw}}$ , then the obtained value presents a good approximation of the average value of Reynolds analogy factor in the turbulent part. These values are presented by blue and red dotted lines in Figure 10b for cooled and heated walls, respectively.

Figures 11a–11f show the contours of Reynolds shear stress for the cases with 1% (A2, C2, and H2) and with 2.4% perturbation intensities (A3, C3, and H3), respectively. As discussed earlier, with increase in the wall temperature, high Reynolds shear stresses get intensified in the near-wall region. From Figures 11a, c, it can be said that both the RSS and  $C_f$  criteria point out nearly the same transition onset location for A2 and H2 with slight differences in the transition region length as the RSS predicts the end of transition at  $Re_x = 4.48 \times 10^6$  and  $Re_x = 4.50 \times 10^6$  for A2 and H2, respectively. But, for Figure 11b, there exists a considerable difference between the transition onset locations marked by RSS,  $Re_x = 3.38 \times 10^6$  and  $C_f$ ,  $Re_x = 3.74 \times 10^6$ . The RSS criterion predicts the transition onset location far upstream than the  $C_f$  criterion. As pointed out before, the LST partially predicts the flow behavior at 1% perturbation intensity and the diminished growth rate of the disturbances in the flow results in longer streaks and hence an augmented length of the transition region which has been shown by both the  $C_f$  and the RSS criteria. However, the exact dependency of transition length on wall temperature cannot be stated for 1% perturbation intensity cases as both linear and nonlinear mechanisms are comparable here resulting in complex physics. In Figures 11d, e, a small contour corresponding to 1% contour shows up just before the big 1% contour. This small contour corresponds to the position of the blowing and suction strip, and hence the starting of second contour is considered as the transition onset

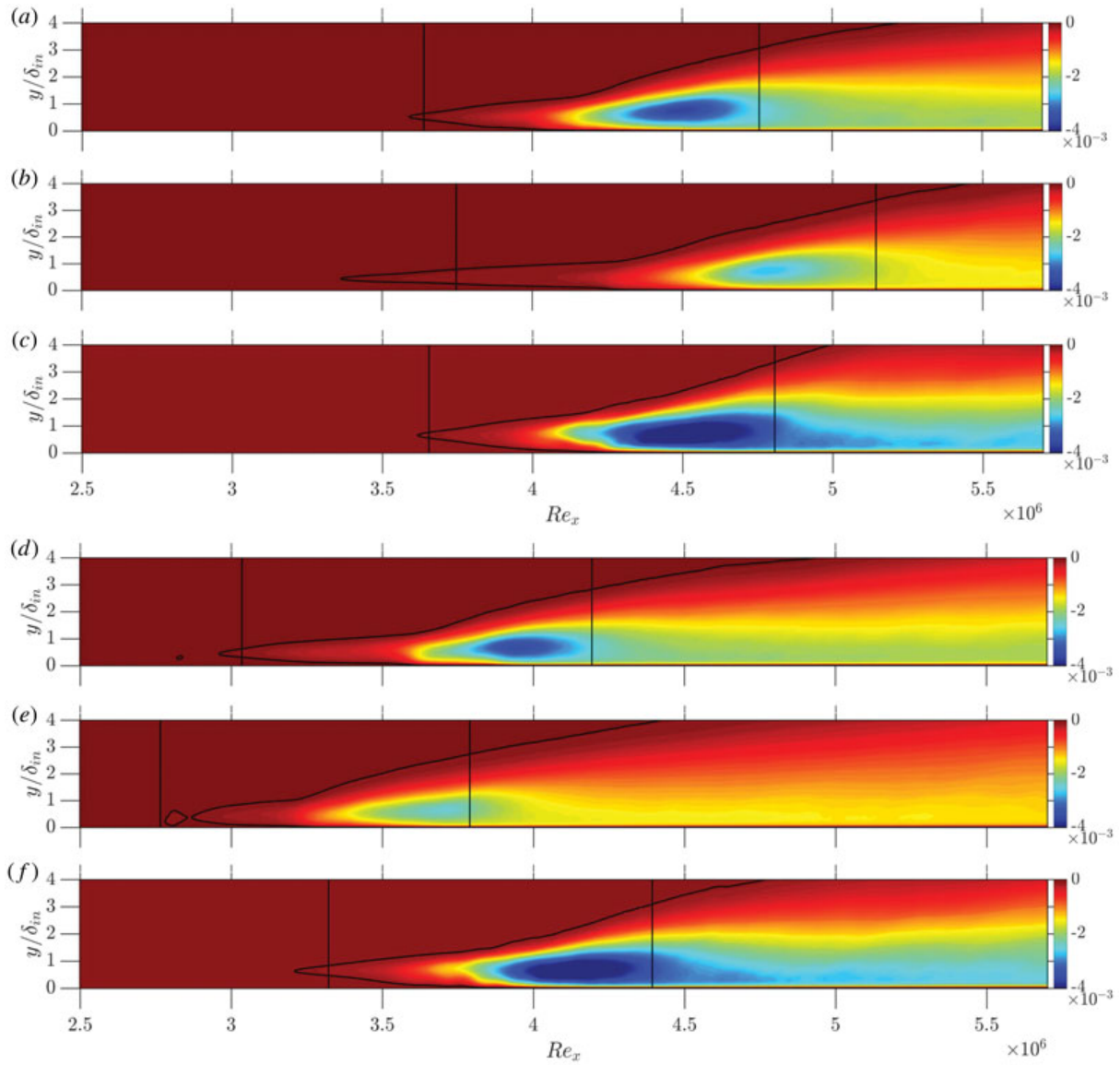


**Figure 11.** Contours of Reynolds shear stress,  $\frac{\overline{\rho u'v'}}{\rho_w U_{\infty}^2}$  for (a) A2, (b) C2, (c) H2, (d) A3, (e) C3, and (f) H3 cases.

location. For nonlinear regime, that is, cases with 2.4% perturbation intensity, high intensity Reynolds shear stresses move closer to the wall; therefore for all the cases with this perturbation intensity lesser difference has been recorded between the transition region lengths predicted by RSS and  $C_f$  criteria. The RSS criterion depicts the transition region extent from  $Re_x = 2.96 \times 10^6$  to  $Re_x = 3.96 \times 10^6$ , from  $Re_x = 2.87 \times 10^6$  to  $Re_x = 3.71 \times 10^6$ , and from  $Re_x = 3.22 \times 10^6$  to  $Re_x = 4.13 \times 10^6$  for A3, C3, and H3, respectively. It can also be clarified from [Figure 11](#) that with increase in wall temperature, the magnitude of the Reynolds shear stress also increases, while the decrease in wall temperature shows the opposite impact. A closer look at [Figures 11d–11f](#) reveals that the cooled and heated walls have the shorter transition region in comparison with the adiabatic wall. In C3 case, we have the fastest and shortest transition to turbulence than A3 while H3 transits farthest of the three with a transition region longer than C3 but shorter than A3.

Contours of wall-normal Reynolds heat flux are presented in [Figures 12a–12f](#) for cases with 1% and 2.4% perturbation intensities, respectively. It can be inferred from these figures that an increment in the wall temperature increases the peak value of wall-normal Reynolds shear stress. [Figures 12a–12c](#) show better agreement between the transition onset locations predicted by RHF and  $C_f$  criteria as compared to the RSS criterion as shown in [Figures 11a–11c](#). However, the transition region lengths predicted by RHF criterion are shorter in comparison with the ones

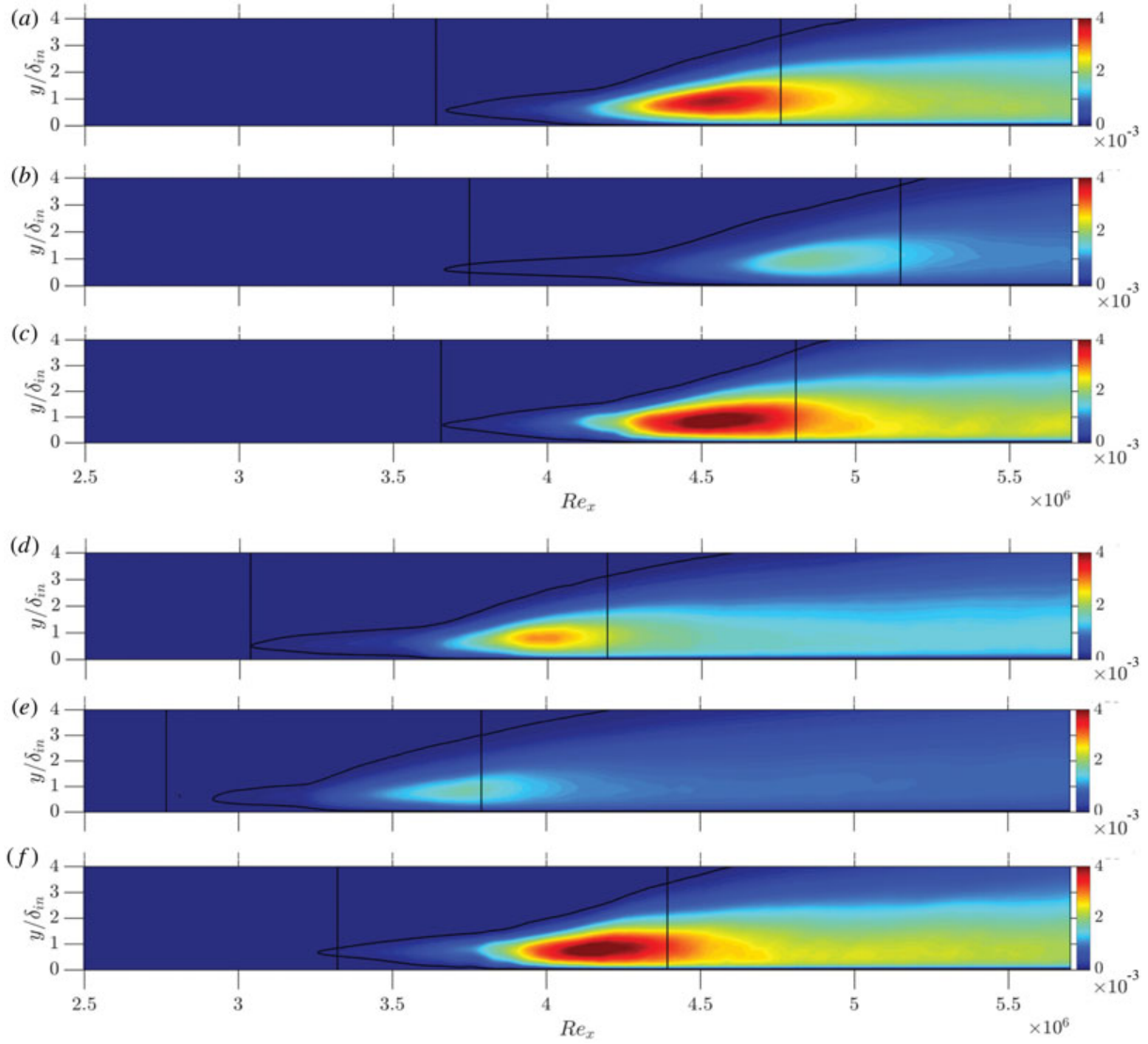


**Figure 12.** Contours of wall-normal Reynolds heat flux,  $\frac{\rho v'' T''}{\rho_w U_\infty T_w}$  for (a) A2, (b) C2, (c) H2, (d) A3, (e) C3, and (f) H3 cases.

predicted by RSS and  $C_f$  criteria. As heat transfer is a consequence of the shear stress, therefore, the effects of increasing temperature are more contained in Figure 12 when compared to Figure 11. Likewise the RSS, for 2.4% perturbation intensity cases, RHF presents better agreements with  $C_f$  criterion in predicting the transition onset location and length of the transition region. From the comparisons of corresponding cases of Figures 11 and 12, it can be concluded that the change in perturbation intensity has more impact on Reynolds shear stress than the wall-normal Reynolds heat flux for the cooled and the heated walls. However, the inverse is true for the adiabatic wall.

Figure 13 depicts the streamwise evolution of the modes  $m_1$  to  $m_4$  for C2 and H2 cases. This figure shows that the transition region extends from  $Re_x = 3.67 \times 10^6$  to  $Re_x = 4.87 \times 10^6$  for C2 case and from  $Re_x = 3.68 \times 10^6$  to  $Re_x = 4.18 \times 10^6$  for H2 case. Hence, the MD also predicts a longer transition region for C2. In Figure 13a, longer transition region for C2 is characterized by distinctively clear levels of energy possessed by different modes. Due to the slower growth rate, the considered modes do not show much interactions with each other until the end of the transition. The evolution of the modes is the same for H2 as discussed before for other cases. Similar modal evolution trend has been observed for the cases with 2.4% perturbation intensity (not shown here). Throughout this study, it has been observed that the MD criterion consistently predicted the shortest length of the transition region in comparison with the other criteria used.

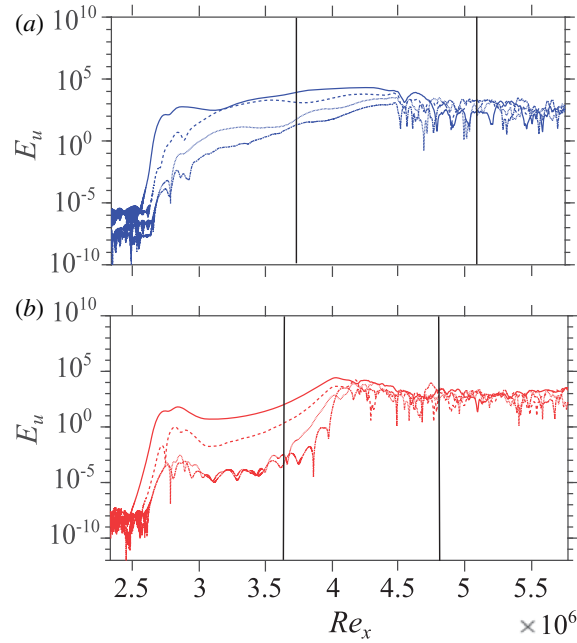


**Figure 13.** Spatial evolution of different modes throughout the computational domain for (a) C2 and (b) H2 cases, each point is integrated in time. Here, different line topologies represent different modes:  $m_1$  (—),  $m_2$  (---),  $m_3$  (· · · · ·), and  $m_4$  (- · - · -).

**Table 2.** Details of transition region (beginning, end, and length of transition region) in terms of  $Re_x$  as predicted by different analyses

Case	Start of transition ( $\times 10^6$ )					End of transition ( $\times 10^6$ )					Transition length ( $\times 10^6$ )				
	$C_f$	RSS	RHF	MD	St	$C_f$	RSS	RHF	MD	St	$C_f$	RSS	RHF	MD	St
A1	4.12	4.17	4.24	4.19	×	5.23	4.98	4.98	4.86	×	1.11	0.81	0.74	0.67	×
A2	3.64	3.59	3.68	3.66	×	4.75	4.48	4.50	4.35	×	1.11	0.89	0.82	0.69	×
A3	3.03	2.96	3.04	3.11	×	4.20	3.96	3.99	4.01	×	1.17	1.00	0.95	0.90	×
C1	×	×	×	×	×	×	×	×	×	×	×	×	×	×	×
C2	3.74	3.38	3.68	3.67	3.80	5.14	4.78	4.82	4.87	5.15	1.40	1.40	1.14	1.20	1.35
C3	2.76	2.87	2.92	2.77	2.89	3.79	3.71	3.74	3.41	3.79	1.03	0.84	0.82	0.64	0.90
H1	3.95	3.95	3.99	4.04	4.02	5.11	4.86	4.90	4.54	5.10	1.16	0.91	0.91	0.50	1.08
H2	3.65	3.63	3.66	3.68	3.73	4.81	4.50	4.53	4.18	4.82	1.16	0.87	0.87	0.50	1.09
H3	3.32	3.22	3.26	3.35	3.37	4.39	4.13	4.13	3.89	4.40	1.07	0.91	0.87	0.54	1.03

RSS, RHF, and MD represent different analyses performed which stand for Reynolds shear stress, wall-normal Reynolds heat flux, and modal decomposition, respectively.

### 3.4. Comparison of transition onset based on different analyses

Throughout this study, we have discussed about the transition in SBLs. Different analyses have been employed in order to unravel the physical explanation of the observed trends of variation in transition onset, which include streamwise evolution of skin-friction coefficient ( $C_f$ ), contours of Reynolds shear stress (RSS), contours of wall-normal component of Reynolds heat flux (RHF), modal decomposition (MD), and streamwise evolution of Stanton number ( $St$ ). For all of the cases investigated, it has been observed that each of these analyses has predicted slightly varied positions for the beginning and the end of transition region presenting the difficulty in uniquely determining the definite transition location. Table 2 presents a comparative overview of different transition region parameters according to these analyses. Symbol (×) in this table means that the stated parameter could not be determined for the given case. On comparing the various locations of the end of transition from Table 2, we can observe that  $C_f$  criterion consistently predicts the end of transition located at the farthest downstream among all the analyses. Transition lengths predicted by different criteria clearly suggest that the  $C_f$  criterion always predicts a longer

transition region in comparison with other criteria while on the other hand MD consistently predicts the shortest. Franko and Lele [22] have also uncovered in their study that  $C_f$  criterion predicts a prolonged length of transition region. A closer look at the transition region lengths predicted by various analyses points out that the transition region gets prolonged with increase in perturbation intensity for adiabatic walls. Table 2 also suggests that at low perturbation intensity, 0.05% wall heating advances the start of transition and increases the length of the transition region while the flow remains laminar for wall cooling. On the other hand, for the nonlinear regime of 2.4% perturbation intensity, both isothermal walls possess shorter transition length in comparison with the adiabatic one. However, among them cooled wall has the shortest transition length signifying the faster transition of the flow to turbulence.

Based on our discussion so far about different parameters to predict the transition onset and length, it is still not conclusive to point out the best suited analysis to define the exact position for the onset and the end of transition. The choice should be made on the basis of the application, that is, for performing deep physical analysis about the mechanisms of transition, MD can be utilized alongside with RSS and RHF criteria while for general engineering applications the  $C_f$  and  $St$  can be used as first.

#### 4. Conclusion

Direct numerical simulations of SBL were performed to study the BL receptivity growth and transition to fully turbulent. A total of nine cases were considered to show the effects of various factors like changing perturbation intensity and wall heat transfer over a flat plate at the free-stream Mach number of  $M_\infty = 2.2$ . We tried to quantify the transition region start and end using different analyses, namely streamwise evolution of skin-friction coefficient, contours of Reynolds shear stress, contours of wall-normal Reynolds heat flux, modal decomposition, and streamwise evolution of Stanton number as a function of  $Re_x$ .

It was observed that an increase in the perturbation intensity shifted the transition onset location upstream for adiabatic walls. All the analyses had also predicted an increasing transition region length, resulting from longer streaks generation for intense perturbations. The effects of wall heat transfer were also investigated and the obtained results were compared against the predictions of LST as initially reported in Shadloo and Hadjadj [24]. The results of DNS and LST were in good agreement. It was revealed that at low perturbation intensity, that is, 0.5%, wall cooling stabilized the flow and it did not transit to turbulence while the wall heating destabilized the flow and it transited to turbulence upstream in comparison with adiabatic wall.

Joint effects of perturbation intensity and wall heat transfer were analyzed for larger perturbation intensities, that is, 1% and 2.4%. As 1%, which is the limit of the linear regime, cooling down the wall did stabilize the flow but there were not any significant differences between the heated wall and the adiabatic wall. As a result of slower growth rate for cooled wall as predicted by the LST, C2 had an unusually long transition region resulting from the formation of elongated streaks. But for nonlinear regime, with 2.4% perturbation intensity, cooling down the wall destabilized the flow and it transited upstream as compared to the adiabatic wall and heating up the plate resulted in flow stabilization and delayed transition. These results are in agreement with those obtained in Shadloo et al. [23] and Shadloo and Hadjadj [24]. This behavior is in direct contrast with the one observed for 0.5% showing the limit of LST prediction for highly perturbed flow. The nonlinear interactions in the flow could be accounted for this contrasting trend. It was also observed that the impact of wall cooling was more amplified than the impact of wall heating. This difference could be explained the way in which the perturbation was imposed, that is, perturbing  $v$  at the wall. As the product  $\rho v$  should remain constant in a compressible regime, the density varies. As a result of density variation, the value of this product decreases in the near wall region for the heated wall and increases for the cooled walls resulting in a difference in

receptivity. Regarding the turbulent regime, it was found out that cooled and heated walls attain different values of Reynolds analogy factor which differ from the value given by  $Pr^{-2/3}$ . Dimensional analysis revealed that multiplying this value by the product of density and viscosity ratios of the corresponding wall to the adiabatic wall,  $Pr^{-2/3} \times \frac{\rho_w \mu_w}{\rho_{aw} \mu_{aw}}$  presented a good approximation of the average value of Reynolds analogy factor attained by both the cooled and the heated walls in the fully turbulent region.

A comparison among the obtained parameters of transition region revealed that  $C_f$  predicted the longest transition region and MD being consistently the shortest one.

## Acknowledgment

This work was granted access to HPC resources of IDRIS under the allocation 2017-100752 made by GENCI (Grand Equipement National de Calcul Intensif – A0022A10103). The authors acknowledge the access to HPC resources of French regional computing center of Normandy named CRIANN (Centre Régional Informatique et d'Applications Numériques de Normandie) under the allocations 1998022 and 2017002. Authors would also like to acknowledge the insightful comments and suggestions made by Prof. F. Hussain (Texas Tech University), Prof. S.K. Lele (Stanford University), Prof. M.J. Kloker (University of Stuttgart) and Dr D.J. Bodony (University of Illinois at Urbana-Champaign).

## Funding

The funding resources provided from European project entitled “NEPTUNE” are gratefully acknowledged.

## ORCID

M. S. Shadloo  <http://orcid.org/0000-0002-0631-3046>

A. Hadjadj  <http://orcid.org/0000-0002-1415-0443>

## References

- [1] L. Duan, I. Beekman, and M. P. Martin, “Direct numerical simulation of hypersonic turbulent boundary layers. Part 2: Effect of wall temperature,” *J. Fluid Mech.*, vol. 655, pp. 419–445, 2010. DOI: [10.1017/S0022112010000959](https://doi.org/10.1017/S0022112010000959).
- [2] M. Tutar and Ü. Sönmez, “The computational modeling of transitional flow through a transonic linear turbine: Comparative performance of various turbulence models,” *Numer. Heat Tr. A-Appl.*, vol. 58, no. 5, pp. 403–427, 2010. DOI: [10.1080/10407782.2010.508432](https://doi.org/10.1080/10407782.2010.508432).
- [3] K. Bensayah, A. Hadjadj, and A. Bounif, “Heat transfer in turbulent boundary layers of conical and bell shaped rocket nozzles with complex wall temperature,” *Numer. Heat Tr. A-Appl.*, vol. 66, no. 3, pp. 289–314, 2014. DOI: [10.1080/10407782.2013.873283](https://doi.org/10.1080/10407782.2013.873283).
- [4] D. C. Reda, M. C. Wilder, and D. K. Prabhu, “Transition experiments on blunt bodies with isolated roughness elements in hypersonic flight,” *J. Spacecr. Rockets.*, vol. 47, no. 5, pp. 828–835, 2010. DOI: [10.2514/1.49112](https://doi.org/10.2514/1.49112).
- [5] G. B. Schubauer and H. K. Skramstad, “Laminar boundary-layer oscillations and stability of laminar flow,” *J. Aeronautical Sci.*, vol. 14, no. 2, pp. 69–78, 1947. DOI: [10.2514/8.1267](https://doi.org/10.2514/8.1267).
- [6] P. S. Klebanoff, “Effect of free-stream turbulence on a laminar boundary layer,” *Bulletin of the American Physical Society.*, vol. 16, no. 11, pp. 1323–1334, 1971.
- [7] P. S. Klebanoff, K. D. Tidstrom, and L. M. Sargent, “The three-dimensional nature of boundary-layer instability,” *J. Fluid Mech.*, vol. 12, no. 1, pp. 1–34, 1962. DOI: [10.1017/S0022112062000014](https://doi.org/10.1017/S0022112062000014).
- [8] J. Kendall, “Experimental study of disturbances produced in a pre-transitional laminar boundary layer by weak freestream turbulence,” presented at the *18th Fluid Dynamics and Plasmadynamics and Lasers Conference*. Cincinnati, Ohio, USA, Jul. 16–18, 1985.
- [9] T. Herbert, “Secondary instability of boundary layers,” *Annu. Rev. Fluid Mech.*, vol. 20, no. 1, pp. 487–526, 1988. DOI: [10.1146/annurev.fl.20.010188.002415](https://doi.org/10.1146/annurev.fl.20.010188.002415).

- [10] J. Lee, S. Y. Jung, H. J. Sung, and T. A. Zaki, "Effect of wall heating on turbulent boundary layers with temperature-dependent viscosity," *J. Fluid. Mech.*, vol. 726, pp. 196–225, 2013. DOI: [10.1017/jfm.2013.211](https://doi.org/10.1017/jfm.2013.211).
- [11] H. B. E. Kurz and M. J. Kloker, "Mechanisms of flow tripping by discrete roughness elements in a swept-wing boundary layer," *J. Fluid Mech.*, vol. 796, pp. 158–194, 2016. DOI: [10.1017/jfm.2016.240](https://doi.org/10.1017/jfm.2016.240).
- [12] M. Bernardini, S. Pirozzoli, P. Orlandi, and S. K. Lele, "Parameterization of boundary-layer transition induced by isolated roughness elements," *AIAA J.*, vol. 52, no. 10, pp. 2261–2269, 2014. DOI: [10.2514/1.J052842](https://doi.org/10.2514/1.J052842).
- [13] J. P. J. P. Van den Eynde and N. D. Sandham, "Numerical simulations of transition due to isolated roughness elements at Mach 6," *AIAA J.*, vol. 54, no. 1, pp. 53–65, 2015. DOI: [10.2514/1.J054139](https://doi.org/10.2514/1.J054139).
- [14] G. Groskopf and M. J. Kloker, "Instability and transition mechanisms induced by skewed roughness elements in a high-speed laminar boundary layer," *J. Fluid Mech.*, vol. 805, pp. 262–302, 2016. DOI: [10.1017/jfm.2016.563](https://doi.org/10.1017/jfm.2016.563).
- [15] N. De Tullio, P. Paredes, N. D. Sandham, and V. Theofilis, "Laminar–turbulent transition induced by a discrete roughness element in a supersonic boundary layer," *J. Fluid Mech.*, vol. 735, pp. 613–646, 2013. DOI: [10.1017/jfm.2013.520](https://doi.org/10.1017/jfm.2013.520).
- [16] S. P. Schneider, "Effects of roughness on hypersonic boundary-layer transition," *J. Spacecr. Rockets.*, vol. 45, no. 2, pp. 193–209, 2008. DOI: [10.2514/1.29713](https://doi.org/10.2514/1.29713).
- [17] J. A. Redford, N. D. Sandham, and G. T. Roberts, "Numerical simulations of turbulent spots in supersonic boundary layers: Effects of Mach number and wall temperature," *Prog. Aerospace Sci.*, vol. 52, pp. 67–79, 2012. DOI: [10.1016/j.paerosci.2011.08.002](https://doi.org/10.1016/j.paerosci.2011.08.002).
- [18] J. A. Redford, N. D. Sandham, and G. T. Roberts, "Direct numerical simulation of transitional flow at high Mach number coupled with a thermal wall model," *Comput. Fluids.*, vol. 45, no. 1, pp. 37–46, 2011. DOI: [10.1016/j.compfluid.2010.11.024](https://doi.org/10.1016/j.compfluid.2010.11.024).
- [19] P. Ricco, D. Tran, and G. Ye, "Wall heat transfer effects on Klebanoff modes and Tollmien–Schlichting waves in a compressible boundary layer," *Phys. Fluids.*, vol. 21, no. 2, p. 024106, 2009. DOI: [10.1063/1.3054155](https://doi.org/10.1063/1.3054155).
- [20] K. J. Franko and S. Lele, "Effect of adverse pressure gradient on high speed boundary layer transition," *Phys. Fluids.*, vol. 26, no. 2, p. 024106, 2014. DOI: [10.1063/1.4864337](https://doi.org/10.1063/1.4864337).
- [21] T. P. Wadhams, E. Mundy, M. G. MacLean, and M. S. Holden, "Ground test studies of the hifire-1 transition experiment Part 1: Experimental results," *J. Spacecr. Rockets.*, vol. 45, no. 6, pp. 1134–1148, 2008. DOI: [10.2514/1.38338](https://doi.org/10.2514/1.38338).
- [22] K. J. Franko and S. K. Lele, "Breakdown mechanisms and heat transfer overshoot in hypersonic zero pressure gradient boundary layers," *J. Fluid Mech.*, vol. 730, pp. 491–532, 2013. DOI: [10.1017/jfm.2013.350](https://doi.org/10.1017/jfm.2013.350).
- [23] M. S. Shadloo, A. Hadjadj, D. J. Bodony, F. Hussain, and S. K. Lele, "Effects of heat transfer on transitional states of supersonic boundary layers," in *Proceedings of Summer program* (Center of Turbulence Research, Stanford University, USA, 2016) pp. 175–184.
- [24] M. S. Shadloo and A. Hadjadj, "Laminar-turbulent transition in supersonic boundary layers with surface heat transfer: A numerical study," *Numer. Heat Tr. A-Appl.*, vol. 72, no. 1, pp. 1–14, 2017. DOI: [10.1080/10407782.2017.1353380](https://doi.org/10.1080/10407782.2017.1353380).
- [25] M. S. Shadloo, A. Hadjadj, and A. Chaudhuri, "On the onset of postshock flow instabilities over concave surfaces," *Phys. Fluids.*, vol. 26, no. 7, p. 076101, 2014. DOI: [10.1063/1.4890482](https://doi.org/10.1063/1.4890482).
- [26] O. Ben-Nasr, A. Hadjadj, A. Chaudhuri, and M. S. Shadloo, "Assessment of subgrid-scale modeling for large-eddy simulation of a spatially-evolving compressible turbulent boundary layer," *Comput. Fluids*, vol. 151, pp. 144–158, 2016. DOI: [10.1016/j.compfluid.2016.07.004](https://doi.org/10.1016/j.compfluid.2016.07.004).
- [27] S. Pirozzoli, F. Grasso, and T. B. Gatski, "Direct numerical simulation and analysis of a spatially evolving supersonic turbulent boundary layer at  $M=2.25$ ," *Phys. Fluids.*, vol. 16, no. 3, pp. 530–545, 2004. DOI: [10.1063/1.1637604](https://doi.org/10.1063/1.1637604).
- [28] K. Stetson and R. Kimmel, "On hypersonic boundary-layer stability," in *30th Aerospace Sciences Meeting and Exhibit*, Reno, NV, Jan. 6–9, 1992, p. 737. DOI: [10.2514/6.1992-737](https://doi.org/10.2514/6.1992-737).
- [29] F. M. White and I. Corfield, *Viscous fluid flow.*, vol. 3. Boston, MA: McGraw-Hill Higher Education, 2006).
- [30] C. J. Roy and F. G. Blottner, "Review and assessment of turbulence models for hypersonic flows," *Prog. Aerospace Sci.*, vol. 42, no. 7–8, pp. 469–530, 2006. DOI: [10.1016/j.paerosci.2006.12.002](https://doi.org/10.1016/j.paerosci.2006.12.002).
- [31] P. Bradshaw, "Compressible turbulent shear layers," *Annual Review of Fluid Mechanics.*, vol. 9, no. 1, pp. 33–52, (1977).

# Chapter 5

## Effects of the baseflow variation on the onset of the transition

---

Published in: *Heat and Mass Transfer*



# Effect of thermo-mechanical non-equilibrium on the onset of transition in supersonic boundary layers

S. Sharma<sup>1</sup> · M. S. Shadloo<sup>1</sup> · A. Hadjadj<sup>1</sup>

Received: 22 February 2018 / Accepted: 12 July 2018  
© Springer-Verlag GmbH Germany, part of Springer Nature 2018

## Abstract

Direct numerical simulations (DNS) for supersonic boundary layers (SBLs) with a free-stream Mach number of  $M_\infty = 2.2$  are carried out. Various cases are investigated, involving the adiabatic and the isothermal (cooled and heated) walls. The laminar boundary layer is tripped using a blowing and suction strip with single-frequency and multiple spanwise wave-number excitation. Effects of thermo-mechanical non-equilibrium of thermal boundary layer on laminar-to-turbulent transition (LTT) are presented in detail. Cases with two perturbation intensities are investigated (0.5% and 2.4%). The receptivity analysis of transition onset location towards the thermo-mechanical non-equilibrium is performed using different physical quantities like streamwise evolution of skin-friction coefficient, Stanton number and Dynamic mode decomposition (DMD). The results reveal that thermo-mechanical non-equilibrium tends to advance the transition onset location and also decreases the transition length for the heated walls regardless of the initial perturbation intensity. However, for the cooled walls with 2.4% perturbation intensity, the existence of thermo-mechanical non-equilibrium has a stabilizing effect resulting in delayed transition onset. The flow stays laminar for cooled walls with 0.5% perturbation intensity. The results obtained from DMD analysis uncover two distinct ways of evolution for odd and even harmonics of the perturbation frequency. DMD results also show that the fundamental evolution of the modes is not affected by the physical flow parameters like wall temperature or existence of thermo-mechanical non-equilibrium. It is observed that the imposed frequency mode or the principal mode is dominant in the transition region and eventually breakdown to smaller structures in the turbulent regime.

## 1 Introduction

Transition to turbulence in high-speed flows is an active field of research that has gained quite a lot of interest due to its importance in fundamental/applied research studies and industrial applications. An understanding of main mechanisms responsible for laminar-to-turbulent transition (LTT) in high-speed flows is imperative for the prediction of turbulence production and its possible control. Various engineering applications such as flow over the blades of a gas turbine [1] demand for a better understanding of LTT of supersonic boundary layers (SBLs). Prediction of LTT is of utmost importance in designing the thermal protection system for the spacecraft [2]. Despite of the numerous numerical and experimental investigations [3–5],

the mechanisms of LTT of SBLs is poorly understood due to the difficulties in accurate measurements [6].

External or internal disturbances can perturb the boundary layer and flow can transit from laminar to turbulent state. These disturbances can be introduced numerically by employing roughness elements [7], vortical disturbances [8], blowing and suction of the boundary layer [9] and random noise. For high-speed flows, studies have widely utilized roughness elements to disturb the boundary layer [7, 10–12]. These studies dealt with the impacts of various parameters like shape [10] and orientation [11] of the roughness elements and also the modal evolution [12].

Most of the numerical investigations mentioned so far have been performed over an adiabatic wall. The amount of literature on SBLs involving the effects of heat transfer is even more scarce. Growth mechanism discussed in [8] for Mach numbers 3 and 6, reveals that free-stream Mach number is the main governing parameter for determining the lateral growth rate of turbulent spots followed by wall temperature. Redford et al. [8] also found out that instability of lateral jets which get generated towards the start of

✉ M. S. Shadloo  
msshadloo@coria.fr

<sup>1</sup> CORIA-UMR 6614, CNRS-University, INSA of Rouen and Normandie University, 76000 Rouen, France

the turbulent zone, serve as a trigger for generation of new turbulent spots in the downstream. The study performed by [13] utilizing a thermal wall model coupled at high Mach number showed that as a result of the frictional heating of the wall, the flow tends to re-laminarize with time. Recent study of [14] has investigated the impacts of wall temperature on single- and multi-point statistics of pressure fluctuations at different wall-normal locations. Their results revealed that acoustic sources were mainly concentrated in the near-wall region and wall cooling was found to significantly influence the nonlinear component of the acoustic term by enhancing dilatational fluctuations in the sublayer while damping vortical fluctuations in the buffer and log layers. The results of [15] suggest that wall cooling stabilizes the laminar streaks when spanwise wavelength is quite large in comparison to the boundary layer thickness. But, for Klebanoff modes when the spanwise diffusion is comparable to the wall-normal diffusion, the laminar streaks are stabilized by wall heating. Shadloo et al. [16] investigated the impacts of wall heat-transfer on statistical properties. They found out that the behavior of near-wall turbulence was affected by wall heat-transfer for turbulent Mach numbers less than 0.3. Tong et al. [17] have studied the impact of wall cooling on turbulent structures and shock motions. Their results suggest that wall cooling significantly affects the log region of mean velocity profile downstream of the interaction region. The streamwise coherence of streaks did increase with decrease in temperature, but the shapes of dynamic modes were not sensitive to the wall temperature [17, 18]. Shadloo et al. [19] studied the LTT of SBLs considering the effects of surface heat transfer on transition onset with free-stream Mach number of 2.2. The results of their DNS were in good agreement with the predictions of Linear Stability Theory (LST) for the adiabatic case. But for the isothermal cases (wall heating and cooling) they obtained DNS results which were in contrast to the LST predictions. As LST predicted upstream transition onset for the heated wall and delayed transition onset for the cooled one in comparison to the adiabatic wall, but obtained DNS results revealed the contrasting behavior of the walls. They asserted that this discrepancy might be originating from the thermo-mechanical non-equilibrium of the temperature profiles i.e. when the thermal boundary layer of the incoming flow does not conform with the thermal boundary layer present on the wall. The cases investigated by them had adiabatic inlet temperature profile regardless of the wall temperature. In addition to thermo-mechanical non-equilibrium, they also accounted high perturbation intensities (2.4% and 4%) used at the perturbation strip as one of the possible reasons for observed deviation from LST results. Shadloo and Hadjadj [9] plotted the evolution of the disturbance energy, which is the energy associated with the unsteady streamwise velocity fluctuations, in the streamwise direction and uncovered that the

slopes of the growth-rate did not change and tend to merge together in turbulent part regardless of the wall-temperature. Sharma et al. [20] investigated the effects of different physical mechanisms like perturbation intensity and wall temperature on transition onset location and transition length for compressible supersonic boundary layers. They found that below 1% perturbation intensity, wall cooling stabilized the flow and it remained laminar while wall heating had a destabilizing impact causing the flow to transit upstream in comparison to the adiabatic wall. Beyond the 1% perturbation intensity, wall cooling instead of stabilizing the boundary layer it destabilized it resulting in the upstream shift of transition onset location [20] and inverse was found for the heated wall.

In current study, we address the assertions made in [19] and [9] regarding the receptivity of LTT of SBLs towards the existence of thermo-mechanical non-equilibrium of the boundary layer. Additionally, we have also considered a lower intensity perturbation of 0.5% to capture the joint impact of perturbation intensity and thermo-mechanical non-equilibrium on LTT of SBLs. Dynamic mode decomposition (DMD) analysis has also been performed to uncover the dependency of evolution of dynamic modes on different flow parameters. To the best of our knowledge, the impact of existence of thermo-mechanical non-equilibrium on the LTT of SBLs has not been investigated before else than in [9, 19].

The rest of the paper is organized as follows: details of the computational setup including governing equations and boundary conditions are given in Section 2. Then a detailed discussion of the effects of thermo-mechanical non-equilibrium on transition are presented in Section 3, after presenting a short note on validation in Section 3.1. The paper is concluded in Section 4.

## 2 Computation setup

### 2.1 Governing equations

Generalized form of the *Navier–Stokes equations* (NSE) for any fluid with a given viscosity  $\mu$  and density  $\rho$  can be represented by a set of equations essentially comprising of the equations of conservation of mass, momentum and energy. This set of equations can be written as follows:

$$\frac{\partial \rho}{\partial t} + \frac{\partial \rho u_j}{\partial x_j} = 0 \quad (1)$$

$$\frac{\partial \rho u_i}{\partial t} + \frac{\partial \rho u_i u_j}{\partial x_j} = -\frac{\partial p}{\partial x_i} + \frac{\partial \tau_{ij}}{\partial x_j} \quad (2)$$

$$\frac{\partial \rho E}{\partial t} + \frac{\partial (\rho E + p) u_i}{\partial x_i} = -\frac{\partial q_i}{\partial x_i} + \frac{\partial u_i \tau_{ij}}{\partial x_j} \quad (3)$$

where,

$$p = (\gamma - 1) \left( \rho E - \frac{1}{2} \rho u_i u_i \right) = \frac{1}{\gamma M^2} \rho T \quad (4)$$

and  $\tau$  being the symmetric viscous stress tensor, which is given by:

$$\tau_{ij} = \frac{\mu}{Re} \left( \frac{\partial u_j}{\partial x_i} + \frac{\partial u_i}{\partial x_j} - \frac{2}{3} \frac{\partial u_k}{\partial x_k} \delta_{ij} \right) \quad (5)$$

Here,  $\rho$ ,  $u$  and  $p$  are density, various velocity components and pressure respectively.  $E$ ,  $T$ ,  $\gamma$ ,  $M = u/\sqrt{\gamma r T}$ ,  $Re = \rho_\infty U_\infty \delta_{in}/\mu$ , and  $\mu$  represent total energy, temperature, ratio of specific heats, Mach number, Reynolds number and kinematic viscosity respectively.  $\delta_{ij}$  is the Kronecker delta.

## 2.2 Numerical solver

This study utilizes a well validated DNS-LES numerical solver known as CHOC-WAVES, which solves three-dimensional, compressible, unsteady NSE for perfect gases. The convective fluxes are discretized by a hybrid conservative sixth-order central scheme with fifth-order Weighted Essential Non-Oscillatory (WENO) scheme. The numerical stability has been optimized by splitting the convective terms in a skew-symmetric form in order to minimize the aliasing error and enforce discrete conservation of kinetic energy. The diffusive terms are approximated with fourth or sixth order formulas, and expanded in Laplacian form. The system of equations is time integrated using third-order Runge-Kutta (RK-3) scheme. More details and validation of the solver can be found in [21] and [22].

## 2.3 Problem setup and boundary conditions

In this study, supersonic boundary layers over a flat plate with free-stream Mach number  $M_\infty = 2.2$ , temperature  $T_\infty = 177$  K, pressure  $p_\infty = 23796$  Pa and Prandtl number  $Pr = 0.72$  have been investigated. The subscript  $\infty$  denotes the free-stream values. This Mach number has been chosen because at higher Mach numbers, Mack modes or the acoustic modes start to dominate the flow and effects of wall heat-transfer are eclipsed due to the arising acoustic instabilities [9]. The velocity, temperature and density profiles corresponding to the Blasius solution are forced at the inlet of the computational domain. These profiles are calculated separately in another solver to obtain the similarity solutions of a laminar compressible boundary layer over adiabatic and isothermal walls. This solution is applied at a distance  $x_{in}$  which is present at certain distance upstream of the domain,  $x_{in} = 0.1016$  m. For adiabatic case, the wall temperature is kept as  $T_w = T_{aw}$ , while for cooled and heated walls the temperature is  $T_w = 0.75 T_{aw}$  and  $T_w = 1.5 T_{aw}$ , respectively, where  $T_{aw} \approx 1.82 T_\infty$ . Details of different DNS cases under investigation have been enlisted in Table 1. In this table A, C and H stand for adiabatic, cooled and heated walls, respectively. The cases with suffix N represent the cases with thermo-mechanical non-equilibrium. A0 is the reference adiabatic case which has been used to validate the mesh resolution, as discussed in Section 3.1. The fluid considered is air with constant specific heats. Sutherland's law has been used to calculate the dynamic viscosity:

$$\mu = \frac{C_1 T^{3/2}}{T + S} \quad (6)$$

**Table 1** Computational parameters of the various test cases considered

Cases	$T_w/T_{aw}$	$A/u_\infty$ (%)	$\omega$ (krad/s)	$Re_{\theta, max}$	$\Delta x^+$	$\Delta y_{min}^+$	$\Delta z^+$
A0 [19]	1.00	2.4	150	3748	5.52	0.34	2.85
A1	1.00	0.5	150	6144	11.05	0.34	6.52
A2	1.00	2.4	150	3675	11.05	0.34	6.52
C1	0.75	0.5	150	1896	16.24	0.50	9.58
C2	0.75	2.4	150	3935	16.24	0.50	9.58
NC1	0.75	0.5	150	1429	16.73	0.52	9.87
NC2	0.75	2.4	150	3754	16.70	0.52	9.85
H1	1.50	0.5	150	2888	6.62	0.21	3.91
H2	1.50	2.4	150	3474	6.61	0.20	3.90
NH1	1.50	0.5	150	1472	5.86	0.18	3.46
NH2	1.50	2.4	150	2582	5.87	0.18	3.46

A, C and H stand for adiabatic, cooled and heated walls, respectively and N represents the cases with thermo-mechanical non-equilibrium. Subscripts *min* and *max* are the wall-normal spacing and maximum Reynolds number which can be achieved in the domain respectively. Superscript + denotes the quantities in wall-units

where,  $S = 110.4$  K is Sutherland's temperature for air and  $C_1$  is a constant,  $1.458 \times 10^{-6} \text{ kg/ms} \sqrt{K}$  which can be written as:

$$C_1 = \frac{\mu_r(T_r + S)}{T_r^{3/2}} \quad (7)$$

where  $\mu_r$  is the reference dynamic viscosity of air,  $1.716 \times 10^{-5} \text{ kg/ms}$  at reference temperature,  $T_r$  of 273.15 K. The subscript  $r$  refers to the reference values.

As can be seen in Table 1, a constant excitation frequency,  $\omega = 150 \text{ krad/s}$  is chosen for blowing and suction strip for all the cases which corresponds to the most unstable frequency according to LST for the adiabatic case and is close to the most unstable frequency for the heated and the cooled walls too, as presented in [19] and [9]. However, [19] have utilized  $\omega = 75 \text{ krad/s}$  for their study following the work mentioned in [23].

Figure 1 shows the schematic of the computational domain with boundary conditions. Considered domain is large enough ( $L_x/\delta_{in} \approx 390$ ) to satisfactorily capture the transition and the fully grown turbulent regions. The height and the width of the domain are chosen such that the flow properties are not compromised by wall-normal outflow and periodicity in the spanwise direction ( $L_y/\delta_{in} \approx 31$  and  $L_z/\delta_{in} \approx 16$ ). The dimensions of the domain are similar to the ones used in [9, 19, 20]. Supersonic inflow and outflow conditions are imposed at the inlet ( $x = x_{in}$ ) and at the outlet ( $x = x_{in} + L_x$ ) of the computational domain respectively. Uniform supersonic flow boundary condition is employed for the upper face of the domain so that the flow remains undisturbed and no confinement effect is there. At the outlet of the domain, no buffer layer has been utilized to compensate the edge effects because here our focus is on the transition region, and far-field turbulent region (towards the end of the domain) is of no interest.

No-slip boundary condition is used at the wall surface ( $y = 0$ ), except for the region between  $x_a = x_{in} + 0.3 \delta_{in}$  and  $x_b = x_{in} + 0.6 \delta_{in}$  where the boundary layer is excited by suction and blowing, as in [19, 20]. In this part of the domain, the wall-normal component of velocity is prescribed by single-frequency and multiple-spanwise wavenumber boundary condition given as:

$$v(x, z, t) = A f(x) \left[ \frac{g(z)}{\max(g(z))} \right] \left[ \frac{h(t)}{\max(h(t))} \right] \quad (8)$$

where  $A$  is the amplitude of disturbance,  $f(x)$ ,  $g(z)$  and  $h(t)$  are the streamwise, spanwise and time-dependent variations respectively and are defined as follows:

$$f(x) = 4 \sin \theta (1 - \cos \theta) \sqrt{27} \quad (9)$$

$$g(z) = \sum_{l=1}^{l_{max}} Z_l \sin(2\pi l(z/L_z + \phi_l)) \quad (10)$$

$$h(t) = \sum_{m=1}^{m_{max}} T_m \sin(\omega t + \phi_m) \quad (11)$$

Here,  $\omega$  is the fundamental frequency of the induced perturbations,  $\theta = 2\pi(x - x_a)/(x_b - x_a)$ , and  $\phi_l$  and  $\phi_m$  are the random numbers between 0 and 1.  $\sum_{l=1}^{l_{max}} Z_l = 1$ ,  $Z_l = 1.25 Z_{l-1}$ , with  $l_{max} = 20$  and  $\sum_{m=1}^{m_{max}} T_m = 1$ ,  $T_m = 1.25 T_{m-1}$ , with  $m_{max} = 20$ .

Uniform mesh spacing is used in both the streamwise and the spanwise directions with  $N_x = 2048$  and  $N_z = 140$  being the number of points in the stated directions. In order to properly resolve the boundary layer, the points are more concentrated close to the wall in the wall-normal direction with  $N_y = 150$ . The stretching function in wall-normal direction is given by:

$$y = L_y \frac{1 + \tanh(\kappa_o y)}{\tanh(\kappa_o)} \quad (12)$$

**Fig. 1** Computational domain and boundary conditions

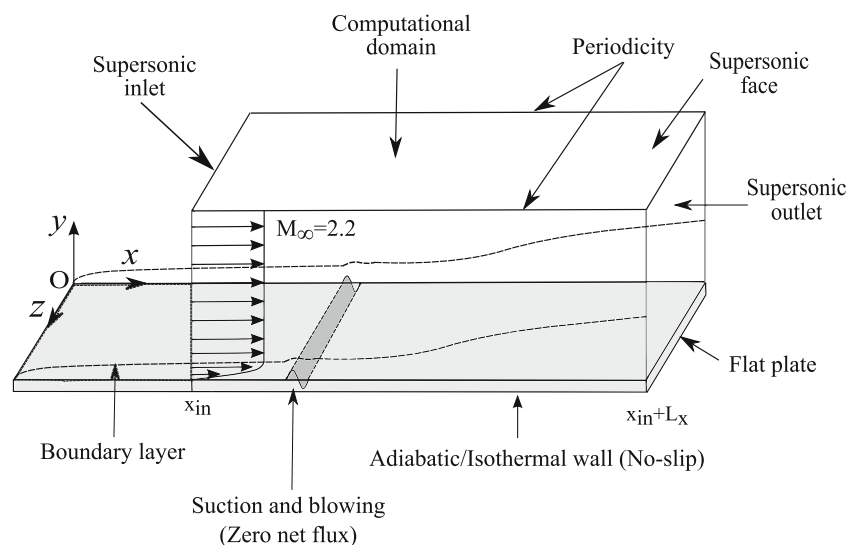
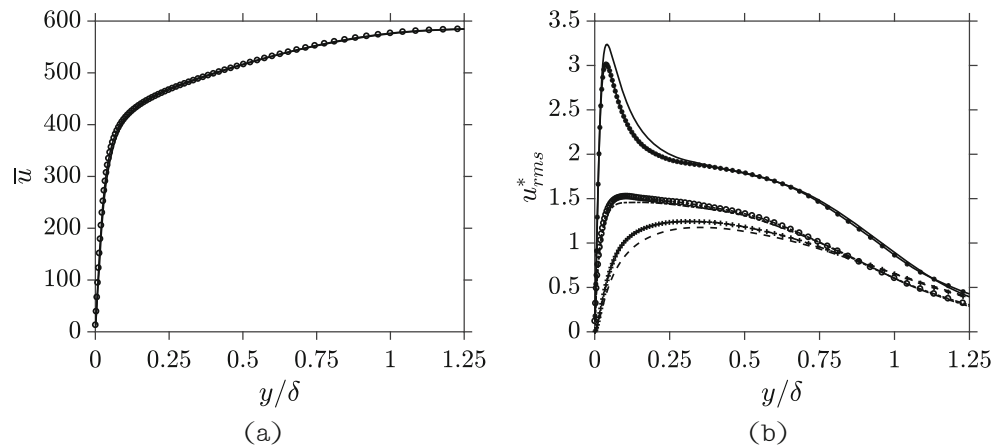


**Fig. 2** Comparison of (a) mean streamwise velocity profiles of A2 (—) with A0 (○), and (b) distribution of rms velocity components as a function of  $y/\delta$  between A0 and A2 at  $Re_x = 4.207 \times 10^6$ , here  $u_{rms}$ ,  $v_{rms}$  and  $w_{rms}$  are represented by (—), (---) and (-·-·), respectively for A2 and by (●), (○) and (+) for A0



with,  $\kappa_o \approx 3$  being the stretch parameter.

### 3 Results and discussion

#### 3.1 Validation

A grid convergence study has been performed, Fig. 2a and b display the comparison between the mean streamwise velocity profiles and  $u_{rms}^*$  values of A0 and A2. It can be seen from these figures that the curves show a good collapse. Therefore, it can be concluded that we have a good grid-resolution even with half the number of points in streamwise and spanwise directions in comparison to [19] and still having sufficient  $\Delta z^+$ ,  $\Delta x^+$  (Table 1) and exactly the same  $\Delta y^+$ . A slight deviation in the rms curves of A0 and A2 cases can be seen in Fig. 2b, which is because of the lesser grid resolution of A2 case in comparison to that of A0 case.

The adequacy of domain in spanwise direction is ensured by plotting two-point correlation function of the fluctuations of different velocity components for the cases

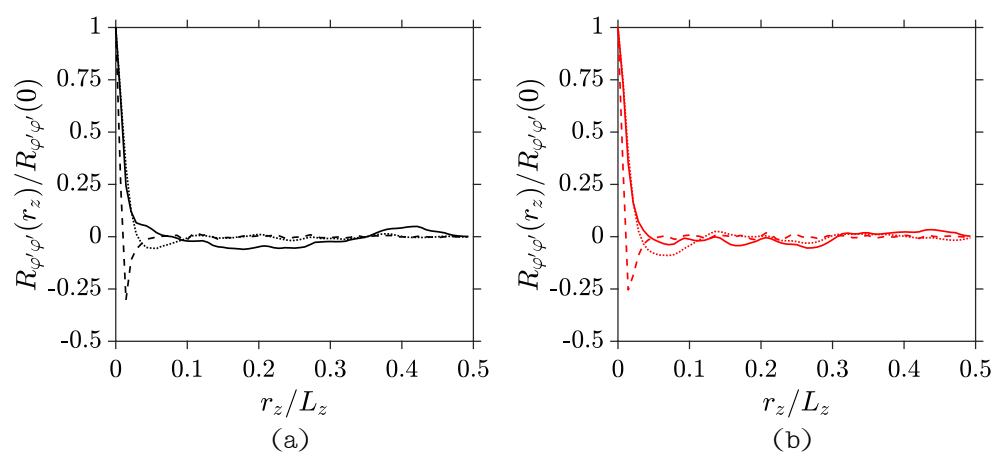
under investigation. Two-point correlation function can be expressed as:

$$R_{\phi'\phi'} = \sum_k^{N_z/2} \langle \phi'_k \phi'_{k+k_r} \rangle_H \tag{13}$$

where  $k_r = 0, 1, \dots, N_z/2$ ,  $r_z = k_r \Delta z$ ,  $\langle \rangle_H$  is the averaging operation over homogeneous direction, superscript(') denotes the fluctuations about Reynolds averaging for any physical quantity and  $\phi$  corresponds to various physical and flow parameters.

Figure 3 represents the two-point correlation functions of different parameters like fluctuations of streamwise, wall-normal and spanwise velocity components for A2, C2 and H2 cases. It can be seen from the figure that all the parameters oscillate around a fixed value well before the half span length,  $L_z/2$  for all the cases. Hence, it can be concluded from these plots that the computation domain is wide enough in the spanwise direction to avoid any kind of hindrance for the principal turbulence mechanisms due to periodicity. The same behavior was also recorded for other cases (not shown here).

**Fig. 3** Two-point correlation coefficients for streamwise (u), spanwise (v) and wall-normal velocity components (w) (represented by  $\phi$  in the Y axes) for, (a) A1 and (b) H1 cases, where (—) represents u, (---) is v and (····) is w



### 3.2 Influence of thermo-mechanical non-equilibrium

Shadloo and Hadjadj [9] asserted that the existence of thermo-mechanical non-equilibrium might be responsible for the observed variations in the transition onset locations. In compressible regimes, the velocity of the flow is coupled with the temperature profile via pressure through energy equation, therefore, thermo-mechanical non-equilibrium is indeed vital for investigation.

Curves comparing the streamwise evolution of skin-friction coefficient,  $C_f$  as a function of  $Re_x$  for the cases with 0.5% perturbation intensity are displayed in Fig. 4a.  $C_f$  can be expressed as

$$C_f = \frac{\tau_w}{\frac{1}{2}\rho_\infty U_\infty^2} \quad (14)$$

where  $\tau_w$  is the local shear stress.

$C_f$  is the most widely used criterion to mark transition region. We use the minimum and maximum time-averaged values of  $C_f$  as the beginning and the end of transition region, respectively. As can be seen in Fig. 4a, in laminar regime, the values of  $C_f$  are the same for all the cases. No transition is observed in case of any of the cooled walls i.e. for C1 and NC1 cases. Due to this reason, we cannot comment about the effect of thermo-mechanical equilibrium on transition for cooled walls with 0.5% perturbation intensity. Figure 4a also shows that NH1 case transits upstream at  $Re_x = 3.47 \times 10^6$  as compared to H1 case which transits at  $Re_x = 3.95 \times 10^6$ . Therefore, it can be inferred that the existence of thermo-mechanical non-equilibrium tends to destabilize the flow and transition onset gets advanced for the heated wall with 0.5% perturbation intensity. However, both the NH1 and H1 cases transit sooner in comparison to the A1 case (at  $Re_x = 4.12 \times 10^6$ ) highlighting the destabilizing nature of wall heating at low perturbation intensity. This observation is consistent with the findings of [20]. These curves also reveal a advanced

transition to turbulence due to thermo-mechanical non-equilibrium as the flow becomes turbulent at  $Re_x = 4.60 \times 10^6$  for NH1 case in comparison to  $Re_x = 5.11 \times 10^6$  for the H1 case highlighting a decrease in transition length for NH1 case in comparison to H1 case. It can also be noted here that the amount of overshoot in the  $C_f$  curve is slightly more for the case with thermo-mechanical non-equilibrium. In the turbulent region, it can be seen that  $C_f$  values are lesser for the heated walls than the adiabatic wall which signifies decreasing shear stress with increase in surface temperature, hence, resulting in lesser values of  $C_f$ . The turbulent part also reveals that  $C_f$  values of NH1 are lesser than H1 which means that the existence of thermo-mechanical non-equilibrium also results in a decrease in shear stress for heated walls. However for C1 and NC1 cases, the  $C_f$  values are exactly the same and the curves closely follow the trend of laminar blasius solution.

Figure 4b shows the trends of streamwise evolution of the Stanton number,  $St$  as a function of  $Re_x$ . It characterizes the wall heat-transfer and can be written as

$$St = \frac{q_w}{\rho_\infty U_\infty C_p (T_{aw} - T_w)} \quad (15)$$

where  $q_w$  denotes the heat transfer from the wall. For turbulent regimes, the adiabatic wall temperature  $T_{aw}$  is calculated by using the approximation for recovery factor,  $Pr^{1/3}$  [24]:

$$T_{aw} = T_\infty \left( 1 + Pr^{1/3} \times \frac{\gamma - 1}{2} \times M_\infty^2 \right) \quad (16)$$

where  $Pr$  is the Prandtl number.

As with the  $C_f$ , here also we have used the minimum and the maximum time-averaged values of  $St$  as the beginning and the end of transition region, respectively. This criterion also predicts an advanced transition onset due to the presence of thermo-mechanical non-equilibrium, as the transition onset location moves from  $Re_x = 4.02 \times 10^6$  for H1 case to  $Re_x = 3.74 \times 10^6$  for NH1 case. Likewise the

**Fig. 4** Streamwise evolution of (a) skin-friction coefficient,  $C_f$  and (b) Stanton number,  $St$  as a function of  $Re_x$  for A1 (—), C1 (—), H1 (—), NC1 (---) and NH1 (---) cases

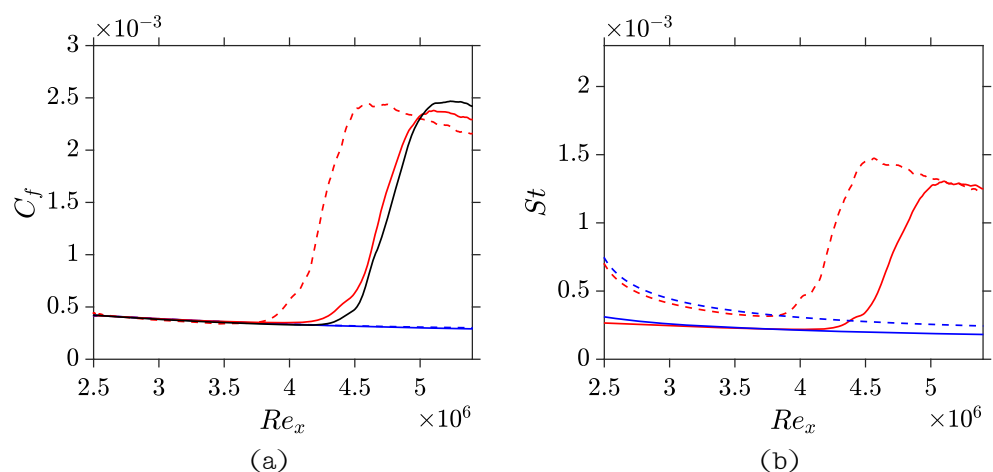
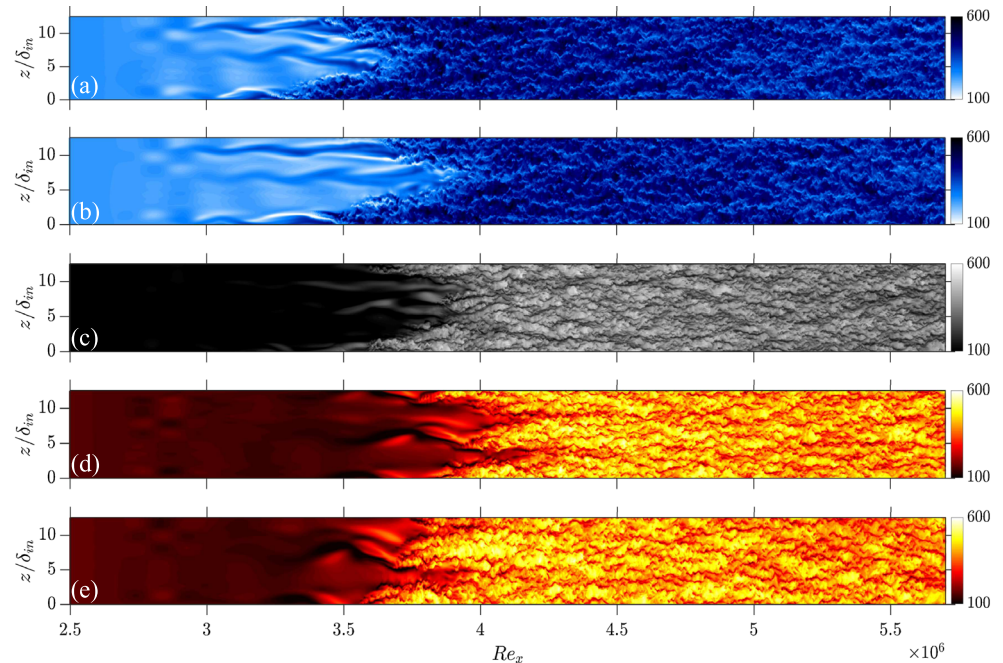


**Fig. 5** Instantaneous flow-fields colored by streamwise velocity component in x-z plane for **a** C2, **b** NC2, **c** A2, **d** H2 and **e** NH2 at  $y/\delta_{in} = 0.29$

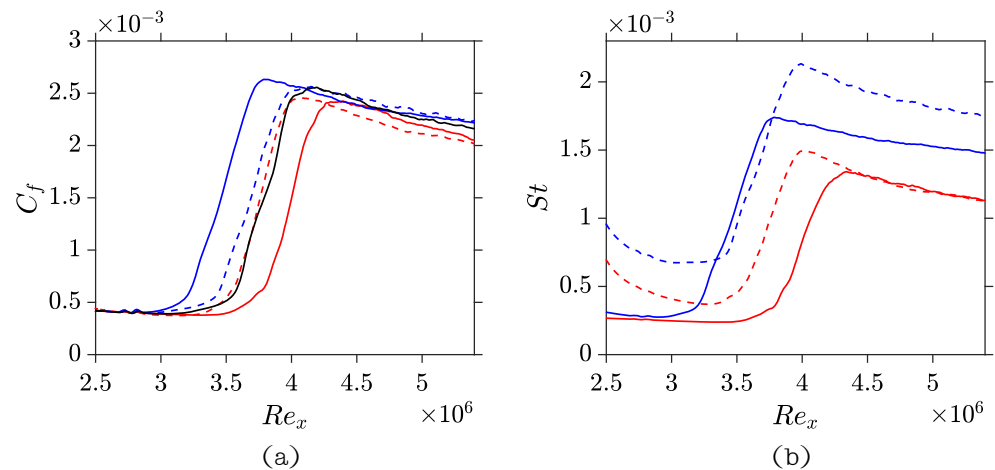


$C_f$  criterion,  $St$  also predicts a shorter length of transition region due to the existence of thermo-mechanical non-equilibrium as the fully developed turbulent regions begin at  $Re_x = 5.10 \times 10^6$  and  $Re_x = 4.56 \times 10^6$  for H1 and NH1 cases, respectively. It can be pointed out here that there exists a prominent difference in the values of the Stanton number of corresponding thermo-mechanical non-equilibrium and thermo-mechanical equilibrium cases in the early laminar region which is due to the difference in the temperature profile of the wall and the incoming flow. This difference is almost the same in case of wall heating and cooling. It can be seen from this figure that the  $St$  values for C1 and NC1 cases do not converge until the very end of the considered domain which means that the flow never attains thermo-mechanical equilibrium in the domain. The  $St$  curve for NC1 case is almost asymptote to the C1 case which signifies that these two curves may converge at infinite length. As a consequence of initial difference in the values of  $St$ , NH1 case exhibits more heat transfer in comparison to the H1 case in laminar part and these values become the same in the turbulent portion. Likewise the  $C_f$  curve, towards the end of the transition region, the amount of overshoot in the  $St$  values is more for the NH1 case underlining an enhanced amount of wall heat-transfer in the turbulent portion in comparison to H1. The equal values of Stanton number in the turbulent regime means that as a result of turbulent mixing, NH1 case eventually attains thermo-mechanical equilibrium with the surface. A comparison between Fig. 4a and b points out that the existence of thermo-mechanical non-equilibrium surges the overshoot for both  $C_f$  and  $St$ .

The instantaneous flow-fields colored by streamwise velocity component in x-z plane at  $y/\delta_{in} = 0.29$  are shown in Fig. 5a-e for C2, NC2, A2, H2 and NH2 cases, respectively. The existence of streamwise streaks can be seen in the transition region for all the cases (distinctively for cooled cases, C2 and NC2). A comparison between Fig. 5a and b highlights that the existence of thermo-mechanical non-equilibrium for cooled walls (NC2 case) results in the formation of elongated streaks and hence a longer transition region in comparison to C2 case. However, the difference in the length of transition region cannot be clearly seen for the heated walls with/without thermo-mechanical non-equilibrium. This set of figures also shows that the transition onset location moves upstream for cooled walls and moves downstream for the heated walls in comparison to adiabatic wall.

Figure 6a depicts the streamwise evolution of  $C_f$  as a function of  $Re_x$  with 2.4% perturbation intensity. It can be seen from this figure that in the laminar regime, the values of  $C_f$  are the same for all the cases. This figure shows that NC2 case transits downstream at  $Re_x = 2.88 \times 10^6$  as compared to C2 case which transits at  $Re_x = 2.76 \times 10^6$ , therefore, thermo-mechanical non-equilibrium tends to have a stabilizing effect for cooled walls with 2.4% perturbation intensity. For the heated walls, similar to 0.5% perturbation intensity cases, the existence of thermo-mechanical non-equilibrium tends to destabilize the flow. As a result of this destabilization, the transition onset location moves upstream to  $Re_x = 3.14 \times 10^6$  for NH2 case in comparison to H2 case at  $Re_x = 3.32 \times 10^6$ . Additionally, Fig. 6a reveals that for intense perturbations i.e. 2.4%, wall heating has a stabilizing

**Fig. 6** Streamwise evolution of (a) skin-friction coefficient,  $C_f$  and (b) Stanton number,  $St$  as a function of  $Re_x$  for A2 (—), C2 (—), H2 (—), NC2 (---) and NH2 (---) cases



effect resulting in delayed transition of H2 in comparison to A2 case which transits at  $Re_x = 3.03 \times 10^6$  while wall cooling has a destabilizing effect. Sharma et al. [20] also found this trend in their study. This can be explained, as mentioned in [25] that for certain disturbance levels, strong mean flow distortions tend to delay or even suppress the transition process for the heated walls. Although the results in [25] are for the hypersonic regime, but it seems that this particular transition delay mechanism does apply here (for supersonic regime). Owing to the stabilizing effect induced by thermo-mechanical non-equilibrium, NC2 case has a longer transition region in comparison to C2 as the flow becomes turbulent at  $Re_x = 4.15 \times 10^6$  for NC2 case and at  $Re_x = 3.79 \times 10^6$  for C2 case. On contrary to this, NH2 case shows faster and shorter transition to turbulence than H2 case with NH2 turning turbulent at  $Re_x = 4.07 \times 10^6$  and H2 at  $Re_x = 4.39 \times 10^6$ . This figure also reveals that the amount of overshoot in the  $C_f$  curve is more for the C2 case than NC2 case highlighting an enhanced amount of shear. However, this overshoot is slightly more for NH2 case in comparison to the H2 case. Likewise in Fig. 4a, the  $C_f$  values are quite close to each-other in turbulent regime for all the cases. In the turbulent part of the domain, it can be seen that wall heating decreases the shear stress resulting in the lesser values of  $C_f$  (likewise Fig. 4a) when compared to A2 case, and wall cooling is found to have an inverse impact. These findings are in accordance with the findings presented in [18]. A closer look of the figure reveals that the existence of thermo-mechanical non-equilibrium tends to decrease the  $C_f$  values for the heated case (i.e. NH1 < H1) and does the opposite for the cooled case (i.e. NC1 > C1).

Figure 6b shows the trends of streamwise evolution of the Stanton number as a function of  $Re_x$ . The laminar regime in this figure also depicts large difference in the values of Stanton number due to different imposed temperature profiles at the inlet as in Fig. 4b. This criterion also predicts delayed transition onset for NC2 case (at  $Re_x = 2.91 \times 10^6$ )

in comparison to C2 case (at  $Re_x = 2.89 \times 10^6$ ) and an early onset of transition for NH2 case (at  $Re_x = 3.14 \times 10^6$ ) compared to H2 case (at  $Re_x = 3.37 \times 10^6$ ). Likewise the  $C_f$  criterion, this criterion also reveals an elongated transition region in case of cooled wall and shorter transition length for the heated case due to the existence of thermo-mechanical non-equilibrium as the fully turbulent region begins from  $Re_x = 3.84 \times 10^6$  for NC2 case and from  $Re_x = 4.01 \times 10^6$  for NH2 case. Due to a large difference in the  $St$  values of NC2 and C2 cases in laminar regime, considerable difference persists in the  $St$  values until the end of the domain despite of the turbulent mixing happening towards the end of the domain. On the other hand, NH2 case eventually attains thermo-mechanical equilibrium in the turbulent portion. In the same way as in Fig. 4b, Fig. 6b also depicts a prominent overshoot for the cases with thermo-mechanical non-equilibrium signifying enhanced heat-transfer.

Table 2 enlists various parameters of the transition region predicted by  $C_f$  and  $St$  criteria. It can be clearly seen from this table that the existence of thermo-mechanical non-equilibrium increases the transition length for the cooled walls while it has the opposite impact on the heated walls irrespective of the perturbation intensity. This table also highlights the effects of other physical parameters like wall temperature on transition onset which agree with the findings of [20].

### 3.3 Dynamic mode decomposition

Dynamic mode decomposition (DMD) method has been utilized to reveal the behavior and evolution of induced perturbation frequency and its super-harmonics throughout the computational domain. This method was introduced by [26], focusing on extracting the information about fluid-dynamical and transport processes. Various methods and algorithms were developed later on as mentioned by

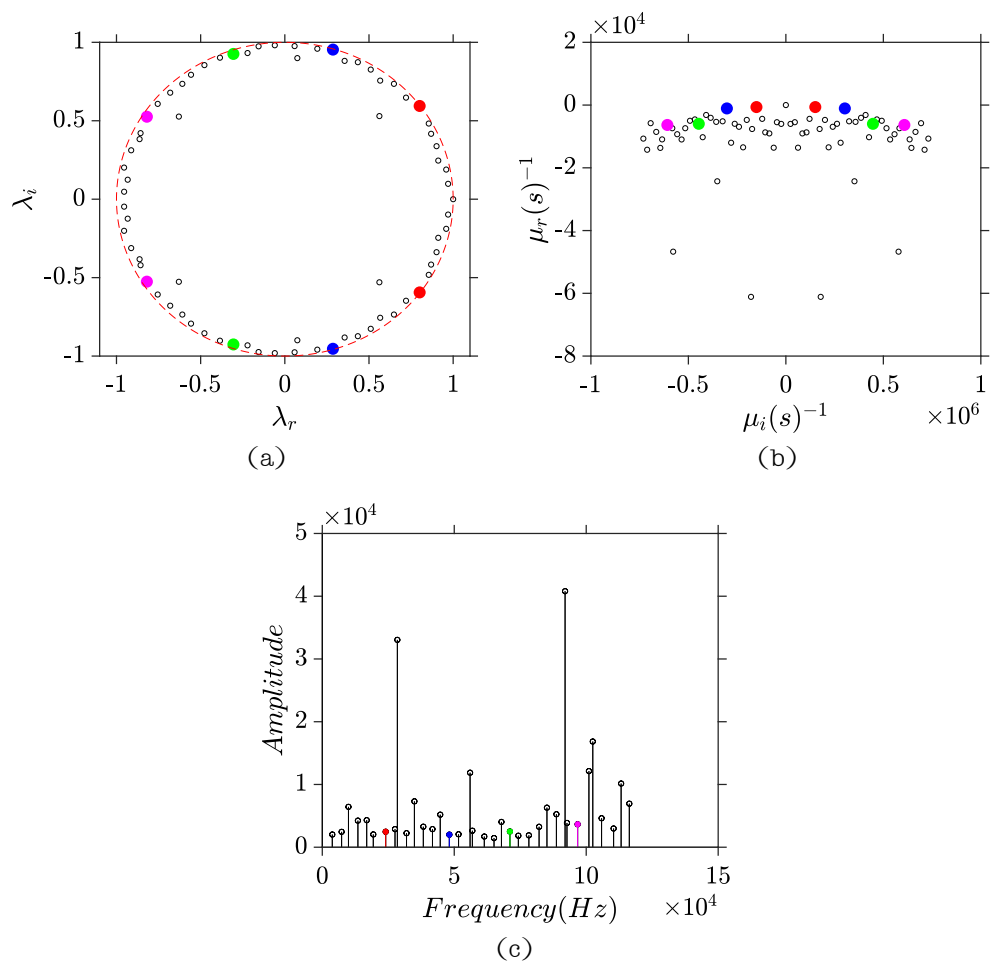
**Table 2** Description of the transition region (the beginning, end and length of transition region) in terms of  $Re_x$  for different cases under investigation as predicted by  $C_f$  and  $St$  criteria

Case	Onset of transition ( $\times 10^6$ )		End of transition ( $\times 10^6$ )		Transition length ( $\times 10^6$ )	
	$C_f$	$St$	$C_f$	$St$	$C_f$	$St$
A1	4.12	$\times$	5.23	$\times$	1.11	$\times$
A2	3.03	$\times$	4.20	$\times$	1.17	$\times$
C1	$\times$	$\times$	$\times$	$\times$	$\times$	$\times$
C2	2.76	2.89	3.79	3.79	1.03	0.90
NC1	$\times$	$\times$	$\times$	$\times$	$\times$	$\times$
NC2	2.88	2.91	4.15	3.84	1.27	0.93
H1	3.95	4.02	5.11	5.10	1.16	1.08
H2	3.32	3.37	4.39	4.40	1.07	1.03
NH1	3.47	3.74	4.60	4.56	1.13	0.82
NH2	3.14	3.14	4.07	4.01	0.93	0.87

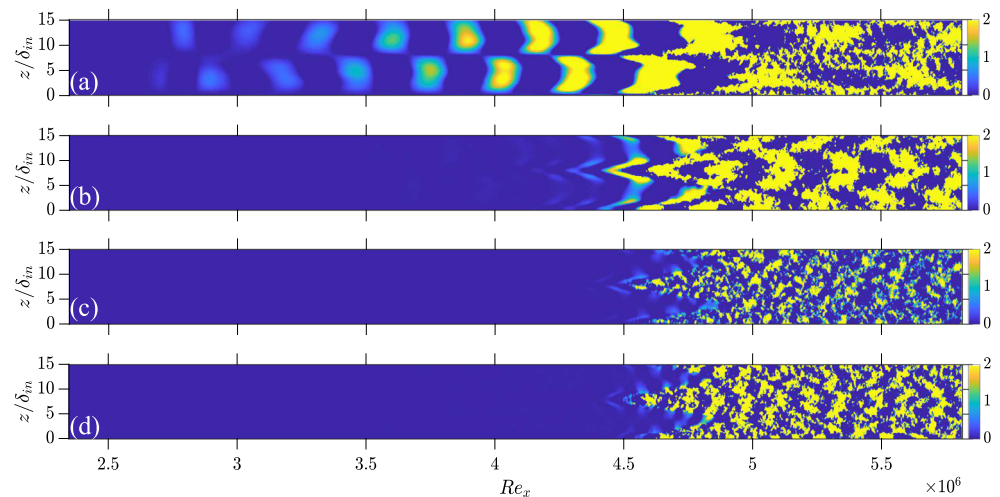
[27] and [28]. This method tracks modal growth in the computational domain. We have analyzed the evolution of induced perturbation frequency and its first three superharmonics which are denoted by  $m_1, m_2, m_3$  and  $m_4$ , respectively. A series of snapshots have been investigated

which are separated from each-other well above the Nyquist criterion [26], which states that the sampling frequency of snapshot should be at least two times more than the frequency being investigated for getting satisfactory results. We have utilized the sampling frequency as high as ten times

**Fig. 7** Eigenvalues spectrum obtained from DMD analysis of A1 case, **a** discrete spectrum with the unit circle, **b** DMD spectrum representing growth rate for various modes and **c** amplitude vs frequency distribution of different modes



**Fig. 8** Reconstructed flow-field for A1 case, showing the evolution of **a**  $m_1$ , **b**  $m_2$ , **c**  $m_3$  and **d**  $m_4$  in the computational domain, colored by streamwise velocity component (m/s)



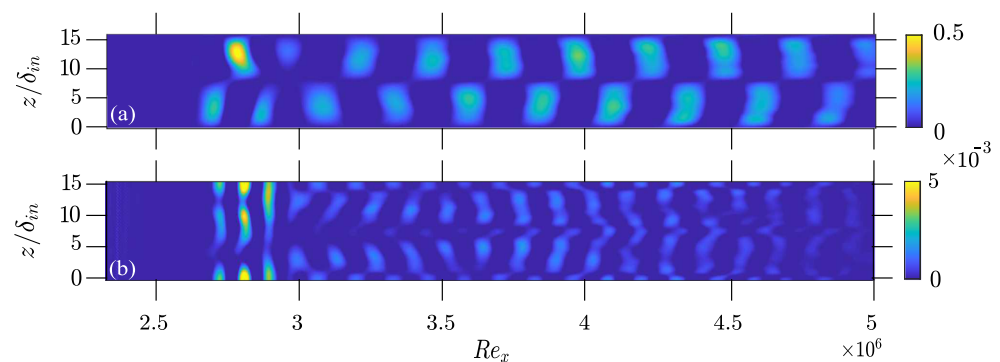
than the lowest frequency under question. Because of this choice, up to third super-harmonic could successfully be captured by using same set of snapshots.

Figure 7 represents various eigenvalues spectra obtained by DMD analysis of A1 case (other cases have not been shown). Figure 7a shows the discretized spectrum for A1 case with the unit circle which represents the limit for the stable modes. The points which are close to the boundary, or at the boundary of this circle are the stable modes while those out of the circle represent the unstable modes. Points inside of the circle represent the decaying modes. In this figure red, blue, green and magenta dots represent  $m_1$ ,  $m_2$ ,  $m_3$  and  $m_4$  modes, respectively. Y-axis of DMD spectrum in Fig. 7b represents the growth rate of the modes. It can be seen in this figure that  $m_1$  has positive growth rate which means that it grows with time and could be a probable cause for triggering turbulence. On the other hand, super-harmonics are the stable modes with slightly positive or negative values of growth rate.

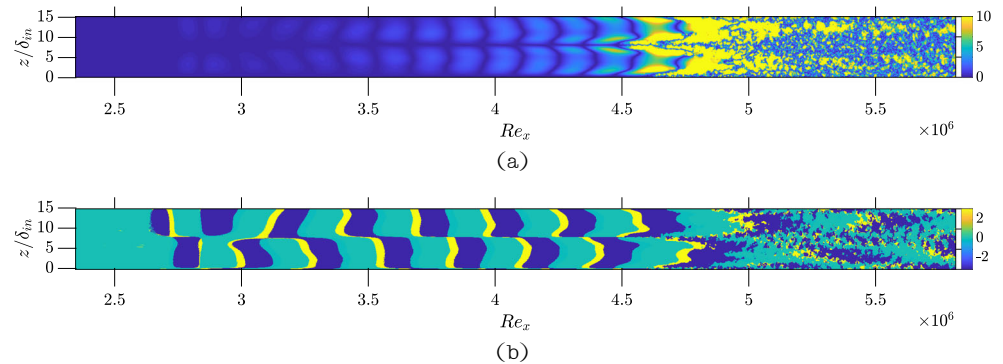
Fast Fourier transform (FFT) is performed for all the points in the computational domain in the streamwise direction which reveal the frequency peaks corresponding to the imposed perturbation frequency and its first three super-harmonics (not shown here). Those corresponding

frequency modes are depicted in Fig. 7c. The flow-field is reconstructed using each individual frequency to track its behavior in the domain. Figures 8 and 9 show the reconstructed flow-field for A1 and C1 cases respectively, colored by the streamwise component of velocity. The relative error during the reconstruction of the flow-field using these modes along with the background mode ranges from 5% to 11%. For other cases under investigation (not shown here), this error is below 15%, therefore, it can be concluded that the considered modes meticulously represent the flow field. From the evolutionary trend of the modes, as could be seen in Fig. 8,  $m_1$  being the principal mode starts just at the location of blowing and suction strip used for exciting the boundary layer and evolves further downstream in staggered manner. Throughout the computational domain,  $m_1$  maintains the evolution in the checkered board pattern in which the large scale structures gain energy downstream and get elongated in the transition region. Being the principal mode, they possess the highest energy content which justifies their elongated shapes in the streamwise direction before getting broken down into smaller structures. The structural integrity of  $m_1$  could be seen until the early turbulent region. It is worth noting here that  $m_2$ , however, has fundamentally different form

**Fig. 9** Reconstructed flow-field for C1 case, showing the evolution of **a**  $m_1$  and **b**  $m_2$  in the computational domain, colored by streamwise velocity component (m/s)



**Fig. 10** Reconstructed flow-field for A1 case, showing the evolution of **a** the magnitude, and **b** phase angle for mode  $m_1$  in the computational domain



of evolution than  $m_1$ . It shows up later in the domain and propagates in parallel lambda shaped structures. Some of these structures seem to replicate the shape of the alternate voids present in the evolutionary pattern of  $m_1$ . A closer look to Fig. 8 reveals that the  $m_1$  and  $m_3$  propagate downstream in staggered pattern while  $m_2$  and  $m_4$  replicate parallel propagation pattern. This highlights two distinct ways of evolution for odd and even harmonics. This trend might be due to the type of blowing and suction employed for flow excitation because the phase difference is introduced to the equation in temporal sense and also in the streamwise direction by random numbers between 0 and 1.

From this figure, it can be observed that all of these modes show up at different locations in the streamwise direction which are based on the level of energy which they attain prior to turbulence. Due to the energy content of each mode, they show up in same sequence as  $m_1$ , followed by  $m_2$ ,  $m_3$  and  $m_4$ , respectively, and disappear in the turbulent portion in reverse order. For C1 case, as the flow remains laminar and eventually the perturbations fade off, therefore, in Fig. 9 only  $m_1$  and  $m_2$  are shown which possess very less amount of energy and they get completely vanished towards the end of the domain. The pattern of evolution of  $m_1$  and  $m_2$  is the same as discussed before for Fig. 8. It has been uncovered that the evolution of the modes is independent of the imposed physical parameters like wall temperature or the thermo-mechanical non-equilibrium. DMD analyses for other cases (not shown here) also showed the same trend of evolution. The observed behavior of dynamic modes agrees well with the results of [17] and [12].

Figure 10a shows the evolution of the magnitude of mode  $m_1$  throughout the computational domain, colored by the magnitude of streamwise component of velocity. The interest behind tracking the evolution of magnitude of this mode is to find out the regions in the computational domain where  $m_1$  is dominant. It can be clearly seen from this figure that the  $m_1$  start to originate from the perturbation strip and progressively becomes dominant in the streamwise direction. The amplitude is highly magnified in the region extending from  $Re_x \approx 4.5 \times 10^6$  to  $Re_x \approx 5 \times 10^6$ , which is a part of the transition region for A1 case, as

shown in Fig. 4a. Afterwards in the turbulent regime, big structures get broken down into smaller ones as a part of energy transfer process. The streamwise evolution of the magnitude of all four modes considered here have the same pattern (not shown here). Figure 10b displays the evolution of phase angle for  $m_1$  in the computational domain. This plot highlights the leads and lags present in the propagating wavefronts. It is important to mention here that the propagation pattern of the phase angles is exactly the same as that of the mode itself (see Fig. 8a), but, as can be seen in Fig. 10b that each propagating mode is composed of wavefronts with opposite phase angles. This figure also reveals that lagging wavefront is more dominant in the domain in comparison to the leading one.

## 4 Conclusion

Direct numerical simulations (DNS) for supersonic boundary layers (SBLs) with a free-stream Mach number of  $M_\infty = 2.2$  were carried out. A total of ten cases were investigated in order to unravel the effects of thermo-mechanical non-equilibrium on transition region. Receptivity of the boundary layer was analyzed using the streamwise evolution of skin-friction coefficient, Stanton number and Dynamic mode decomposition (DMD). The cases were investigated for 0.5% and 2.4% perturbation intensities. The results revealed that the existence of thermo-mechanical non-equilibrium destabilized the flow and transition onset location was shifted upstream irrespective of the induced intensity of perturbation for heated walls. Moreover, it was also uncovered that the heated walls with thermo-mechanical non-equilibrium had a shorter transition region. From the evolution of Stanton number in the domain it was clear that despite of the large difference in the values of Stanton number in the laminar part, the heated walls with thermo-mechanical non-equilibrium eventually did attain thermo-mechanical equilibrium in the turbulent part of the domain resulting from the turbulent mixing taking place. The cooled walls didn't show any signs of transition and the flow remained laminar throughout the

computational domain for 0.5% perturbation intensity. In contrast to the heated wall, for 2.4% perturbation intensity, thermo-mechanical non-equilibrium was found to delay the transition onset location and also a longer transition region was observed in case of the cooled walls. The cooled walls never attained thermo-mechanical equilibrium, neither for 0.5% nor for 2.4% perturbation intensities. Curves of streamwise evolution of Stanton number as a function of  $Re_x$  revealed that the cases with thermo-mechanical non-equilibrium had more overshoot than their thermo-mechanical equilibrium counterparts which highlighted the increased amount of heat-transfer for the cases with thermo-mechanical non-equilibrium. It is important to mention that it was found that for 0.5% perturbation intensity, wall cooling had a stabilizing effect on the flow and it remained laminar throughout the domain while wall heating destabilized the flow and it transitioned before the adiabatic case. On the other hand for 2.4% perturbation intensity, wall cooling destabilized the flow while heating was found to have a stabilizing effect resulting in delayed transition onset in comparison to the adiabatic wall.

The results obtained from DMD analysis uncovered two distinct ways of evolution for odd and even harmonics. It was concluded that the evolution of the modes is independent of the imposed physical parameters like wall temperature or the thermo-mechanical non-equilibrium. For cooled wall with 0.5% perturbation intensity, it was found that the modes disappeared towards the end of the domain but the manner of propagation was the same as in the other cases for corresponding modes. It was found that the considered mode was dominant in the transition region and eventually broke-down to smaller structures in the turbulent regime. The lead and lag in the propagating wavefronts were revealed by the plot of phase angles which uncovered that each propagating mode was comprised of wavefronts with opposite phase angles.

**Acknowledgments** This work was granted access to HPC resources of IDRIS under the allocation 2017-100752 made by GENCI (Grand Equipement National de Calcul Intensif- A0022A10103). The authors acknowledge the access to HPC resources of French regional computing center of Normandy named CRIANN (Centre Régional Informatique et d'Applications Numériques de Normandie) under the allocations 1998022 and 2017002. This project is co-financed by the European Union with the European Regional Development Fund (FEDER) and the Normandy regional council through project 'NEPTUNE'.

**Publisher's Note** Springer Nature remains neutral with regard to jurisdictional claims in published maps and institutional affiliations.

## References

- Tutar M, Sönmez Ü (2010) The computational modeling of transitional flow through a transonic linear turbine: comparative performance of various turbulence models. *Numer Heat Tran Part A: Appl* 58:403–427
- Berry S, Horvath T, Hollis B, Thompson RA, Hamilton HH (2001) X-33 hypersonic boundary layer transition. *J Spacecr Rocket* 38:646–657
- Duan L, Huang J, Deegan C, Choudhari MM, Chou A, Radespiel R, Ali S, Munoz F, Marineau EC, Casper KM et al Characterization of freestream disturbances in conventional hypersonic wind tunnels. In: 2018 AIAA aerospace sciences meeting, p 0347
- Horvath T, Berry S, Hollis B, Singer B, Chang CL Boundary layer transition on slender cones in conventional and low disturbance Mach 6 wind tunnels. In: 32nd AIAA fluid dynamics conference and exhibit, p 2743
- Kosinov A, Maslov A, Semionov N (1997) An experimental study of generation of unstable disturbances on the leading edge of a plate at  $m=2$ . *J Appl Mech Techn Phys* 38:45–51
- Schneider SP (2001) Effects of high-speed tunnel noise on laminar-turbulent transition. *J Spacecr Rocket* 38:323–333
- Bernardini M, Pirozzoli S, Orlandi P, Lele SK (2014) Parameterization of boundary-layer transition induced by isolated roughness elements. *AIAA J* 52:2261–2269
- Redford J, Sandham N, Roberts G (2012) Numerical simulations of turbulent spots in supersonic boundary layers: effects of mach number and wall temperature. *Prog Aerosp Sci* 52:67–79
- Shadloo M, Hadjadj A (2017) Laminar-turbulent transition in supersonic boundary layers with surface heat transfer: a numerical study. *Numer Heat Transfer, Part A: Appl* 72(1):40–53
- Van den Eynde JP, Sandham N (2015) Numerical simulations of transition due to isolated roughness elements at Mach 6, *AIAA Journal*
- Groskopf G, Kloker M (2016) Instability and transition mechanisms induced by Skewed roughness elements in a high-speed laminar boundary layer. *J Fluid Mech* 805:262–302
- Fezer A, Kloker M (2000) Spatial direct numerical simulation of transition phenomena in supersonic flat-plate boundary layers. In: *Laminar-turbulent transition*. Springer, pp 415–420
- Redford J, Sandham N, Roberts G (2011) Direct numerical simulation of transitional flow at high mach number coupled with a thermal wall model. *Comput Fluids* 45:37–46
- Zhang C, Duan L, Choudhari MM (2017) Effect of wall cooling on boundary-layer-induced pressure fluctuations at Mach 6. *J Fluid Mech* 822:5–30
- Ricco P, Tran DL, Ye G (2009) Wall heat transfer effects on klebanoff modes and tollmien-schlichting waves in a compressible boundary layer. *Phys Fluids* 21:024106
- Shadloo M, Hadjadj A, Hussain F (2015) Statistical behavior of supersonic turbulent boundary layers with heat transfer at  $M_\infty = 2$ . *Int J Heat Fluid Flow* 53:113–134
- Tong F, Tang Z, Yu C, Zhu X, Li X (2017) Numerical analysis of shock wave and supersonic turbulent boundary interaction between adiabatic and cold walls. *J Turbul* 18(6):569–588
- Hadjadj A, Ben-Nasr O, Shadloo M, Chaudhuri A (2015) Effect of wall temperature in supersonic turbulent boundary layers: A numerical study. *Int J Heat Mass Transfer* 81:426–438
- Shadloo M, Hadjadj A, Bodony DJ, Hussain F, Lele SK (2016) Effects of heat transfer on transitional states of supersonic boundary layers. In: *Proceedings of summer program, center of turbulence research*. Stanford University, USA, pp 175–184
- Sharma S, Shadloo M, Hadjadj A (2018) Laminar-to-turbulent transition in supersonic boundary layer: effects of initial perturbation and wall heat transfer. *Numer Heat Transfer, Part A: Appl* 73(9):583–603
- Shadloo M, Hadjadj A, Chaudhuri A (2014) On the onset of postshock flow instabilities over concave surfaces. *Phys Fluids* 26:076101

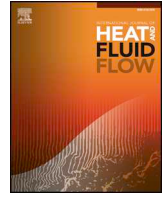
22. Ben-Nasr O, Hadjadj A, Chaudhuri A, Shadloo M (2016) Assessment of subgrid-scale modeling for large-eddy simulation of a spatially-evolving compressible turbulent boundary layer. *Computers & Fluids*
23. Pirozzoli S, Grasso F, Gatski T (2004) Direct numerical simulation and analysis of a spatially evolving supersonic turbulent boundary layer at  $M = 2.25$ . *Phys Fluids* 16:530–545
24. White FM, Corfield I (2006) *Viscous fluid flow*, vol 3. McGraw-Hill Higher Education, Boston
25. Fezer A, Kloker M (1999) Transition processes in Mach 6.8 boundary layers at varying temperature conditions investigated by spatial direct numerical simulation. In: *New results in numerical and experimental fluid mechanics II*. Springer, pp 138–145
26. Schmid PJ (2010) Dynamic mode decomposition of numerical experimental data. *J Fluid Mech* 656:5–28
27. Tu JH, Rowley CW, Luchtenburg DM, Brunton S, Kutz J (2013) On dynamic mode decomposition: theory and applications, arXiv:1312.0041
28. Kutz J, Grosek J, Fu X, Brunton S (2015) Multi-resolution time-scale separation of video content using dynamic mode decomposition. In: *International workshop on video processing and quality metrics for consumer electronic, VPQM*

## **Chapter 6**

# **Implications of the wall temperature on the turbulent flow topology**

---

Published in: *International Journal of Heat and Fluid Flow*



## Turbulent flow topology in supersonic boundary layer with wall heat transfer

S. Sharma, M.S. Shadloo\*, A. Hadjadj

CORIA-UMR 6614, CNRS-University & INSA of Rouen, Normandie University, France



### ARTICLE INFO

#### Keywords:

Supersonic boundary layer  
Turbulent flow  
Direct numerical simulation (DNS)  
Joint probability distribution function (JPDF)  
distribution  
Covariance integrand analysis

### ABSTRACT

Direct numerical simulations (DNS) are performed for the supersonic boundary layers (SBLs) with a free-stream Mach number  $M_\infty = 2.2$ . Different cases including the adiabatic and the isothermal (cooled and heated) walls are investigated. The laminar boundary layer is excited by means of a blowing and suction strip with single-frequency and multiple spanwise wave-numbers. The incoming laminar flow is strongly perturbed with a perturbation intensity of 2.4% of the free-stream velocity to obtain the turbulent boundary layer. In the fully developed turbulent regions, the joint probability density function (JPDF) distribution and the covariance integrands' analyses of different parameters are performed to find out the contribution of various physical mechanisms towards different transfer processes. The results reveal that behavior of the turbulent shear stress is similar to its incompressible counterpart and the wall-temperature impacts are dominant in the buffer layer region (at  $y^+ = 10$ ). The inclination angles of coherent structures show variations arising from the wall-temperature in both the buffer-layer and the log region. The covariance integrands' analyses of different components of the heat flux reveal the dominance of a different transfer process in case of the cooled wall, and as a result of this difference, the cooled wall acts as a heat sink.

### 1. Introduction

An increasing focus towards the improvement in the designs of the supersonic aircraft, calls for a better understanding of the high-speed flows. Various other applications such as the flow through a supersonic propulsive nozzle (Bensayah et al., 2014), demand for better characterization of the supersonic turbulent boundary layers. Due to the complexity posed by the compressibility effects in case of the high-speed flows, it therefore becomes necessary to explore the implications of different physical parameters such as the surface temperature on the flow itself (Duan et al., 2010).

The scientific community is trying to characterize the turbulent flows from a very long period of time. The study performed by Theodorsen (1952) brings out the importance of the coherent structures in case of the incompressible turbulent wall-bounded flows. Their results shed light on the fact that these structures are responsible for low-momentum fluid transport and Reynolds shear-stress production. The morphology of these structures were experimentally verified by Head and Bandyopadhyay (1981). The investigation presented in Stanislas et al. (2008) suggests that in the turbulent boundary layer, the asymmetric one-legged hairpin vortex is the most-probable shape of the coherent structures. Later on, the numerical study performed by

Wu and Moin (2009) stated that the forests of hairpin vortices dominate the turbulent boundary layer. Experimentally, the events of ejections and sweeps which are responsible for Reynolds shear-stress production were visualized by Corino and Brodkey (1969). Wallace et al. (1972) quantified the turbulent processes and provided further insight about Reynolds stress production in the near-wall region for the incompressible turbulent channel flows. Their results revealed that ejections and sweeps together contribute more than 100% to the Reynolds stress, and the additional stress was countered by other contributing factors named interactions.

For the incompressible turbulent channel flows, Wallace and Brodkey (1977) performed the joint probability density distribution function (JPDF) and the covariance integrands' analyses for the streamwise and wall-normal velocity fluctuations in order to find out the contribution of different transport processes towards the Reynolds shear-stress. Their results suggest that when moving from the near wall-region i.e.  $y^+ = 5$  to the end of the log region, different physical phenomena dominate the transfer processes. They also showed that the most-probable velocity pairs did not have the largest contribution towards the shear-stress. Major contribution of ejections towards the Reynolds shear stress was also reported by the experimental investigation of Willmarth and Lu (1972). The results presented by

\* Corresponding author.

E-mail addresses: [msshadloo@coria.fr](mailto:msshadloo@coria.fr), [mostafa.safdari-shadloo@insa-rouen.fr](mailto:mostafa.safdari-shadloo@insa-rouen.fr) (M.S. Shadloo).

<https://doi.org/10.1016/j.ijheatfluidflow.2019.108430>

Received 9 July 2018; Received in revised form 6 May 2019; Accepted 13 June 2019  
0142-727X/© 2019 Elsevier Inc. All rights reserved.

Ong and Wallace (1998) highlighted the ability of the JPDF and covariance analyses in determining the topology of the turbulent flows. The results of this study helped in determining the most probable angles of inclination of the vorticity filaments using the covariance integrands' analyses. The events of vortex stretching and compression were also discussed in detail. It was found that the average stretching of the filaments was greater than compression at all of the considered locations (Ong and Wallace, 1998). Direct numerical simulations (DNS) of Le et al. (2000) investigated the changes in three-dimensional turbulent boundary layer by employing a combination of different statistical and visualization methods. Their results uncovered that mean three-dimensionality was responsible for breaking up the symmetry and alignment of the near-wall coherent structures disrupting their self-sustaining mechanisms, and resulting in the reduction of the turbulent kinetic energy.

Fewer investigations have been performed so-far for the compressible turbulent boundary layers. For low Mach number turbulent boundary layers, the DNS results of Bechlers and Sandberg (2017b) found the potential backscatter mechanism for the transfer of the kinetic energy from smaller scales to the larger scales. The effects on the first three invariants of the velocity gradient tensor with wall-normal distance for weakly compressible flow are studied by Bechlers and Sandberg (2017a). The experimental database available for the compressible problems is scarce due to the difficulty in measurements. The experimental investigation of Spina et al. (1994) revealed that the compressibility has little impact on the statistical properties of the flow. One of the first investigations reported by Morkovin (1962) suggests that the effects of compressibility on turbulence are due to the variations of the thermodynamic properties across the boundary layer. The experimental data also confirms that the supersonic boundary layers bear close similarities to the incompressible ones (Smits and Dussauge, 2006; Li and Xi-Yun, 2011). Li and Xi-Yun (2011) have reported that the angles of inclination of the vortical structures with the streamwise direction increases from sub-layer to buffer layer and then decreases from the buffer layer to the wake region. Maeder et al. (2001) and Pirozzoli et al. (2004) have investigated the structural characteristics of the supersonic turbulence and found the presence of the organized motions in the outer layer. The study presented in Pirozzoli et al. (2008) tried to quantitatively characterize the statistical features of the coherent structures for the case of turbulent supersonic boundary layer and found that the inner layer was mostly populated by the quasi-streamwise vortices while the outer layer (including the log and the wake regions) was populated by different types of structures such as the hairpin vortices and the hairpin packets.

The careful examination of the existing scientific literature reveals that the studies pertaining to the effects of wall heat-transfer on turbulent flow topology for the compressible supersonic boundary layer are scarce (almost none for the heated wall). The study investigating the supersonic cooled turbulent channel flows in Lechner et al. (2001) deals with the effects of compressibility on the pressure-strain correlation and the dissipation rate tensors in the Reynolds stress budgets. The results of this study revealed that the fluctuations conditioned on ejections and sweeps in the wall-layer were instructive, and showed that the positive temperature fluctuations were mainly due to sweeps in case of the cooled wall. Moreover, the comparison with the incompressible flow data underlined that the compressibility effects persisted in the wall-layer only. Relevant statistical properties of the compressible turbulent flows (including the heated wall) are assessed in Shadloo et al. (2015). This study found that the Morkovin's hypothesis was neither valid for the heated walls nor for the cooled walls. The analysis of the turbulent kinetic energy budget showed that the dilatational to solenoidal dissipation ratio increases/decreases with heating/cooling of the wall. Later on, Trettel and Larsson (2016) proposed the transformations of the velocity and the wall-coordinate simultaneously for the supersonic isothermal turbulent channel flows and the turbulent boundary layers, relating the compressible mean velocity profile at any given Mach

number. For low-Mach number heated channel flows, Patel et al. (2017) found that the van Driest transformed mean temperature profiles of variable property cases collapsed with the constant property cases if the semilocal Reynolds number and the local Prandtl number distributions are constant across the channel. Chu et al. (2013) studied the effects of wall temperature on the orientation of the vortical structures and other statistical properties like Morkovin's scaling. It was found that with increasing wall-temperature, the spanwise distance between the legs of the hairpin vortex increased, the mean swirling strength and the angle of the vorticity filament with the wall also increased in the inner layer. However, the statistical properties of the vortical structures were nearly insensitive to the wall temperature in the outer layer. Moreover, they also put forward a new criteria for better characterizing the angles of inclination of the vortical structures. Other works characterized the factors influencing the transition scenarios for the compressible supersonic flows (Shadloo et al., 2016; Shadloo and Hadjadj, 2017; Sharma et al., 2018b).

For the supersonic boundary layers, it is important to address the impacts of wall-heating and cooling on the arrangement and the orientation of the vortical structures, and the heat-transfer mechanisms, which are the fundamental and still open questions for the community. In this study, the JPDF and the covariance integrands' analyses are utilized to unravel the physical mechanisms responsible for the heat-transfer in the streamwise and the wall-normal directions. Various quadrant analyses have been put forward to find out the most-significant and contributing transfer process responsible for the turbulent shear stress, the vortical structures' orientation and the turbulent heat-flux.

This paper is structured as follows: the governing equations and details of the computational setup including the boundary conditions are given in Section 2, followed by the description of the turbulent boundary layer in Section 3. Then a detailed discussion about the turbulent shear stress, topology of the coherent structures and different components of the turbulent heat-transfer is presented in Sections 4.1, 4.2 and 4.3, respectively. The conclusions of the paper are presented in Section 5.

## 2. Description of the numerical setup

### 2.1. Governing equations

The motion of a Newtonian fluid is governed by the set of equations known as the Navier – Stokes equations (NSE) comprising of the equations of conservation of mass, momentum and total energy. The NSE are non-dimensionalized using the free-stream quantities and the boundary layer thickness at the inlet  $\delta_{in}^*$  as the reference length:

$$\frac{\partial \rho}{\partial t} + \frac{\partial \rho u_j}{\partial x_j} = 0, \quad (1)$$

$$\frac{\partial \rho u_i}{\partial t} + \frac{\partial \rho u_i u_j}{\partial x_j} = -\frac{\partial p}{\partial x_i} + \frac{\partial \tau_{ij}}{\partial x_j}, \quad (2)$$

$$\frac{\partial \rho E}{\partial t} + \frac{\partial (\rho E + p) u_i}{\partial x_i} = -\frac{\partial q_i}{\partial x_i} + \frac{\partial u_i \tau_{ij}}{\partial x_j}, \quad (3)$$

where, density  $\rho = \rho^*/\rho_\infty^*$ , velocity  $u = u^*/u_\infty^*$ , time  $t = t^* \times u_\infty^*/\delta_{in}^*$ , pressure  $p = p^*/(\rho_\infty^* u_\infty^{*2})$  and energy  $E = E^*/u_\infty^{*2}$ . Throughout this paper, the free-stream quantities are marked by the subscript  $\infty$  and the dimensional quantities are marked by the asterisk superscript (\*).

$\tau$  being the symmetric viscous stress tensor, which is given by:

$$\tau_{ij} = \frac{\mu}{Re} \left( \frac{\partial u_j}{\partial x_i} + \frac{\partial u_i}{\partial x_j} - \frac{2}{3} \frac{\partial u_k}{\partial x_k} \delta_{ij} \right). \quad (4)$$

where, viscosity  $\mu = \mu^*/\mu_\infty^*$ , Reynolds number  $Re = \rho_\infty^* u_\infty^* \delta_{in}^*/\mu_\infty^*$  and  $\delta_{ij}$  is the Kronecker delta. The pressure and the heat-flux are computed using

the equation of state and the Fourier law of heat conduction respectively:

$$p = (\gamma - 1) \left( \rho E - \frac{1}{2} \rho u_i u_i \right) = \frac{1}{\gamma M_\infty^2} \rho T, \quad (5)$$

and

$$q = \frac{-\mu}{(\gamma - 1) M_\infty^2 Re Pr} \frac{\partial T}{\partial x_j}. \quad (6)$$

with temperature  $T = T^*/T_\infty^*$ , constant specific heat ration  $\gamma = 1.4$  and Mach number  $M_\infty = u_\infty^*/\sqrt{\gamma R^* T_\infty^*}$  with gas constant  $R^* = 287 \text{ J/Kkg}^{-1}$  and Prandtl number  $Pr = 0.72$ .

The Sutherland's law has been used to calculate the dynamic viscosity:

$$\mu^*(T^*) = \frac{C_1^* T^{*3/2}}{T^* + S^*}, \quad (7)$$

where,  $S^* = 110.4 \text{ K}$  is Sutherland's temperature for air and  $C_1^*$  is a constant,  $1.458 \times 10^{-6} \text{ kg/ms} \sqrt{\text{K}}$  which can be written as:

$$C_1^* = \frac{\mu_r^*}{T_r^{*3/2}} (T_r^* + S^*), \quad (8)$$

where  $\mu_r^*$  is the reference dynamic viscosity of the air,  $1.716 \times 10^{-5} \text{ kg/ms}$  at the reference temperature,  $T_r^*$  of  $273.15 \text{ K}$ . The subscript  $r$  refers to the reference values.

## 2.2. Numerical solver

We have utilized a well validated DNS - LES numerical solver named CHOC-WAVES to solve the three-dimensional, compressible, unsteady NSE for perfect gases. This solver discretizes the convective fluxes by a hybrid conservative sixth-order central scheme with fifth-order Weighted Essential Non-Oscillatory (WENO) scheme (Chaudhuri et al., 2011; Jiang and Shu, 1996). Convective terms are splitted in a skew-symmetric form to minimize the aliasing error and to enforce discrete conservation of the kinetic energy which results in better numerical stability. Approximation of the diffusive terms is done with the fourth or the sixth order formulas, and they are expanded in the Laplacian form. The time integration is performed using the third-order Runge-Kutta (RK-3) scheme. More details on validation can be found in Chaudhuri et al. (2012), Ngomo et al. (2010) and Ben-Nasr et al. (2016).

## 2.3. Problem setup

This study utilizes the supersonic flow over a flat plate with free-stream Mach number  $M_\infty = 2.2$ , temperature  $T_\infty^* = 177 \text{ K}$ , pressure  $p_\infty^* = 23796 \text{ Pa}$  and viscosity  $\nu_\infty^* = 2.55 \times 10^{-5} \text{ m}^2/\text{s}$ . The choice of the Mach number is based on the fact that at higher Mach numbers, the second mode instabilities or the Mack modes (Mack, 1984) dominate the flow and hence the effects of wall heat-transfer could not be distinguished prominently (Shadloo et al., 2016; Shadloo and Hadjadj, 2017; Sharma et al., 2018b). The computational domain is free of the shocks generated at the leading edge of the flat-plate because the inlet is placed downstream of the leading edge at  $x_{in}^* = 0.1016 \text{ m}$  with inlet Reynolds number  $Re_{x_{in}} = 2.33 \times 10^6$  and unit Reynolds number  $Re_{unit}^* = 2.293 \times 10^7/\text{m}$ . The length and the height of the domain are  $L_x^* = 0.15 \text{ m}$  and  $L_y^* = 0.0127 \text{ m}$  respectively. The height of the computational domain is chosen such that the boundary layer thickness towards the end of the domain is approximately one-third of the height of the domain. The spanwise width of the domain is set equal to the fundamental wavelength of the excited mode i.e.  $L_z^* = \lambda_z^* = 0.00605 \text{ m}$  corresponding to the most-unstable mode predicted by the Linear stability theory (LST) (Shadloo et al., 2016; Shadloo and Hadjadj, 2017). Two-point correlations in the spanwise direction are plotted (not shown here) which assure that the periodicity does not affect the generated

**Table 1**

Computational parameters for various test cases. A, C and H stand for the adiabatic, the cooled and the heated walls, respectively. Subscript  $min$  denotes the wall-normal spacing. Superscript  $+$  denotes the quantities in wall-units.  $I$  is the disturbance amplitude of blowing and suction ( $I = v_{wall,max}^*/u_\infty^*$ ).

Cases	$T_w^*/T_{aw}^*$	$I(\%)$	$\omega^*$ (krad/s)	$\Delta x^+$	$\Delta y_{min}^+$	$\Delta z^+$
A0 (Shadloo et al., 2016)	1.00	2.4	150	5.52	0.34	2.85
A	1.00	2.4	150	5.52	0.34	3.26
C	0.75	2.4	150	8.11	0.50	4.78
H	1.50	2.4	150	3.30	0.20	1.95

turbulence. Uniform mesh spacing is used in both the streamwise and the spanwise directions with  $N_x = 4096$  and  $N_z = 280$  being the number of points in the given directions. However, in the wall-normal direction ( $N_y = 150$ ), points are more concentrated close to the wall in order to resolve the boundary layer. The stretching function in the wall-normal direction is given by:

$$y^* = L_y^* \frac{1 + \tanh(\kappa_0 y^*)}{\tanh(\kappa_0)}, \quad (9)$$

with,  $\kappa_0 \approx 3$  being the stretch parameter.

Details about various DNS cases under investigation are enlisted in Table 1. In this table, A, C and H stand for the adiabatic, cooled and heated walls respectively. As seen in Table 1, constant excitation frequency i.e.  $\omega^* = 150 \text{ krad/s}$  (or  $23.87 \text{ kHz}$ ) is chosen for the blowing and suction strip for all the cases which corresponds to the most-unstable frequency according to the LST (Shadloo et al., 2016; Shadloo and Hadjadj, 2017). Moreover, the perturbation intensity is kept high i.e. 2.4% of the free-stream velocity in order to strongly excite the boundary layer, so that the turbulent boundary layer exists in the majority of the computational domain ( $> 50\%$ ).

### 2.3.1. Boundary conditions

Fig. 1 represents a schematic the computational domain and the boundary conditions. At the inlet of the domain, the streamwise and the wall-normal velocities, as well as the density profile are set to the laminar Blasius profile, without any disturbance. These profiles are calculated using a dedicated solver to obtain similarity solutions for adiabatic and isothermal compressible laminar boundary layers which utilizes the Illingworth transformation (White and Corfield, 2006; Masatsuka, 2009). The boundary layer thickness at the inlet of the domain  $\delta_{in}^*$  for A, C and H cases are  $4.44 \times 10^{-4} \text{ m}$ ,  $3.91 \times 10^{-4} \text{ m}$  and  $4.86 \times 10^{-4} \text{ m}$  respectively. For the adiabatic case, the wall temperature  $T_w^* = T_{aw}^*$  (adiabatic wall temperature), while for cooled and heated walls the temperature is set as  $T_w^* = 0.75 T_{aw}^*$  and  $T_w^* = 1.5 T_{aw}^*$  respectively, where  $T_{aw}^* \approx 1.82 T_\infty^*$ .  $T_{aw}^*$  is calculated using the recovery factor approximation  $Pr^{1/3}$ , (White and Corfield, 2006):

$$T_{aw}^* = T_\infty^* \left( 1 + Pr^{1/3} \times \frac{\gamma - 1}{2} \times M_\infty^2 \right) \quad (10)$$

Supersonic inflow and outflow boundary conditions are imposed at the inlet ( $x_{in}^*$ ) and at the outlet ( $x_{out}^* = x_{in}^* + L_x^*$ ) respectively. The side-walls of the domain are periodic and for the upper face of the domain, zero boundary-normal gradient is imposed. No-slip and no-penetration condition is used for at the surface of the wall ( $y = 0$ ), except for the narrow strip of blowing and suction existing between  $x_a^* = x_{in}^* + 0.0127 \text{ m}$  to  $x_b^* = x_{in}^* + 0.0254 \text{ m}$ . The wall-normal component of the velocity in the blowing and suction strip is prescribed by the single-frequency and multiple-spanwise wavenumber boundary condition given as:

$$v^*(x, y = 0, z, t) = I u_\infty^* f(x) \left[ \frac{g(z)}{\max(g(z))} \right] \left[ \frac{h(t)}{\max(h(t))} \right], \quad (11)$$

where  $I$  is the disturbance amplitude,  $f(x)$ ,  $g(z)$  and  $h(t)$  are the

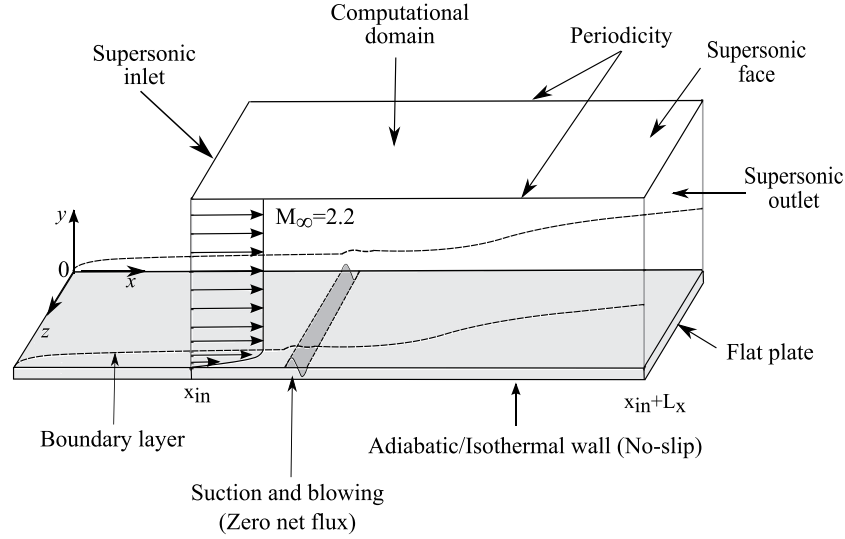


Fig. 1. Computational domain and boundary conditions.

streamwise, spanwise and time-dependent variations respectively, defined as:

$$f(x) = 4 \sin \theta (1 - \cos \theta) / \sqrt{27}, \quad (12)$$

$$g(z) = \sum_{l=1}^{l_{\max}} Z_l \sin(2\pi l(z^*/L_z^* + \phi_l)), \quad (13)$$

$$h(t) = \sum_{m=1}^{m_{\max}} T_m \sin(\omega^* t^* + \phi_m). \quad (14)$$

Here,  $\omega^*$  is the fundamental frequency of the induced disturbance,  $\theta = 2\pi(x^* - x_a^*)/(x_b^* - x_a^*)$ , and  $\phi_l$  and  $\phi_m$  are the random numbers between 0 and 1. The random numbers are generated using the FORTRAN subroutines of RANDOM\_NUMBER and RANDOM\_SEED which generate the pseudo-random numbers with uniform distribution between 0 and 1.  $\sum_{l=1}^{l_{\max}} Z_l = 1$ ,  $Z_l = 1.25Z_{l-1}$ , with  $l_{\max} = 20$  and  $\sum_{m=1}^{m_{\max}} T_m = 1$ ,  $T_m = 1.25T_{m-1}$ , with  $m_{\max} = 20$ . The above mentioned methodology for generating fully developed turbulent boundary layer is a modified version of the method used by Pirozzoli et al. (2004). This methodology has been used by Shadloo et al. (2016) and Shadloo and Hadjadj (2017), and their results present good agreement with the turbulent boundary layer results of Shadloo et al. (2015) (cf. Figs. 4 and 8 in Shadloo and Hadjadj, 2017).

### 3. State of the turbulent boundary layer

Fig. 2 represents the evolution of the compressible and the incompressible skin-friction coefficients  $C_f$  and  $C_{f,inc}$  (averaged in time and the spanwise direction) in the domain for all the cases under consideration. In this study, we would regard the maximum value of  $C_f$  to mark the beginning of the fully developed turbulent region.  $C_f$  can be defined as:

$$C_f = \frac{\tau_w^*}{\frac{1}{2}\rho_\infty^* U_\infty^{*2}} \quad (15)$$

where,  $\tau_w^*$  is the shear stress at the wall.

It can be seen from Fig. 2a that the boundary layer begins the transition to turbulence towards the end of the blowing/suction strip because of the high intensity of perturbation, which sets-in the by-pass transition scenario and no secondary instability region (usually marked by the formation of the streaks) is formed. The effect of disturbance is visible in the plot due to the high intensity of perturbation. Moreover, the levels of skin-friction coefficients rise consistently with decreasing

wall-temperature in the transitional and the turbulent parts of the domain, because of the increasing local density close to the wall. More details regarding the effects of various physical parameters on the onset of transition can be found in Sharma et al. (2018b,a). However, a contrasting trend is observed in case of the incompressible  $C_{f,inc}$  (see Fig. 2b). These trends agree well with the findings reported by Shadloo et al. (2016) and Shadloo and Hadjadj (2017).

Empirically, the compressible skin-friction coefficient for the laminar regime (marked by ..... in Fig. 2a) is given by White and Corfield (2006):

$$C_{f,lam} = 0.664 \times \frac{\sqrt{\rho_w^* \mu_w^* / \rho_\infty^* \mu_\infty^*}}{\sqrt{Re_x}} \quad (16)$$

while the analytical relation for the incompressible skin-friction coefficient for the fully developed turbulent region can be given as (Shadloo et al., 2016):

$$C_{f,inc(turb)} = 0.074 \times \sqrt{\frac{\rho_{aw}^*}{\rho_w^*}} \times Re_x^{-0.2} \quad (17)$$

Hence, it can be seen in Fig. 2a that the fully developed turbulent region starts from  $Re_x = 3.42 \times 10^6$ ,  $Re_x = 3.46 \times 10^6$  and  $Re_x = 3.57 \times 10^6$  for cooled, adiabatic and heated walls, respectively. Fig. 3 displays the instantaneous flow visualizations of different cases showing the existence of the turbulent region in the majority of the domain.

Frequency spectra for the adiabatic case in the middle of the domain i.e. at  $z^*/\delta_{in}^* = 7$  and  $y^+ = 90$  at different streamwise locations;  $Re_x = 3.02 \times 10^6$ ,  $3.94 \times 10^6$  and  $5.40 \times 10^6$  along with the -5/3rd slope of turbulence decay are plotted in Fig. 4a–c. It can be clearly seen in these spectra plots that as we move from the transition region to the fully developed turbulent regime, the excitation frequency (23.87 kHz) does no longer remain prominently visible in the frequency spectrum. Therefore, it can be stated that the resulting turbulent statistics are not affected by the forcing frequency of the blowing and suction strip. Fig. 4d shows the comparison of the Van-Driest transformed velocity profiles at  $Re_x = 5.40 \times 10^6$  for the adiabatic case vs. Shadloo et al. (2015) revealing the existence of fully developed turbulent flow because the viscous sublayer and the logarithmic regions are distinctly visible.

### 4. Joint probability density function and covariance integrands analyses

In this section, we will extensively employ the JPFD distribution and

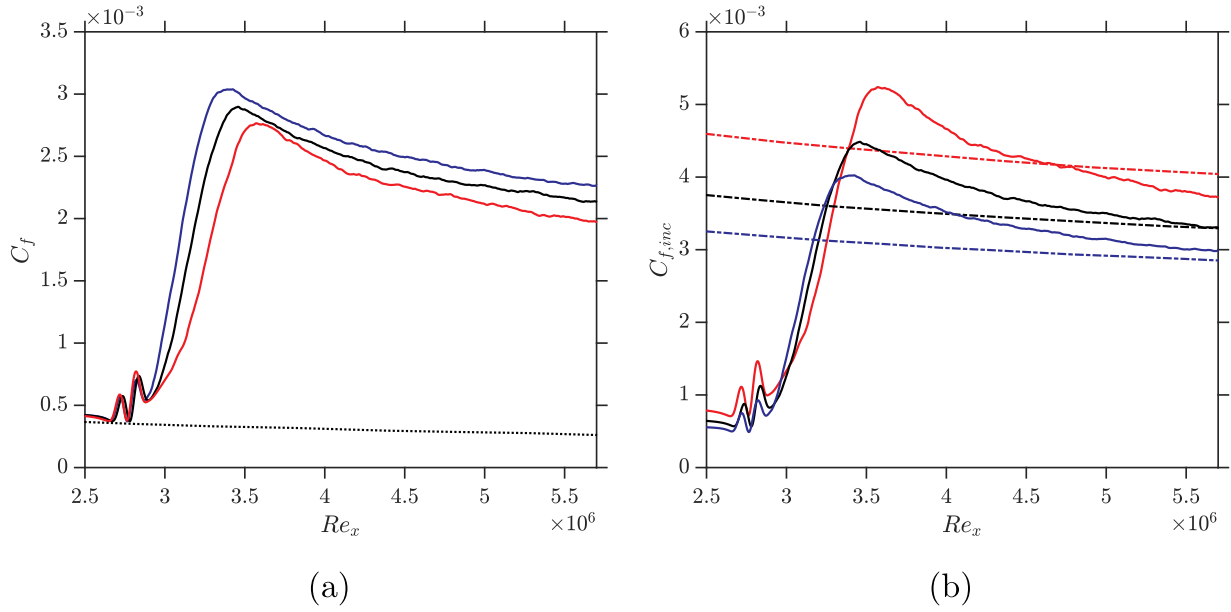


**Fig. 2.** Streamwise evolution of (a) compressible, and (b) incompressible skin-friction coefficients as a function of  $Re_x$  for cooled (—), adiabatic (—) and heated (—) cases. Here, (.....) is  $(C_{f,lam} = 0.664 \times \frac{\sqrt{\rho_w \mu_w^* / \rho_\infty \mu_\infty^*}}{\sqrt{Re_x}})$  and (---) is  $(C_{f,inc(turb)} = 0.074 \times \sqrt{\frac{\rho_w^* \mu_w^*}{\rho_w}} \times Re_x^{-0.2})$  lines represent the theoretical curves for the laminar and the turbulent regimes respectively.

the covariance integrand analyses for investigating different properties affecting the flow topology of the supersonic turbulent boundary layers. These analyses would be used to describe various structural and dynamical aspects of the vortical structures and also to get a deeper insight about the physical mechanisms contributing the most to the turbulent shear-stress and the turbulent heat-flux. Both the JPDFs and the covariance integrands are plotted using the same bin size. It is to be noted that the results are reported for a fixed streamwise location in the fully turbulent part of the domain i.e. at  $Re_x = 5.40 \times 10^6$ . A grayscale color palette is used to represent the levels of the contours ranging from white (the minimum value) to black (the maximum value).

#### 4.1. Velocity fluctuations

**Fig. 5** depicts the contour plots of the JPDF distribution of the fluctuations of the streamwise ( $u'^*$ ) and wall-normal ( $v'^*$ ) velocity components scaled by the local friction velocity  $u_\tau^* = \sqrt{\tau_w^* / \rho_w^*}$  at various  $y^+$  locations. In this figure,  $u' = u'^* / u_\tau^*$  and  $v' = v'^* / u_\tau^*$ .

**Table 2** enlists the peak locations for the cases mentioned in **Fig. 5** (marked by the yellow \*). The JPDF contours point out that the distribution of the  $v'$  is confined to a very small area in the buffer layer i.e.  $y^+ = 10$ , hence, the distribution is quite flat (**Fig. 5a-c**). A comparison of **Fig. 5a-c** shows that, for the near-wall region, the peak tends to move towards zero (see first row of **Table 2**) with increasing wall-temperature confirming the presence of the accelerated flow due to the increase in

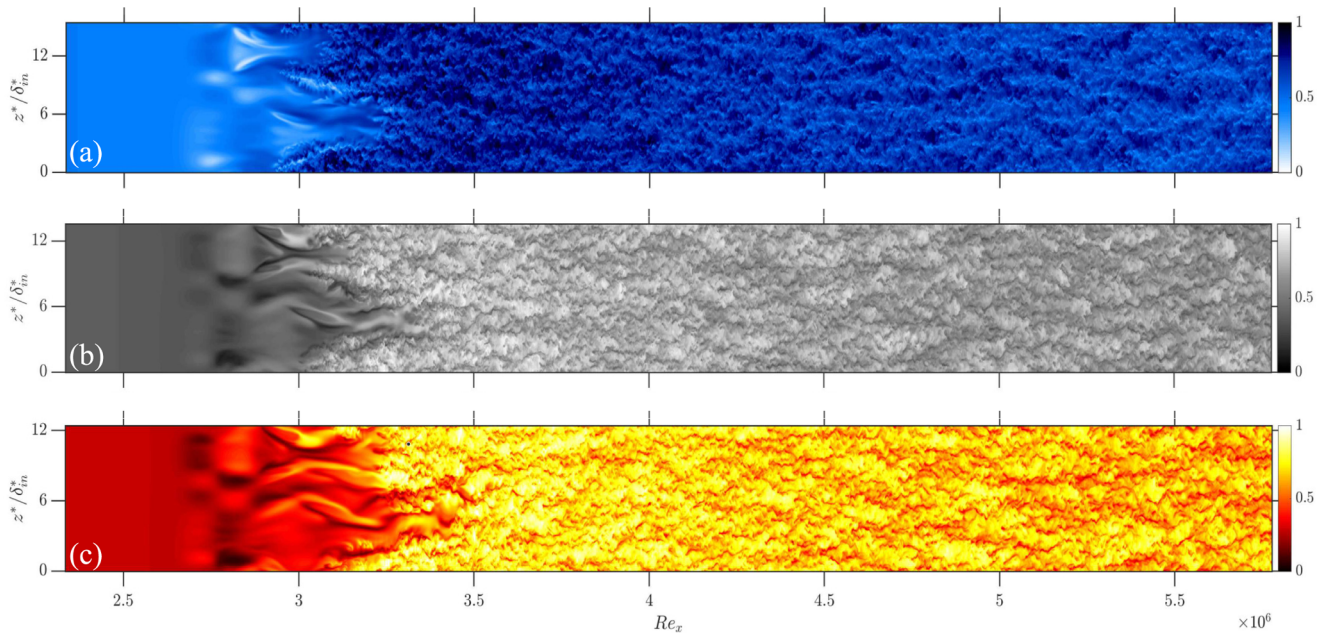


**Fig. 3.** Instantaneous flow fields for (a) cooled, (b) adiabatic and (c) heated walls: contours of  $u^*/u_\infty^*$ , shown at  $y^*/\delta_m^* = 0.29$ .

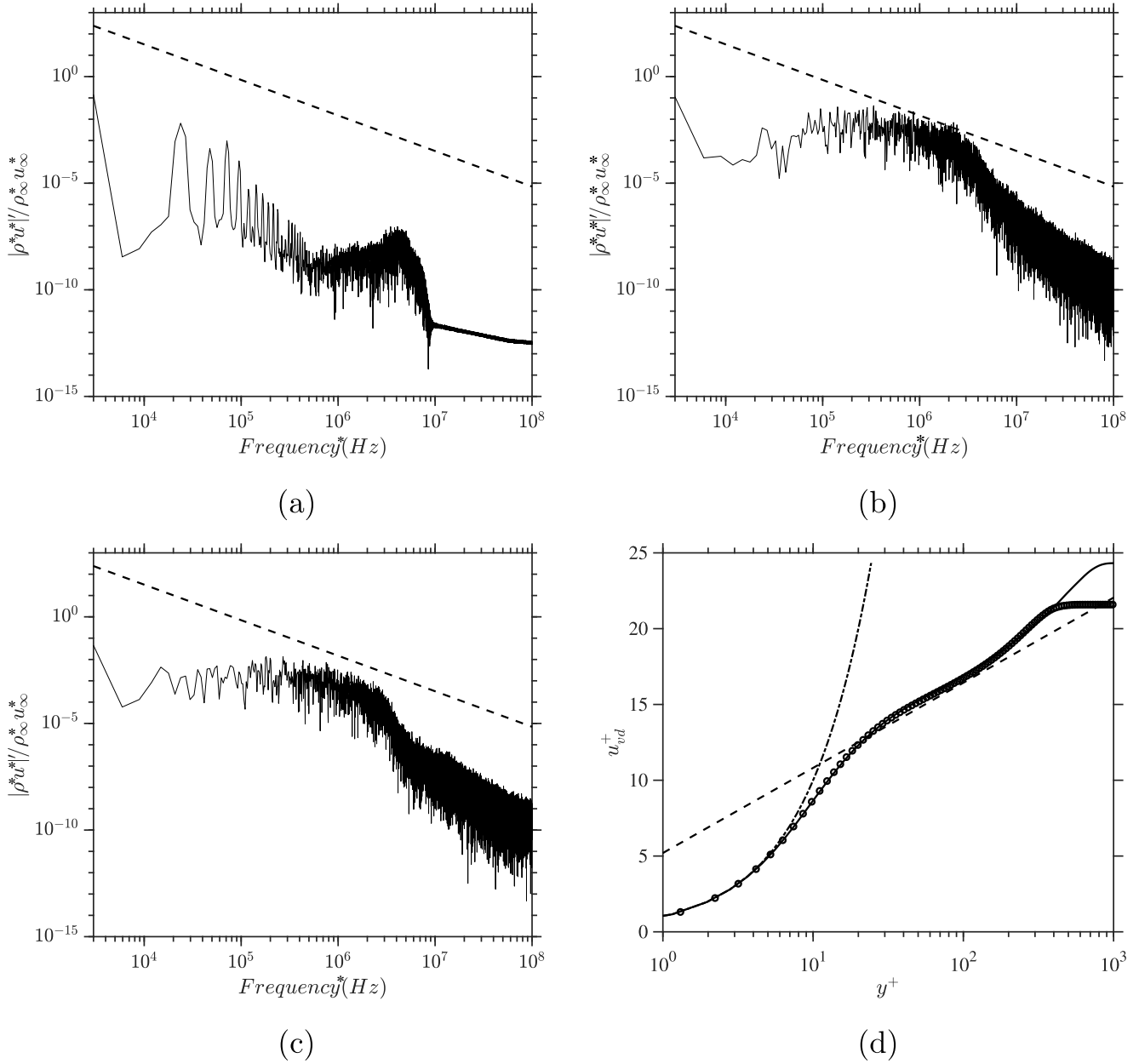


**Fig. 4.** Frequency spectra of  $|\rho^*u^*'|/\rho_\infty^*u_\infty^*$  for the adiabatic wall at (a)  $Re_x = 3.02 \times 10^6$ , (b)  $Re_x = 3.94 \times 10^6$ , (c)  $Re_x = 5.40 \times 10^6$ ; where (—) represents the  $(-5/3)$  law of turbulence decay, and (d) Van-Driest transformed mean velocity profile for the adiabatic case compared with (Shadloo et al., 2015) (symbols) at  $Re_x = 5.40 \times 10^6$ , where (—) is  $(1/0.41 \log y^+ + 5.2)$  and (---) is  $u_{vd}^+ = y^+$ .

the momentum transfer process. Moreover, the peak locations marked in the first row of Table 2 show negligible effects of the wall-temperature on the  $v'$  which is due to the strong viscous forces close to the wall. Similar behavior has been reported by Wallace and Brodkey (1977) in case of the incompressible turbulent boundary layer. The comparison of the first and the second rows of Fig. 5, reveals that on moving from the buffer layer to the log-region i.e.  $y^+ = 10$  to 35, the peak moves in the direction of the fourth quadrant which means that an increasing amount of fast moving flow going towards the wall (more details on the quadrant analysis will follow subsequently). However in the log-region, at  $y^+ = 90$  (Fig. 5g-i), the positions of the peaks do not show a prominent variation (also see the third row of Table 2) with respect to the wall-temperature. This means that the effects of the wall-temperature are confined to the near-wall region only. On comparing Fig. 5d to f with Fig. 5g to i, it can be observed that the distribution of  $v'$  grows more rapidly and dramatically with increase in  $y^+$  as the wall

temperature increases. This trend of growth mechanism shows an increased amount of wall-normal fluctuations in the log region with increasing wall-temperature, which generates higher levels of the turbulent shear-stress in the heated case. It should be noted here that the JPDF distribution tends to align its major axis with the corresponding dominant quadrants. From our discussion of this set of figures, it can be said that impact of wall heat transfer on the distribution of  $u'$  and  $v'$  can be seen predominantly in the buffer layer region.

In order to have a better insight about the flow topology, we would now use the quadrant analysis previously reported in Wallace et al. (1972), Wallace and Brodkey (1977) and Willmarth and Lu (1972). The quadrant analysis of the contour plots of the covariance integrands provides a better understanding of various physical phenomena related to the corresponding quantities. Each quadrant represents a particular transfer process and the dominant quadrant represents the most influential of these. The turbulent shear-stress

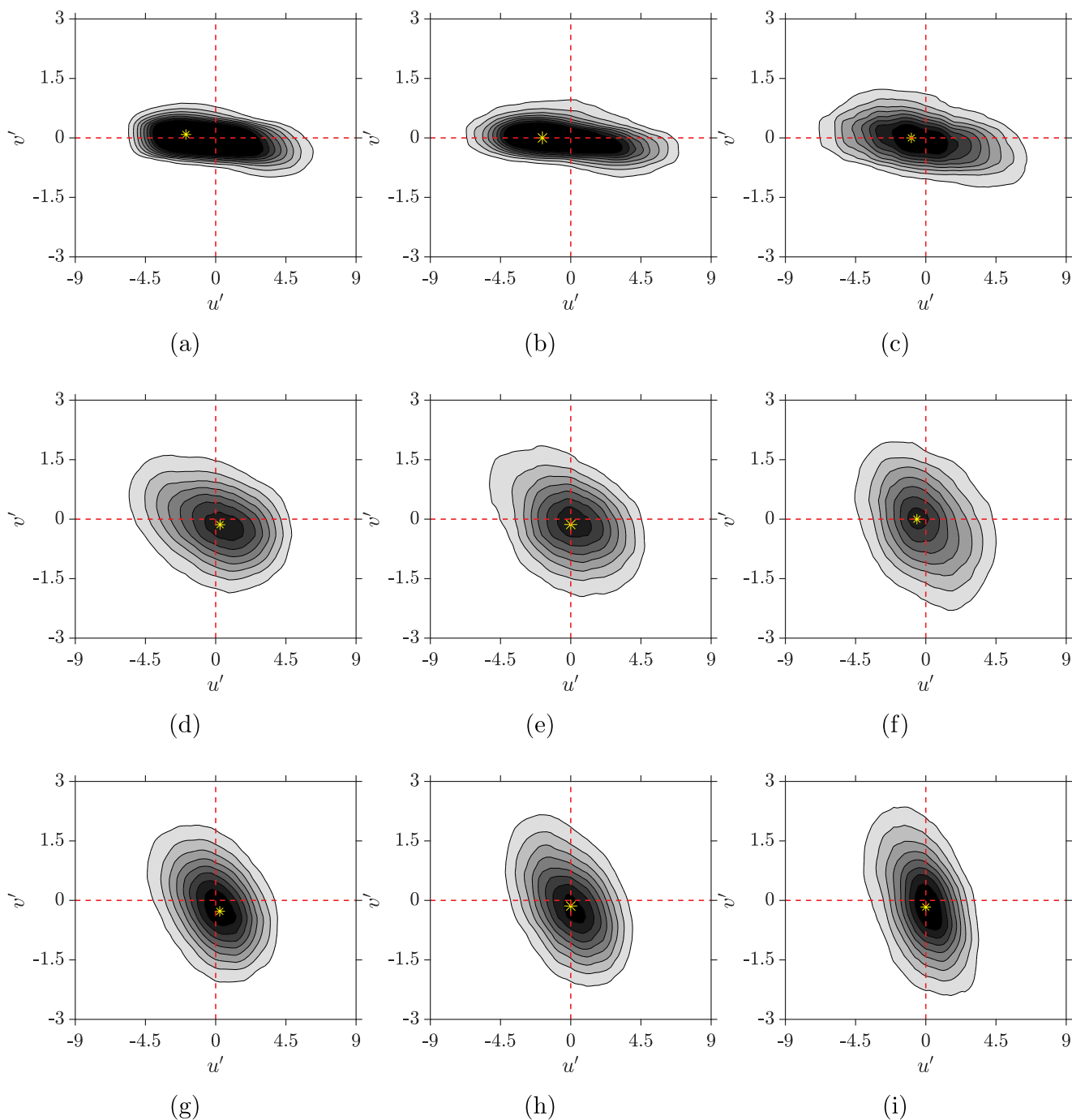


Fig. 5. Contours of the joint probability density function (JPDF) distribution of the  $u'$  and  $v'$  at  $y^+ = 10$  ((a)–(c)), 35 ((d)–(f)) and 90 ((g)–(i)). The colors of the contour levels vary from 1 to 8 (light to dark). Here the first, second and third columns represent the cooled, adiabatic and heated walls, respectively. (For interpretation of the references to color in this figure legend, the reader is referred to the web version of this article.)

**Table 2**  
Locations of the peaks for different cases shown in Fig. 5. The coordinates are marked as the  $(u', v')$  tuple.

$y^+$	C	A	H
10	(-1.906, 0.086)	(-1.815, 0.000)	(-0.926, 0.000)
35	(0.280, -0.139)	(0.000, -0.135)	(-0.571, 0.000)
90	(0.264, -0.276)	(0.000, -0.142)	(0.000, -0.166)

covariance,  $\overline{u'v'}$  can be written as

$$\overline{u'v'} = \int \int_{-\infty}^{\infty} u'v'P(u', v')du'dv', \tag{18}$$

where,  $P(u', v')$  is the joint probability density function of the  $u'$  and  $v'$  over a bin area of  $du'dv'$  and the quantity  $u'v'P(u'v')$  is known as the covariance integrand.

The contour plots of the covariance integrands of  $u'v'$  represent the contribution of signs and magnitude of a given component of velocity i.e.  $u'$  or  $v'$  towards the turbulent shear-stress covariance,  $\overline{u'v'}$ . The first quadrant ( $Q_1$ ), where  $u' > 0$  and  $v' > 0$ , represents the outward interactions. The second quadrant ( $Q_2$ ), where  $u' < 0$  and  $v' > 0$ , represents the events of ejections. The third quadrant ( $Q_3$ ), where  $u' < 0$  and

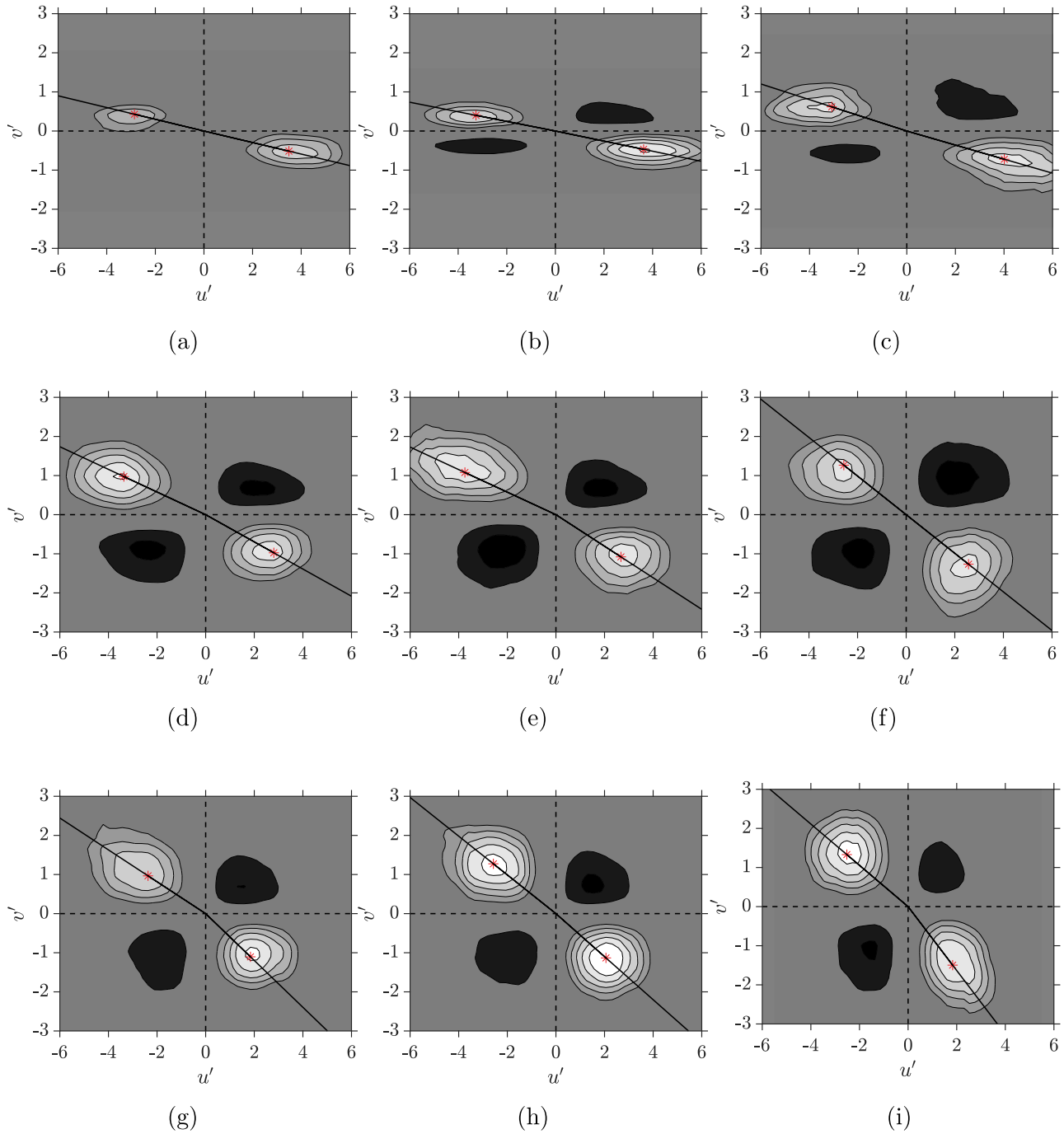


**Fig. 6.** Contours of the covariance integrands of the  $u'$  and  $v'$  at  $y^+ = 10$  ((a)–(c)), 35 ((d)–(f)) and 90 ((g)–(i)). The colors of the contour levels vary from -8 to 2, excluding the zero level (light to dark). Here the first, second and third columns represent the cooled, adiabatic and heated walls, respectively. (For interpretation of the references to color in this figure legend, the reader is referred to the web version of this article.)

$v' < 0$ , represents the inward interactions, and the fourth one ( $Q_4$ ), with  $u' > 0$  and  $v' < 0$ , represents the sweeps (Wallace and Brodkey, 1977; Willmarth and Lu, 1972; Li and Xi-Yun, 2011).

Fig. 6 represents the contour plots of the covariance integrands of the  $u'$  and  $v'$  for the corresponding  $y^+$  positions mentioned in Fig. 5. In this figure, dark contours signify the positive contour levels i.e. levels 1 and 2 while the light ones are the negative contour levels (levels -8 to -1, see Fig. 5). The solid black lines in each plot serve as a visual reference for determining the angles of inclination with respect to the positive  $u'$  axis. These lines originate from the origin and pass through the peaks of the most dominant quadrants (marked by the red \*). The

changes in the angles of inclination quantify the shift in the observed physical phenomenon for the corresponding quadrant. At a glance of Fig. 6, it can be said that for all of the cases  $Q_2$  and  $Q_4$  are the dominant quadrants which means that the ejection and sweep mechanisms contribute the most to the turbulent shear stress. For incompressible channel flows, as per the findings of Wallace et al. (1972), the ejections and sweeps contribute more than 100% towards the shear-stress, and additional stress generated is countered by the positive and negative interactions represented by the events of  $Q_1$  and  $Q_3$  respectively. Hence, the results shown in Fig. 6 are in good agreement with their incompressible counterparts. A closer look to this figure reveals that in

the buffer region, at  $y^+ = 10$ , the sweeps are more important in comparison to the ejections in case of the cooled and to some extent for the adiabatic wall (Fig. 6a and b) because there exists an additional lower contour level. This means that the high-speed fluid moving towards the wall is the major contributor to the turbulent shear-stress. However, Fig. 6c suggests that for  $y^+ = 10$ , the ejections and sweeps become comparable for the heated wall. Therefore, it can be said that in the buffer-region, decrease in wall-temperature favors the sweep events. At  $y^+ = 35$  (Fig. 6d–f), it can be seen that the ejection events are dominant for the cooled and the adiabatic walls, whereas for the heated wall, both the ejections and sweeps become comparable, which means that the decreasing wall-temperature favors the ejections. Towards the end of the log-region, at  $y^+ = 90$ , the ejections and the sweeps are comparable for the cases A and H while for the case C sweeps contribute the most towards the shear-stress covariance.

#### 4.2. Vorticity fluctuations

In this section we would talk about the topology and the physical orientation of the coherent structures in the flow field. The JPDF and the covariance integrand contours of the vorticity components shed some light on the flow topology. The alignment of these contours indicates the most-likely orientation of the projections of the coherent structures at that given position in different planes. It should be noted here that this representation is global in nature and reveals the most-likely inclinations of the projections of the coherent structures in three-dimensional sense. The structures present in the turbulent field can have any sense of rotation or they may exist in pairs of counter-rotating vortices which in three-dimensional sense represent a hairpin (or lambda) structure. Other possibilities of flow configuration also exist such as the hairpin forests (Wu and Moin, 2009), or the cane structures (or asymmetrical hairpins) (Li and Xi-Yun, 2011) among others.

Fig. 7 displays the contours of the JPDF distribution of the streamwise and wall-normal vorticity components;  $\Omega_x^*$  and  $\Omega_y^*$  respectively which are normalized by the local vorticity magnitude i.e.  $\Omega_x = \Omega_x^*/\Omega^*$  and  $\Omega_y = \Omega_y^*/\Omega^*$ , where  $(\langle\Omega^*\rangle = \sqrt{\Omega_x^{*2} + \Omega_y^{*2} + \Omega_z^{*2}})$ ,  $\langle\rangle$  represents local time-averaged quantity, and  $\Omega_x^* = \frac{\partial w^*}{\partial y^*} - \frac{\partial v^*}{\partial z^*}$ ,  $\Omega_y^* = \frac{\partial u^*}{\partial z^*} - \frac{\partial w^*}{\partial x^*}$  and  $\Omega_z^* = \frac{\partial v^*}{\partial x^*} - \frac{\partial u^*}{\partial y^*}$ . These contours represent the most probable projections of the coherent structures in the streamwise-wall-normal plane (x-y plane) at some angle to the wall that can vary along the length of the vortical structure (Ong and Wallace, 1998). The orientation of these contours shows the positive correlation between the two quantities which is obvious due to the high-speed of the flow in the streamwise direction. On comparing the first, second and third rows of Fig. 7 it can be stated that the contours' orientation increases in the streamwise direction which is due to the increment in the streamwise velocity with increasing  $y^+$ . Moreover, it can be seen from these figures that the wall-temperature does not have significant impact on the inclination of the contours.

The contours of the covariance integrands of  $\Omega_x$  and  $\Omega_y$  i.e.  $\Omega_x\Omega_yP(\Omega_x, \Omega_y)$  are shown in Fig. 8. It should be noted that, for this quadrant analysis, the physical significance of each quadrant is not the same as stated before for Fig. 6. In this case, the dominant quadrants highlight the most-likely orientation of the vorticity filaments (their projections) at the given locations which contribute to the covariance  $\Omega_x\Omega_y$ . It can be clearly seen from these plots that as a result of the positive correlation between the two quantities,  $Q_1$  and  $Q_3$  are the dominant quadrants here. The orientation of the projections of the vorticity filaments in the (x-y) plane can be given as

$$\alpha = \tan^{-1}\left(\frac{\Omega_y}{\Omega_x}\right) \quad (19)$$

$\alpha$  is the angle made by the peaks of the dominant quadrants ( $Q_1$  and  $Q_3$  here) with respect to the positive  $\Omega_x$ -axis. The solid black lines are marked to serve as a visual aid to estimate the angles of inclination. In

Fig. 8a–c, the white regions surrounding the gray rectangles are the areas with no data. On comparing the inclinations of the vorticity filaments at different  $y^+$  positions, it can be observed that  $\alpha$  is  $54^\circ$ ,  $44^\circ$  and  $38^\circ$  in  $Q_1$  and  $-134^\circ$ ,  $-136^\circ$  and  $-142^\circ$  in  $Q_3$  for  $y^+ = 10, 35$  and  $90$ , respectively for the cooled wall (i.e. Fig. 8a, d and g). This trend suggests that on moving from the buffer layer ( $y^+ = 10$ ) to the log region ( $y^+ = 35$ ), the filaments tend to rotate in the streamwise direction. The same trend is observed for all the three cases when moving from  $y^+ = 10$  to  $35$  (see first two rows of Table 4). However, for the adiabatic wall, the  $\alpha$  is about  $46^\circ$ ,  $41^\circ$  and  $42^\circ$  in  $Q_1$  and  $-139^\circ$ ,  $-144^\circ$  and  $-139^\circ$  in  $Q_3$  respectively. Hence, the adiabatic wall shows subtle variation in the log-region (angles in  $Q_1$ ), this trend is similar to the one reported by Ong and Wallace (1998) for the incompressible turbulent flows (keeping in mind the  $\pm 5^\circ$  error for the bin size used by them). The visual inspection of the orientation and dominance of the quadrants with the literature reveals that the results of both the cooled as well as the adiabatic walls bear close similarities with the results of the compressible flows (Chu et al., 2013) (due to the different  $y^+$  locations reported, a direct comparison is not possible). However, for the heated wall, the inclination angles decrease in the early log region followed by a strong increase i.e.  $42^\circ$ ,  $39^\circ$  and  $48^\circ$  in  $Q_1$  for  $y^+ = 10, 35$  and  $90$ , respectively. This variation in the trend of inclination means that in the log region the wall-normal vorticity component is still on the rise due to increased heat-transfer from the wall. A comparison between the angles of inclination of the second and the third rows of Fig. 8 (see Table 4) reveals that on moving from  $y^+ = 35$  to  $90$ , the vortical filaments tend to orient themselves lesser in the streamwise direction (as evident from the increasing values of  $\alpha$ ) with increasing wall-temperature. Therefore, from our discussion of about this set of figures, it can be stated that the wall temperature affects the usual orientation of the vorticity filaments in the buffer-layer region as well as in the log-region due to the strong heat transfer.

Now, we consider the orientation of the projections of the coherent structures in the x-z plane (streamwise-spanwise plane). Fig. 9 shows the JPDF distribution,  $P(\Omega_x, \Omega_z)$  of the streamwise and the wall-normal vorticity components,  $\Omega_x^*$  and  $\Omega_z^*$ , respectively which are normalized by the time-averaged local vorticity magnitude  $\langle\Omega^*\rangle$  at different  $y^+$  positions for all the three cases (A, C and H), and Table 3 enlists the peak locations for the same cases. It can be seen in these figures that in the buffer layer,  $y^+ = 10$  (Fig. 9a–c) the JPDF contours are somewhat triangular in shape. This triangular shape becomes predominant with increasing wall-temperature which indicates a net increase in the magnitude of  $\Omega_x$  as the wall-temperature rises. As we progress farther from the buffer-layer region ( $y^+ = 10$ ) to the log-region ( $y^+ = 35$ ), the contours start to get more dilated in the  $\Omega_x$  direction irrespective of the wall-temperature, however, the peak remains in the vicinity of zero for the  $\Omega_x$ -axis (see Table 3). The dilatation of the contours gets increased with increasing wall-temperature (Fig. 9a–f) which means that increasing wall-temperature also increases the net magnitude of  $\Omega_x$ . These triangular shapes of JPDF contours imply that the vorticity filaments do not show much inclination in the streamwise direction and the spanwise vorticity component ( $\Omega_z$ ) largely remains negative, meaning that it has the same sign as that of the mean shear. It can be clearly seen from Table 3 that there exists a considerable shift in the location of the peak towards the positive  $\Omega_z$ -axis ( $\approx 50\%$ ) irrespective of the wall-temperature as one moves to the higher  $y^+$  locations which implies a sudden and dramatic increase of the wall-normal vorticity component. This comparison of the peak location also reveals that the shift of the peak locations is less significant with increasing wall-temperature. From Fig. 9, it can be concluded that  $\Omega_z$  is dominant in comparison to  $\Omega_x$  because the location of the peak never changed considerably in the  $\Omega_x$ -axis.

Fig. 10 shows the plots of the contours of the covariance integrand of the  $\Omega_x$  and  $\Omega_z$  at different  $y^+$  locations. The white regions around the dark rectangles in Fig. 10a–d and i are the regions without any data. In the buffer-layer ( $y^+ = 10$ , Fig. 10a–c), no contour levels exist in the  $Q_1$

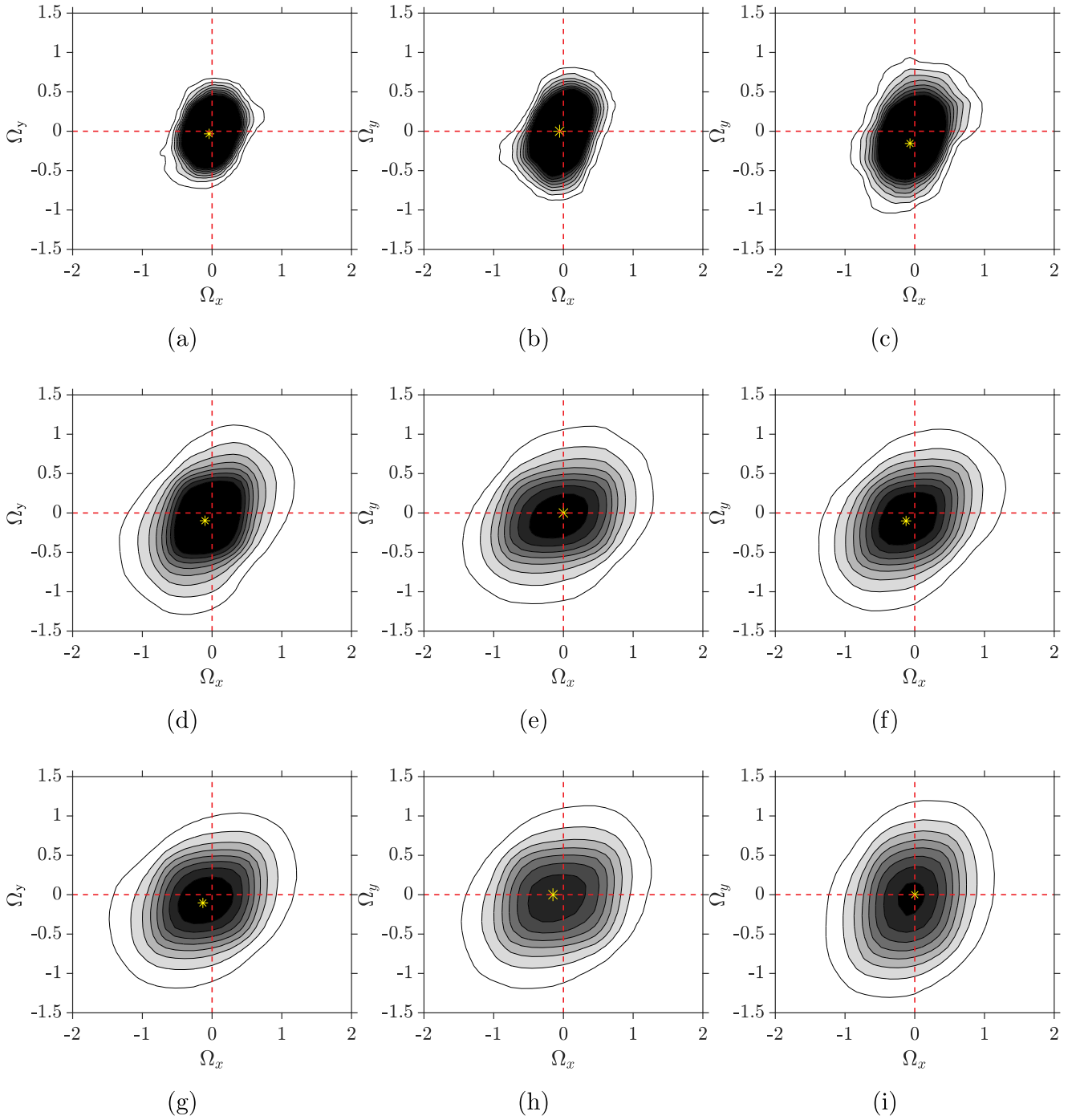


**Fig. 7.** Contours of the JPDF distribution of the  $\Omega_x$  and  $\Omega_y$  at  $y^+ = 10$  ((a)–(c)), 35 ((d)–(f)) and 90 ((g)–(i)). The colors of the contour levels vary from 5 to 40 (light to dark). Here, the first, second and third columns represent the cooled, adiabatic and heated walls, respectively. (For interpretation of the references to color in this figure legend, the reader is referred to the web version of this article.)

nor in the  $Q_2$  which is consistent with Fig. 9a–c which show that the JPDF distribution of  $\Omega_x$  and  $\Omega_z$  exists only in the  $Q_3$  and  $Q_4$ . Therefore, Fig. 10 clearly shows that the  $Q_3$  and  $Q_4$  are the dominant quadrants. The angles of inclination of projections of the vorticity filaments in the  $x$ - $z$  plane (represented by the solid black lines) can be defined as

$$\beta = \tan^{-1}\left(\frac{\Omega_x}{\Omega_z}\right). \quad (20)$$

These inclinations are mentioned here with respect to the negative  $\Omega_z$ -axis. Like before, the counter-clockwise sense is considered as the positive sense of rotation while the clockwise sense is the negative one.

On moving from the buffer-layer to the log-region; from  $y^+ = 10$  to 35, the inclination angles increase for all the cases (see Table 4). Moreover, for these locations, the angles of inclination increase with increasing wall-temperature. For case C, in the buffer layer region, i.e.  $y^+ = 10$  (Fig. 10a), the vortical filament projections are inclined at  $11^\circ$  and  $-13^\circ$  in the  $Q_4$  and  $Q_3$  quadrants, respectively. These low values imply that in the  $x$ - $z$  plane, the coherent structures are primarily oriented in the negative spanwise direction. However, with an increment in the distance from the wall, the filaments tend to rotate in the streamwise direction resulting in the augmentation of the angles of inclination to  $27^\circ$  and  $-31^\circ$  for the  $Q_4$  and  $Q_3$ , respectively at  $y^+ = 35$ , and to  $36^\circ$  and  $-41^\circ$

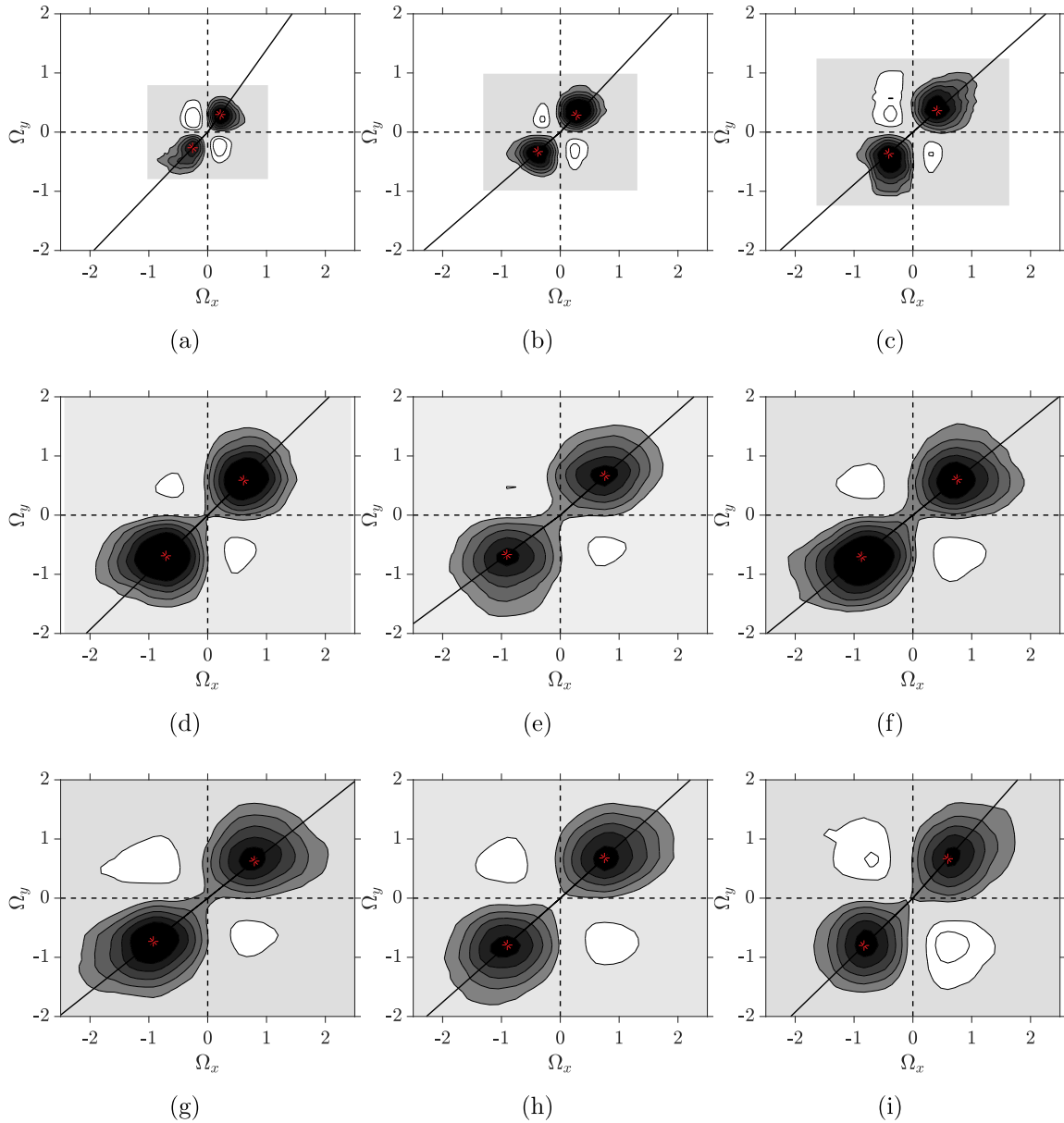


**Fig. 8.** Contours of the covariance integrands of the  $\Omega_x$  and  $\Omega_y$  at  $y^+ = 10$  ((a)–(c)), 35 ((d)–(f)) and 90 ((g)–(i)). The colors of the contour levels vary from  $-0.5$  to  $3$ , excluding the zero level (light to dark). Here the first, second and third columns represent the cooled, adiabatic and heated walls, respectively. (For interpretation of the references to color in this figure legend, the reader is referred to the web version of this article.)

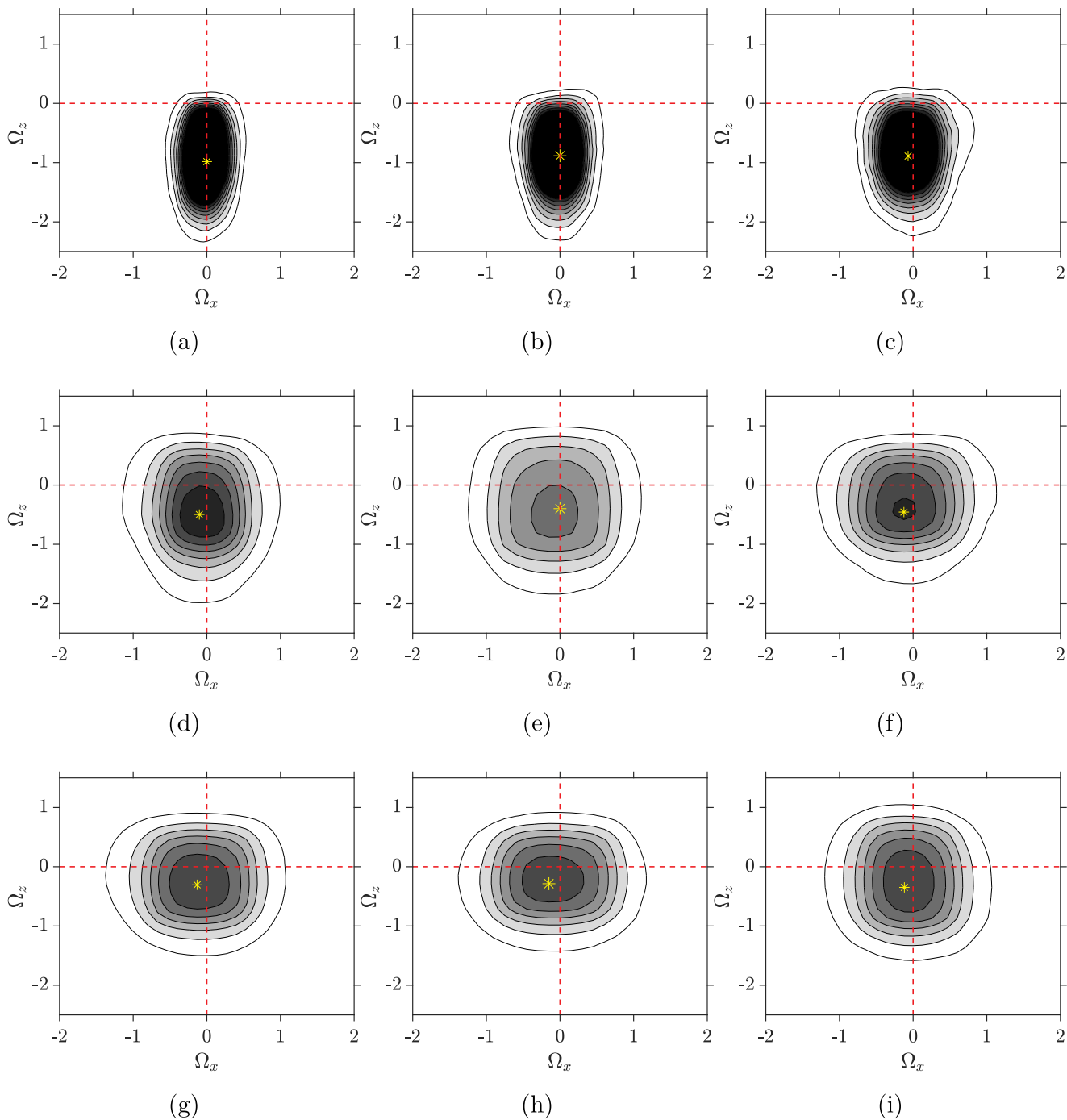
at  $y^+ = 90$ . The same trend is observed for the adiabatic wall as well (see Table 4). Significant differences exist regarding the angles of inclination for the heated wall at different  $y^+$  locations because of the increased transfer processes due to higher wall-temperature. Notably, at  $y^+ = 90$ , the values of  $\beta$  decrease for the heated wall (see Table 4). This can be explained by the JPFD distribution shown in Fig. 9i, which shows a dramatic increase in the distribution of the  $\Omega_z$  as a consequence of the increased wall-temperature. Hence, the distribution of  $\Omega_x$  slightly shrinks. Therefore, it can be said that the wall-temperature affects the topology of the vortical elements in the  $x$ - $z$  plane also in both the buffer-layer and the log-region.

Table 4 enlists all the values of  $\alpha$  and  $\beta$  for all the cases at different  $y^+$  positions, and also brings out the impacts of wall temperature on these angles. From this table, it can be clearly interpreted that the wall-temperature affects the turbulent flow topology in both the buffer-layer as well as the log-region for the SBLs.

#### 4.3. Streamwise velocity component and temperature fluctuations

So far, we have discussed the kinetic aspects of the flow in detail which dealt with the velocity fluctuations and the vorticity components. For this study, we are utilizing different wall temperatures, hence, it becomes vital to investigate the implications of the wall-temperature on the heat-flux. Moreover, in the supersonic regime, the wall-temperature is one of the important factors to be looked into because it is impacted by different physical quantities like the local density and viscosity which themselves are affected by the compressibility.

Fig. 11 shows the JPFD distribution of the streamwise velocity fluctuations ( $u'^*$ ) and the temperature fluctuations ( $T'^*$ ) for all the cases at different  $y^+$  locations, and Table 5 enlists the locations of the peaks for the corresponding cases. In this figure, an additional location in the viscous sub-layer ( $y^+ = 5$ ) is also shown, in order to explore the near-wall region in greater detail. Here, the temperature axis is scaled by the time-averaged local temperature,  $\langle T^* \rangle$  and the velocity by the local friction velocity ( $u_\tau^*$ ). The relation between the  $u'$  and the  $T'$  represents



**Fig. 9.** Contours of the JPDF distribution of the  $\Omega_x$  and  $\Omega_z$  at  $y^+= 10$  ((a)–(c)), 35 ((d)–(f)) and 90 ((g)–(i)). The color of the contour levels vary from 5 to 40 (light to dark). Here the first, second and third columns represent the cooled, adiabatic and heated walls, respectively. (For interpretation of the references to color in this figure legend, the reader is referred to the web version of this article.)

**Table 3**  
Locations of the peaks for different cases shown in Fig. 9. The coordinates are marked as the  $(\Omega_x, \Omega_z)$  tuple.

$y^+$	C	A	H
10	(0.000, -0.983)	(0.000, -0.884)	(-0.068, -0.889)
35	(-0.102, -0.497)	(0.000, -0.398)	(-0.125, -0.456)
90	(-0.132, -0.304)	(-0.150, -0.286)	(-0.119, -0.348)

**Table 4**  
Angles of inclination of the projections of the vorticity filaments for different cases at various  $y^+$  positions.

$y^+$	Cooled wall				Adiabatic wall				Heated wall			
	$\alpha$		$\beta$		$\alpha$		$\beta$		$\alpha$		$\beta$	
	$Q_1$	$Q_3$	$Q_3$	$Q_4$	$Q_1$	$Q_3$	$Q_3$	$Q_4$	$Q_1$	$Q_3$	$Q_3$	$Q_4$
10	54	-134	-13	11	46	-139	-18	14	42	-138	-22	19
35	44	-136	-31	27	41	-144	-37	32	39	-141	-39	34
90	38	-142	-41	36	42	-139	-40	35	48	-136	-34	30

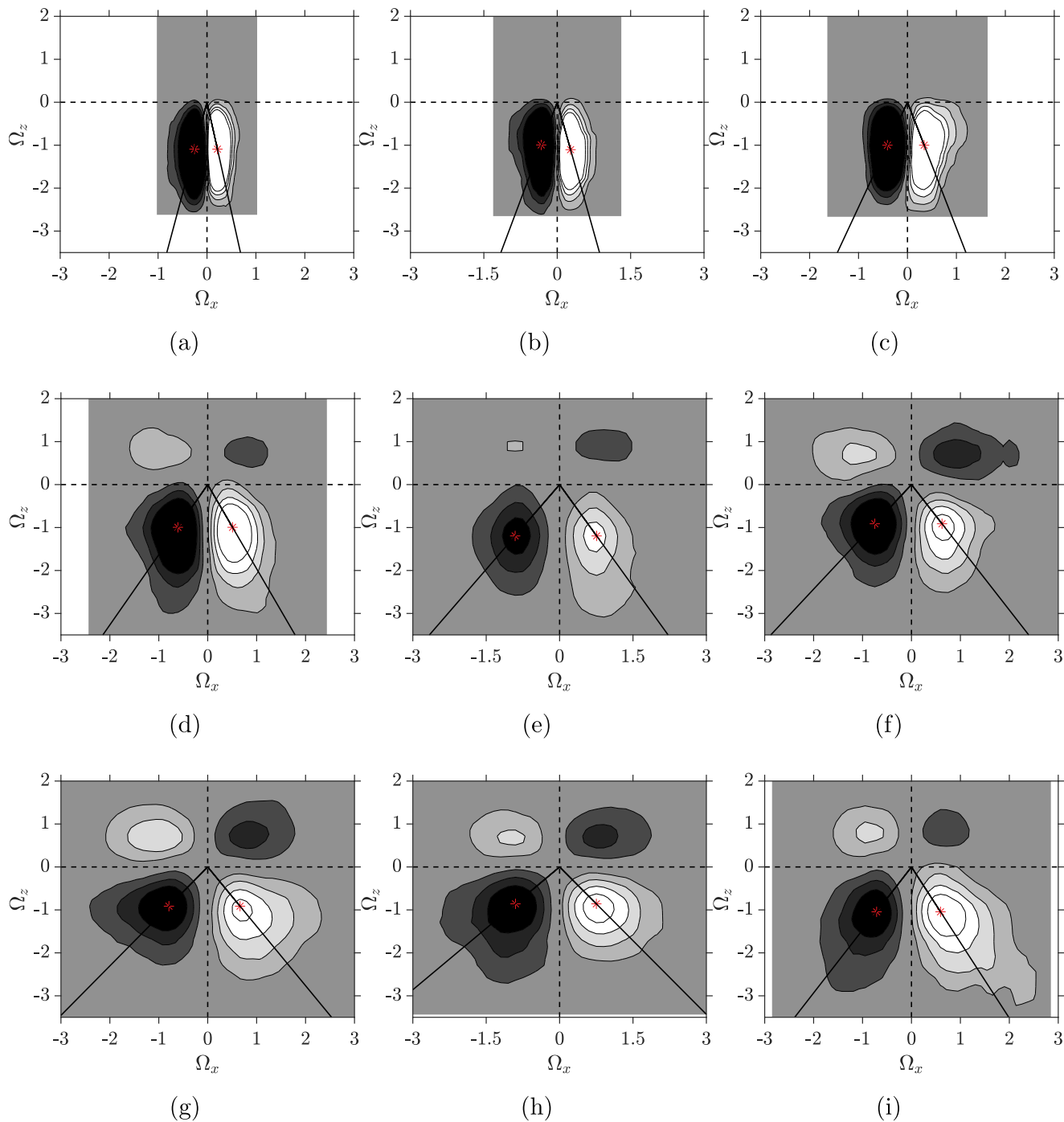


**Fig. 10.** Contours of the covariance integrands of the  $\Omega_x$  and  $\Omega_z$  at  $y^+ = 10$  ((a)–(c)), 35 ((d)–(f)) and 90 ((g)–(i)). The color of the contour levels vary from -2 to 1.5, excluding the zero level (light to dark). Here the first, second and third columns represent the cooled, adiabatic and heated walls, respectively. (For interpretation of the references to color in this figure legend, the reader is referred to the web version of this article.)

the turbulent heat-flux in the streamwise direction. For the rest of the manuscript, the correlation and the anti-correlation between the mentioned quantities refers to the existence of the positive, and the negative slopes respectively of the JPFD contours with the axis of abscissae. A comparison of Fig. 11a to c highlights the effects of the wall-temperature in the viscous sub-layer. It can be seen that in case of the cooled wall, in the viscous sub-layer, the  $u'$  and  $T'$  are directly correlated, while a clear anti-correlation can be seen in case of the adiabatic and the heated walls. This trend has been reported by Duan et al. (2010), Lechner et al. (2001) and Shadloo et al. (2015) for the supersonic turbulent flat plates and the channel flows. This set of figures clearly

reveals a trend of change in the orientation of the major axis of the JPFD contours with increment in the  $y^+$  with respect to the  $u'$  axis. For case C, in the buffer layer region (at  $y^+ = 10$ ), the JPFD contours become parallel to the  $u'$  axis representing a flat distribution. It can be seen from Fig. 11d that the peak of  $u'$  is shifted to the negative side (see first column of Table 5) which implies the existence of the retarded flow in the streamwise direction. On the other hand, the flow is comparatively less retarded for the adiabatic and the heated walls. This clearly indicates that in the buffer-layer region  $y^+ = 10$ , the increasing wall-temperature tends to decrease the deceleration of the flow in the streamwise direction. For the higher  $y^+$ , the  $u'$  and the  $T'$  become anti-

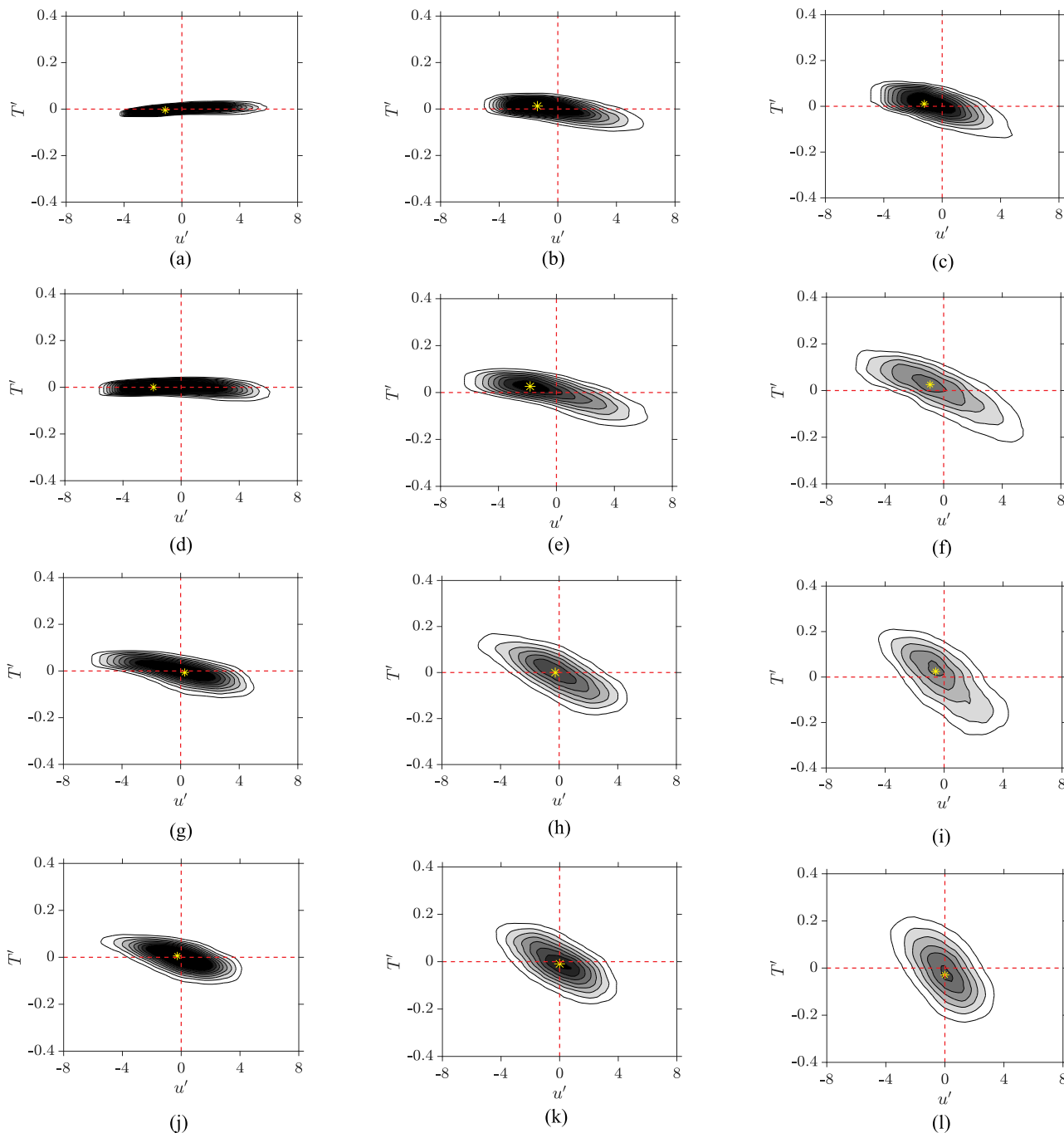


**Fig. 11.** Contours of the JPDF distribution of the  $u'$  and  $T'$  at  $y^+= 5$  ((a)–(c)), 10 ((d)–(f)), 35 ((g)–(i)) and 90((j)–(k)). Here the first, second and third columns represent the cooled, adiabatic and heated walls, respectively. the color of the contour levels vary from 15 to 120 (light to dark). (For interpretation of the references to color in this figure legend, the reader is referred to the web version of this article.)

**Table 5**  
Locations of the peaks for different cases shown in Fig. 11. The coordinates are marked as the  $(u', T')$  tuple.

$y^+$	C	A	H
5	(-1.145, -0.004)	(-1.391, 0.013)	(-1.221, 0.011)
10	(-1.906, -0.000)	(-1.815, 0.026)	(-0.926, 0.026)
35	(0.280, -0.006)	(-0.268, 0.000)	(-0.570, 0.025)
90	(-0.264, -0.006)	(0.000, -0.009)	(0.000, -0.029)

correlated for the cooled wall. However, the adiabatic and the heated cases remain anti-correlated from the viscous sub-layer itself. It can be clearly seen from Fig. 11g–l that in the log-region, for all the cases, the peak location remains very close to zero (see Table 5) which indicates the existence of the homogenous turbulence. This set of figures also clarifies that the increasing wall-temperature favors the anti-correlation between the  $u'$  and the  $T'$ .

The contours of the covariance integrands of the  $u'$  and  $T'$ , i.e.  $u'T'P(u', T')$  are shown in Fig. 12 which represent the contributions of the  $u'$  and the  $T'$  towards the streamwise component of the heat-flux,  $\overline{u'T'}$ . In order to understand the physical phenomena responsible for this

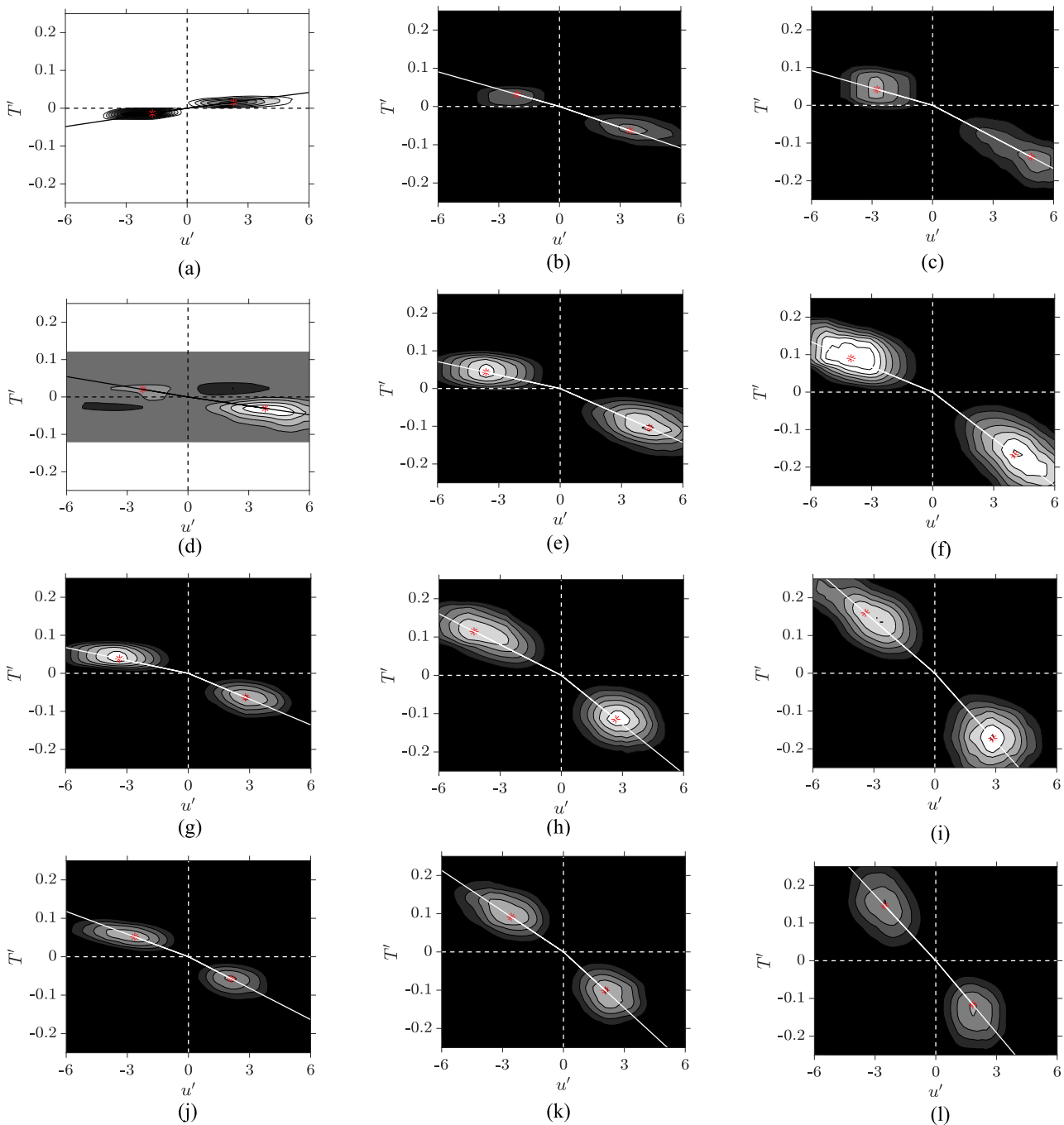


**Fig. 12.** Contours of the covariance integrands of the  $u'$  and  $T'$  for  $y^+ = 5$  ((a)–(c)), 10 ((d)–(f)), 35 ((g)–(i)) and 90((j)–(l)). Here the first, second and third columns represent the cooled, adiabatic and heated walls, respectively. The colors of the contour levels vary from 2 to 9 (light to dark) for (a), from  $-5$  to 2, excluding the zero level for (d) and from  $-16$  to  $-4$  for the rest. (For interpretation of the references to color in this figure legend, the reader is referred to the web version of this article.)

transfer process, we present the following quadrant analysis. The first quadrant ( $Q_1$ ), where  $u' > 0$  and  $T' > 0$ , indicates fast moving heated fluid. The second quadrant ( $Q_2$ ), with  $u' < 0$  and  $T' > 0$ , indicates slow moving heated fluid. The third quadrant ( $Q_3$ ), having  $u' < 0$  and  $T' < 0$ , means that the cooled fluid is moving slower while the fourth quadrant ( $Q_4$ ), where  $u' > 0$  and  $T' < 0$ , denotes the events of fast moving cooled fluid. As can be seen, in all the figures except Fig. 12a where clear dominance of the  $Q_1$  and  $Q_3$  can be seen, the  $Q_2$  and  $Q_4$  are the dominant quadrants owing to the anti-correlation between the  $u'$  and  $T'$ . For the cooled wall, at  $y^+ = 5$  (Fig. 12a),  $Q_3$  is dominant in comparison to  $Q_1$  which means that the slow moving cold fluid contributes

more to the turbulent heat-flux in the streamwise direction than the fast moving hot fluid. In the buffer-layer, at  $y^+ = 10$  (Fig. 12d), where the change in the inclination of the contours is registered, it can be seen that  $Q_4$  is more dominant in comparison to  $Q_2$ , highlighting the fact that fast moving cooled fluid has more contribution towards the streamwise turbulent wall heat-transfer. In case of the adiabatic and the heated walls, it can be seen that the major contribution comes from  $Q_2$  than  $Q_4$ , extending from the viscous sub-layer to the log region. The comparable dominance of the  $Q_2$  and  $Q_4$  implies the existence of homogeneous turbulence towards the outer layer. It can also be observed from these figures that on moving away from the surface of the wall i.e. towards

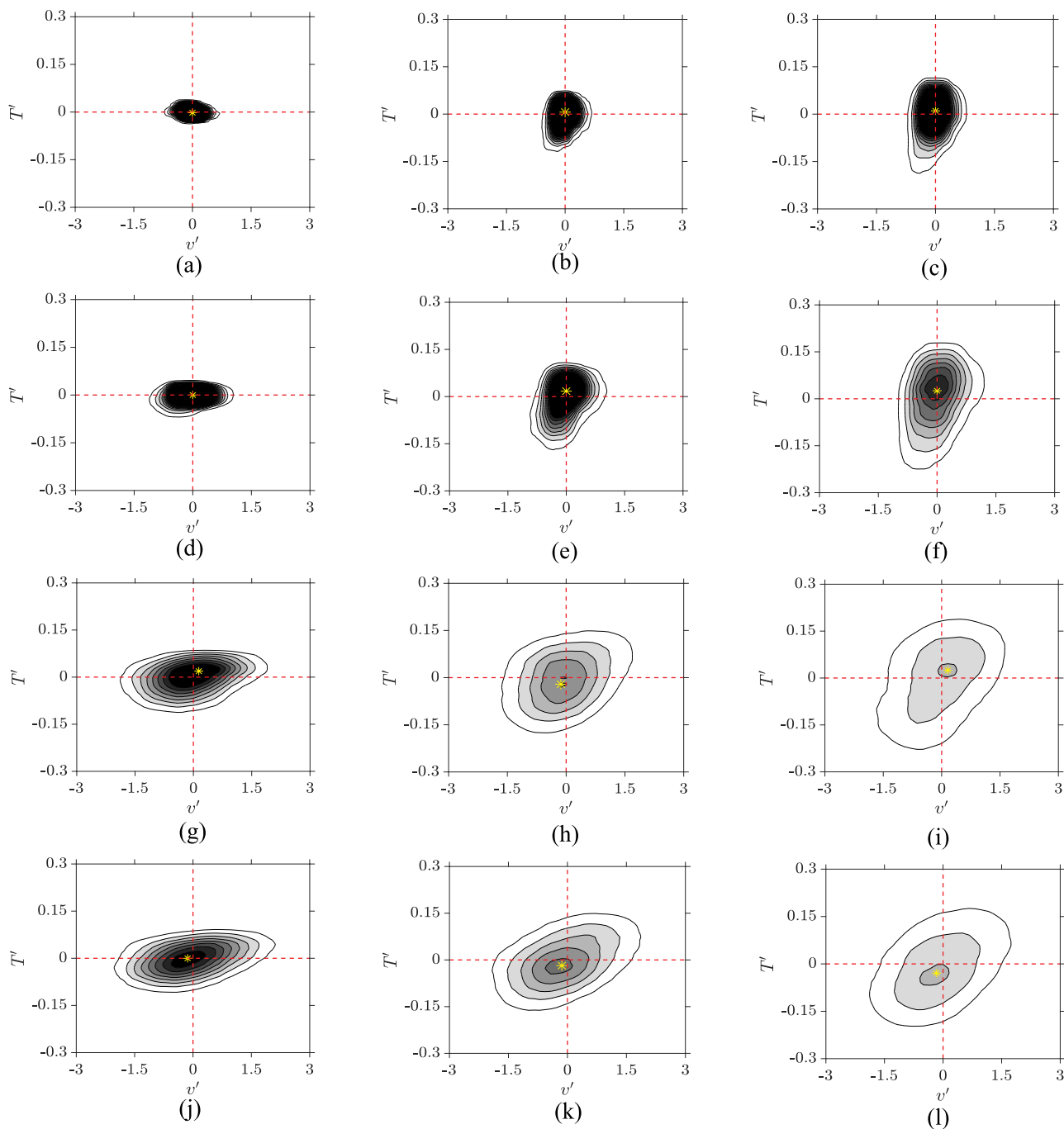


**Fig. 13.** Contours of the JPDF distribution of the  $v'$  and  $T'$  for  $y^+ = 5$  ((a)–(c)), 10 ((d)–(f)), 35 ((g)–(i)) and 90 ((j)–(l)). Here the first, second and third columns represent the cooled, adiabatic and heated walls, respectively. The color of the contour levels vary from 40 to 320 (light to dark). (For interpretation of the references to color in this figure legend, the reader is referred to the web version of this article.)

the higher  $y^+$ , the angles of inclination of the contours also increase because of the increased perturbations. From this comparison we can state that for the cooled wall, the effects of wall temperature on the streamwise turbulent heat-flux can be seen from the viscous sub-layer to the buffer-layer. And, in the log-region, the wall temperature does not have significant effects due to the turbulent mixing happening in the outer layers.

#### 4.4. Wall-normal velocity component and temperature fluctuations

In order to have a complete overview of the heat-transfer phenomenon, we would now focus on the wall-normal component of the

turbulent heat-flux which is given by the covariance of the wall-normal velocity and temperature fluctuations. The contours plots of the JPDF distribution of the wall-normal velocity fluctuations ( $v'^*$ ) and temperature fluctuations ( $T'^*$ ) are shown in Fig. 13. Here, the velocity and the temperature fluctuations are scaled by the local friction velocity ( $u_\tau^*$ ) and the time-averaged local temperature  $\langle T^* \rangle$ , respectively. Likewise in Fig. 11, a comparison between Fig. 13a to c highlights a different trend in case of the cooled wall, as in the viscous sub-layer the quantities  $v'$  and  $T'$  are weakly anti-correlated while they exhibit a subtle correlation for the other two cases (A and H). For case C, on moving towards higher  $y^+$ , we see that at  $y^+ = 10$ , the major axis of the JPDF contours becomes parallel to the  $v'$  axis and the distribution

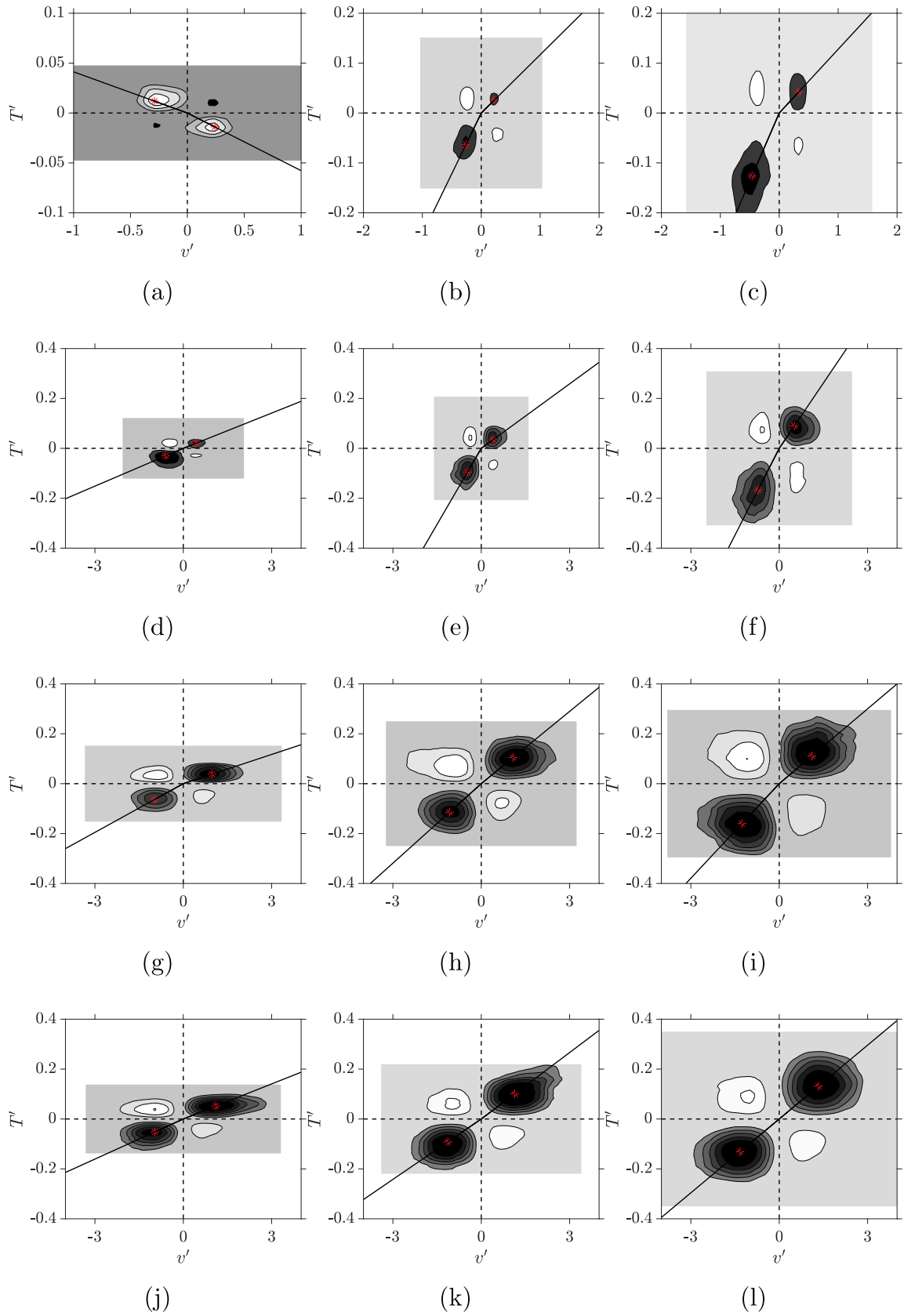


**Fig. 14.** Contours of the covariance integrands of the  $v'$  and  $T'$  at  $y^+ = 5$  ((a)–(c)), 10 ((d)–(f)), 35 ((g)–(i)) and 90 ((j)–(l)). Here, the first, second and third columns represent the cooled, adiabatic and heated walls, respectively. The colors of the contour levels vary from  $-2.5$  to  $1$ , excluding the zero level (light to dark) for (a), from  $-1$  to  $1$ , excluding the zero level for (d) and from  $-3$  to  $6$  for the rest. (For interpretation of the references to color in this figure legend, the reader is referred to the web version of this article.)

becomes flat, and the peak of the contours remains close to the origin. However, in the log region, Fig. 13g and j, the major axis of the contours aligns itself in the  $Q_1$  and  $Q_3$  in an anti-clockwise sense which means that more amount of fluid is going towards the wall. This set of figures shows that for the adiabatic and the heated walls, the quantities  $v'$  and  $T'$  show correlation from the viscous sublayer itself. This means that the effects of temperature on the turbulent boundary layers can be seen from the viscous sublayer to the buffer-layer region. Afterwards, for  $y^+ \geq 35$ , as a result of the turbulent mixing, the differences arising from the wall-temperature are not so significant in terms of the peak position, but the maximum value of the JPFD contours does decrease with increasing wall-temperature.

We would now discuss about the contour plots of the covariance integrand of the  $v'$  and  $T'$  i.e.  $v'TP(v', T')$  in order to reveal the contributions of different physical phenomena towards the turbulent wall-normal heat-flux covariance,  $\overline{v'T'}$ . Following quadrant analysis is presented for the  $v'T'$  plane. The first quadrant ( $Q_1$ ), with  $v' > 0$  and  $T' > 0$ , indicates that the heated fluid is moving away from the wall. The second quadrant ( $Q_2$ ), where  $v' < 0$  and  $T' > 0$ , means that the heated fluid moving down towards the wall. The third quadrant ( $Q_3$ ), with  $v' < 0$  and  $T' < 0$ , highlights the events where cooled fluid moves towards the wall while the fourth quadrant ( $Q_4$ ), with  $v' > 0$  and  $T' < 0$ , indicates the events of the cooled fluid moving away from the wall. The contours of the covariance integrands of the  $v'$  and  $T'$  are shown in Fig. 14 for all the cases at different  $y^+$  locations. Like before, the white region surrounding the gray rectangles represents the region with no data. It should be noted here that in order to have a clear representation, Fig. 14a, and b and c are zoomed-in by four and two times respectively for both the axes with reference to the planes' dimensions used for Fig. 14d-l. It can be seen in Fig. 14 that for all the cases the  $Q_1$  and  $Q_3$  are the dominant quadrants except for Fig. 14a where the  $Q_2$  and  $Q_4$  are dominant. In the viscous sub-layer, at  $y^+ = 5$ , it can be seen that for the cooled wall, the  $Q_2$  is more dominant in comparison to the  $Q_4$  which means that the heated fluid is going towards the wall has more contribution towards the turbulent wall-normal heat-flux which is the reason why the wall is behaving as the heat sink here, as pointed out by Lechner et al. (2001). On the other hand, for the adiabatic and the heated cases, at the same  $y^+$  location (Fig. 14b and c), the  $Q_3$  is more dominant in comparison to the  $Q_1$  which means that the cooled fluid moving towards the wall is the major contributor to the turbulent wall-normal heat-flux. Therefore, in these cases, the wall is acting as a heat source. In the buffer layer,  $y^+ = 10$ , the  $Q_3$  is more dominant than the  $Q_1$  irrespective of the wall temperature. From Fig. 14g-l, it can be seen that in the log region from  $y^+ = 35$  to 90, the  $Q_1$  is more dominant than the  $Q_3$  for all of the cases highlighting that the principal contribution is coming from the events of the  $Q_1$  than the events of the  $Q_3$ . From the observations drawn from this set of figures, it can be concluded that the wall-cooling has significant effect on the heat-transfer mechanisms for the compressible turbulent boundary layer which is clearly highlighted in the near-wall region (up to  $y^+ = 5$ ). In the higher  $y^+$  regions, the physical mechanisms responsible for the heat-transfer do not change significantly with the wall-temperature, but slight variations in their amplitudes are registered. This explains the difference in the levels of the wall-normal Reynolds heat-flux observed for the heated and the cooled walls found by Sharma et al. (2018b).

## 5. Conclusion

Direct numerical simulations (DNS) for the supersonic boundary layers (SBLs) with free-stream Mach number of  $M_\infty = 2.2$  were carried out. Three DNS test cases were investigated in order to unravel the effects of the wall-temperature on the turbulent flow topology for the SBLs. The implications on the important physical parameters like the turbulent shear-stress, the orientation of the projections of the coherent structures in different planes, and different components of the turbulent

heat-flux were analyzed using the joint probability density function (JPFD) distribution and the covariance integrands' analyses.

The results showed that the sweeps were the dominant physical phenomenon majorly contributing to the turbulent shear-stress in the buffer layer. But, for the heated wall, both the ejections and the sweeps became comparable transfer processes. In the log-region, ejections had the dominant contribution to the shear-stress irrespective of the wall-temperature. These trends showed similarities with the findings reported by Wallace et al. (1972) and Ong and Wallace (1998) regarding the adiabatic incompressible boundary layers. The results presented also highlighted different trends for the angles of inclination ( $\alpha$  and  $\beta$ ) of the projections of the coherent structures in case of the heated wall, as a result of the increased heat transfer from the surface of the wall. The trends of  $\alpha$  and  $\beta$  showed good agreement with the compressible and the incompressible counterparts reported in the literature.

The plots of the covariance integrands of the  $u'$  and  $T'$  showed that for the adiabatic and the heated walls, the  $Q_2$  and  $Q_4$  were the dominant quadrants implying the principal contribution of the fast moving cooled fluid towards the streamwise turbulent wall heat-transfer extending from the viscous sub-layer to the log-region. Whereas for the cooled wall, the  $Q_1$  and  $Q_3$  were found to be the major contributors in the viscous sub-layer. A similar contrasting trend was observed for the cooled wall again, for the wall-normal component of the turbulent heat-flux in the viscous sub-layer where the  $Q_2$  had dominance in comparison to the  $Q_4$ , meaning that heated fluid going towards the wall had more contribution towards the turbulent wall-normal heat-flux. For the rest, the  $Q_1$  and  $Q_3$  were the dominant quadrants.

## Acknowledgments

This work was granted access to HPC resources of IDRIS under the allocation 2017-100752 made by GENCI (Grand Equipement National de Calcul Intensif- A0022A10103). The authors acknowledge the access to HPC resources of French regional computing center of Normandy named CRIANN (Centre Régional Informatique et d'Applications Numériques de Normandie) under the allocations 1998022 and 2017002. The funding resources provided from European projects entitled FEDER and NEPTUNE 1 are gratefully acknowledged. Authors would also like to extend their gratitude to both the reviewers whose critical comments helped us to substantially improve the quality of the paper.

## References

- Bechlers, P., Sandberg, R., 2017. Evolution of the velocity gradient tensor invariant dynamics in a turbulent boundary layer. *J. Fluid Mech.* 815, 223–242.
- Bechlers, P., Sandberg, R., 2017. Variation of enstrophy production and strain rotation relation in a turbulent boundary layer. *J. Fluid Mech.* 812, 321–348.
- Ben-Nasr, O., Hadjadj, A., Chaudhuri, A., Shadloo, M., 2016. Assessment of subgrid-scale modeling for large-eddy simulation of a spatially-evolving compressible turbulent boundary layer. *Comput. Fluids*.
- Bensayah, K., Hadjadj, A., Bounif, A., 2014. Heat transfer in turbulent boundary layers of conical and bell shaped rocket nozzles with complex wall temperature. *Numer. Heat Transf. Part A* 66 (3), 289–314.
- Chaudhuri, A., Hadjadj, A., Chinnayya, A., Palerm, S., 2011. Numerical study of compressible mixing layers using high-order weno schemes. *J. Sci. Comput.* 47 (2), 170–197.
- Chaudhuri, A., Hadjadj, A., Sadot, O., Glazer, E., 2012. Computational study of shock-wave interaction with solid obstacles using immersed boundary methods. *Int. J. Numer. Methods Eng.* 89 (8), 975–990.
- Chu, Y.-B., Zhuang, Y.-Q., Lu, X.-Y., 2013. Effect of wall temperature on hypersonic turbulent boundary layer. *J. Turbul.* 14 (12), 37–57.
- Corino, E.R., Brodkey, R.S., 1969. A visual investigation of the wall region in turbulent flow. *J. Fluid Mech.* 37 (1), 1–30.
- Duan, L., Beekman, I., Martin, M., 2010. Direct numerical simulation of hypersonic turbulent boundary layers. Part 2. Effect of wall temperature. *J. Fluid Mech.* 655, 419–445.
- Head, M., Bandyopadhyay, P., 1981. New aspects of turbulent boundary-layer structure. *J. Fluid Mech.* 107, 297–338.
- Jiang, G.-S., Shu, C.-W., 1996. Efficient implementation of weighted eno schemes. *J. Comput. Phys.* 126 (1), 202–228.
- Le, A.-T., Coleman, G.N., Kim, J., 2000. Near-wall turbulence structures in three-

- dimensional boundary layers. *Int. J. Heat Fluid Flow* 21 (5), 480–488.
- Lechner, R., Sesterhenn, J.r., Friedrich, R., 2001. Turbulent supersonic channel flow. *J. Turbul.* 2 (1), 001.
- Li, W., Xi-Yun, L., 2011. Statistical analysis of coherent vortical structures in a supersonic turbulent boundary layer. *Chin. Phys. Lett.* 28 (3), 034703.
- Mack, L.M., 1984. Boundary-Layer Linear Stability Theory. Technical Report. California Inst of Tech Pasadena Jet Propulsion Lab.
- Maeder, T., Adams, N.A., Kleiser, L., 2001. Direct simulation of turbulent supersonic boundary layers by an extended temporal approach. *J. Fluid Mech.* 429, 187–216.
- Masatsuka, K., 2009. I Do Like CFD. PKatate Masatsuka.
- Morkovin, M.V., 1962. Effects of compressibility on turbulent flows. *Méc. Turbul.* 367, 380.
- Ngomo, D., Chaudhuri, A., Chinnayya, A., Hadjadj, A., 2010. Numerical study of shock propagation and attenuation in narrow tubes including friction and heat losses. *Comput. Fluids* 39 (9), 1711–1721.
- Ong, L., Wallace, J.M., 1998. Joint probability density analysis of the structure and dynamics of the vorticity field of a turbulent boundary layer. *J. Fluid Mech.* 367, 291–328.
- Patel, A., Boersma, B.J., Pecnik, R., 2017. Scalar statistics in variable property turbulent channel flows. *Phys. Rev. Fluids* 2 (8), 084604.
- Pirozzoli, S., Bernardini, M., Grasso, F., 2008. Characterization of coherent vortical structures in a supersonic turbulent boundary layer. *J. Fluid Mech.* 613, 205–231.
- Pirozzoli, S., Grasso, F., Gatski, T., 2004. Direct numerical simulation and analysis of a spatially evolving supersonic turbulent boundary layer at  $M = 2.25$ . *Phys. fluids* 16 (3), 530–545.
- Shadloo, M., Hadjadj, A., 2017. Laminar-turbulent transition in supersonic boundary layers with surface heat transfer: a numerical study. *Numer. Heat Transf. Part A* 72 (1), 40–53.
- Shadloo, M., Hadjadj, A., Hussain, F., 2015. Statistical behavior of supersonic turbulent boundary layers with heat transfer at  $M_\infty = 2$ . *Int. J. Heat Fluid Flow* 53, 113–134.
- Shadloo, M.S., Hadjadj, A., Bodony, D.J., Hussain, F., Lele, S.K., 2016. Effects of heat transfer on transitional states of supersonic boundary layers. *Proceedings of Summer Program. Center of Turbulence Research, Stanford University, USA*, pp. 175–184.
- Sharma, S., Shadloo, M., Hadjadj, A., 2018. Effect of thermo-mechanical non-equilibrium on the onset of transition in supersonic boundary layers. *Heat Mass Transf.* 1–13. <https://doi.org/10.1007/s0023>.
- Sharma, S., Shadloo, M.S., Hadjadj, A., 2018. Laminar-to-turbulent transition in supersonic boundary layer: effects of initial perturbation and wall heat transfer. *Numer. Heat Transf. Part A* 73 (9), 583–603. <https://doi.org/10.1080/10407782.2018.1464785>.
- Smits, A.J., Dussauge, J.-P., 2006. *Turbulent Shear Layers in Supersonic Flow*. Springer Science & Business Media.
- Spina, E.F., Smits, A.J., Robinson, S.K., 1994. The physics of supersonic turbulent boundary layers. *Ann. Rev. Fluid Mech.* 26 (1), 287–319.
- Stanislas, M., Perret, L., Foucaut, J.-M., 2008. Vortical structures in the turbulent boundary layer: a possible route to a universal representation. *J. Fluid Mech.* 602, 327–382.
- Theodorsen, T., 1952. Mechanisms of turbulence. *Proceedings of the 2nd Midwestern Conference on Fluid Mechanics*, 1952.
- Trettel, A., Larsson, J., 2016. Mean velocity scaling for compressible wall turbulence with heat transfer. *Phys. Fluids* 28 (2), 026102.
- Wallace, J.M., Brodkey, R.S., 1977. Reynolds stress and joint probability density distributions in the u-v plane of a turbulent channel flow. *Phys. Fluids* 20 (3), 351–355.
- Wallace, J.M., Eckelmann, H., Brodkey, R.S., 1972. The wall region in turbulent shear flow. *J. Fluid Mech.* 54 (1), 39–48.
- White, F.M., Corfield, I., 2006. *Viscous Fluid Flow*. vol. 3 McGraw-Hill New York.
- Willmarth, W., Lu, S., 1972. Structure of the Reynolds stress near the wall. *J. Fluid Mech.* 55 (1), 65–92.
- Wu, X., Moin, P., 2009. Direct numerical simulation of turbulence in a nominally zero-pressure-gradient flat-plate boundary layer. *J. Fluid Mech.* 630, 5–41.

# Chapter 7

## Conclusions and perspectives

---

### 7.1 Conclusions

This research work was performed under the framework of the European project Neptune 1 focused at better understanding of the flow physics of wall-bounded flows. Complex transition scenarios like the O-type breakdown and the by-pass transition in supersonic boundary layer were investigated. Implications of various physical parameters such as the wall temperature, the initial perturbation intensity, and the variations in the baseflow were studied. The study also presented the relevant results regarding the successful control of the O-type breakdown using the streak modes, no experimental or numerical investigation have reported this type of control so far.

The flow solver was validated with the existing DNS results of [Fezer & Kloker \(2000\)](#), [Mayer et al. \(2011\)](#) (O-type breakdown) at  $M_\infty = 2.0$ . The same setup was utilized to demonstrate the successful control of full oblique-type breakdown of a supersonic adiabatic boundary layer using control streaks. The investigated streaks with, in various cases, three to six times the spanwise wavenumber of the fundamental, obliquely running modes and maximal  $\rho u$ -amplitudes of 20% - 10% have been introduced by steady spanwise periodic suction/blowing at the wall within one or two control strips. Generally, higher wavenumbers of the decaying streaks are found to be more effective to suppress the unsteady most amplified fundamental mode (1,1) but need higher initial amplitudes due to a stronger streamwise decay. This can cause a significant shock-like, detrimental steady pressure wave. The oblique-breakdown streak mode (0,2) is not much influenced directly, rather by lowering the oblique travelling modes (1,1) that feed it.

It was found that the spanwise wavelength of effective control streaks lies between 20-25% of the fundamental oblique mode. Modified DNS with suppressed 2-D disturbance parts and thus MFD could show that, for the 3-D part to be effective in growth attenuation, the spanwise wavelength must be smaller than about 2.5 times the local boundary-layer thickness ( $\lambda_{control}^*/\delta^* < 2.5$ ). This value is about the one of modes with optimal transient growth in theory. At the considered Reynolds number,  $Re_x = 2 \times 10^5$ , of the first spanwise suction/blowing control strip, all steady control modes monotonically decay directly downstream of the strip, the stronger the shorter the wavelength is. Starting with the ideal  $\lambda_{control}^*/\delta^*$  would lead to a fast decay of the streaks and no significant control can be achieved. For the streaks found effective on the whole, the ideal  $\lambda_{control}^*/\delta^*$  is reached downstream near  $Re_x = 5.5 - 6 \times 10^5$  when their control  $\rho u$ -amplitudes have decayed from initially about 20% to 10%, but at the same time the beneficial MFD induced falls eventually below 3% and gets inactive. In the first streamwise part downstream of the control strip, the MFD amplitude

ranges from 10%-3%, and the observed oblique-mode suppression is thus solely provided by the MFD. Globally, the MFD and the 3-D part of the control contribute each with a comparable share in the reduction of the fundamental-mode amplitude.

The MFD may become maleficial (locally) if the blowing part is too strong and not pointed enough; generalized inflection points occur in the spanwise-averaged velocity profiles, invoking inviscid instability. In refreshing the control strip downstream, the oncoming low-velocity streaks must not be widened locally which would otherwise trigger transition. The initial penalties in the wall-shear and wall-temperature increase are marginal by the control, shifting their increase by turbulence significantly downstream. Simulations with a broader disturbance spectrum comprising higher spanwise wavenumbers  $k$  and frequencies  $h$ , modes ( $h = 1 - 2, k = 1 - 3$ ) and significantly increased total amplitude show that the basic suppressing mechanisms work also in this case. The additional streak modes generated ( $0, k = 4, 6$ ) are much closer to the control mode and were considered critical a priori, but they do not degrade the control (Sharma, Shadloo, Hadjadj & Kloker 2019).

The DNS investigations regarding the by-pass transition scenario were also performed. Implications of various factors like initial perturbation intensity, and wall heat-transfer on the onset transition were investigated. We tried to quantify the onset and the end of the transition region using different quantities namely streamwise evolution of the skin-friction coefficient, contours of the Reynolds shear stress, contours of the wall-normal Reynolds heat-flux, the modal decomposition and the streamwise evolution of the Stanton number as a function of  $Re_x$ .

It was observed that an increase in the perturbation intensity of blowing and suction shifted the transition onset location upstream for the adiabatic walls. The analyses have predicted an increase in length of the transition region with increasing levels of perturbation. The DNS results of the effects of wall heat-transfer were compared against the predictions of LST (initially reported in Shadloo & Hadjadj (2017)). The results of DNS and LST were in good agreement. It was also found that at low perturbation intensity, i.e. 0.5%, the wall cooling tends to stabilize the flow and it remains laminar, while the wall heating advanced the onset of the transition to turbulence in comparison to the adiabatic wall.

Joint effects of perturbation intensity and wall heat-transfer were analyzed for stronger perturbation intensities of 1% and 2.4%. At 1%, wall-cooling did stabilize the flow and the transition location shifted downstream, but there weren't any significant differences between the heated and the adiabatic walls. As a result of a weaker growth rate for cooled wall, as predicted by the LST, the cooled wall had a longer transition region. But, for the non-linear regime, with 2.4% perturbation intensity, cooling down the wall destabilized the flow and it transitioned upstream as compared to the adiabatic wall. However, heating up the plate resulted in a delayed transition. These results are in agreement with the DNS results obtained by Shadloo et al. (2016), Shadloo & Hadjadj (2017). This behavior is in direct contrast with the one observed for 0.5% showing the limitation of the LST for strongly perturbed flow. The non-linear interactions in the flow could be accounted for this contrasting

trend. It was also observed that the impact of wall cooling was more amplified than wall heating which could be explained by the way in which the perturbation was imposed i.e. by perturbing the  $v$  component at the wall. The product  $\rho v$  should remain constant, but in a compressible regime the density varies. As a result of density variation, the value of this product decreases in the near wall region for heated walls and increases for cooled ones resulting in a difference in the receptivity. Regarding the turbulent part of the domain, it was found that the cooled and the heated walls attain different values of Reynolds analogy factor which differ from the value given by  $Pr^{-2/3}$ . Dimensional analysis revealed that multiplying this value by the product of density and viscosity ratios of the isothermal wall to the adiabatic wall,  $Pr^{-2/3} \times \frac{\rho_w}{\rho_{aw}} \frac{\mu_w}{\mu_{aw}}$  presented a good approximation of the average value of the Reynolds analogy factor attained by both the cooled and the heated walls in the fully turbulent region (Sharma et al. 2018a).

Receptivity of the boundary layer towards the variations in the baseflow was analyzed using the streamwise evolution of skin-friction coefficient, Stanton number and DMD. The cases were investigated for 0.5% and 2.4% perturbation intensities. The results revealed that the existence of the thermo-mechanical non-equilibrium destabilized the flow, and transition onset location was shifted upstream irrespective of the induced intensity of perturbation for heated walls. Moreover, it was also found that the heated walls with thermo-mechanical non-equilibrium had a shorter transition region. From the evolutionary trend of the Stanton number in the streamwise direction, it was clear that despite of the large difference in the values of Stanton number in the laminar part, the heated walls with thermo-mechanical non-equilibrium eventually did attain the thermal equilibrium in the turbulent part of the domain resulting from the turbulent mixing. The cooled walls didn't show any signs of transition and the flow remained laminar throughout the computational domain for 0.5% perturbation intensity. In contrast to the heated wall, for 2.4% perturbation intensity, the existence of the thermo-mechanical non-equilibrium was found to delay the transition onset location, and also a longer transition region was observed for the cooled walls. However, the cooled walls never attained the thermal equilibrium, neither for 0.5% nor for 2.4% perturbation intensities. Moreover, the curves of the streamwise evolution of Stanton number as a function of  $Re_x$  revealed that the cases with thermo-mechanical non-equilibrium had more overshoot than their thermo-mechanical equilibrium counterparts due to the increased amount of heat-transfer (Sharma et al. 2018b).

The results obtained from the DMD analysis show two distinct ways of evolution for the odd and the even harmonics of the forcing frequency. It was found that the evolution of these harmonics was independent of the imposed physical parameters like the wall-temperature or the thermo-mechanical non-equilibrium. However, for the cooled wall with 0.5% perturbation intensity, the modes disappeared towards the end of the domain but the manner of propagation was the same as in the other cases for the corresponding modes. It was also found that the considered mode grew strongly and became dominant in the transition region before eventually breaking down in to smaller structures in the turbulent regime. The

lead and lag in the propagating wavefronts were revealed by the plot of phase angles which uncovered that each propagating mode was comprised of the wavefronts with opposite phase angles (Sharma et al. 2018b).

The DNS investigations for the turbulent supersonic boundary layers were also carried out in order to unravel the effects of wall temperature on the turbulent flow topology for the SBLs. The implications on the important physical parameters like the turbulent shear-stress, the orientation of the projections of the coherent structures in different planes, and different components of the turbulent heat-flux were analyzed using the JPDF distribution and the covariance integrands' analyses (Sharma, Shadloo & Hadjadj 2019).

The results showed that the sweeps were the dominant physical phenomenon largely contributing to the turbulent shear-stress in the buffer layer. But, for the heated wall, both the ejections and the sweeps became comparable transfer processes. In the log-region, ejections had the dominant contribution to the shear-stress irrespective of the wall-temperature. These trends showed similarities with the findings reported by Wallace et al. (1972), Ong & Wallace (1998) regarding the adiabatic incompressible boundary layers. The results presented also highlighted different trends for the angles of inclination ( $\alpha$  and  $\beta$ ) of the projections of the coherent structures in case of the heated wall, as a result of the increased heat transfer from the surface of the wall. The trends of  $\alpha$  and  $\beta$  showed good agreement with the compressible and the incompressible counterparts reported in the literature.

The plots of the covariance integrands of the  $u'$  and  $T'$  showed that for the adiabatic and the heated walls, the  $Q_2$  and  $Q_4$  were the dominant quadrants implying the principal contribution of the fast moving cooled fluid towards the streamwise component of the turbulent wall heat-transfer extending from the viscous sub-layer to the log-region. Whereas for the cooled wall, the  $Q_1$  and  $Q_3$  were found to be the major contributors in the viscous sub-layer. A similar contrasting trend was observed for the cooled wall again, for the wall-normal component of the turbulent heat-flux in the viscous sub-layer where the  $Q_2$  had dominance in comparison to the  $Q_4$ , meaning that heated fluid going towards the wall had more contribution towards the turbulent wall-normal heat-flux. For the rest, the  $Q_1$  and  $Q_3$  were the dominant quadrants.

## 7.2 Perspectives

Taking into account the work presented in this dissertation, many important results were put forward which undoubtedly enhanced our knowledge of the supersonic transitional boundary layers. Moreover, the implications of the physical parameters on the behavior and the topology of the flow were also insightful.

This research investigation was one of the very first ventures of our Shock-Waves Research Group at CORIA, Rouen in the domain of transitional flows, and has open the following directions for the future research works:

- As presented in chapter 3, the control mechanism to counter the O-type breakdown

can be looked deeper in details. Simulations with a broader disturbance spectrum comprising higher spanwise wavenumbers  $k$  and frequencies  $h$ , modes ( $h = 1-2, k = 1-3$ ) showed that the additional streak modes generated by the control modes ( $0, k = 4, 6$ ) do not degrade the control. Therefore, the robustness of the control streaks to cope up with more complex disturbance situations must be the subject of immediate next-step investigations.

- The typical next step following the previous one would be to investigate the effectiveness of the control mode in suppressing the transition in case of slightly heated/cooled walls. It should be noted here that only slight changes of temperature should be investigated in the beginning otherwise the thermal effects would destroy the amplification of the modes.
- It would be interesting to investigate the applicability of the streak modes for higher Mach numbers i.e.  $M_\infty = 4$ , because at such regimes, second modes instabilities (Mack modes) dominate the flow.
- Some cases involving the gradual heating/cooling of the wall could also be investigated. These scenarios represent the descent/ascent phase of the aircraft. The gradual change of wall-temperature should dynamically shift the transition onset location.
- DNS with the in-flight conditions can also be performed for a cross-flow case which represents the swept-wing configuration of the supersonic aircraft.

# Bibliography

---

- Åkervik, E., Brandt, L., Henningson, D. S., Hoepffner, J., Marxen, O. & Schlatter, P. (2006), ‘Steady solutions of the navier-stokes equations by selective frequency damping’, *Physics of Fluids* **18**(6), 068102. (Cited on page 21).
- Andersson, P., Brandt, L., Bottaro, A. & Henningson, D. S. (2001), ‘On the breakdown of boundary layer streaks’, *Journal of Fluid Mechanics* **428**, 29–60. (Cited on page 24).
- Avellaneda, J., Bataille, F. & Toutant, A. (2019), ‘DNS of turbulent low mach channel flow under asymmetric high temperature gradient: Effect of thermal boundary condition on turbulence statistics’, *International Journal of Heat & Fluid Flow* **77**, 40–47. (Cited on page 26).
- Bagheri, S. & Hanifi, A. (2007), ‘The stabilizing effect of streaks on tollmien-schlichting and oblique waves: A parametric study’, *Physics of Fluids* **19**(7), 078103. (Cited on page 24).
- Barkley, D., Song, B., Mukund, V., Lemoult, G., Avila, M. & Hof, B. (2015), ‘The rise of fully turbulent flow’, *Nature* **526**(7574), 550. (Cited on page 5).
- Bechlars, P. & Sandberg, R. (2017a), ‘Evolution of the velocity gradient tensor invariant dynamics in a turbulent boundary layer’, *Journal of Fluid Mechanics* **815**, 223–242. (Cited on page 26).
- Bechlars, P. & Sandberg, R. (2017b), ‘Variation of enstrophy production and strain rotation relation in a turbulent boundary layer’, *Journal of Fluid Mechanics* **812**, 321–348. (Cited on page 26).
- Ben-Nasr, O. (2012), Étude numérique des transferts pariétaux en écoulements turbulents supersoniques, PhD thesis, INSA de Rouen, France. (Cited on pages 33, 34, 35 & 40).
- Ben-Nasr, O., Hadjadj, A., Chaudhuri, A. & Shadloo, M. (2016), ‘Assessment of subgrid-scale modeling for large-eddy simulation of a spatially-evolving compressible turbulent boundary layer’, *Computers & Fluids* . (Cited on pages 32 & 40).
- Bensayah, K., Hadjadj, A. & Bounif, A. (2014), ‘Heat transfer in turbulent boundary layers of conical and bell shaped rocket nozzles with complex wall temperature’, *Numerical Heat Transfer, Part A: Applications* **66**(3), 289–314. (Cited on page 15).
- Bernardini, M., Pirozzoli, S., Orlandi, P. & Lele, S. K. (2014), ‘Parameterization of boundary-layer transition induced by isolated roughness elements’, *AIAA Journal* **52**(10), 2261–2269. (Cited on page 20).
- Berry, S. A., Horvath, T. J., Hollis, B. R., Thompson, R. A. & Hamilton, H. H. (2001), ‘X-33 hypersonic boundary-layer transition’, *Journal of Spacecraft & Rockets* **38**(5), 646–657. (Cited on page 18).
- Bewley, T. R. (2001), ‘Flow control: new challenges for a new renaissance’, *Progress in Aerospace Sciences* **37**(1), 21–58. (Cited on page 9).

- Bippes, H. (1999), 'Basic experiments on transition in three-dimensional boundary layers dominated by crossflow instability', *Progress in Aerospace Sciences* **35**(4), 363–412. (Cited on page 9).
- Bonfigli, G. & Kloker, M. (1999), Spatial navier-stokes simulation of crossflow-induced transition in a three-dimensional boundary layer, in 'New Results in Numerical & Experimental Fluid Mechanics II', Springer, pp. 61–68. (Cited on page 10).
- Bonfigli, G. & Kloker, M. (2007), 'Secondary instability of crossflow vortices: validation of the stability theory by direct numerical simulation', *Journal of Fluid Mechanics* **583**, 229–272. (Cited on page 21).
- Chaudhuri, A., Hadjadj, A., Chinnayya, A. & Palerm, S. (2011), 'Numerical study of compressible mixing layers using high-order weno schemes', *Journal of Scientific Computing* **47**(2), 170–197. (Cited on pages 32 & 40).
- Chaudhuri, A., Hadjadj, A., Sadot, O. & Glazer, E. (2012), 'Computational study of shock-wave interaction with solid obstacles using immersed boundary methods', *International Journal for Numerical Methods in Engineering* **89**(8), 975–990. (Cited on pages 32 & 40).
- Choudhari, M., Li, F., Chang, C.-L., Edwards, J., Kegerise, M. & King, R. (2010), Laminar-turbulent transition behind discrete roughness elements in a high-speed boundary layer, in '48th AIAA aerospace sciences meeting including the new horizons forum and aerospace exposition', p. 1575. (Cited on page 21).
- Choudhari, M., Norris, A., Li, F., Chang, C.-L. & Edwards, J. (2013), Wake instabilities behind discrete roughness elements in high speed boundary layers, in '51st AIAA aerospace sciences meeting including the new horizons forum and aerospace exposition', p. 81. (Cited on page 21).
- Chu, Y.-B., Zhuang, Y.-Q. & Lu, X.-Y. (2013), 'Effect of wall temperature on hypersonic turbulent boundary layer', *Journal of Turbulence* **14**(12), 37–57. (Cited on page 28).
- Cliffe, K. A., Hall, E. J., Houston, P., Phipps, E. T. & Salinger, A. G. (2012), 'Adaptivity and a posteriori error control for bifurcation problems iii: Incompressible fluid flow in open systems with O(2) symmetry', *Journal of Scientific Computing* **52**(1), 153–179. (Cited on page 5).
- Corino, E. R. & Brodkey, R. S. (1969), 'A visual investigation of the wall region in turbulent flow', *Journal of Fluid Mechanics* **37**(1), 1–30. (Cited on page 25).
- Cossu, C. & Brandt, L. (2002), 'Stabilization of tollmien–schlichting waves by finite amplitude optimal streaks in the blasius boundary layer', *Physics of Fluids* **14**(8), L57–L60. (Cited on page 24).
- Dagenhart, J. & Mangalam, S. (1986), Disturbance functions of the görtler instability on an airfoil, in '4th Joint Fluid Mechanics, Plasma Dynamics and Lasers Conference', p. 1048. (Cited on page 5).

- De Tullio, N., Paredes, P., Sandham, N. D. & Theofilis, V. (2013), 'Laminar–turbulent transition induced by a discrete roughness element in a supersonic boundary layer', *Journal of Fluid Mechanics* **735**, 613–646. (Cited on pages 20 & 21).
- Dörr, P. C. & Kloker, M. J. (2017), 'Numerical investigations on tollmien–schlichting wave attenuation using plasma-actuator vortex generators', *AIAA Journal* **56**(4), 1305–1309. (Cited on page 25).
- Dörr, P. & Kloker, M. (2015), 'Stabilisation of a three-dimensional boundary layer by base-flow manipulation using plasma actuators', *Journal of Physics D: Applied Physics* **48**(28), 285205. (Cited on page 24).
- Duan, L., Beekman, I. & Martin, M. P. (2010), 'Direct numerical simulation of hypersonic turbulent boundary layers. part 2. effect of wall temperature', *Journal of Fluid Mechanics* **655**, 419–445. (Cited on page 15).
- Duan, L., Huang, J., Deegan, C., Choudhari, M. M., Chou, A., Radespiel, R., Ail, S., Munoz, F., Marineau, E. C., Casper, K. M. et al. (2018), Characterization of freestream disturbances in conventional hypersonic wind tunnels, in '2018 AIAA Aerospace Sciences Meeting', p. 0347. (Cited on page 18).
- Ducoin, A., Shadloo, M. & Roy, S. (2017), 'Direct numerical simulation of flow instabilities over savonius style wind turbine blades', *Renewable Energy* **105**, 374–385. (Cited on pages 5 & 6).
- Ducros, F., Ferrand, V., Nicoud, F., Weber, C., Darracq, D., Gacherieu, C. & Poinsot, T. (1999), 'Large-eddy simulation of the shock/turbulence interaction', *Journal of Computational Physics* **152**(2), 517–549. (Cited on page 37).
- Durbin, P. & Wu, X. (2007), 'Transition beneath vortical disturbances', *Annual Review of Fluid Mechanics* **39**, 107–128. (Cited on page 15).
- Fasel, H. F., Thumm, A. & Bestek, H. (1993), Direct numerical simulation of transition in supersonic boundary layers: oblique breakdown, in 'Fluids Engineering Conference', Publ by ASME, pp. 77–92. (Cited on page 13).
- Fedorov, A. (2011), 'Transition and stability of high-speed boundary layers', *Annual Review of Fluid Mechanics* **43**, 79–95. (Cited on pages viii & 18).
- Fedorov, A., Shipluk, A., Maslov, A., Burov, E. & Malmuth, N. (2003), 'Stabilization of a hypersonic boundary layer using an ultrasonically absorptive coating', *Journal of Fluid Mechanics* **479**, 99–124. (Cited on page 24).
- Fezer, A. & Kloker, M. J. (2000), Spatial direct numerical simulation of transition phenomena in supersonic flat-plate boundary layers, in 'Laminar-Turbulent Transition', Springer, pp. 415–420. (Cited on pages viii, xvi, 13, 41, 43, 44 & 126).
- Franko, K. J. & Lele, S. (2014), 'Effect of adverse pressure gradient on high speed boundary layer transition', *Physics of Fluids* **26**(2), 024106. (Cited on page 22).

- Franko, K. J. & Lele, S. K. (2013), 'Breakdown mechanisms and heat transfer overshoot in hypersonic zero pressure gradient boundary layers', *Journal of Fluid Mechanics* **730**, 491–532. (Cited on page 22).
- Fransson, J. H., Talamelli, A., Brandt, L. & Cossu, C. (2006), 'Delaying transition to turbulence by a passive mechanism', *Physical Review Letters* **96**(6), 064501. (Cited on pages 15 & 24).
- Friederich, T. & Kloker, M. J. (2012), 'Control of the secondary cross-flow instability using localized suction', *Journal of Fluid Mechanics* **706**, 470–495. (Cited on page 24).
- Görtler, H. (1940), Über eine dreidimensionale Instabilität laminarer Grenzschichten an konkaven Wänden, PhD thesis, Vandenhoeck & Ruprecht. (Cited on page 5).
- Groskopf, G. & Kloker, M. J. (2012), 'Stability analysis of three-dimensional hypersonic boundary-layer flows with discrete surface roughness', *Univ. of Stuttgart, NATO RTO-MP-AVT-200-30, Stuttgart, Germany* pp. 1–19. (Cited on page 21).
- Groskopf, G. & Kloker, M. J. (2016), 'Instability and transition mechanisms induced by skewed roughness elements in a high-speed laminar boundary layer', *Journal of Fluid Mechanics* **805**, 262–302. (Cited on pages 20 & 69).
- Groskopf, G., Kloker, M. J. & Marxen, O. (2010), Bi-global crossplane stability analysis of high-speed boundary-layer flows with discrete roughness, in 'Seventh IUTAM Symposium on Laminar-Turbulent Transition', Springer, pp. 171–176. (Cited on page 21).
- Hadjadj, A., Ben-Nasr, O., Shadloo, M. & Chaudhuri, A. (2015), 'Effect of wall temperature in supersonic turbulent boundary layers: A numerical study', *International Journal of Heat & Mass Transfer* **81**, 426–438. (Cited on pages 27 & 40).
- Haynes, T. & Reed, H. (1996), Computations in nonlinear saturation of stationary crossflow vortices in a swept-wing boundary layer, in '34th Aerospace Sciences Meeting and Exhibit', p. 182. (Cited on page 10).
- Haynes, T. S. & Reed, H. L. (2000), 'Simulation of swept-wing vortices using nonlinear parabolized stability equations', *Journal of Fluid Mechanics* **405**, 325–349. (Cited on page 10).
- Head, M. & Bandyopadhyay, P. (1981), 'New aspects of turbulent boundary-layer structure', *Journal of Fluid Mechanics* **107**, 297–338. (Cited on page 25).
- Henrick, A. K., Aslam, T. D. & Powers, J. M. (2005), 'Mapped weighted essentially non-oscillatory schemes: achieving optimal order near critical points', *Journal of Computational Physics* **207**(2), 542–567. (Cited on page 33).
- Herbert, T. (1988), 'Secondary instability of boundary layers', *Annual Review of Fluid Mechanics* **20**(1), 487–526. (Cited on pages 10 & 11).
- Horvath, T., Berry, S., Hollis, B., Singer, B. & Chang, C.-L. (2002), Boundary layer transition on slender cones in conventional and low disturbance mach 6 wind tunnels, in '32nd AIAA Fluid Dynamics Conference and Exhibit', p. 2743. (Cited on page 18).

- Hultgren, L. S. & Gustavsson, L. H. (1981), 'Algebraic growth of disturbances in a laminar boundary layer', *Physics of Fluids* **24**(6), 1000–1004. (Cited on page 10).
- Jameson, A., Schmidt, W. & Turkel, E. (1981), Numerical solution of the euler equations by finite volume methods using runge kutta time stepping schemes, in '14th Fluid and Plasma Dynamics Conference', p. 1259. (Cited on page 37).
- Janke, E. & Balakumar, P. (2000), 'On the secondary instability of three-dimensional boundary layers', *Theoretical & Computational Fluid Dynamics* **14**(3), 167–194. (Cited on page 10).
- Jiang, G.-S. & Shu, C.-W. (1996), 'Efficient implementation of weighted eno schemes', *Journal of Computational Physics* **126**(1), 202–228. (Cited on pages 32, 33 & 34).
- Joslin, R. D., Erlebacher, G. & Hussaini, M. Y. (1996), 'Active control of instabilities in laminar boundary layers-overview and concept validation', *Journal of Fluids Engineering* **118**(3), 494–497. (Cited on page 9).
- Kawakami, M., Kohama, Y. & Okutsu, M. (1999), Stability characteristics of stationary crossflow vortices in three-dimensional boundary layer, in '37th Aerospace Sciences Meeting and Exhibit', p. 811. (Cited on page 9).
- Kendall, J. (1985), Experimental study of disturbances produced in a pre-transitional laminar boundary layer by weak freestream turbulence, in '18th Fluid Dynamics and Plasma-dynamics and Lasers Conference', p. 1695. (Cited on page 11).
- Kim, J. & Bewley, T. R. (2007), 'A linear systems approach to flow control', *Annual Review of Fluid Mechanics* **39**, 383–417. (Cited on page 9).
- Klebanoff, P. S. (1971), Effect of free-stream turbulence on a laminar boundary layer, in 'Bulletin of the American Physical Society', Vol. 16, AMER INST PHYSICS 1305 WALT WHITMAN RD, STE 300, MELVILLE, NY 11747-4501 USA, pp. 1323–+. (Cited on page 11).
- Klebanoff, P. S., Tidstrom, K. D. & Sargent, L. M. (1962), 'The three-dimensional nature of boundary-layer instability', *Journal of Fluid Mechanics* **12**(1), 1–34. (Cited on page 11).
- Kleiser, L. & Zang, T. A. (1991), 'Numerical simulation of transition in wall-bounded shear flows', *Annual Review of Fluid Mechanics* **23**(1), 495–537. (Cited on pages 8 & 9).
- Kloker, M. (2002), 'DNS of transitional boundary-layer flows at sub-and hypersonic speeds', *DGLR Paper JT2002-017, DGLR-Jahrestagung, Stuttgart* . (Cited on pages viii & 20).
- Kloker, M. (2008), Advanced laminar flow control on a swept wing-useful crossflow vortices and suction, in '38th Fluid dynamics conference and exhibit', p. 3835. (Cited on page 24).
- Kloker, M. J. (2018), 'Mechanisms of laminar-to-turbulent transition', *Lecture notes, Institute of Aerodynamics and Gas Dynamics, University of Stuttgart* . (Cited on pages viii, 11, 15, 17, 19, 20 & 24).

- Koch, W., Bertolotti, F. P., Stolte, A. & Hein, S. (2000), 'Nonlinear equilibrium solutions in a three-dimensional boundary layer and their secondary instability', *Journal of Fluid Mechanics* **406**, 131–174. (Cited on pages 10 & 21).
- Kohama, Y., Saric, W. S. & Hoos, J. A. (1991), 'A high-frequency, secondary instability of crossflow vortices that leads to transition'. (Cited on page 9).
- Kosinov, A. D., Semionov, N. V., Shevel'kov, S. G. & Zinin, O. I. (1994), Experiments on the nonlinear instability of supersonic boundary layers, in 'Nonlinear instability of nonparallel flows', Springer, pp. 196–205. (Cited on page 13).
- Kosinov, A., Maslov, A. & Semionov, N. (1997), 'An experimental study of generation of unstable disturbances on the leading edge of a plate at  $M=2$ ', *Journal of Applied Mechanics and Technical Physics* **38**(1), 45–51. (Cited on page 18).
- Kubacki, S., Jonak, P. & Dick, E. (2019), 'Evaluation of an algebraic model for laminar-to-turbulent transition on secondary flow loss in a low-pressure turbine cascade with an endwall', *International Journal of Heat & Fluid Flow* **77**, 98–112. (Cited on page 5).
- Kurz, H. B. E. & Kloker, M. J. (2016), 'Mechanisms of flow tripping by discrete roughness elements in a swept-wing boundary layer', *Journal of Fluid Mechanics* **796**, 158–194. (Cited on page 10).
- Kutz, J., Grosek, J., Fu, X. & Brunton, S. (2015), Multi-resolution time-scale separation of video content using the dynamic mode decomposition, in 'International Workshop on Video Processing and Quality Metrics for Consumer Electronic, VPQM 2015'. (Cited on page 23).
- Laible, A. C. & Fasel, H. F. (2016), 'Continuously forced transient growth in oblique breakdown for supersonic boundary layers', *Journal of Fluid Mechanics* **804**, 323–350. (Cited on pages 13 & 19).
- Le, A.-T., Coleman, G. N. & Kim, J. (2000), 'Near-wall turbulence structures in three-dimensional boundary layers', *International Journal of Heat & Fluid Flow* **21**(5), 480–488. (Cited on page 26).
- Lebon, B., Nguyen, M. Q., Peixinho, J., Shadloo, M. S. & Hadjadj, A. (2018), 'A new mechanism for periodic bursting of the recirculation region in the flow through a sudden expansion in a circular pipe', *Physics of Fluids* **30**(3), 031701. (Cited on pages viii, 5 & 6).
- Lechner, R., Sesterhenn, J. R. & Friedrich, R. (2001), 'Turbulent supersonic channel flow', *Journal of Turbulence* **2**(1), 001–001. (Cited on page 27).
- Lee, J., Jung, S. Y., Sung, H. J. & Zaki, T. A. (2013), 'Effect of wall heating on turbulent boundary layers with temperature-dependent viscosity', *Journal of Fluid Mechanics* **726**, 196–225. (Cited on page 21).
- Lerche, T. (1996), Experimental investigation of nonlinear wave interactions and secondary instability in three-dimensional boundary-layer flow, in 'Advances in Turbulence VI', Springer, pp. 357–360. (Cited on page 9).

- Li, W. & Xi-Yun, L. (2011), ‘Statistical analysis of coherent vortical structures in a supersonic turbulent boundary layer’, *Chinese Physics Letters* **28**(3), 034703. (Cited on page 26).
- Mack, L. M. (1984), Boundary-layer linear stability theory, Technical report, CALIFORNIA INST OF TECH PASADENA JET PROPULSION LAB. (Cited on page 19).
- Mack, L. M. (1987), Review of linear compressible stability theory, in ‘Stability of time dependent and spatially varying flows’, Springer, pp. 164–187. (Cited on page 19).
- Maeder, T., Adams, N. A. & Kleiser, L. (2001), ‘Direct simulation of turbulent supersonic boundary layers by an extended temporal approach’, *Journal of Fluid Mechanics* **429**, 187–216. (Cited on page 27).
- Malik, M., Li, F. & Chang, C.-L. (1994), ‘Crossflow disturbances in three-dimensional boundary layers: nonlinear development, wave interaction and secondary instability’, *Journal of Fluid Mechanics* **268**, 1–36. (Cited on page 10).
- Malik, M. R., Li, F., Choudhari, M. M. & Chang, C.-L. (1999), ‘Secondary instability of crossflow vortices and swept-wing boundary-layer transition’, *Journal of Fluid Mechanics* **399**, 85–115. (Cited on page 10).
- Martín, M. P., Taylor, E. M., Wu, M. & Weirs, V. G. (2006), ‘A bandwidth-optimized weno scheme for the effective direct numerical simulation of compressible turbulence’, *Journal of Computational Physics* **220**(1), 270–289. (Cited on page 33).
- Marxen, O., Iaccarino, G. & Shaqfeh, E. S. (2010), ‘Disturbance evolution in a mach 4.8 boundary layer with two-dimensional roughness-induced separation and shock’, *Journal of Fluid Mechanics* **648**, 435–469. (Cited on page 21).
- Masatsuka, K. (2009), ‘I do like cfd’, *Published by Katate Masatsuka* . (Cited on page 39).
- Mayer, C. S. J., Wernz, S. & Fasel, H. F. (2011), ‘Numerical investigation of the nonlinear transition regime in a mach 2 boundary layer’, *Journal of Fluid Mechanics* **668**, 113–149. (Cited on pages xvi, 13, 41, 43 & 126).
- Méndez, M., Shadloo, M., Hadjadj, A. & Ducoin, A. (2018), ‘Boundary layer transition over a concave surface caused by centrifugal instabilities’, *Computers & Fluids* **171**, 135–153. (Cited on page 6).
- Moin, P. & Bewley, T. (1994), ‘Feedback control of turbulence’, *Applied Mechanics Reviews* **47**(6S), S3–S13. (Cited on page 9).
- Morkovin, M. (1994), ‘Transition in open flow systems-a reassessment’, *Bulletin of American Physical Society* **39**, 1882. (Cited on pages viii & 18).
- Morkovin, M. V. (1962), ‘Effects of compressibility on turbulent flows’, *Mécanique de la Turbulence* **367**, 380. (Cited on page 26).
- Mouronval, A.-S. (2004), Étude numérique des phénomènes aéroélastiques en aérodynamique supersonique. Application aux tuyères propulsives, PhD thesis, INSA de Rouen, France. (Cited on page 38).

- Ngomo, D., Chaudhuri, A., Chinnayya, A. & Hadjadj, A. (2010), 'Numerical study of shock propagation and attenuation in narrow tubes including friction and heat losses', *Computers & Fluids* **39**(9), 1711–1721. (Cited on page 32).
- Nolan, K. P. & Zaki, T. A. (2013), 'Conditional sampling of transitional boundary layers in pressure gradients', *Journal of Fluid Mechanics* **728**, 306–339. (Cited on page 10).
- Oliveira, P. J. & Pinho, F. T. d. (1997), 'Pressure drop coefficient of laminar newtonian flow in axisymmetric sudden expansions', *International Journal of Heat & Fluid Flow* **18**(5), 518–529. (Cited on page 5).
- Ong, L. & Wallace, J. M. (1998), 'Joint probability density analysis of the structure and dynamics of the vorticity field of a turbulent boundary layer', *Journal of Fluid Mechanics* **367**, 291–328. (Cited on pages xix, 26 & 129).
- Paredes, P., Choudhari, M. M. & Li, F. (2017), 'Instability wave–streak interactions in a supersonic boundary layer', *Journal of Fluid Mechanics* **831**, 524–553. (Cited on pages 24, 25 & 69).
- Patel, A., Boersma, B. J. & Pecnik, R. (2017), 'Scalar statistics in variable property turbulent channel flows', *Physical Review Fluids* **2**(8), 084604. (Cited on page 27).
- Peixinho, J. & Mullin, T. (2007), 'Finite-amplitude thresholds for transition in pipe flow', *Journal of Fluid Mechanics* **582**, 169–178. (Cited on page 5).
- Piquet, A. (2017), Physical analysis and numerical simulation of the separation phenomenon in over-expanded nozzle flow, PhD thesis, INSA de Rouen, France. (Cited on pages 38 & 40).
- Pirozzoli, S. (2010), 'Generalized conservative approximations of split convective derivative operators', *Journal of Computational Physics* **229**(19), 7180–7190. (Cited on pages 32, 34, 35, 36 & 37).
- Pirozzoli, S. (2011), 'Numerical methods for high-speed flows', *Annual Review of Fluid Mechanics* **43**, 163–194. (Cited on page 38).
- Pirozzoli, S., Bernardini, M. & Grasso, F. (2008), 'Characterization of coherent vortical structures in a supersonic turbulent boundary layer', *Journal of Fluid Mechanics* **613**, 205–231. (Cited on page 27).
- Pirozzoli, S., Grasso, F. & Gatski, T. (2004), 'Direct numerical simulation and analysis of a spatially evolving supersonic turbulent boundary layer at  $M=2.25$ ', *Physics of fluids* **16**(3), 530–545. (Cited on pages 27 & 41).
- Radeztsky, R. H., Reibert, M. S. & Saric, W. S. (1999), 'Effect of isolated micron-sized roughness on transition in swept-wing flows', *AIAA journal* **37**(11), 1370–1377. (Cited on page 9).
- Reda, D. C., Wilder, M. C. & Prabhu, D. K. (2010), 'Transition experiments on blunt bodies with isolated roughness elements in hypersonic flight', *Journal of Spacecraft & Rockets* **47**(5), 828–835. (Cited on page 18).

- Redford, J. A., Sandham, N. D. & Roberts, G. T. (2011), 'Direct numerical simulation of transitional flow at high mach number coupled with a thermal wall model', *Computers & Fluids* **45**(1), 37–46. (Cited on page 22).
- Redford, J. A., Sandham, N. D. & Roberts, G. T. (2012), 'Numerical simulations of turbulent spots in supersonic boundary layers: Effects of mach number and wall temperature', *Progress in Aerospace Sciences* **52**, 67–79. (Cited on page 21).
- Reed, H. L., Haynes, T. S. & Saric, W. S. (1998), 'Computational fluid dynamics validation issues in transition modeling', *AIAA journal* **36**(5), 742–751. (Cited on page 10).
- Reibert, M., Saric, W., Carrillo, Jr, R. & Chapman, K. (1996), Experiments in nonlinear saturation of stationary crossflow vortices in a swept-wing boundary layer, in '34th Aerospace Sciences Meeting and Exhibit', p. 184. (Cited on page 9).
- Reibert, M., Saric, W., Reibert, M. & Saric, W. (1997), Review of swept-wing transition, in '28th Fluid Dynamics Conference', p. 1816. (Cited on page 9).
- Ren, J. & Fu, S. (2015), 'Secondary instabilities of görtler vortices in high-speed boundary layer flows', *Journal of Fluid Mechanics* **781**, 388–421. (Cited on page 6).
- Rennels, D. C. & Hudson, H. M. (2012), *Pipe flow: A practical and comprehensive guide*, John Wiley & Sons. (Cited on page 5).
- Reynolds, O. (1883), 'Xxix. an experimental investigation of the circumstances which determine whether the motion of water shall be direct or sinuous, and of the law of resistance in parallel channels', *Philosophical Transactions of the Royal society of London* **174**, 935–982. (Cited on page 5).
- Ricco, P., Tran, D. & Ye, G. (2009), 'Wall heat transfer effects on klebanoff modes and tollmien-schlichting waves in a compressible boundary layer', *Physics of Fluids* **21**(2), 024106. (Cited on page 22).
- Sanmiguel-Rojas, E., Del Pino, C. & Gutiérrez-Montes, C. (2010), 'Global mode analysis of a pipe flow through a 1: 2 axisymmetric sudden expansion', *Physics of Fluids* **22**(7), 071702. (Cited on page 5).
- Saric, W. S., Carrillo, R. B. & Reibert, M. S. (1998), 'Nonlinear stability and transition in 3-d boundary layers', *Meccanica* **33**(5), 469–487. (Cited on page 9).
- Saric, W. S., Reed, H. L. & Kerschen, E. J. (2002), 'Boundary-layer receptivity to freestream disturbances', *Annual Review of Fluid Mechanics* **34**(1), 291–319. (Cited on pages viii, 13 & 15).
- Saric, W. S., Reed, H. L. & White, E. B. (2003), 'Stability and transition of three-dimensional boundary layers', *Annual Review of Fluid Mechanics* **35**(1), 413–440. (Cited on page 24).
- Sayadi, T., Hamman, C. W. & Moin, P. (2013), 'Direct numerical simulation of complete h-type and k-type transitions with implications for the dynamics of turbulent boundary layers', *Journal of Fluid Mechanics* **724**, 480–509. (Cited on pages viii, 12 & 14).

- Schmid, P. J. (2010), 'Dynamic mode decomposition of numerical and experimental data', *Journal of fluid mechanics* **656**, 5–28. (Cited on page 23).
- Schmidt, O. T. & Rist, U. (2011), 'Linear stability of compressible flow in a streamwise corner', *Journal of Fluid Mechanics* **688**, 569–590. (Cited on page 21).
- Schneider, S. P. (2001), 'Effects of high-speed tunnel noise on laminar-turbulent transition', *Journal of Spacecraft & Rockets* **38**(3), 323–333. (Cited on page 18).
- Schneider, S. P. (2008), 'Effects of roughness on hypersonic boundary-layer transition', *Journal of Spacecraft & Rockets* **45**(2), 193–209. (Cited on page 21).
- Schrader, L.-U., Brandt, L. & Zaki, T. A. (2011), 'Receptivity, instability and breakdown of Görtler flow', *Journal of Fluid Mechanics* **682**, 362–396. (Cited on page 6).
- Schubauer, G. B. & Skramstad, H. K. (1947), 'Laminar boundary-layer oscillations and stability of laminar flow', *Journal of the Aeronautical Sciences* **14**(2), 69–78. (Cited on page 8).
- Selvam, K., Peixinho, J. & Willis, A. P. (2015), 'Localised turbulence in a circular pipe flow with gradual expansion', *Journal of Fluid Mechanics* **771**. (Cited on page 5).
- Shadloo, M., Hadjadj, A. & Chaudhuri, A. (2014), 'On the onset of postshock flow instabilities over concave surfaces', *Physics of Fluids* **26**(7), 076101. (Cited on page 40).
- Shadloo, M., Hadjadj, A. & Hussain, F. (2015), 'Statistical behavior of supersonic turbulent boundary layers with heat transfer at  $M_\infty = 2$ ', *International Journal of Heat & Fluid Flow* **53**, 113–134. (Cited on pages 27 & 40).
- Shadloo, M. S. & Hadjadj, A. (2017), 'Laminar-turbulent transition in supersonic boundary layers with surface heat transfer: A numerical study', *Numerical Heat Transfer, Part A: Applications* pp. 1–14. (Cited on pages xvii, xviii, 23, 28 & 127).
- Shadloo, M. S., Hadjadj, A., Bodony, D. J., Hussain, F. & Lele, S. K. (2016), Effects of heat transfer on transitional states of supersonic boundary layers, in 'Proceedings of Summer program', Center of Turbulence Research, Stanford University, USA, pp. 175–184. (Cited on pages xviii, 22, 28 & 127).
- Shahinfar, S., Sattarzadeh, S. S., Fransson, J. H. M. & Talamelli, A. (2012), 'Revival of classical vortex generators now for transition delay', *Physical Review Letters* **109**(7), 074501. (Cited on page 24).
- Sharma, S. & Ducoin, A. (2018), 'Direct numerical simulation of the effect of inlet isotropic turbulence on centrifugal instabilities over a curved wall', *Computers & Fluids* **174**, 1–13. (Cited on pages viii, 6 & 7).
- Sharma, S., Shadloo, M. & Hadjadj, A. (2018a), 'Laminar-to-turbulent transition in supersonic boundary layer: Effects of initial perturbation and wall heat-transfer', *Numerical Heat Transfer, Part A: Applications* **73**(9), 583–603. (Cited on pages xv, xviii, 23, 28, 29 & 128).

- Sharma, S., Shadloo, M. S. & Hadjadj, A. (2018b), 'Effect of thermo-mechanical non-equilibrium on the onset of transition in supersonic boundary layers', *Heat & Mass Transfer* pp. 1–13. (Cited on pages [xv](#), [xviii](#), [xix](#), [23](#), [29](#), [128](#) & [129](#)).
- Sharma, S., Shadloo, M. S. & Hadjadj, A. (2019), 'Turbulent flow topology in supersonic boundary layer with wall heat transfer', *International Journal of Heat & Fluid Flow* **78**, 1–19. (Cited on pages [xv](#), [xix](#), [29](#) & [129](#)).
- Sharma, S., Shadloo, M. S., Hadjadj, A. & Kloker, M. J. (2019), 'Control of oblique-type breakdown in a supersonic boundary layer employing streaks', *Journal of Fluid Mechanics* **873**, 1072–1089. (Cited on pages [xv](#), [xvii](#), [29](#) & [127](#)).
- Smits, A. J. & Dussauge, J.-P. (2006), *Turbulent shear layers in supersonic flow*, Springer Science & Business Media. (Cited on page [26](#)).
- Soni, V. (2016), Parallel adaptive multiscale numerical methods for complex compressible flows, PhD thesis, INSA de Rouen, France. (Cited on pages [38](#) & [40](#)).
- Soni, V., Hadjadj, A., Chaudhuri, A. & Ben-Dor, G. (2017), 'Shock-wave reflections over double-concave cylindrical reflectors', *Journal of Fluid Mechanics* **813**, 70–84. (Cited on page [40](#)).
- Spina, E. F., Smits, A. J. & Robinson, S. K. (1994), 'The physics of supersonic turbulent boundary layers', *Annual Review of Fluid Mechanics* **26**(1), 287–319. (Cited on page [26](#)).
- Stanislas, M., Perret, L. & Foucaut, J.-M. (2008), 'Vortical structures in the turbulent boundary layer: a possible route to a universal representation', *Journal of Fluid Mechanics* **602**, 327–382. (Cited on page [25](#)).
- Sundaram, P., Sengupta, T. K. & Sengupta, S. (2019), 'Is tollmien-schlichting wave necessary for transition of zero pressure gradient boundary layer flow?', *Physics of Fluids* **31**(3), 031701. (Cited on page [10](#)).
- Tandiono, T., Winoto, S. & Shah, D. (2013), 'Spanwise velocity component in nonlinear region of görtler vortices', *Physics of Fluids* **25**(10), 104104. (Cited on page [6](#)).
- Tandiono, W. & Shah, D. (2009), 'Wall shear stress in görtler vortex boundary layer flow', *Physics of Fluids* **21**(8). (Cited on page [6](#)).
- Theodorsen, T. (1952), Mechanisms of turbulence, in 'Proceedings of the 2<sup>nd</sup> Midwestern Conference on Fluid Mechanics, 1952'. (Cited on page [25](#)).
- Theofilis, V. (2011), 'Global linear instability', *Annual Review of Fluid Mechanics* **43**, 319–352. (Cited on page [21](#)).
- Thomas, A. S. (1983), 'The control of boundary-layer transition using a wave-superposition principle', *Journal of Fluid Mechanics* **137**, 233–250. (Cited on page [9](#)).
- Thomas, A. S. (1990), 'Active wave control of boundary-layer transition', *Viscous drag reduction in boundary layers* **123**. (Cited on page [9](#)).

- Thumm, A. (1991), 'Numerische untersuchungen zum laminar-turbulenten strömungsumschlag in transsonischen grenzschnittströmungen', *Dr.-Ing. dissertation, Inst. for Aerodynamics and Gasdynamics, University of Stuttgart* . (Cited on page 13).
- Tong, F., Tang, Z., Yu, C., Zhu, X. & Li, X. (2017), 'Numerical analysis of shock wave and supersonic turbulent boundary interaction between adiabatic and cold walls', *Journal of Turbulence* pp. 1–20. (Cited on page 27).
- Trettel, A. & Larsson, J. (2016), 'Mean velocity scaling for compressible wall turbulence with heat transfer', *Physics of Fluids* **28**(2), 026102. (Cited on page 27).
- Tu, J. H., Rowley, C. W., Luchtenburg, D. M., Brunton, S. L. & Kutz, J. N. (2013), 'On dynamic mode decomposition: theory and applications', *arXiv preprint arXiv:1312.0041* . (Cited on page 23).
- Tutar, M. & Sönmez, Ü. (2010), 'The computational modeling of transitional flow through a transonic linear turbine: comparative performance of various turbulence models', *Numerical Heat Transfer, Part A: Applications* **58**(5), 403–427. (Cited on page 15).
- UNFCCC (2015), 'Adoption of the paris agreement (fccc/cp/2015/l. 9/rev. 1)', *United Nations Framework Convention on Climate Change* . (Cited on pages xiv & 2).
- Van den Eynde, J. P. J. P. & Sandham, N. D. (2015), 'Numerical simulations of transition due to isolated roughness elements at mach 6', *AIAA Journal* **54**(1), 53–65. (Cited on page 20).
- Wadhams, T. P., Mundy, E., MacLean, M. G. & Holden, M. S. (2008), 'Ground test studies of the hifire-1 transition experiment part 1: experimental results', *Journal of Spacecraft & Rockets* **45**(6), 1134–1148. (Cited on page 22).
- Wagner, A., Hannemann, K. & Kuhn, M. (2014), 'Ultrasonic absorption characteristics of porous carbon-carbon ceramics with random microstructure for passive hypersonic boundary layer transition control', *Experiments in fluids* **55**(6), 1750. (Cited on page 24).
- Wallace, J. M. & Brodkey, R. S. (1977), 'Reynolds stress and joint probability density distributions in the u-v plane of a turbulent channel flow', *The Physics of Fluids* **20**(3), 351–355. (Cited on page 26).
- Wallace, J. M., Eckelmann, H. & Brodkey, R. S. (1972), 'The wall region in turbulent shear flow', *Journal of Fluid Mechanics* **54**(1), 39–48. (Cited on pages xix, 25 & 129).
- Wassermann, P. & Kloker, M. (2000), Dns-investigations of the development and control of crossflow vortices in a 3-d boundary-layer flow, in 'Laminar-Turbulent Transition', Springer, pp. 565–570. (Cited on page 24).
- Wassermann, P. & Kloker, M. J. (2002), 'Mechanisms and passive control of crossflow-vortex-induced transition in a three-dimensional boundary layer', *Journal of Fluid Mechanics* **456**, 49–84. (Cited on pages 9, 24 & 25).
- White, E. B. & Saric, W. S. (2005), 'Secondary instability of crossflow vortices', *Journal of Fluid Mechanics* **525**, 275–308. (Cited on page 9).

- White, E., Saric, W., Gladden, R. & Gabet, P. (2001), Stages of swept-wing transition, in '39th Aerospace Sciences Meeting and Exhibit', p. 271. (Cited on page 9).
- White, F. M. & Corfield, I. (2006), *Viscous fluid flow*, Vol. 3, McGraw-Hill New York. (Cited on pages viii, 19 & 39).
- Willmarth, W. & Lu, S. (1972), 'Structure of the reynolds stress near the wall', *Journal of Fluid Mechanics* **55**(1), 65–92. (Cited on page 26).
- Wu, X. & Moin, P. (2009), 'Direct numerical simulation of turbulence in a nominally zero-pressure-gradient flat-plate boundary layer', *Journal of Fluid Mechanics* **630**, 5–41. (Cited on page 25).
- Zaki, T. A. (2013), 'From streaks to spots and on to turbulence: exploring the dynamics of boundary layer transition', *Flow, Turbulence & combustion* **91**(3), 451–473. (Cited on page 13).
- Zaki, T. A., Liu, Y. & Durbin, P. A. (2010), Boundary layer transition by interaction of streaks and tollmien–schlichting waves, in 'Seventh IUTAM Symposium on Laminar-Turbulent Transition', Springer, pp. 439–444. (Cited on page 10).
- Zhang, C., Duan, L. & Choudhari, M. M. (2017), 'Effect of wall cooling on boundary-layer-induced pressure fluctuations at mach 6', *Journal of Fluid Mechanics* **822**, 5–30. (Cited on page 27).
- Zhang, M. & Zheng, Z. C. (2018), Analysis of wakes downstream of a heaving airfoil by decomposition methods, in '2018 Fluid Dynamics Conference', p. 2904. (Cited on page 23).